

Analytical Formalism to Study the 21 cm Signal from Cosmic Dawn and Epoch of Reionization

A Thesis

Submitted for the Degree of

Doctor of Philosophy

in the Faculty of Science

by

Janakee Raste



Joint Astronomy Programme
Department of Physics
Indian Institute of Science
Bengaluru – 560 012 (INDIA)

June, 2019

© Janakee Raste

June 2019


All rights reserved

Declaration

I, Janakee Raste, hereby declare that the work presented in this thesis titled “Analytical Formalism to Study the 21 cm Signal from Cosmic Dawn and Epoch of Reionization” is entirely original. This work has been carried out by me under the supervision of Prof. Shiv Sethi (Raman Research Institute) and Prof. Tarun Deep Saini (Indian Institute of Science) at the Department of Astronomy and Astrophysics, Raman Research Institute under the Joint Astronomy Program hosted by the Department of Physics, Indian Institute of Science.

I further declare that the subject matter presented in this thesis has not previously formed the basis for the award of any degree, diploma, membership, associateship or any other similar title of any university or institution.

Department of Physics
Indian Institute of Science
Bengaluru-560012
India


Janakee Raste
Date: November 14, 2019

To my parents...

Acknowledgements

I was ten years old when I decided that I wanted to become an Astrophysicist. I am grateful to everyone who has since then supported my dream and has helped me fulfill it. I begin with thanking my parents for believing in me and supporting me in every way possible. Their love, support and wisdom have always been my biggest strength.

I am grateful to my Ph.D. guide Prof. Shiv Sethi for insightful lectures and discussions on various areas of physics. I thank him for encouraging me to work on projects of my interest, bearing with my unusual working schedule and counselling me during challenging times. Over the past six years, I have been able to learn many things from him during many academic and non-academic discussions and arguments. He claims that one's Ph.D. is not over until one comes to hate their guide; fortunately, it is only his opinion and not a formal requirement. I am really lucky to have him as my advisor.

I thank Prof. Biman Nath and Prof. S. Sridhar for providing constructive criticism of my work as part of my academic advisory committee and for sending reference letters for me. I thank them as well as Prof. Tarun Deep Saini, Prof. Joseph Samuel and Prof. Pravabati Chingangbam for their excellent introduction to various fields of astrophysics and cosmology during course work. I have often turned back to their notes and lectures during my research work. I express my gratitude to Prof. Steven Furlanetto for providing valuable comments and criticism on my research work and for sending reference letters for post-doctoral applications.

Saurabh, thanks for bearing with my weirdness for years and for helping me through every new phase of Ph.D. life. Akash, thanks for helping me through tough times. I admire you for your philosophy of life (or the lack of it) and I am fortunate to have been able to learn many things from you - from watching animes to solving quantum mechanics. I thank both of you for countless stimulating discussion on almost anything in and out of this world. Thank you for lending an ear, irrespective of whether I was rehearsing talks or having disheartened rant about life, and for always providing constructive criticism.

Anirudh, I am grateful to you for being an amazing friend who has stood by me and helped me through every phase of life. I will miss the time spent with you over five years; without you, Ph.D. life would have been surely difficult. I thank my seniors Nazma, Meera, Abir, Karam, and Anjan for always providing advice and support. Ravi, thanks for discussions and occasional coffee during late working hours. Priyanka, Kshitija, Nancy, Sanhita, Ranita, Palak, Shruti, Samskruthi and Sindhu, I thank all of you multi-talented girls for friendship and inspiration over the years. From exotic dark chocolates to home-cooked food, from singing and dancing to movies, from trekking to shopping, I have been fortunate to have had your company.

Acknowledgements

Aditi, I admire you for teaching me to look at life from different perspectives and for clicking great pictures, writing great poems and cracking jokes (great and otherwise). Manami and Gunjan, thank you for always bringing a smile to people and making awesome coffee. Varun, Raj, Siddhartha and Chaitanya, I have had so much fun celebrating festivals and other special occasions with you, especially with the unique dancing and singing styles which all of you have. Mugundhan, thanks for having discussions on books and regular ice-cream trips. To everyone at RRI, I will miss our discussions at tea-time, side trips during conferences, visits to Sankey Tank, freshers trips, celebrating in-house cultural evening and festivals. Thank you all for helping me maintain my sanity and enthusiasm over the past six years.

I thank Akanksha, Sandeep, and many many people whom I met during conferences and schools; you all made these events memorable. Prasun da and Nirupam da, thank you for being sources of inspiration, knowledge and occasional treats. Jordan, I enjoyed discussing my work with you; your comments were very helpful.

Finally, I express my gratitude to all teachers, doctors, cooks, administrative and library staff, security guards, friends, family, and strangers, who have helped me through this awesome adventure of Ph.D.

Synopsis

The epoch of cosmic dawn and reionization (CD/EoR) is one of the most important time periods of the history of the universe when the first sources of radiation like stars and galaxies were formed. These sources emitted a wide spectrum of radiation and changed the properties of their surrounding medium. This epoch is not completely understood theoretically and is poorly constrained with observations. 21 cm radiation emitted due to the hyperfine splitting of neutral hydrogen (HI) is one of the most important probes to study the state and dynamics of the neutral medium during this epoch. In this thesis, we present an analytical formalism to study the fluctuating component of the HI signal from the epoch of cosmic dawn and reionization.

We use excursion set formalism to calculate the size distribution of randomly distributed self-ionized regions. These ionization bubbles are surrounded by isotropically heated neutral regions. The spin temperature (T_S) of HI in these regions might be fully or partially coupled to the kinetic temperature of the medium. We model the ionization, X-ray heating, and Lyman- α coupling using five parameters: efficiency of ionization (ζ), number of X-ray photons emitted per stellar baryon (N_{heat}), the spectral index of X-ray photons (α), minimum frequency of X-ray photons (ν_{min}), and the ratio of source luminosity of Lyman- α to ionizing photon (f_L).

We develop a formalism to compute the two-point correlation function for this topology, taking into account the autocorrelation of the ionization field and spin temperature field, and cross-correlation between ionization and spin temperature. Using geometric and probabilistic arguments, we compute the global HI signal, its autocorrelation and power spectrum in the redshift range $10 \leq z \leq 30$ for the Λ CDM model. We check the validity of this formalism for various limits and simplified cases and develop a few toy models to explore the results more intuitively.

Our results agree reasonably well with existing results from N -body simulations in spite of following an entirely different approach and requiring orders of magnitude less computational power and time. We further apply our formalism to study the fluctuating component corresponding to the recent EDGES observation that shows an unexpectedly deep absorption trough in global HI signal in the redshift range $15 < z < 19$. We show that, generically, this observation predicts larger signal in this redshift range, but smaller signal at higher redshifts. We also explore the possibility of negative real-space auto-correlation of spin temperature in the early universe.

Chapter 1: Introduction

In the first chapter, we explore the current observational bounds on the early history of the universe and their theoretical implications. We briefly present current theoretical understanding of how the large scale structures collapsed and first sources of radiation were formed within them. We list the expected properties of these first sources and their effect on their surrounding medium. We summarise the excursion set formalism used in our work to find the size distribution of isolated ionization bubbles at any redshift. We also discuss the hyperfine line splitting of neutral hydrogen and the mechanisms that affect the population of these two states, and hence the spin temperature of HI; these mechanisms are background radiation, collisions, and Lyman- α photons. We conclude with listing ongoing effort to theoretically understand the epoch of CD/EoR through simulations and analytical methods.

Chapter 2: Temperature Evolution of the IGM

In this chapter, we compute X-ray heating of the intergalactic medium (IGM) surrounding the ionization bubbles due to photoionization of neutral atoms. We calculate the temperature evolution at a point as a function of its distance from the centre of the X-ray source. We also compute the background temperature evolution due to the combined effect of all the faraway sources. Since the X-rays have a large mean free path, the temperature profiles are large; therefore, we explore various possible methods to truncate these profiles while allowing them to overlap with one another and ensuring that they merge smoothly with the background values far away from any source. We also study a fiducial model where the baryonic gas might be coupled to cold dark matter through velocity-dependent interaction.

Chapter 3: Spin Temperature Coupling

In this chapter, we present the physics of HI spin temperature T_S coupling with the matter kinetic temperature T_K through Lyman- α photons and collisions. We calculate the number density of Lyman- α photons as a function of distance from a source, taking into account the effect of higher-order Lyman- n transitions. We also compute the background value of Lyman- α number density far away from any sources. We also calculate the Lyman- α mean free path in the neutral medium and the average number of scattering experience by a typical Lyman- α photon before it is redshifted out of the resonance width. Combined with the kinetic temperature profiles calculated in the previous section, we can use the value of coupling coefficients to calculate the final spin temperature profiles around ionization bubbles.

Chapter 4: Correlations

We present our formalism to calculate the two-point correlation function of HI 21 cm signal in this chapter. We use geometric arguments to find pairs of points at any separation r and find the probability of such a pair occurring given our geometry of self-ionized bubbles and large overlapping spin temperature profiles around them. We verify that our formalism gives expected results in various limits and simplifications. We also study two simple models which help us identify the effect of ionization, heating and coupling on correlation at various scales. We extend our formalism to a simple scenario where ionization bubble centres

are correlated and show that such correlations introduce new scales in the results. We calculate the power spectrum by taking a Fourier transform of our correlation function.

Chapter 5: Results

We present results of our formalism in this chapter and study their dependence on five modelling parameters. We show the evolution of global HI 21 cm brightness temperature signal as a function of redshift. We also show the evolution of the fluctuating component (correlation functions and power spectrum) at various scales and for various combination of modelling parameters. We compare our results with results of N -body simulations and find that our results match the simulations in general, but differ in details. We also calculate the spin temperature profiles for a fiducial model of dark matter-baryon coupling, which matches the unexpectedly deep absorption trough observed by the EDGES group. We compute the expected correlation function and power spectrum for such a model and show that if the global signal detected by EDGES is confirmed, then the value of fluctuating component of 21 cm signal during those redshifts would also be enhanced.

Chapter 6: Conclusion

We summarise the current and upcoming instrumental projects to detect the global 21 cm signal and its fluctuating component. We list the upper limits placed by these instruments as well as the possible implications of the detection of global absorption trough by EDGES. We conclude with a brief overview of our work and possible future extensions.

Publications from the Thesis

Refereed Journals

1. **Janakee Raste** and Shiv Sethi, *An Analytic Formulation of the 21 cm Signal from the Early Phase of the Epoch of Reionization*, 2018, *The Astrophysical Journal*, 860, 55
2. **Janakee Raste** and Shiv Sethi, *Analytic formulation of 21 cm signal from cosmic dawn: Ly α fluctuations*, 2019, *The Astrophysical Journal*, 876, 56

Contents

List of Figures	xvii
1 Introduction	1
1.1 The Universe	1
1.1.1 The Early Universe	2
1.1.2 Matter Radiation Equality, Recombination and Decoupling	3
1.1.3 Structure Formation	6
1.1.4 Photoionization	9
1.2 Observations	13
1.2.1 Scattering of Lyman- α due to Neutral Hydrogen at High Redshift	14
1.2.2 Cosmic Microwave Background Radiation	16
1.2.3 Other Probes	17
1.3 The 21 cm Signal	17
1.3.1 Spin Temperature	17
1.3.2 Brightness Temperature	20
1.3.3 21 cm Signal from Early Universe	22
1.3.4 Simulations and Analytical Formalisms	23
1.4 Thesis Plan	24
2 Temperature Evolution of the IGM	25
2.1 X-Ray Heating	25
2.1.1 Photoionization and Heating of the Medium	27
2.1.2 Temperature Profile around X-ray Sources	29
2.1.3 Background Temperature	31
2.1.4 Modelling Profiles	32
2.1.5 Overlap of Profiles	35
2.2 Baryon Interaction with Cold Dark Matter	39
3 Spin Temperature Coupling	40
3.1 Lyman- α Coupling	40
3.1.1 Lyman- α in the Intergalactic Medium	40
3.1.2 Lyman- α Photons Number Density	43

3.1.3	Coupling Coefficient	46
3.2	Collisional Coupling	49
4	Correlation	50
4.1	Auto-correlation of Brightness Temperature T_B	51
4.2	Simplifying Cases and Limits	53
4.2.1	Ignoring Density Inhomogeneities ($\xi = 0$)	53
4.2.2	Uniform Temperature T_S	53
4.2.3	Very Large Scale	54
4.2.4	Very Small Scale	54
4.2.5	Complete Coupling	55
4.3	Notations and Modelling	55
4.4	Complete Model	58
4.4.1	Correlation of Neutral Region ($\langle n_1 n_2 \rangle$)	58
4.4.2	Correlation between Neutral region and Temperature ($\langle n_1 s_2 \rangle$)	62
4.4.3	Correlation of Temperature ($\langle s_1 s_2 \rangle$)	66
4.4.4	Alternative Method ($\langle \phi_1 \phi_2 \rangle$)	70
4.5	Simple Models	73
4.5.1	Uniform Temperature T_S	73
4.5.2	Uniform Bubble Size	74
4.5.3	Toy Model: One Bubble Size, Flat Temperature Profile	76
4.5.4	Toy Model: One Bubble Size, Two Shells, $\langle \phi \rangle = 0$	81
4.6	Correlation between Ionization Bubble Centres	84
5	Results	87
5.1	Modelling Parameters	87
5.2	Global Brightness Temperature	88
5.3	Two-point Correlation Function	90
5.4	Power Spectrum	93
5.5	Non-Standard Scenarios	96
5.5.1	Negative Correlation	96
5.5.2	Possible Explanations for EDGES Detection	97
5.6	Certain Assumptions and their Impact on Results	99
6	Conclusion	103
6.1	Detecting HI 21 cm Signal	103
6.1.1	Global Signal	104
6.1.2	Fluctuating Components	105
6.2	Summary and Conclusions	107
6.3	Future Prospects	107
	Appendix	109

A	Physical Constants	109
B	Hydrogen and Helium	109
C	Cosmology	110
D	Radiative Transfer	113
E	Probability	114
F	Geometry	114
	F.1 $D(x, R)$	115
	F.2 $E(x, Q, R)$	116
	F.3 $C(x, P, Q, R)$	117
	Bibliography	123

List of Figures

1.1	Cosmic microwave background anisotropies (Courtesy: ESA/Planck Collaboration).	4
1.2	Evolution of n_e/n_H with redshift calculated using CMBFAST (Seljak and Zaldarriaga [1996]). The two bumps at high redshifts indicate the first and second ionization of helium.	5
1.3	Evolution of CMB and matter (gas) temperature with redshift, as function of residual electron fraction x_{res} . Matter decouples from CMB earlier for smaller value of x_{res}	5
1.4	Cooling efficiency for a halo consisting of primordial gas of atomic hydrogen ($n_H = 0.045 \text{ cm}^{-3}$) and helium (solid red curve) and a halo with additional molecular hydrogen ($n_{H_2} = 0.001 n_H$) (dashed blue curve) as function of temperature. The two peaks in the red curve correspond to the characteristic temperature for excitation of HI and HeII. (Courtesy: Barkana and Loeb [2001])	8
1.5	Evolution of global ionization fraction (f_i) for different values of ζ . Reionization is completed earlier for higher value of ζ	13
1.6	Evolution of size distribution of self-ionized regions as function of halo mass for $\zeta = 10$	13
1.7	Absorption troughs in spectra of SDSS quasars from redshift $5.74 < z < 6.42$, indicating presence of HI in the IGM. These observations suggest that the reionization might have completed around $z \sim 6$ (Courtesy: Fan et al. [2006b]).	15
1.8	Evolution of T_{CMB} (blue curve), T_K (T_{gas} , red curve) and T_S (black curve) for a fiducial model. The dashed red curve shows the evolution of T_K without any heating sources.	23
2.1	Heating (T_K) profiles around a bubble at $z = 17$ for various values of α and v_{min} with $\zeta = 10$ and $N_{\text{heat}} = 1.0$. For $v_{\text{min}} > 1 \text{ keV}$ the temperature is smaller and the profile around a source is shallow.	34
2.2	Evolution of the T_K profile around a fiducial ionized bubble for $\alpha = 1.5$, $v_{\text{min}} = 100 \text{ eV}$, $\zeta = 10$, and $N_{\text{heat}} = 1.0$. The size of the ionization bubble is assumed to grow as $R_x \sim f_i^{1/3}$	34
2.3	Evolution of the size distribution of heated regions as a function of halo mass for $\zeta = 10$, $\alpha = 1.5$ and $N_{\text{heat}} = 1.0$	35
3.1	The 1s and 2p levels of hydrogen atom. The numbers in the centre are relative strengths. (Courtesy: Field [1958])	47

4.1	Cartoons for topology of the ionized region and its surrounding IGM. The colour scheme shows the kinetic temperature T_K (left panel) and dimensionless brightness temperature ψ (right panel). T_K in the ionization bubble of radius R_x (with sharp boundary) is 10^4 K. It falls as the distance from the source increases and smoothly merges with the background at radius R_h . $\psi_i = 0$ in the ionized region. It might be positive in the neutral, heated and coupled region, and negative in neutral, non-heated and coupled region. The background is not coupled in this case ($\psi_{bg} = 0$). We can randomly choose a point and find correlation with its neighbour at distance r	57
4.2	Finding pairs of points separated by distance r is equivalent to finding points and their neighbours at distance r	59
4.3	If one point is ionized, what is the probability of its neighbour at distance r being neutral? .	60
4.4	A toy model: an ionization bubble ($\phi_i = 0$) has one T_S shells around it. Background is unheated.	77
4.5	Evolution of ionized and heating fractions for a fiducial model for $\zeta = 10$, $N_{\text{heat}} = 1.0$ and $\alpha = 1.5$	80
4.6	Evolution of correlation function for a set of scales for a model in Figure 4.5. The background temperature and profile temperature is allowed to increase in the left panel, whereas they are held constant in the right panel.	80
4.7	A toy model: an ionization bubble ($\phi_i = 0$) has two T_S shells around it. The background is uncoupled ($\phi_b = 0$).	82
4.8	A case with negative correlation for certain scales. The ionization fraction $f_i = 0.01$ and heated fraction $f_s = 0.55$. The distance scale would depend on the size of ionization bubble, which is chosen to be 0.1 Mpc.	84
4.9	Evolution of correlation function for a set of scales for a model in which the background temperature is held constant. Here the curves from bottom to top show cases for no correlation (left panel of Figure 4.6), correlation with $b = 1$ and with $b = 2$	85
5.1	Global brightness temperature as function of redshift for various values of α , N_{heat} , and v_{min} . All plots have $\zeta = 10.0$ and $f_L \rightarrow \infty$ ($T_S = T_K$).	89
5.2	Global brightness temperature as function of redshift for various values of f_L ranging from 1.0 to 1000 and for $N_{\text{heat}} = 10$ (solid lines), 1.0 (long dashed lines), and 0.1 (short dashed lines). All plots have $\zeta = 7.5$, $\alpha = 1.5$, and $v_{\text{min}} = 100$ eV.	89
5.3	Evolution of auto-correlation of HI brightness temperature for $r = 0.5$ Mpc (top left panel), $r = 2.0$ Mpc (top right panel), $r = 4$ Mpc (bottom left panel) and $r = 8$ Mpc (bottom right panel) for $\zeta = 7.5$, a range of f_L varying from 0.1 to 1000 and three values of N_{heat} : 10 (solid lines), 1.0 (long dashed curves) and 0.1 (short dashed lines). The dot-dashed line represents a fiducial model that matches with EDGES observations.	90
5.4	Evolution of two-point correlation function for a range of scales (including the RMS corresponding to $r = 0$) for $\alpha = 1.5$, and $\zeta = 10$. The thick curves are for $v_{\text{min}} = 100$ eV and the thin curves are for $v_{\text{min}} = 1$ keV. N_{heat} is 0.1 (top left panel), 0.5 (top right panel), 1.0 (bottom left panel), and 5.0 (bottom right panel).	91

5.5	Evolution of auto-correlation of HI brightness temperature for $r = 0.5$ Mpc, including density perturbations (left panel) and without density perturbations ($\xi = 0$) (right panel), for $\zeta = 7.5$, a range of f_L varying from 0.1 to 1000 and three values of N_{heat} : 10 (solid lines), 1.0 (long dashed curves) and 0.1 (short dashed lines). The dot-dashed line represents a fiducial model that matches with EDGES observations.	92
5.6	The evolution of auto-correlation of HI brightness temperature at various scales, including density perturbations (left panel) and without density perturbations ($\xi = 0$) (right panel), for $\zeta = 10$, $f_L = 10$, and $N_{\text{heat}} = 0.5$	93
5.7	Evolution of $\Delta^2(k) = k^3 P(k)/2\pi^2$ for $k = 2 \text{ Mpc}^{-1}$ (top left panel), $k = 1 \text{ Mpc}^{-1}$ (top right panel), $k = 0.5 \text{ Mpc}^{-1}$ (bottom left panel) and $k = 0.125 \text{ Mpc}^{-1}$ (bottom right panel) for $\zeta = 7.5$, a range of f_L varying from 0.1 to 1000 and three values of N_{heat} : 10 (solid lines), 1.0 (long dashed lines) and 0.1 (short dashed lines). The dot-dashed line represents a fiducial model that matches with EDGES detection.	94
5.8	Evolution of $\Delta^2 = k^3 P(k)/2\pi^2 ((mK)^2)$ for a range of scales for $\alpha = 1.5$, and $\zeta = 10$. The thick curves are for $v_{\text{min}} = 100$ eV and the thin curves are for $v_{\text{min}} = 1$ keV. The left and right panels correspond to $N_{\text{heat}} = 0.1$ and $N_{\text{heat}} = 0.5$, respectively.	95
5.9	Neglecting density perturbations ($\xi = 0$), the auto-correlation of HI signal at $z = 20$ for $\zeta = 7.5$, $f_L = 1.0$ and $N_{\text{heat}} = 1.0$	96
5.10	Global brightness temperature as function of redshift for $\zeta = 7.5$, various values of f_L ranging from 0.1 to 1000, and three value of N_{heat} : 10 (solid lines), 1.0 (long dashed lines) and 0.1 (short dashed lines). We have assumed dark matter-baryon interaction with $\sigma_1 = 5 \times 10^{-24} \text{ cm}^2$ and $m_{\text{dm}}/m_p = 0.001$	97
5.11	Global brightness temperature as function of redshift for $\zeta = 7.5$, various values of f_L ranging from 1.0 to 1000, and three value of N_{heat} : 10 (solid lines), 1.0 (long dashed lines) and 0.1 (short dashed lines). The dot-dashed line represents the fiducial model of Figure 5.10 with $f_L = 2$ and $N_{\text{heat}} = 0.08$	97
F.1	Case a: $x \leq R$	115
F.2	Case b: $R \leq x \leq 2R$	115
F.3	Case c: $x \geq 2R$	115
F.4	Case a: $x \leq R - Q$	118
F.5	Case b: $x \leq P - R$	118
F.6	Case c: $x \geq R + Q$	118
F.7	Case d.a: $R - Q \leq x \leq R - P, x \leq Q - R$	118
F.8	Case d.b: $R - Q \leq x \leq R - P, x \geq Q - R$	118
F.9	Case e.a: $P - R \leq x \leq Q - R, x \geq P + R$	119
F.10	Case e.b: $P - R \leq x \leq Q - R, x \leq P + R$	119
F.11	Case f.b: $R + P \leq x \leq R + Q, x \geq Q - R$	120
F.12	Case g: $x \geq Q - R, x \geq R - P, x \leq P + R$	120

Chapter 1

Introduction

“There is a theory which states that if ever anyone discovers exactly what the Universe is for and why it is here, it will instantly disappear and be replaced by something even more bizarre and inexplicable. There is another theory which states that this has already happened.”

— Douglas Adams, *The Restaurant at the End of the Universe*

1.1 The Universe

According to the standard model of cosmology, the universe as we know it began as a hot dense state in an event called the ‘big bang’. The universe expanded with time, cooled and the energy was converted into radiation and matter. This matter collapsed under self-gravity and formed stars, galaxies and clusters of galaxies. Within the core of these stars and their energetic remnants, heavy elements were created which formed the planets like earth. So, about 13.7 billion years after the formation of our universe, we look up into the sky and wonder how was it created, what is it made up of, how does it evolve and how will it end.

There are many parts of this narrative which are not well understood. On the one hand, we have a fair understanding of our Solar system, Milky Way galaxy and the local universe at large. For billions and billions of lightyears in any direction, we observe a universe that is made up of galaxies, which are made up of stars, gas and dust. There are about 10^{11} galaxies in the observable universe and about 10^{11} stars per galaxy. These galaxies are further part of even larger structures. When we do fail to detect these structures, it is largely due to the limitations of our current instruments and not because there is nothing to detect.

On the other hand, we have observed the cosmic microwave background (CMB), the fading afterglow of the young universe (Penzias and Wilson [1965], Dicke et al. [1965]). Unlike our present universe, it is remarkably uniform with the temperature of 2.7 K. The fluctuations of CMB temperature are about 1 part in 10^5 (Mather et al. [1990], Hinshaw et al. [2013], Planck Collaboration et al. [2018]). This is the universe where most of the matter is in the form of hot, uniform, partly ionized gas.

However, between these two extremes, we are left to fill up a lot of blanks. How and when did the gas start condensing to form sources of radiation such as we see today? Where did these sources form? What were the properties of these first sources? The physics of first stars and galaxies is only partially understood theo-

retically and poorly constrained with observations. It is one of the outstanding goals of modern cosmology to try to answer these questions. This thesis is a small contribution towards understanding this period in the history of the universe.

1.1.1 The Early Universe

Inflation: Soon after the universe came into existence, for a brief period, it expanded exponentially. This time period is called ‘inflation’. The quantum fluctuations during this exponential phase caused density fluctuations in matter and radiation at the end of the inflation. This is the initial condition for density perturbations that grew via gravitational collapse into the universe that we see today.

Baryogenesis and Big bang Nucleosynthesis (BBNS): All observational evidences suggest that our universe contains an excess of baryons over anti-baryons. Starting from an initial condition which is symmetric with respect to the number of baryons/anti-baryons, it is possible to achieve an excess of baryons through a process known as baryogenesis (Sakharov [1967]) during and after the inflationary era. This process was responsible for creating the photon to baryon ratio, $\eta_b = 10^9$; this ratio is invariant under the expansion of the universe.

The next important phase of the early universe is the formation of heavy nuclei. At temperature $T \gg 10^{10}$ K, there was an equilibrium between proton and neutron number density with,

$$p^+ + e^- \leftrightarrow n^0 + \nu_e.$$

As the rate of weak interactions fell below the expansion rate, this process fell out of equilibrium. However, the free neutrons continued to decay until the temperature dropped further to allow them to form deuteron and helium nuclei. The proton to neutron ratio at this epoch ($n_p/n_n \sim 1/7$) determined the abundance of helium nucleus ($\sim 25\%$ by mass). The nucleosynthesis also created trace amounts of deuteron (^2H), Helium-3 (^3He), Lithium-7 (^7Li) and Beryllium (^7Be) (Wagoner [1973], Boesgaard and Steigman [1985], Kolb and Turner [1990]).

During this phase, the universe has the following components: photons, non-relativistic matter (dark matter, baryonic matter (ionized and strongly coupled to photons)), neutrinos (decoupled for other matter and free streaming).

The small density fluctuations in matter and radiation generated during inflation grew via self-gravitational collapse. As the universe is dominated by the energy density of radiation (photons and neutrinos), these fluctuations can only grow logarithmically on scales smaller than the horizon, H^{-1} . In addition, the baryonic matter plasma is strongly coupled to photons, whose main effect is: (a) The baryonic matter remains ionized, (b) Through repeated scattering between photons and baryons, density fluctuations in the baryonic matter are washed out¹ (Silk [1968]), (c) The baryon temperature T_K and the radiation temperature T_γ are the same and both fall as $1/(1+z)$ owing to expansion (Appendix C).

¹This is one of the reasons why we need dark matter that does not interact with radiation. The structures we see today could not have been formed if the only matter component in the universe was baryonic, because in that case radiation would have wiped out all fluctuations on small scales (Blumenthal et al. [1984]).

1.1.2 Matter Radiation Equality, Recombination and Decoupling

Matter-Radiation Equality: When the universe made a transition from the radiation-dominated to the matter-dominated era at $z_{\text{eq}} \simeq 3380$ (Appendix C), the expansion rate slowed enough to allow the dark matter to start collapsing. However, the potential wells thus created were incapable of trapping the ionized baryonic matter since it was still strongly coupled to the radiation field.

Hydrogen Recombination: Around $z_{\text{rec}} \sim 1100$, the number of hydrogen-ionizing photons in the background radiation fell sufficiently to allow hydrogen atoms to be formed (Epoch of Recombination).

However, if a proton and an electron directly combined to form a hydrogen atom, the emitted photon of energy $\simeq 13.6$ eV would be immediately absorbed by another hydrogen atom and the net recombination would be zero. Therefore, for the recombination process to be successful, the electron and proton should combine to an excited state. The majority of such recombinations took place through the first excited state of the hydrogen atom. From this state, it can de-excite to the ground state by one of the two processes: (1) $2s \rightarrow 1s$: This is a forbidden transition, and hence $2s$ is a metastable state. The hydrogen atom can still make this transition with the rate $\Lambda = 8.23 \text{ s}^{-1}$ through the emission of two photons. (2) $2p \rightarrow 1s$: The Lyman- α photon emitted in this process is also immediately absorbed by another neutral hydrogen. However, after multiple scattering, this photon will redshift out of the resonance line, leaving one successfully recombined atom¹. Both these processes made a similar contribution to the process of recombination (Peebles [1993]).

Helium Recombination: Helium ionization energy is higher than the hydrogen (24.6 eV and 54.4 eV for neutral and singly-ionized helium). Therefore, the number of photons with energy higher than this in the background radiation fell below the number of helium atoms at $z \sim 6000$ and $z \sim 2000$ (Switzer and Hirata [2008]) respectively for first and second recombination of helium and these events took place before hydrogen recombination.

Cosmic Microwave Background (CMB) Radiation: In a neutral universe, the background radiation was finally able to free stream. The last scattering of this background radiation occurred during the end of the epoch of recombination, which is called the ‘the last scattering’ surface. The small fluctuations in the density and hence the temperature of the baryonic matter at this epoch were imprinted into CMB radiation as temperature and polarization inhomogeneities. These inhomogeneities are seen as anisotropy of the order of 10^{-5} in the CMB maps across the sky (Figure 1.1) (Planck Collaboration et al. [2018]). CMB is currently the strongest probe to study the early universe and the deciding factor in support of the hot big bang model (Dodelson [2003]). Since this epoch, there are very few known mechanisms which substantially alter the properties of the CMB. The free streaming radiation cools as $1/(1+z)$ and its temperature at any redshift is given by $T_{\text{CMB}}(z) = T_0(1+z)$, where $T_0 = 2.73$ is its observed temperature at the present.

Residual Ionization: Towards the end of the epoch of recombination, rapid reduction of the number density of electrons and protons caused the rate of recombination to fall. Hence a small fraction of free electrons and protons was left in the universe. This ‘residual’ electron fraction remains fairly constant for a

¹The photons which have energy slightly smaller than Lyman- α due to redshifting are not absorbed by anything at that epoch. Whereas the redshifted recombination photon would excite the neutral atom to a high energy state, from where it can get easily ionized through collisions. Thus, redshifting does not destroy the recombination photons, but it destroys the Lyman- α photons.

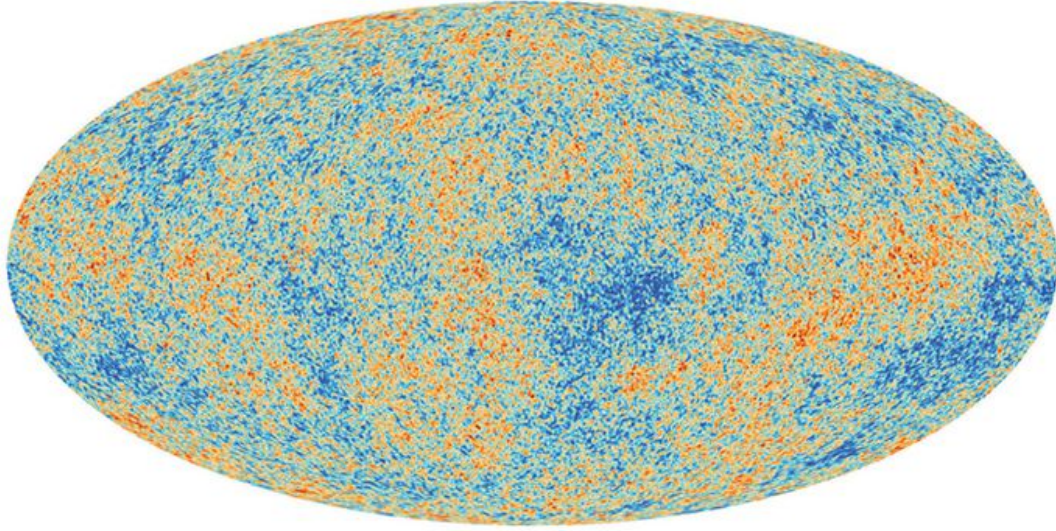


Figure 1.1: Cosmic microwave background anisotropies (Courtesy: ESA/Planck Collaboration).

long time as it becomes increasingly difficult for free electrons and protons to encounter each other in the rapidly expanding universe¹ (Figure 1.2). In our calculations we take the fraction of residual electron to be $x_e \simeq 2 \times 10^{-4}$, and assume that it is independent of redshift.

At the end of the epoch of recombination, the universe has following components: Radiation (free streaming), Matter (dominant) (dark matter (forming structures), baryonic matter (almost neutral, thermally coupled to radiation)), neutrinos (free streaming).

Thermal Decoupling: After recombination, the mostly free streaming CMB photons were still being scattered from the residual electron fraction. The electron interaction time scale with both the ionized gas and neutral medium is smaller than the time scale of electron-photon interaction; therefore, these electrons exchanged energy with the CMB through inverse Compton scattering and shared it with the baryonic gas, which kept all the components of the gas at the same temperature. The evolution of matter temperature T_K is given by,

$$\frac{dT_K}{dt} = -\frac{2\dot{a}}{a}T_K + \frac{x_e}{1+x_e} \frac{8\sigma_T}{3} \frac{a_r T_{\text{CMB}}^4}{m_e c} (T_{\text{CMB}} - T_K). \quad (1.1)$$

¹ We can compare the recombination rate and expansion rate in the present universe ($z = 0$). For $T = 10^4$ K within the ionized regions ($x_e = 1$), the case A recombination coefficient is, $\alpha_A = 4.18 \times 10^{-13} \text{cm}^3 \text{s}^{-1}$; and the recombination rate is $R = \alpha_A n_e$, where $n_e = x_e n_{b,0}$ is electron number density. The ratio of recombination rate to Hubble expansion rate is,

$$\frac{R}{H_0} = 4.18 \times 10^{-13} \frac{n_{b,0}}{H_0} \simeq 0.046.$$

This ratio suggests that even without sources of ionizing radiation, the gas will not recombine since the rate of current expansion is higher than rate of recombination.

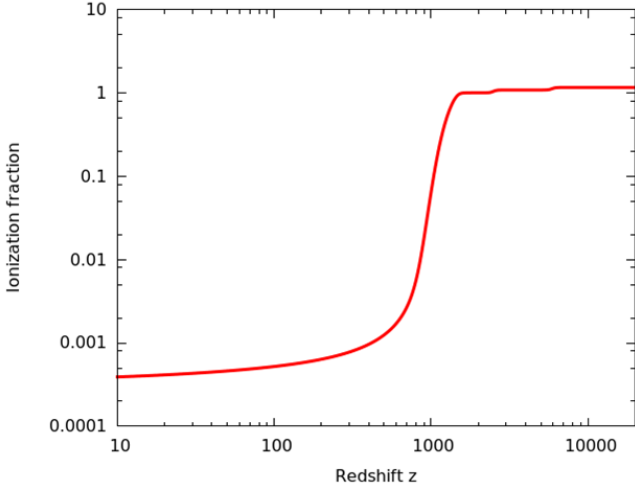


Figure 1.2: Evolution of n_e/n_H with redshift calculated using CMBFAST (Seljak and Zaldarriaga [1996]). The two bumps at high redshifts indicate the first and second ionization of helium.

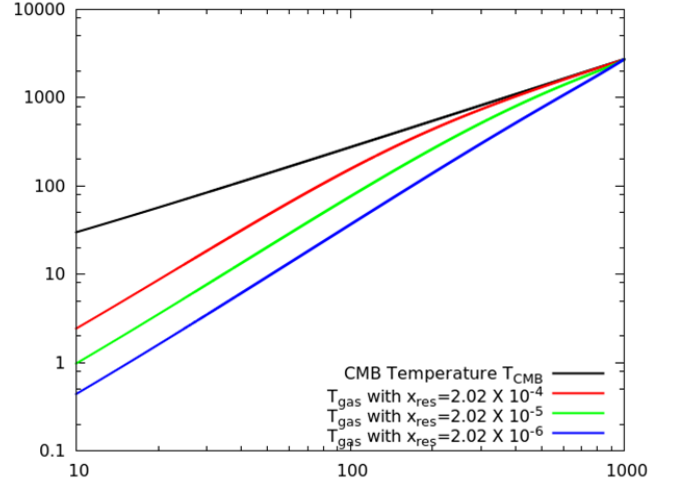


Figure 1.3: Evolution of CMB and matter (gas) temperature with redshift, as function of residual electron fraction x_{res} . Matter decouples from CMB earlier for smaller value of x_{res} .

Here, the first term is the adiabatic cooling of matter due to the expansion of the universe, and the second term is the heating/cooling due to thermal coupling with CMB (Peebles [1993]). σ_T is the Thomson scattering cross-section of electrons and photons, a_r is radiation constant, and m_e is electron mass. The $x_e/(1+x_e)$ factor is the ratio of number density electrons to all the particles which share its energy (e.g. electrons, ions, atoms)¹. This equation states that even though baryons are cooling faster than CMB due to the expansion of the universe, as long as there is sufficient interaction between residual electrons and CMB photons, the baryons are *thermally* coupled to CMB and their temperature falls as $1/(1+z)$. Given the large heat capacity of CMB photons, this process did not sufficiently alter the CMB spectrum².

When the rate of this interaction fell below the cooling rate (i.e. the expansion rate of the universe), the thermal coupling became inefficient and the baryons started cooling as $1/(1+z)^2$. The timescale for the heating (photon-electron thermal coupling) is,

$$t_c = \frac{1+x_e}{x_e} \frac{3m_e c}{8\sigma_t a_r T_{\text{CMB}}^4}. \quad (1.2)$$

Comparing this time scale with the Hubble expansion time scale for the matter dominated universe ($H(z)^{-1} \sim t_c$) we get,

$$\frac{1}{H_0 \Omega_m^{1/2} (1+z)^{3/2}} \sim \frac{1+x_e}{x_e} \frac{3m_e c}{8\sigma_t a_r T_{\text{CMB}}^4} \frac{1}{(1+z)^4}. \quad (1.3)$$

Therefore, the redshift when the cooling rate overtook the heating rate is dependent on the residual electron

¹If non-baryonic matter (with number density $n_d = x_d n_b$) was coupled to baryonic matter at this epoch, its effect can be incorporated by modifying this ratio to $x_e/(1+x_e+x_d)$.

²One way to describe this process is that *the CMB has decoupled from baryonic matter, but the matter has not decoupled from CMB*.

fraction as

$$(1+z)^{5/2} \sim 45.15 \frac{1+x_e}{x_e}. \quad (1.4)$$

With $x_e = 2.7 \times 10^{-4}$, the thermal decoupling redshift is $z_{\text{dec}} \sim 122$. If the residual electron fraction was smaller, the baryons would decouple and start cooling sooner and their temperatures would be lower. On the other hand, if the residual electron fraction was larger, then the final baryon temperature would be higher (and closer to CMB temperature). For example, taking $x_e = 2.7 \times 10^{-5}$, we get $z_{\text{dec}} \sim 308$, and taking $x_e = 2.7 \times 10^{-3}$, we get $z_{\text{dec}} \sim 48$. Figure 1.3 shows the evolution of CMB and matter temperature as function of three different residual electron fractions.

Components of the universe after thermal decoupling are: Radiation (free streaming), Matter (dominant) (dark matter (forming structures), baryonic matter (almost neutral, decoupled from radiation)), neutrinos (free streaming).

Dark Ages: The time period after recombination is referred to as ‘dark ages’ since there was minimal interaction between matter and radiation and the sources of radiation had not formed yet. During this epoch, the baryonic matter started falling into the dark matter potential wells and these high-density regions collapsed into halos of various masses. This epoch ended when the sources of radiation were created in these collapsed structures. There are no current observations to study the nature and dynamics of the universe during this time period and our understanding of this epoch is based on theoretical models.

1.1.3 Structure Formation

In a perfectly homogeneous¹ universe, every point of matter will remain stationary since it feels the equal force from every direction. This is an unstable equilibrium since a slight inhomogeneity would grow under self-gravity. The evolution of such density inhomogeneities in different components of the universe is the key to understand the formation of structures in the universe, as these inhomogeneities eventually collapse to form galaxies and other large scale structures.

We can begin with a patch of the universe which has a density

$$\rho = \bar{\rho}(1 + \delta), \quad (1.5)$$

where, $\bar{\rho}$ is the average density of the universe. If $\delta > 0$, then the selected patch has density higher than the average density (overdense region); if $\delta < 0$, then the patch has density lower than the average density (underdense region). The ‘overdensity’ parameter δ has minimum value of -1 . In the early universe, $\delta \ll 1$ and with the expansion of the universe, this overdensity grows. The evolution of the overdensity in different components of the universe (baryons, photons, massless and massive neutrinos, etc.) is important for understanding the details of this process in the early universe. But the dominant component of the matter at late times is the cold dark matter (CDM) and to gauge the salient aspects of the growth of these perturbations, it suffices to underline the evolution of the perturbations for this component of the universe.

¹Such a universe will need to be infinite or closed.

An important outcome of CDM domination is that the structures grow hierarchically, i.e. smaller structures form before the bigger structures.

At early times and/or large enough scales, we can study the evolution of inhomogeneities with linear perturbation theory. In this approximation, the perturbations grow independently for each Fourier mode. The factor enhancing these fluctuations is called the ‘growing mode’ (D_+). The assumption of linear theory breaks down when $\delta > 1$. The fluctuations at different scales become nonlinear at different time (redshift). The non-linear phase of density perturbations can be studied using the top-hat spherical model. At the time of the collapse, the full nonlinear overdensity of a spherical overdense region is $\delta_{nl} = 178$, which corresponds to linear overdensity of $\delta_L = 1.686$. Therefore, if the linear analysis predicts a region with an overdensity of $\delta > 1.686$, in full nonlinear theory, this region has collapsed into a halo (Peebles [1980], Padmanabhan [1993]).

Virialization: Slight asymmetry in the mass distribution of a halo will prevent it from collapsing to a point. During the collapse, shocks and heating of the halo gas will lead to ‘virial equilibrium’, where the total potential binding energy of the halo is twice the kinetic energy of its particles ($-W = 2K$). This virialization takes place on the same time scale as the collapse of the halo. The region with higher initial overdensity virializes sooner.

Jeans Mass: Within a virialized halo, the baryonic matter exerts pressure which starts to balance the effect of gravity. This prevents further collapse of the baryonic halo. If a halo is collapsing faster than the speed of sound, it will continue to collapse before the pressure can build up to counter it. Once it has reached equilibrium, further gravitational instability will create pressure waves. For a halo of radius R and density ρ , the dynamical collapse time scale and the time scale for a pressure wave to travel through it (acoustic response time) are, respectively,

$$t_c \sim \frac{1}{\sqrt{G\rho}} \quad \text{and} \quad t_a \sim \frac{R}{c_s}, \quad (1.6)$$

where c_s is speed of sound in the medium. Both these processes depend on the mass, temperatures and density of the halo. The threshold mass (‘Jeans mass’) is (Barkana and Loeb [2001]),

$$M_J \sim \left(\frac{5k_b T}{Gm_p} \right)^{3/2} \left(\frac{3}{4\pi\rho} \right)^{1/2}. \quad (1.7)$$

When the halo is more massive than the Jeans mass, the gravity dominates, and the halo can collapse. Halos smaller than Jeans mass will not form structures¹.

Cooling: The temperature of baryons within a collapsing halo rises owing to increasing density which causes more collisions between particles. These energetic collisions can ionize or excite an atom, molecule, or ion. When this particle de-excites or recombines, a photon will be emitted which might escape the cloud. Thus the kinetic (thermal) energy of the particles can be carried away by the radiation. In a halo consisting of primordial gas, the emission of HI atomic lines constitutes the most important channel of cooling. The

¹For the cold dark matter, the Jeans mass is formally zero as it is pressureless, therefore a halo of any mass can collapse. However, the halos with masses below the baryonic Jeans mass contain only dark matter and no baryonic matter.

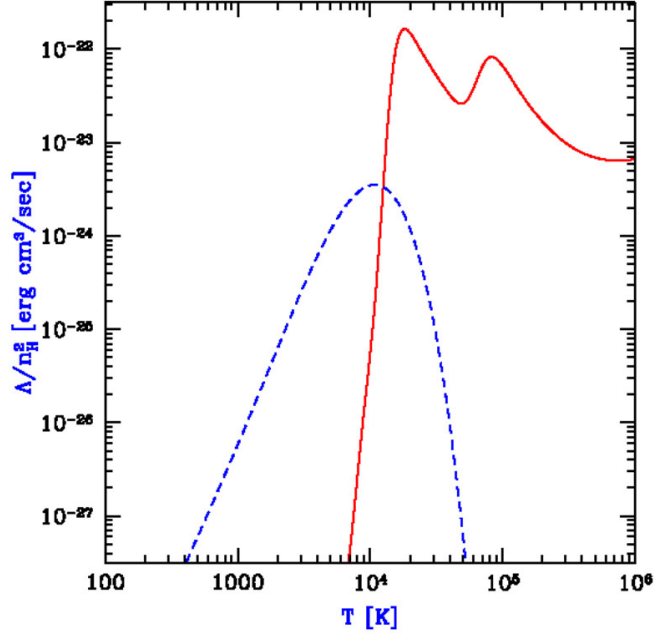


Figure 1.4: Cooling efficiency for a halo consisting of primordial gas of atomic hydrogen ($n_{\text{H}} = 0.045 \text{ cm}^{-3}$) and helium (solid red curve) and a halo with additional molecular hydrogen ($n_{\text{H}_2} = 0.001n_{\text{H}}$) (dashed blue curve) as function of temperature. The two peaks in the red curve correspond to the characteristic temperature for excitation of HI and HeII. (Courtesy: [Barkana and Loeb \[2001\]](#))

minimum temperature required to excite these lines is about 10^4 K and this is the minimum temperature that can be attained with HI cooling.

If there were molecules, then the halo can cool further through excitation of their rotational or vibrational lines, which takes place at a lower temperature. Moreover, the radiation emitted through molecular lines can escape the halo with greater ease, since their mean free path is very large due to the smaller number densities of molecules. However, in the early universe, the ‘metals’ (elements heavier than helium) are negligible as they are primarily formed in stellar core and supernova remnants, none of which have been formed at this epoch. It is possible to form H_2 molecule in the early universe, but it is extremely difficult since we need catalysts like ‘dust’ (heavy molecules) or electrons.

In our work, we assume that halos are cooled only through atomic hydrogen. As this requires a virial temperature $T_{\text{vir}} > 10^4$ K, we obtain a lower bound on the mass of the collapsing halo ([Barkana and Loeb \[2001\]](#), [Dayal and Ferrara \[2018\]](#)):

$$M_{\text{min}} = 3.915 \times 10^8 (\Omega_m h^2)^{-1/2} (1+z)^{-3/2} M_{\odot}. \quad (1.8)$$

Fragmentation: Within a virialized halo, if cooling time is shorter than the dynamical time ($t_{\text{cool}} < t_{\text{dyn}}$), then the collapse is isothermal. In such a scenario, the temperature remains constant, but the density incre-

ases. This leads to decrease in the Jeans mass $M_J \propto \rho^{-1/2} T^{3/2}$. Therefore, within the original halo, now smaller structures can collapse. Shocks and density inhomogeneity within the halo will lead to fragmentation of the halo. This is a runaway process in which the clouds keep fragmenting and collapsing until eventually, the density is so high that the clouds become optically thick to the cooling radiation (Ciardi and Ferrara [2005]).

Cosmic Dawn: The more efficient the cooling is, the longer the sub halos and clouds fragment. Thus, strong cooling leads to the formation of stars which have small masses. Given the inefficient atomic cooling of the primordial halos, the first stars that formed were very massive. These are called ‘Population III’ (Pop III) stars. They are believed to be isolated, very bright and short-lived (Barkana and Loeb [2001], Ciardi and Ferrara [2005]).

Feedback: Chemical: When these Pop III stars died (and caused supernova explosions), they enriched their surrounding medium with metals, which helped the formation of H_2 molecules. This lead to easier channels for cooling of the medium and the new sources which formed there had properties different from the first stars; these are called the Population II (Pop II) stars (e.g. Loeb and Barkana [2001], Ciardi and Ferrara [2005] and the references therein).

Mechanical: Violent supernova explosions injected energy into the medium and threw out the gas. This depletion of gas prevented further stars formation in the neighbourhood.

Radiative: These stars emitted a spectrum of radiation which changed the properties of their surrounding medium (Haiman et al. [2000], Barkana and Loeb [2001], Pritchard and Loeb [2012], Natarajan and Yoshida [2014], Morales and Wyithe [2010]). The ultraviolet (UV) photons ionized and heated their surrounding neutral gas. X-ray photons emitted from the accretion of gas around binaries and black holes, heated up the medium, increased the electron fraction and formation of H_2 molecules. However, the Lyman-Werner photons (11.26 to 13.6 eV) can cause dissociation of H_2 molecules (Haiman et al. [1997]). Heating and ionization of the medium lead to increase in Jeans mass to about $10^9 M_\odot$ (Sethi [2005]).

We study the effect of three most important components of this radiation: UV, Lyman- α ¹ and X-ray photons with a wide spectrum.

1.1.4 Photoionization

The ultraviolet (UV) photons emitted by first sources are absorbed in their immediate vicinity and carve out ionized HII regions in the neutral Intergalactic Medium (IGM). The number density and spectrum of ionizing photons depend on the type of the source (e.g. black holes emit with harder spectrum than stars). With the formation of new sources and the expansion of the universe, these HII regions expand and merge. This epoch is called the ‘Epoch of Reionization’ (EoR).

HII Region: Within an ionized region, there is a balance between the recombination of HI atoms and their ionization due to UV photons. Due to this constant recombination and ionization, the ionization photon is scattered until it reaches the boundary of the ionized region where it is absorbed. Given the small mean free

¹While studying this epoch, all the radiation between Lyman- α and Lyman-limit *emitted* from the source is referred to as Lyman- α radiation. Whereas the Lyman- α radiation *received* at a point only refers to photons with Lyman- α frequency.

path of the UV photon in a neutral region, the boundary of an HII region is very sharp. However, towards the end of EoR the global volume fraction of the ionized gas (f_i) is close to 1 and the ionizing photon mean free path is very large. This leads to non-local ionization. The temperature of the ionized region is $\sim 10^4$ K.

This scenario is called ‘inside out’ reionization where the medium surrounding the sources is ionized first. This model is currently favoured by the numerical simulations (Choudhury et al. [2009]), but it was earlier proposed that the reionization process would be dominated by recombination time scale instead of ionization. If that was the case, the regions far away from sources would be ionized first, since due to their low density, recombinations would be slower. This is called an ‘outside-in’ reionization scenario (Miralda-Escudé et al. [2000]). We only use inside-out reionization model in our work.

Clumping Factor: In the IGM, there are regions which are dense and massive ($M > M_J$) enough to be gravitationally bound, but not massive enough to collapse into a star. These clouds have very high recombination rate due to high density and they remain neutral for a long time even when their surrounding medium has been ionized. Such regions act as UV sink (Sethi [2005]), as inside such a region, the ionization and recombination processes are not in balance. Clumping factor is defined as,

$$C = \frac{\langle n_b^2 \rangle}{\langle n_b \rangle^2}, \quad (1.9)$$

where, n_b is baryon number density and $\langle \rangle$ is the ensemble average¹. We could have defined C with number density of hydrogen instead of baryons, but hydrogen and helium are not expected to cluster differently. C usually has a value between 1 and 5 (McQuinn et al. [2007]). We assume it to have a constant value of 2.

Strömgren sphere: If \dot{N}_γ is the number of ionizing photons emitted (isotropically) by a source per unit time, then we can balance the number of recombination and ionization to calculate radius R of the ionization region as (Shapiro and Giroux [1987], Shu [1992]),

$$\dot{N}_\gamma = \frac{4\pi}{3} R^3 \alpha_B C n_e n_p, \quad (1.10)$$

where, n_e and n_p are electron and proton number density respectively, and α_B is Case-2 recombination coefficient (Appendix B). The physical radius of a Strömgren sphere is,

$$R = \left(\frac{3}{4\pi} \frac{\dot{N}_\gamma}{\alpha_B C n_e n_p} \right)^{1/3}. \quad (1.11)$$

This radius is increasing with the expansion of the universe. The comoving radius,

$$R_0 = R(z)(1+z) = \frac{1}{1+z} \left(\frac{3}{4\pi} \frac{\dot{N}_\gamma}{\alpha_B C n_{e,0} n_{p,0}} \right)^{1/3},$$

is also increasing with the expansion of the universe, because the number density of particles and hence recombination efficiency is decreasing.

¹Assumption of Ergodicity: we use volume average and ensemble average interchangeably.

Self-Ionized Regions: For Λ CDM model of the universe, the ionized regions are larger than the Strömgen sphere of a single source, because they are created by highly clustered multiple sources. Self-ionized regions are defined as regions which have enough sources to ionize all the gas in them and no more (Furlanetto et al. [2004]). If within such a region, collapsed mass m_{coll} can produce enough sources to ionize total of m_{ion} mass, then we can define ‘ionization efficiency parameter’ as,

$$\zeta = \frac{m_{\text{ion}}}{m_{\text{coll}}}. \quad (1.12)$$

It is a function of properties of the sources and their surrounding medium. Balancing total recombination with total ionization per hydrogen atom within a self-ionized region, we get,

$$\begin{aligned} n_{\text{rec}} &= \frac{\text{received photons}}{\text{total hydrogen}} \\ &= \frac{\text{received photons}}{\text{emitted photons}} \frac{\text{emitted photons}}{\text{stellar baryons}} \frac{\text{stellar baryons}}{\text{collapsed baryons}} \frac{\text{collapsed baryons}}{\text{total baryons}} \\ &= f_{\text{esc}} N_{\gamma/b} f_{\star} f_{\text{coll}} \end{aligned} \quad (1.13)$$

Here, $f_{\text{coll}} = m_{\text{coll}}/m_{\text{tot}}$ is the fraction the halo mass that has collapsed into structures, f_{\star} is the fraction of collapsed baryons that is converted into stars, f_{esc} is the fraction of ionizing photons that escape the source halo, $N_{\gamma/b}$ is number of UV photons emitted per stellar baryon, while n_{rec} is the number of recombinations per hydrogen atom¹. The collapsed fraction within a self-ionized region is,

$$f_{\text{coll}} = \frac{n_{\text{rec}}}{N_{\gamma/b} f_{\star} f_{\text{esc}}}. \quad (1.14)$$

Inside a self-ionization region all the mass is ionized ($m_{\text{ion}} = m_{\text{tot}}$), therefore, we can write,

$$\zeta = \frac{1}{f_{\text{coll}}} = f_{\star} f_{\text{esc}} \frac{N_{\gamma/b}}{n_{\text{rec}}}. \quad (1.15)$$

Hence, the ionization efficiency parameter ζ incorporates multiple properties of the sources, many of which have uncertainty by a large factor (Gnedin et al. [2008], Benson et al. [2013], Kim et al. [2013]). Therefore, in our work, we only explore various values of ζ and try to constrain it using available observations. The value of ζ would evolve with time because the nature of sources and their surrounding medium change with redshift. However, we assume ζ to be constant over the whole redshift range in our work.

The self-ionized regions (ionization bubbles) need not be spherical, but for the sake of simplicity, we assume them to be spherical, though this assumption will not hold in case of overlapping and merging bubbles. We discuss the implications of these assumptions in Section 5.6.

Excursion Set Formalism: A region which has linear overdensity of $\delta > 1.68$, will have collapsed to form a halo. However, this region could be part of a larger halo. Such a ‘cloud in cloud’ scenario suggests that to figure out if a point in the universe is within a collapsed halo, we should find the largest possible region around it that has collapsed. This method is called the ‘excursion set formalism’ (Press and Schechter

¹We have interchangeably used total baryons number and total hydrogen number, which would make a small difference.

[1974], Bond et al. [1991], Lacey and Cole [1994]).

Around a point, we start with a region of very large radius (and corresponding mass scale), track the value of overdensity parameter δ smoothed¹ at that scale (δ_m), and find the radius (mass) when this value crosses (a barrier of) $\delta_c = 1.68$. We can linearly extrapolate this barrier to present ($z = 0$), which gives the redshift dependent barrier as $\delta_c(z) = 1.68/D_+(z) > \delta_c(0)$. Here $\delta_c(z)$ is the critical density for collapse at redshift z and D_+ is the growing mode of density perturbations. $\delta_c(z) > \delta_c(0)$ because the halos which formed earlier should have higher overdensity.

Defining $\sigma^2(m)$ as the variance of δ_m at present ($z = 0$), if $m_1 > m_2$, then $\sigma(m_1) < \sigma(m_2)$, with the limiting case of $\sigma(m \rightarrow \infty) = 0$. Using the extended Press-Schechter model (Sheth and Tormen [1999], Sheth et al. [2001]), the collapse fraction at any redshift is,

$$f_{\text{coll}} = \text{erfc} \left[\frac{\delta_c(z) - \delta_m}{\sqrt{2[\sigma_{\text{min}}^2 - \sigma^2(m)]}} \right], \quad (1.16)$$

where, $\sigma_{\text{min}}^2 \equiv \sigma^2(m_{\text{min}})$.

We can use a similar method to calculate the size distribution of self-ionized regions in the early universe. By applying a condition that the collapse fraction within a region needs to be greater than ζ^{-1} , we ensure that the region is self-ionized. Using Eq. 1.15 in Eq. 1.16, we get

$$\zeta^{-1} = \text{erfc} \left[\frac{\delta_c(z) - \delta_x(m, z)}{\sqrt{2[\sigma_{\text{min}}^2 - \sigma^2(m)]}} \right].$$

Here $\delta_x(m, z)$ is the overdensity barrier a region must cross to be self-ionized. Using, $\text{erfc}(x) = 1 - \text{erf}(x)$, and defining, $K(\zeta) = \text{erf}^{-1}(1 - \zeta^{-1})$, we can write the barrier as,

$$\delta_x(m, z) = \delta_c(z) - \sqrt{2} K(\zeta) [\sigma_{\text{min}}^2 - \sigma^2(m)]^{1/2}. \quad (1.17)$$

For simplicity, the barrier can be linearised at $m \rightarrow \infty$ as,

$$B(m, z) = \delta_c(z) - \sqrt{2} K(\zeta) \sigma_{\text{min}} + \frac{K(\zeta) \sigma^2(m)}{\sqrt{2} \sigma_{\text{min}}}. \quad (1.18)$$

To find the self-ionized region, we need to find the first up-crossing of δ above the curve described by $B(m, z)$. Finally, this gives the comoving number density of ionization bubbles in mass range $(m, m + dm)$ (Sheth [1998]) as,

$$m \frac{dn}{dm} = \sqrt{\frac{2}{\pi}} \frac{\bar{\rho}}{m} \left| \frac{d \ln \sigma}{d \ln m} \right| \frac{B_0}{\sigma(m)} \exp \left[-\frac{B^2(m, z)}{2\sigma^2(m)} \right]. \quad (1.19)$$

Here $B_0 \equiv \delta_c(z) - \sqrt{2} K(\zeta) \sigma_{\text{min}}$ is the value of barrier at $m \rightarrow \infty$ and $\bar{\rho}$ is the background mass density.

¹Smoothing a field on scale R essentially means that we average out the information on a scale smaller than this. For this we use a window function which determines *how* different points within the smoothed regions are assigned weight.

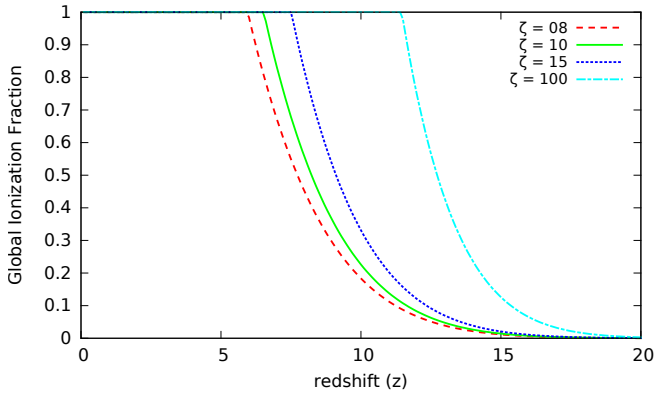


Figure 1.5: Evolution of global ionization fraction (f_i) for different values of ζ . Reionization is completed earlier for higher value of ζ .

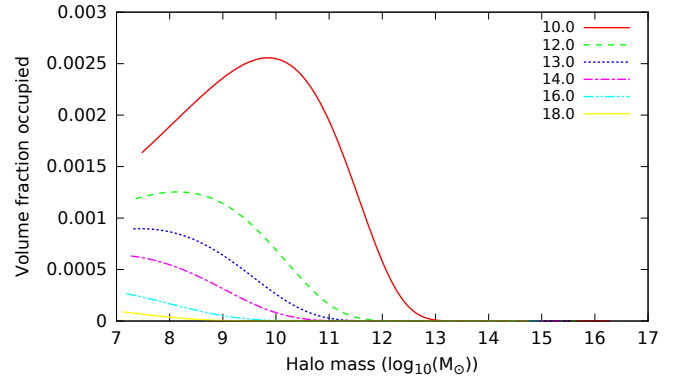


Figure 1.6: Evolution of size distribution of self-ionized regions as function of halo mass for $\zeta = 10$.

Figure 1.5 shows the evolution of the global ionization fraction f_i of the universe as a function of ζ . For higher value of ζ , the reionization is more efficient and is completed earlier (at higher redshift).

In Figure 1.6 we show the distribution of volume fraction occupied by bubbles of different sizes and their evolution with redshift. This figure agrees with the results of [Furlanetto et al. \[2004\]](#) (their Figure 2) for the set of parameters used by them. For the set of parameters used in our work, the self-ionized bubbles are smaller, e.g. at $z = 12$ the peak of the bubble distribution corresponds roughly to a scale of $R_x \simeq 10$ Mpc for [Furlanetto et al. \[2004\]](#), while it peaks at $R_x \simeq 3$ Mpc for our case.

Excursion set formalism has been used extensively for analytic work and semi-numerical simulations of the epoch of reionization, including in the publicly-available code 21cmFAST ([Mesinger et al. \[2011\]](#)). This formalism breaks down when the ionization fraction of the universe is very large since the shapes of the ionized regions become irregular due to significant overlap.

Ionization of Helium: The sources of UV photons which ionized hydrogen were also able to cause first ionization of helium. However, the second ionization of helium requires photons of energy higher than 54.4 eV. Main sources of such hard UV photons are quasars (quasi-stellar objects) which started forming at low redshifts and therefore the complete ionization of helium was delayed until such sources formed ([Morrison et al. \[2019\]](#)).

1.2 Observations

Our understanding of physics during dark ages, cosmic dawn and epoch of reionization is still limited. There is substantial uncertainty about the properties of the dark matter and its interaction with baryons, the formation of large scale structures, the halo cooling mechanism and the feedback processes. Studying these epochs can help us gain useful insights into non-linear structure formation and the evolution of first sources in the universe. It would also provide an independent method to measure cosmological parameters and investigate dark matter models.

To observationally study the physics of this time period, we need to either directly detect the radiation from this epoch or study the distortion (e.g. spectral distortion, spatial inhomogeneity or change in polarization)

of a background radiation that passes through it. For any astrophysical probe, it is essential to ascertain that the signal received had indeed originated from the desired source. For CD/EoR studies, this is a challenge, as we do not completely understand the properties of the sources and medium at high redshifts. We also do not completely understand the properties of local sources (stars, their remnants, dark matter, gas in galaxies and IGM, dust, earth’s atmosphere, other terrestrial sources etc.) which can contaminate or mimic the signal which we are trying to detect. However, if multiple independent probes with different systematics corroborate the same picture, then it would increase our confidence in their detections. We next list the main probes to study the ionization history of the universe (Fan et al. [2006a]).

1.2.1 Scattering of Lyman- α due to Neutral Hydrogen at High Redshift

The high-redshift galaxies and quasars emit radiation around Lyman- α line. These photons are redshifted as they travel in the expanding universe. The photons of higher frequency (bluer) than Lyman- α at the redshift of emission, might redshift into the Lyman- α resonance on their way towards us. At the location where this occurs, if there is substantial neutral hydrogen present in the medium, it will absorb these photons and re-emit them in random directions. This scattering results in an absorption line in the observed spectra of QSOs at frequencies larger than Lyman- α in the rest frame (Field [1962], Scheuer [1965]).

The optical depth of Lyman- α photons in a neutral medium is,

$$\tau_{\text{GP}} \simeq 2.04 \times 10^5 x_{\text{HI}}(1 + \delta)(1 + z)^{3/2},$$

as shall be derived in Section 3.1.1. This optical depth is very large, which means that a very small amount of neutral hydrogen ($x_{\text{HI}}(1 + \delta)$) at a certain point in intergalactic medium is enough to scatter almost all the redshifted Lyman- α radiation. Thus, this test is extremely sensitive to detect the presence of neutral hydrogen, but it can only provide lower bound to the HI number density.

This effect is named after James Gunn and Bruce Peterson, who proposed this as a test of neutral hydrogen in the intergalactic medium at $z \sim 2$ (Gunn and Peterson [1965]). At high redshifts there are multiple lines in the blueward side of such spectra, which suggests the presence of neutral hydrogen in clouds. Studying the distribution of such absorption lines (‘Lyman- α forest’) can help us understand the distribution of HI clouds and the patchiness of the reionization process. Figure 1.7 shows the spectra of quasars from redshift $5.74 < z < 6.42$. Almost complete absorption of radiation of frequency higher than Lyman- α (Gunn Peterson trough) in these spectra, suggests that the universe was transitioning from neutral to ionized state at $z \sim 6$ (Becker et al. [2001], Fan et al. [2006b]).

A similar analysis can also be applied to study the galaxies which emit prominently in the vicinity of Lyman- α line (‘Lyman- α Emitters’) and galaxies which emit prominently in frequency below Lyman-limit, but are dim in Lyman- α (‘Lyman Break galaxies’). Lyman- α fluxes of such galaxies drop between $6 < z < 7$, adding further evidence to the presence of HI at this redshift (Malhotra and Rhoads [2004], Jensen et al. [2013], Dijkstra [2016]). This probe can also be used to study the ionization history of helium through absorption lines of HeI or HeII (Miralda-Escude [1993], Shapiro et al. [1994]). These observations suggest that the ionization of helium was completed by redshift $2 < z < 3$ (Morrison et al. [2019]).

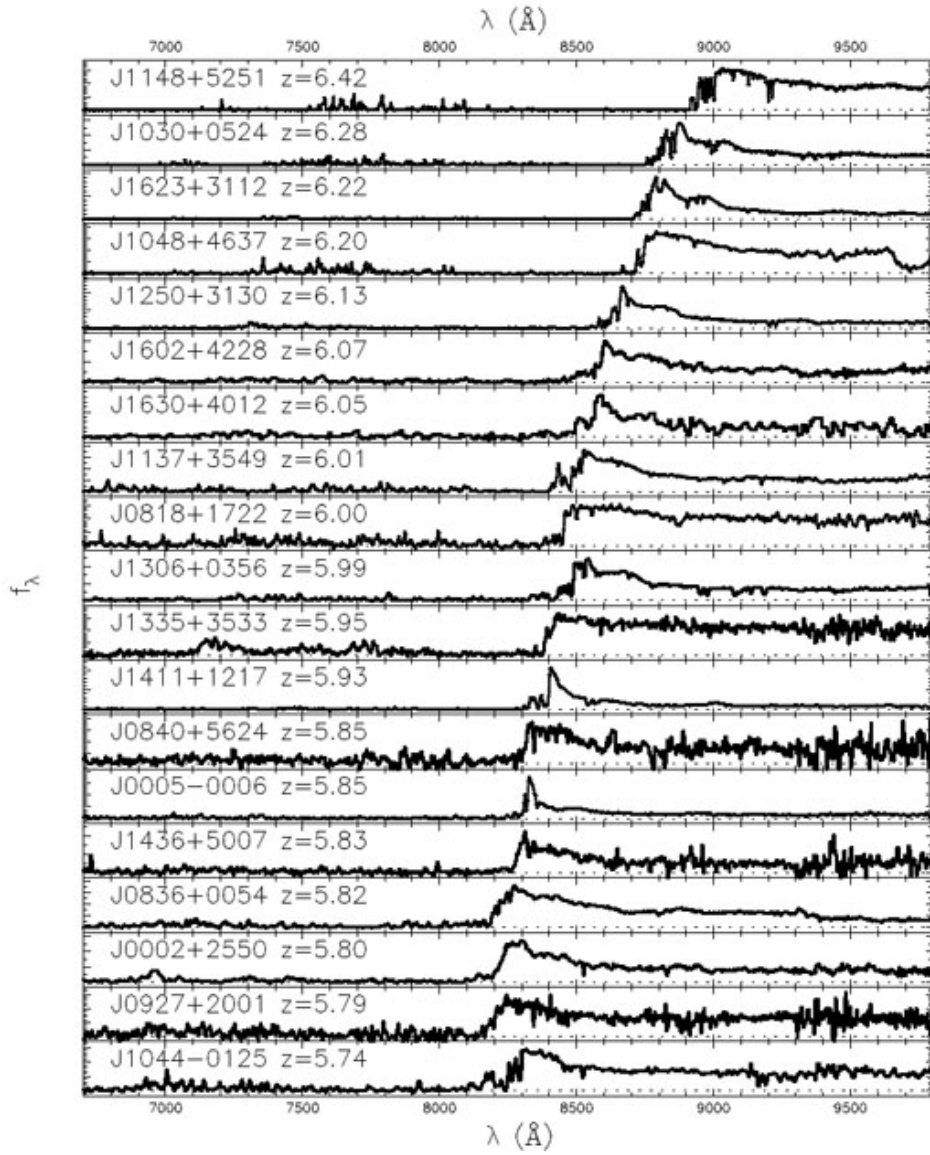


Figure 1.7: Absorption troughs in spectra of SDSS quasars from redshift $5.74 < z < 6.42$, indicating presence of HI in the IGM. These observations suggest that the reionization might have completed around $z \sim 6$ (Courtesy: [Fan et al. \[2006b\]](#)).

1.2.2 Cosmic Microwave Background Radiation

Once the hydrogen in IGM starts getting ionized, the CMB photons once again can interact with the free electrons of the medium they pass through via Thomson scattering. This does not result in complete coupling of CMB and matter, as the number density of the matter particles has fallen by a factor of $\sim 100^3$ since the recombination epoch. The main impact of Thomson scattering of CMB photons with electrons is to cause linear polarization of CMB at large scales (Rees [1968], Hu and White [1997]). The optical depth of scattering is,

$$\begin{aligned}\tau_{\text{reion}} &= \int n_i(z) \sigma_T dl \\ &= \int_0^{z_{\text{ls}}} n_{\text{HI},0} (1+z)^3 f_i(z) \sigma_T \frac{c dz}{(1+z)H(z)},\end{aligned}$$

where, σ_T is Thomson cross-section and $n_i = n_{\text{HI},0} (1+z)^3 f_i$ is the electron number density in the ionized region. Here we have ignored the effect of helium ionization. The upper limit of the integration z_{ls} is the redshift of last scattering surface and we have used light travel distance to calculate integration over photon path. The above equation is useful for calculating the cumulative history of reionization. However, to get a first order approximation, we assume that the universe ionized instantaneously at z_{reion} . We take $f_i = 1$ for $z \leq z_{\text{reion}}$, and 0 otherwise. This gives us,

$$\begin{aligned}\tau_{\text{reion}} &\simeq \frac{c \sigma_T n_{\text{HI},0}}{H_0} \int_0^{z_{\text{reion}}} \frac{(1+z)^2 dz}{[\Omega_\Lambda + (1+z)^3 \Omega_m]^{1/2}} \\ &\simeq \frac{2c \sigma_T n_{\text{HI},0}}{3\Omega_m H_0} [(\Omega_\Lambda + (1+z_{\text{reion}})^3 \Omega_m)^{1/2} - (\Omega_\Lambda + \Omega_m)^{1/2}].\end{aligned}$$

Taking value of $\tau_{\text{reion}} = 0.055$ (Planck Collaboration et al. [2018]), we have, $z_{\text{reion}} \sim 8.43$. By performing more detailed modelling, and including the effect of ionization of helium and the kinetic Sunyaev-Zeldovich effect (Planck Collaboration et al. [2016a]), this value further reduces to $z_{\text{reion}} = 7.75 \pm 0.73$ (Fan et al. [2000], Becker et al. [2001], Hinshaw et al. [2013], Planck Collaboration et al. [2014, 2016b, 2018]). This matches with observations of Gunn-Peterson test¹ since we expect the reionization to be an extended process. Towards the end of EoR, the neutral gas is limited in dense clumps of matter, which are self-shielded from the ionizing photons; and we expect to see them in quasar spectra long after most of the universe has been fully ionized.

The interaction between CMB photons and free electrons also generates a small distortion of the CMB spectrum ('Sunyaev - Zeldovich effect') (Sunyaev and Zeldovich [1972]), which can be also used to probe the history of HI reionization (Carlstrom et al. [2002], McQuinn et al. [2005]).

¹The value of τ_{reion} has changed over the years with better observations. Its initial value, $\tau_{\text{reion}} = 0.17 \pm 0.04$ gave reionization redshift to be $11 < z_{\text{reion}} < 33$ (Spergel et al. [2003]), which was very different from Gunn-Peterson results. Models where the universe was once ionized, became neutral again and ionized again were considered to account for this discrepancy (Cen [2003]). They have been discarded now.

1.2.3 Other Probes

We can observe the bright galaxies from the epoch of reionization and cosmic dawn using deep surveys (e.g. Hubble Space Telescope (Oesch et al. [2013], Ellis et al. [2013], Oesch et al. [2016])) to study the evolution of structures during these epochs. Observational probes to study the redshifted radiation emitted from early sources are expected to be operational in the next decade (e.g. James Webb Space Telescope (JWST), Giant Magellan Telescope (GMT), Extremely Large Telescope (ELT), Thirty Meter Telescope (TMT)). The reionization of hydrogen and helium adds a large amount of energy into the IGM, raising its temperature. After this phase transition, the gas cools with the expansion of the universe. By measuring the IGM temperature at lower redshifts and its evolution, we can potentially determine the redshift of hydrogen and helium reionization (Theuns et al. [2002]).

It is also useful to observe the atomic and ionic lines of the medium surrounding the early sources, which can provide us with indirect information about the nature and distribution of these sources (Meiksin [2009]). These lines include hyperfine splitting of ground state of HI (21 cm line) (Furlanetto et al. [2006], Pritchard and Loeb [2012]) and HeII (Vasiliev et al. [2018]), fine structure line from first excited state of HI (3 cm line) (Dijkstra et al. [2008b]) and the recombination lines from ionized regions. Many ongoing and upcoming experiments are planning to detect the spectral distortion of CMB due to HI 21 cm line from the epoch of cosmic dawn and reionization (summarized in Section 6.1). Experiment to Detect the Global EoR Signature (EDGES) has claimed a detection of a broad global absorption trough of strength 500 mK at $\nu \simeq 78 \pm 10$ MHz (Bowman et al. [2018]); this is the only positive detection of HI signal. In our work, we have explored the possibility of studying the epoch of cosmic dawn and reionization using the 21 cm signal.

1.3 The 21 cm Signal

The ground state of neutral hydrogen splits into two hyperfine levels. The spin of the electron and nucleus (proton) in the ‘triplet’ and ‘singlet’ states are parallel and anti-parallel respectively. When an atom makes a transition from triplet to singlet, it emits a photon of wavelength $\lambda_{21} = 21.1$ cm ($\nu_{21} = 1420.406$ MHz). The triplet state is metastable with transition rate of $A_{21} = 2.85 \times 10^{-15} \text{s}^{-1}$, which makes spontaneous transition from triplet to singlet very difficult. This line was first predicted by Hendrik van de Hulst in 1944 (Van De Hulst [1982]) and was first observed in the HI 21 cm spectra of our Galaxy by Ewen and Purcell [1951].

1.3.1 Spin Temperature

The spin (or excitation) temperature of 21 cm line, T_S , is defined by the ratio of atoms in two hyperfine states,

$$\frac{n_1}{n_0} = \frac{g_1}{g_0} \exp\left(-\frac{h_p \nu_{21}}{k_B T_S}\right). \quad (1.20)$$

Here, h_p is plank constant¹, n_0 and n_1 are number density of atoms in singlet and triplet states respectively², and $g_0 = 1$ and $g_1 = 3$ are degeneracies of these two states. T_S is the thermal temperature the HI gas would have if the number densities of singlet and triplet states were in thermal equilibrium. We can define, $T_\star = h_p \nu_{21}/k_B = 0.068\text{K}$. This value is very small, generally smaller than almost any temperature in the universe if we ignore any exotic physics. Therefore, the ratio of two levels is

$$\frac{n_1}{n_0} \simeq \frac{g_1}{g_0} \left(1 - \frac{T_\star}{T_S}\right) \quad (1.21)$$

$$\text{and} \quad \frac{T_\star}{T_S} \simeq 1 - \frac{g_0 n_1}{g_1 n_0}. \quad (1.22)$$

Given the inefficient spontaneous emission, the value of T_S is determined by the following processes in the early universe which cause transition between these two states (Field [1958]):

1. Background Radiation: 21 cm photons present in the radio background (e.g. CMB) will get absorbed by singlet atoms or cause stimulated emission of triplet atoms. Rate of these two transitions are respectively:

$$P_{01}^\gamma = \frac{g_1}{g_0} \frac{T_\gamma}{T_\star} A_{21}, \quad \text{and} \quad P_{10}^\gamma = \left(1 + \frac{T_\gamma}{T_\star}\right) A_{21}, \quad (1.23)$$

where, T_γ is the radiation temperature. The ratio of upward to downward transition rate for this mechanism is,

$$\frac{P_{01}^\gamma}{P_{10}^\gamma} \simeq \frac{g_1}{g_0} \left(1 - \frac{T_\star}{T_\gamma}\right). \quad (1.24)$$

2. Collisions: The collision of HI with other atoms and charged particles will lead to excitation and de-excitation of hyperfine states, bringing the T_S in equilibrium with kinetic temperature T_K . The ratio of these two rates is,

$$\frac{P_{01}^c}{P_{10}^c} = \frac{g_1}{g_0} \exp\left(-\frac{T_\star}{T_K}\right) \simeq \frac{g_1}{g_0} \left(1 - \frac{T_\star}{T_K}\right). \quad (1.25)$$

We have retained only the first order term for the expansion of exponential because we can assume $T_K \gg T_\star$.

3. Lyman- α : A Lyman- α photon might take an atom from the singlet/triplet state to the first excited state. From there, the atom might de-excited to triple/singlet state, causing a spin-flip (Section 3.1.3). The rate of upward and downward transition is,

$$\frac{P_{01}^\alpha}{P_{10}^\alpha} = \frac{g_1}{g_0} \left(1 - \frac{T_\star}{T_\alpha}\right), \quad (1.26)$$

where, T_α is Lyman- α radiation colour temperature. Repeated scattering of Lyman- α photons by HI atoms at kinetic temperature T_K causes T_α to relax to T_K through Wouthuysen-Field effect (Wouthuysen [1952], Field [1958, 1959], Rybicki and dell'Antonio [1994], Chen and Miralda-Escudé [2004]).

¹We use subscript p to distinguish it from Hubble parameter h .

²For this subsection, the subscript 0 does not indicate $z = 0$.

Detailed Balance: The probability of transition from singlet/triplet state to triplet/singlet state is only a function of atoms in singlet/triplet state and does not depend on the number of atoms already in triplet/singlet state. Therefore, when more than one of these mechanisms is present, the probability of transition by one mechanism will not be affected by the presence of other mechanisms. If singlet and triplet states are in equilibrium, then

$$(P_{01}^\gamma + P_{01}^c + P_{01}^\alpha)n_0 = (P_{10}^\gamma + P_{10}^c + P_{10}^\alpha)n_1. \quad (1.27)$$

Therefore, the ratio of atoms in two levels depends on the transition rates as,

$$\frac{n_1}{n_0} = \frac{P_{01}^\gamma + P_{01}^c + P_{01}^\alpha}{P_{10}^\gamma + P_{10}^c + P_{10}^\alpha}.$$

Using these rates from Eqs. 1.23, 1.25 and 1.26 and ratio of number densities from Eq. 1.21, we get,

$$\frac{g_1}{g_0} \left(1 - \frac{T_\star}{T_S}\right) \simeq \frac{\frac{g_1}{g_0} \frac{T_\gamma}{T_\star} A_{21} + P_{10}^c \frac{g_1}{g_0} \left(1 - \frac{T_\star}{T_K}\right) + P_{10}^\alpha \frac{g_1}{g_0} \left(1 - \frac{T_\star}{T_\alpha}\right)}{\left(1 + \frac{T_\gamma}{T_\star}\right) A_{21} + P_{10}^c + P_{10}^\alpha}.$$

Simplifying this, we get

$$\frac{T_\star}{T_S} \simeq \frac{A_{21} + P_{10}^c \frac{T_\star}{T_K} + P_{10}^\alpha \frac{T_\star}{T_\alpha}}{\left(1 + \frac{T_\gamma}{T_\star}\right) A_{21} + P_{10}^c + P_{10}^\alpha}.$$

Defining collision and Lyman- α coupling coefficients as,

$$y_c = \frac{P_{10}^c}{A_{21}} \frac{T_\star}{T_K} \quad \text{and} \quad y_\alpha = \frac{P_{10}^\alpha}{A_{21}} \frac{T_\star}{T_\alpha} \quad (1.28)$$

respectively, we can write spin temperature as,

$$T_S \simeq \frac{T_\star + T_\gamma + y_c T_K + y_\alpha T_\alpha}{1 + y_c + y_\alpha}. \quad (1.29)$$

In this equation, the T_\star term is negligible compared to other temperatures and is usually dropped. Here, $y_c \propto n_{\text{HI}}, n_e$ (number density of neutral hydrogen atom or electrons) and $y_\alpha \propto n_\alpha$ (number density of Lyman- α photons) determine the efficiency of collisional and Lyman- α coupling, respectively¹ (Chapter 3). Given that $T_\alpha \simeq T_K$, if $y_{\text{tot}} = y_c + y_\alpha \gtrsim T_\gamma/T_K$, then T_S is strongly coupled to T_K . Otherwise, in absence of these coupling mechanisms, it relaxes to T_γ .

In early universe, the only known source of radio background is CMB with blackbody temperature T_{CMB} .

¹If there was any other exotic mechanism (at temperature T_d) which affected the number densities of hydrogen atoms in singlet and triplet states, we can include it as,

$$T_S \simeq \frac{T_\star + T_\gamma + y_c T_K + y_\alpha T_\alpha + y_d T_d}{1 + y_c + y_\alpha + y_d}. \quad (1.30)$$

Hence, we usually assume that $T_\gamma = T_{\text{CMB}}$. However, if other radio sources (with temperature T_R) were present, then we need to use $T_\gamma = T_{\text{CMB}} + T_R$ (Ewall-Wice et al. [2018], Feng and Holder [2018]).

While computing equilibrium between rates of upward and downward transition in Eq. 1.27, we have assumed that all the rates involved are larger than the expansion rate of the universe. Assuming the radiation source to be CMB, the ratio of radiation excitation and the Hubble expansion rate (for matter dominated universe) is,

$$\begin{aligned}\frac{P_{01}^\gamma}{H(z)} &\simeq \frac{3T_0 A_{21}}{T_\star H_0 \sqrt{\Omega_m}} (1+z)^{-1/2} \\ &\simeq 4.17 \times 10^5 (1+z)^{-1/2}.\end{aligned}$$

The de-excitation rate is of the same order of magnitude as the excitation rate. Hence, the hyperfine excitation and de-excitation of HI due to CMB is faster than the expansion rate of the universe at all relevant redshifts. For collisional and Lyman- α coupling,

$$\begin{aligned}\frac{P_{01}^i}{H(z)} &\simeq \frac{T_K}{T_\star} \frac{A_{21}}{H(z)} y_i \\ &\simeq 5.1 \times 10^4 (1+z)^{-3/2} T_K y_i.\end{aligned}$$

This ratio is dependent on the kinetic temperature and the coupling coefficients. When the coupling is weak, the expansion rate of the universe is larger than the excitation and de-excitation rates. However, in this scenario, the balance between hyperfine levels will be mediated by CMB.

Eq. 1.29 can also be written alternatively as (Pritchard and Loeb [2012]),

$$T_S^{-1} = \frac{T_\gamma^{-1} + x_\alpha T_\alpha^{-1} + x_c T_K^{-1}}{1 + x_\alpha + x_c}, \quad (1.31)$$

where the rate coefficients are defined differently as,

$$x_c = \frac{P_{10}^c}{A_{21}} \frac{T_\star}{T_\gamma} \quad \text{and} \quad x_\alpha = \frac{P_{10}^\alpha}{A_{21}} \frac{T_\star}{T_\gamma}. \quad (1.32)$$

1.3.2 Brightness Temperature

When the background CMB radiation passes through a patch of HI at high redshift, 21 cm photons are absorbed from or emitted into this background radiation depending on whether spin temperature of HI is greater than or less than T_{CMB} . The CMB brightness temperature in a patch of sky (r) at redshift z is (Rybicki and Lightman [1979]),

$$T_{\text{CMB}}(r, z) = T_{\text{CMB}}(z) e^{-\tau(r, z)} + T_S(r, z) (1 - e^{-\tau(r, z)}),$$

where τ is the 21 cm optical depth of the patch of HI and $T_{\text{CMB}}(z)$ is the unaltered black body CMB temperature at redshift z . In this expression, the first term is due to the absorption and stimulated emission

of the 21 cm photons in the CMB spectrum by the HI path. The second term accounts for the spontaneous emission from the HI cloud and further absorption and stimulated emission of these photons by the cloud. The change in CMB brightness temperature due to this HI cloud, the *differential* brightness temperature at that patch of sky and redshift, is given as,

$$\begin{aligned}\Delta T_B(r, z) &= T_{\text{CMB}}(r, z) - T_{\text{CMB}}(z) \\ &= -T_{\text{CMB}}(z)(1 - e^{-\tau(r, z)}) + T_S(r, z)(1 - e^{-\tau(r, z)}).\end{aligned}$$

The redshifted 21 cm differential brightness temperature at present is,

$$\Delta T_B(r, \nu_o) = \frac{\Delta T_B(r, z)}{1+z} = \frac{T_S(r, z) - T_{\text{CMB}}(z)}{1+z} (1 - e^{-\tau(r, z)}), \quad (1.33)$$

where, the observed frequency is $\nu_o = \nu_{21}/(1+z)$ due the redshifting of photons. The 21 cm optical depth is the integration of absorption coefficient α_ν along the light travel path, $\tau(r, z) = \int \alpha_\nu(r, z) dl$. The absorption coefficient incorporates the absorption and stimulated emission of 21 cm photon (Rybicki and Lightman [1979]),

$$\alpha_\nu = \frac{h_p \nu}{4\pi} n_0 B_{01} \left(1 - \frac{g_0 n_1}{g_1 n_0} \right) \phi(\nu). \quad (1.34)$$

Here B_{01} is the Einstein B coefficient. The line profile function $\phi(\nu)$ can be approximated as $\phi(\nu) \sim \Delta\nu^{-1}$, where $\Delta\nu$ is the resonance line width. For 21 cm line, the natural broadening is very small, therefore the resonance line width is dominated by the motion (velocity ν) of the atoms. In static cloud of HI, this line width is due to thermal (Doppler) broadening. In cosmological setting, this width is dominated by the cosmic expansion and peculiar velocity of the gas. Hence,

$$\nu \phi(\nu) \simeq \frac{\nu}{\Delta\nu} = \frac{c}{\nu} = \frac{c}{\left(H(z) + \frac{1}{a(t)} \frac{dv}{dt} \right) \Delta l}. \quad (1.35)$$

The peculiar velocity of HI is generally very small compared to the expansion velocity, and we ignore its effect ('Redshift Space Distortion') in our work.

Here Δl is the typical distance a 21 cm photon would travel before it is redshifted out of the resonance width, after which it will not interact with the HI gas. Therefore, this gives the integration limit of optical depth. The value of Δl is very small, therefore we can assume that all the properties of the gas (temperatures, density, etc.) will remain constant over this length. Thus using Eq. 1.34 and 1.35, we have,

$$\tau(r, z) \simeq \alpha_\nu(r, z) \Delta l \simeq \frac{h_p \nu}{4\pi} n_0 B_{01} \left(1 - \frac{g_0 n_1}{g_1 n_0} \right) \frac{c}{\nu H(z)}. \quad (1.36)$$

Substituting the value of T_S from Eq. 1.22 and $g_1/g_0 = 3$ in Eq. 1.36, and exploiting the relation between Einstein A and B coefficients (Appendix D), we have,

$$\tau(r, z) \simeq \frac{h_p \nu}{4\pi} n_0 \left(3A_{21} \frac{c^2}{2h_p \nu^3} \right) \left(\frac{T_\star}{T_S} \right) \frac{c}{\nu H(z)}$$

$$\simeq \frac{3}{8\pi} A_{21} n_0 \frac{c^3 T_\star}{v^3 T_S} \frac{1}{H(z)}. \quad (1.37)$$

The number density of singlet atoms can be approximated as,

$$n_0 = \frac{n_0}{n_0 + n_1} n_{\text{HI}} = \frac{g_0}{g_0 + g_1 \left(1 - \frac{T_\star}{T_S}\right)} n_{\text{HI}} \simeq \frac{1}{4} \left(x_{\text{HI}}(1 + \delta) n_{\text{HI},0} (1 + z)^3\right).$$

Here, we have ignored the $(1 - T_\star/T_S)$ factor in the denominator, since its effect is negligible. Substituting this in Eq. 1.37 and using the value of $n_{\text{HI},0}$ from Appendix C, we get

$$\tau(r, z) \simeq \frac{3}{8\pi} \left(\frac{1}{4} x_{\text{HI}}(1 + \delta)\right) \frac{3}{4} \Omega_b \frac{3H_0^2}{8\pi G m_p} (1 + z)^3 A_{21} \frac{c^3 T_\star}{v^3 T_S} \frac{1}{H(z)}.$$

Here, x_{HI} is the neutral fraction of HI gas and δ is the overdensity. For matter dominated universe, the optical depth is,

$$\begin{aligned} \tau(r, z) &\simeq \frac{3^3}{32^2 \pi^2} \frac{A_{21} h_p c^3}{G m_p k_B v^2} \frac{H_0 x_{\text{HI}}(1 + \delta)}{h T_S} \frac{\Omega_b h^2}{(\Omega_m h^2)^{1/2}} (1 + z)^{3/2} \\ &\simeq 8.435 \times 10^{-3} \frac{x_{\text{HI}}(1 + \delta)}{T_S} \left(\frac{\Omega_b h^2}{0.022}\right) \left(\frac{0.14}{\Omega_m h^2}\right)^{1/2} (1 + z)^{3/2} \text{ K}. \end{aligned} \quad (1.38)$$

As this optical depth is very small ($\tau \ll 1$), we can approximate $1 - e^{-\tau(r, z)} \simeq \tau(r, z)$ in Eq. 1.33. The final value of differential brightness temperature is,

$$\begin{aligned} \Delta T_B(r, \nu_o) &\simeq \frac{T_S(r, z) - T_{\text{CMB}}(z)}{1 + z} \tau(r, z) \\ &\simeq 26.67 x_{\text{HI}}(1 + \delta) \left(1 - \frac{T_{\text{CMB}}(z)}{T_S}\right) \left(\frac{1 + z}{10} \frac{0.14}{\Omega_m h^2}\right)^{1/2} \left(\frac{\Omega_b h^2}{0.022}\right) \text{ mK}. \end{aligned} \quad (1.39)$$

The CMB spectral distortion caused by this effect is observable (Madau et al. [1997], Shaver et al. [1999], Gnedin and Shaver [2004], Sethi [2005]) and it contains information about density (δ), ionization (x_{HI}) and spin temperature (T_S) of the gas from where it originated. The value of ΔT_B is function of both redshift of observation (through ν_o) and the direction. The globally averaged value of this signal at any redshift is

$$\langle \Delta T_B(\nu_o) \rangle \simeq 26.67 \langle x_{\text{HI}} \rangle \left\langle 1 - \frac{T_{\text{CMB}}(z)}{T_S} \right\rangle \left(\frac{1 + z}{10} \frac{0.14}{\Omega_m h^2}\right)^{1/2} \left(\frac{\Omega_b h^2}{0.022}\right) \text{ mK}. \quad (1.40)$$

Here the global average of ionization is the ionization volume fraction of the universe ($\langle x_{\text{HI}} \rangle = f_i$) and the global average of overdensity is zero ($\langle \delta \rangle = 0$).

1.3.3 21 cm Signal from Early Universe

- During the early dark ages ($1000 < z < 150$) the matter temperature T_K is still coupled to T_{CMB} . Therefore, irrespective any coupling mechanism, $T_S = T_{\text{CMB}}$ and the differential brightness temperature $\Delta T_B = 0$.

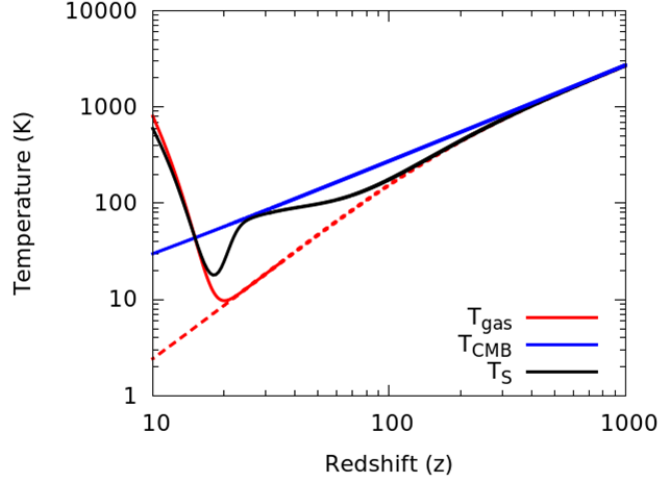


Figure 1.8: Evolution of T_{CMB} (blue curve), T_K (T_{gas} , red curve) and T_S (black curve) for a fiducial model. The dashed red curve shows the evolution of T_K without any heating sources.

- After matter thermally decouples from the CMB ($150 < z < 30$), the baryonic gas cools faster than CMB ($T_K < T_{\text{CMB}}$). Collisions couple T_S to matter temperature T_K , and the $\Delta T_B < 0$ (dark ages absorption trough).
- With the expansion of the universe ($z \sim 30$), the density and temperature of the gas decrease, the collisions become inefficient, driving the $T_S \rightarrow T_{\text{CMB}}$ and $\Delta T_B \rightarrow 0$.
- When the first sources of radiation form during cosmic dawn, the production of Lyman- α photons once again couple T_S to T_K . Initially, the baryonic gas at T_K is colder than the T_{CMB} , and the signal is in absorption with $\Delta T_B \leq 0$ (CD/EoR absorption trough).
- The gas can be heated due to X-rays emitted from the sources ($T_K > T_{\text{CMB}}$) and the signal would be in emission with $\Delta T_B \geq 0$.
- Finally when the gas has completely ionized, $x_{\text{HI}} = 0$ and hence the brightness temperature $\Delta T_B = 0$.

A plot for evolution of T_{CMB} , T_K and T_S for a fiducial model is show in Figure 1.8.

1.3.4 Simulations and Analytical Formalisms

The HI signal from the epoch of cosmic dawn and reionization has been extensively studied in the literature using semi-analytic methods and large-scale simulations (e.g. Pritchard and Furlanetto [2007], Santos et al. [2008], Baek et al. [2010], Santos et al. [2010], Mesinger et al. [2011], Visbal et al. [2012], Tashiro and Sugiyama [2013], Mesinger et al. [2013], Pacucci et al. [2014], Fialkov et al. [2014, 2015], Ghara et al. [2015], Mesinger et al. [2016], Fialkov et al. [2017], Ross et al. [2017]). These N -body simulations are affected by both the box-size of the simulation and grid-size of cells. If the box-size is not large enough, the coupling of short and long scales cannot be computed properly. On the other hand, if the number density of particles in a simulation is not large enough, then small scale structures are not resolved. Given

the complicated physics at very small and large scale, as well as multiple time scales, it is not possible to completely simulate cosmic dawn and EoR in-depth with current technology.

Numerical simulations can provide insight into the morphology and evolution of the sources in the early universe, however, given the uncertainty in the astrophysics of this epoch, analytical methods are better suited to predict the statistical quantities like correlation function and power spectrum. Compared to numerical simulations, these estimates are computationally inexpensive, as well as orders of magnitude faster, which makes it possible to analyse a large set of possible modelling parameters and their degeneracies at a fraction of computational resources and time. The analytical methods are not limited by the size of the simulation box, therefore a variety of physical process happening at very small or very large scale can be easily incorporated.

In our work, we developed a formalism based on geometric and probabilistic arguments to analytically compute the autocorrelation and power spectrum of HI signal in the early phase of CD/EoR. Our method cannot predict the shape of individual regions, but it allows us to compute the statistics of the HI field and compare the observed signal for multiple sets of parameters. It needs to be emphasized that, our formalism is not perfect, as we still need to relax several simplifying assumptions (Section 5.6). However, since N -body simulations, semi-analytical and analytical formalisms each have their own set of assumptions, strengths and weakness, it is beneficial to compare results obtained by different methods. If the predictions of all these methods match, it increases our confidence in the results; if they do not match, it might lead us to a deeper insight of the physics of the early universe and the shortcoming of our methodologies.

1.4 Thesis Plan

In the present chapter, we reviewed the HI signal from CD/EoR and the motivation to study it. In Chapter 2, we calculate the impact of X-ray heating on the medium surrounding ionization bubbles. In Chapter 3, we calculate the strength of HI spin temperature coupling with matter temperature through Lyman- α photons and collisions. In Chapter 4, we present our formalism for computing the two-point correlation function of the HI signal. We also discuss various approximations, assumptions, and limits germane to our formalism. We summarize our results in Chapter 5 and explore their dependence on various modelling parameters as well as the assumptions taken in this work. We make concluding remarks in Chapter 6 and summarise the current status of observational detection of cosmological 21 cm signal. We give a list of useful constants, expressions and geometrical functions used in our work in the Appendix.

In our computations, we assume the spatially-flat Λ CDM model of the universe, with the cosmological parameters from Planck 2015 (Planck Collaboration et al. [2016b]) and Planck 2018 (Planck Collaboration et al. [2018]): $\Omega_m = 0.310$, $\Omega_B = 0.049$, $h = 0.677$ and $n_s = 0.967$, with the overall matter power spectrum normalization corresponding to $\sigma_8 = 0.808$. The matter power spectrum of the Λ CDM model is generated using publicly-available code CMBFAST (Seljak and Zaldarriaga [1996]).

Chapter 2

Temperature Evolution of the IGM

“The idea hovered and shimmered delicately, like a soap bubble, and she dared not even look at it directly in case it burst. But she was familiar with the way of ideas and she let it shimmer, looking away, thinking about something else.”

— Philip Pullman, *Northern Lights*

2.1 X-Ray Heating

Accretion in X-ray binaries and stellar remnants at high redshifts emit X-ray photons (photons of energy higher than 100 eV¹). We assume that the X-ray source luminosity is a power law function (Mesinger et al. [2011]),

$$\dot{N}_\nu = \dot{N}_t \left(\frac{\nu}{\nu_{\min}} \right)^{-\alpha}, \quad (2.1)$$

where ν_{\min} is the lowest frequency (in the rest frame of the source) of X-ray photons escaping from the sources. It is expected that high-mass X-ray binaries would emit harder X-ray spectra than stellar remnants (Fialkov et al. [2014]). Therefore we can use different values of α to represent different types of sources. For higher value of α (more negative power), there are lesser photons with high frequency, which suggests a softer spectrum. By using more than one combination of modelling parameters (α, ν_{\min}), we can model the effect of multiple types of sources, but we do not attempt such modelling in our work. We have,

$$\frac{d\dot{N}_\nu}{d\nu} = -\alpha \dot{N}_t \left(\frac{\nu}{\nu_{\min}} \right)^{-\alpha} \nu^{-1}, \quad (2.2)$$

which shows that the source luminosity decreases with increasing frequency. We drop the negative sign for the rest of the derivation. Given the dynamic nature of X-ray sources, the X-ray luminosity of a halo

¹We use photon energy and frequency interchangeably and both are given in eV.

depends on the number of sources *being formed* per time and not the number of sources *already present*.

$$\begin{aligned}\dot{N}_t &= \frac{\text{number of X-ray photons emitted}}{\text{time}} \\ &= \frac{\text{number of X-rays emitted}}{\text{number of baryons in stars}} \frac{\text{number of baryons in stars}}{\text{number of collapsed baryons}} \frac{\text{number of collapsed baryons}}{\text{time}}.\end{aligned}$$

Here the fraction of collapsed baryons that is converted into stars is f_* , and we define N_{heat} as the number of X-ray photons emitted per stellar baryons.

The number of baryons collapsing per unit time should be calculated at the redshift when the sources were forming in the halo, and not when they started emitting X-rays after being converted into binaries. In our work, we do not study detailed evolution of sources; therefore, we ignore this time delay and calculate the baryons which were collapsing when the X-rays were being emitted. The number of baryons collapsing within an ionization bubble per unit time can be linked to the growth of this bubble. Therefore,

$$\dot{N}_t = N_{\text{heat}} f_* \frac{d(N_{\text{halo}} f_{\text{coll,ion}})}{dt}, \quad (2.3)$$

where, $N_{\text{halo}} = 4\pi/3 R_x^3 n_{b,0}$ is the number of baryons¹ in a self-ionized region of radius R_x . Within this region, the collapse fraction is $f_{\text{coll,ion}} = 1/\zeta$. Given the definition of ζ and self-ionized regions, $f_{\text{coll,ion}}$ remains constant as the size of the halo (N_{ion}) increases (Section 1.1.4).

In our work, we do not follow the evolution of individual ionization bubbles. The only information we have is their size distribution at any redshift calculated using excursion set formalism (Section 1.1.4). Therefore we assume that the growth of an ionization bubble is proportional to the growth of global collapse fraction, $f_{\text{coll,g}}$ at that redshift. We write,

$$\begin{aligned}\frac{d(N_{\text{halo}} f_{\text{coll,ion}})}{dt} &= N_{\text{halo}} f_{\text{coll,ion}} \frac{\dot{f}_{\text{coll,g}}}{f_{\text{coll,g}}} \\ &= \frac{4\pi}{3} R_x^3 n_{b,0} \frac{1}{\zeta} \frac{\dot{f}_{\text{coll,g}}}{f_{\text{coll,g}}}.\end{aligned} \quad (2.4)$$

Here we have ignored the fact that we expect high density regions within an ionized region to be collapsing faster than the average of all sources in every part of the universe. Replacing these values in Eq. 2.2, we get the number of X-ray photons of frequency ν emitted by the source, per unit time, per unit frequency,

$$\frac{d\dot{N}_\nu}{d\nu} = \frac{4\pi}{3} R_x^3 \frac{\alpha N_{\text{heat}} f_* n_{b,0}}{\zeta \nu} \frac{\dot{f}_{\text{coll,g}}}{f_{\text{coll,g}}} \left(\frac{\nu}{\nu_{\text{min}}} \right)^{-\alpha}. \quad (2.5)$$

These X-rays of energy $E \gg 13.6\text{eV}$ are not absorbed in the HI region, but escape into the surrounding neutral medium.

¹We have again used the number of hydrogen atoms and number of baryons interchangeably. This makes a small difference.

2.1.1 Photoionization and Heating of the Medium

X-rays emitted from the sources are absorbed by the neutral hydrogen and helium in the IGM. This process emits an energetic photoelectron, which causes secondary ionization and excitations into the medium. Depending on the electron fraction and temperature of the medium, the energy of the photoelectron gets divided into heating, ionization and excitation of the medium (Shull and van Steenberg [1985], Venkatesan et al. [2001]).

A neutral medium is ionized up to 10% by X-rays, after which the energy gone into further ionization is negligible. In our work, we neglect the effect of this partial ionization caused by X-rays and assume the medium outside an ionization bubble to be comprised of neutral hydrogen and neutral helium with primordial abundances. For small ionization fraction of the medium, the fraction of energy of the photoelectron that goes into heating of the medium is $f_H = 0.15$ (Shull and van Steenberg [1985], Venkatesan et al. [2001]). This is a function of ionization fraction and approximately independent of X-ray frequency for $\nu > 100$ eV.

In this subsection, we try to calculate the kinetic temperature profile around an ionization bubble of X-ray sources. Here primed quantities are calculated at the receiving point (point P), un-primed quantities are at the source (point S), and quantities with 0 subscript are comoving quantities. The probability of ionization of species i by a photon of frequency ν' in a shell of thickness dl' is,

$$P(i, \nu') = n'_i \sigma_i(\nu') dl'. \quad (2.6)$$

Here $n'_i = x'_i n_{b,0} (1 + z')^3$ is the local number density of species i , with x'_i being the local number fraction of species i . Assuming that in the mostly neutral medium, the fraction of ionized hydrogen and singly ionized helium is the same, we have

$$\begin{aligned} x_{\text{HI}} &= \frac{12}{13} x_n & x_{\text{HII}} &= \frac{12}{13} (1 - x_n) \\ x_{\text{HeI}} &= \frac{1}{13} x_n & x_{\text{HeII}} &= \frac{1}{13} (1 - x_n), \end{aligned}$$

where, x_n is the neutral fraction of the medium. We have ignored the effects of doubly ionized helium, which require very high energy photons. $n_{b,0} = 9.14 \times 10^{-6} \Omega_b h^2$ is the number density of baryons at present (Appendix C). The photoionization cross-section of species i by an X-ray photon of frequency ν' is,

$$\sigma_i(\nu') = \sigma_{i,0} \left(\frac{\nu'}{\nu_i} \right)^{-3}, \quad (2.7)$$

where, ν_i is the ionization threshold frequency and $\sigma_{i,0}$ is the ionization cross-section of a particle of species i . We have used the approximate expressions for the frequency dependence of the ionization cross-section of HI and HeI; for more precise expressions see Osterbrock [1989]. This gives the probability of absorption:

$$P(i, \nu') = x'_i n_{b,0} (1 + z')^3 \sigma_{i,0} \left(\frac{\nu'}{\nu_i} \right)^{-3} dl'. \quad (2.8)$$

The ratio of probability of absorption by HI and HeI is,

$$\frac{P(\text{HI}, \nu')}{P(\text{HeI}, \nu')} \simeq \frac{x_{\text{H}} \sigma_{\text{H},0} \nu_{\text{H}}^3}{x_{\text{He}} \sigma_{\text{He},0} \nu_{\text{He}}^3} \simeq 0.52. \quad (2.9)$$

Therefore, $\sim 2/3$ X-ray photons are absorbed by helium.

Mean Free Path of X-rays: The physical mean free path of an X-ray photon of frequency ν , is

$$\begin{aligned} \bar{l} &= \frac{1}{n\sigma} \simeq \frac{1}{(1+z)^3} \frac{\nu^3}{n_{\text{HI},0} \sigma_{\text{HI},0} \nu_{\text{HI}}^3 + n_{0,\text{He}} \sigma_{\text{HeI},0} \nu_{\text{HeI}}^3} \\ &\simeq 3.76 \times 10^{-5} \left(\frac{\nu}{1+z} \right)^3 \text{ Mpc}, \end{aligned} \quad (2.10)$$

which agrees with [Furlanetto et al. \[2006\]](#). As the photon travels through the medium, its frequency decreases, which increases the cross-section. But the decrease in number density of hydrogen atoms with redshift cancels this effect and the probability of the absorption of the X-ray photon is not altered significantly.

The low-frequency X-ray photons have lower mean free paths and they are absorbed with higher probability. They heat up the medium immediately surrounding the HII regions, whereas the high-frequency photons free stream through the medium and might get absorbed far away from any source. For example, at $z = 20$, the physical¹ mean free path of X-ray photons of frequency $\nu \simeq 100$ eV and $\nu \simeq 1$ keV are $l \simeq 4.06$ kpc and $l \simeq 4.06$ Mpc respectively. At $z = 15$, these mean free path are $l = 9.18$ kpc and $l = 9.18$ Mpc respectively.

Hard X-rays with large mean free paths heat up the whole IGM to some uniform background temperature T_{bg} . The heating caused by soft X-rays around individual sources adds to the spatial fluctuations of kinetic temperature. In our work, we divide the neutral regions into two zones. In the *near zone* the heating is dominated by X-ray photons from an individual self-ionized region and in the *far zone*, the average contribution from the all the background sources is taken into account.

Very high energy photons are not absorbed until the completion of the reionization of the universe. We do not consider the increase in UV flux due to redshifted X-ray photons. The frequency of an X-ray photon emitted at the beginning of cosmic dawn $z \sim 30$ will decrease by a factor of 5 by the completion of reionization. Since the soft X-rays photons are absorbed locally, they will not have a chance to redshift to the UV band; and the redshifting of hard X-ray photons will not put them in this band.

Optical Depth of the Medium: The X-ray optical depth of the medium (at z') between source S (at z) and receiving point P (at z'') is,

$$\tau = \int_S^P dl' \sum_i n'_i \sigma'_i.$$

Using Eq. 2.8, we get

$$\tau = \int_S^P dl' \sum_i n_{b,0} x'_i (1 + \delta') (1 + z')^3 \sigma_{i,0} \left(\frac{\nu_i}{\nu'} \right)^3$$

¹Given the large mean free paths for high frequency photons, these distances should be interpreted as *light travel* distance.

$$= n_{b,0} \int_S^P dl' \frac{x'_n(1+\delta')(1+z')^3}{v'^3} \sum_i x_i \sigma_{i,0} v_i^3. \quad (2.11)$$

We have divided the fraction of a species in two factors as $x'_i = x'_n x_i$, where x'_n is the neutral fraction of the medium and x_i is the primordial fraction of species i . If the point P is very close to the source, then the quantities within the distance integral will remain constant over the integral. X-ray photons are not absorbed in the ionized region, so we integrate this term from the boundary of the ionization bubble (at X) to point P . Assuming $\delta' = 0$,

$$\begin{aligned} \tau &= n_{b,0} \int_X^P dl' \frac{(1+\delta')(1+z')^3}{v'^3} \sum_i x_i \sigma_{i,0} v_i^3 \\ &\simeq \frac{n_{b,0}(1+z')^3}{v'^3} R_\gamma \sum_i x_i \sigma_{i,0} v_i^3, \end{aligned} \quad (2.12)$$

where R_γ is the light travel distance between X and P . We note here that since the mean free path of soft photons is a few kpc, calculating the optical depth from the centre of the ionization bubble and calculating it from the boundary of the bubble changes the temperature immediately surrounding the ionization bubble drastically. However, the temperature far away from the source is not affected much due to this effect. The optical depth of the medium for a photon of fixed frequency ν is decreasing with the expansion of the universe since the number density of the particle decreases.

2.1.2 Temperature Profile around X-ray Sources

First, we assume that an X-ray photon is emitted by the source at z (point S) and it is absorbed by an atom at z' (point P). Energy obtained by electrons due to ionization of species i , per unit time, per unit comoving volume, per unit frequency at comoving distance R_0 from the source is,

$$\frac{dE'_{\nu'}(i)}{dt' d\nu' dV_0} = (h_p \nu' - h_p \nu_i) \frac{dN'_{\nu'}}{dt' d\nu' dV_0} P(i, \nu'), \quad (2.13)$$

where, $dN'_{\nu'}/(dt' d\nu' dV_0)$ is the number of photons of frequency ν' arriving at distance R_0 , per unit time, per unit frequency, and per unit comoving volume. $P(i, \nu')$ is the probability of atom of species i getting ionized by a photon of frequency ν' if such a photon were present (Eq. 2.8) and $(h_p \nu' - h_p \nu_i)$ is the energy of the emitted photoelectron if an atom of species i was ionized by photon of frequency ν' . Assuming a neutral medium and taking into account the contribution due to all species, we get,

$$\begin{aligned} \frac{dE'_{\nu'}}{dt' d\nu' dV_0} &= \frac{dN'_{\nu'}}{dt' d\nu' dV_0} \sum_i h_p (\nu' - \nu_i) x_i n_{b,0} (1+z')^3 \sigma_{i,0} \left(\frac{\nu'}{\nu_i}\right)^{-3} dl' \\ &= h_p n_{b,0} \frac{dN'_{\nu'}}{dt' d\nu' dA_0} \frac{dl'}{dl_0} \frac{(1+z')^3}{v'^3} \sum_i (\nu' - \nu_i) x_i \sigma_{i,0} v_i^3. \end{aligned} \quad (2.14)$$

The number of photons of frequency ν' received at distance R_0 from the source per unit area, per unit time, per unit frequency are,

$$\frac{dN'_{\nu'}}{dt'd\nu'dA_0} = \frac{d\dot{N}_\nu}{d\nu} \frac{1}{4\pi R_0^2} e^{-\tau(R_0, \nu')}, \quad (2.15)$$

where, $d\dot{N}_\nu/d\nu$ are the number of photons emitted from the source per unit time, per unit frequency and $\tau(R_0, \nu')$ is the optical depth of the medium. Using Eq. 2.15 in Eq. 2.14, and noting that $dl_0 = dl'(1+z')$ we get,

$$\frac{dE'_{\nu'}}{dt'd\nu'dV_0} = h_p n_{b,0} \frac{d\dot{N}_\nu}{d\nu} \frac{1}{4\pi R_0^2} e^{-\tau(R_0, \nu')} \frac{(1+z')^2}{\nu'^3} \sum_i (\nu' - \nu_i) x_i \sigma_{i,0} \nu_i^3. \quad (2.16)$$

Using the value of source luminosity from Eq. 2.5, we get,

$$\begin{aligned} \frac{dE'_{\nu'}}{dt'd\nu'dV_0} &= h_p n_{b,0} \left(\frac{4\pi}{3} R_x^3 \frac{\alpha N_{\text{heat}} f_\star n_{b,0} \dot{f}_{\text{coll,g}}}{\zeta \nu} \left(\frac{\nu}{\nu_{\text{min}}} \right)^{-\alpha} \right) \frac{1}{4\pi R_0^2} e^{-\tau(R_0, \nu')} \frac{(1+z')^2}{\nu'^3} \sum_i (\nu' - \nu_i) x_i \sigma_{i,0} \nu_i^3 \\ &= h_p n_{b,0}^2 \frac{\alpha N_{\text{heat}} f_\star \nu_{\text{min}}^\alpha}{3 \zeta} \frac{R_x^3 \dot{f}_{\text{coll,g}}}{R_0^2 f_{\text{coll,g}}} \frac{(1+z')^2}{\nu'^{\alpha+4}} \left(\frac{1+z'}{1+z} \right)^{\alpha+1} e^{-\tau(R_0, \nu')} \sum_i (\nu' - \nu_i) x_i \sigma_{i,0} \nu_i^3. \end{aligned} \quad (2.17)$$

We integrate this over all frequencies $\nu > \nu_{\text{min}}$ to get energy per emitted photoelectron, per unit time, per unit comoving volume at distance R_0 from the centre of a self-ionized region of radius R_x . We assume that $f_H = 0.15$ fraction of the energy of these photoelectrons goes into heating the medium, which gives,

$$\frac{dE_{\text{heat}}}{dt'dV_0} = \frac{h_p n_{b,0}^2}{3} \frac{f_H \alpha N_{\text{heat}} f_\star \nu_{\text{min}}^\alpha}{\zeta} \frac{(1+z')^{\alpha+3}}{(1+z)^{\alpha+1}} \frac{R_x^3 \dot{f}_{\text{coll,g}}}{R_0^2 f_{\text{coll,g}}} \int_{\nu'_{\text{min}}}^{\infty} d\nu' \frac{e^{-\tau(R_0, \nu')}}{\nu'^{\alpha+4}} \sum_i (\nu' - \nu_i) x_i \sigma_{i,0} \nu_i^3, \quad (2.18)$$

where, $\nu'_{\text{min}} = \nu_{\text{min}}(1+z')/(1+z)$ is the minimum frequency from the source that reaches P . We can integrate Eq. 2.18 over the history of the source to get the total energy converted into heating the medium. However, with the expansion of the universe, the medium is also cooling adiabatically. If z'_c is the redshift at which we want to compute the temperature profile, then the source redshift is z_c . We multiply the energy received at higher redshift (z') by $(1+z'_c)^2/(1+z')^2$ factor to account for this effect. Therefore,

$$\begin{aligned} \frac{dE'_{\text{heat}}}{dV_0} &= \frac{h_p n_{b,0}^2}{3} \frac{f_H \alpha N_{\text{heat}} f_\star \nu_{\text{min}}^\alpha}{\zeta} \int_{t(z_\star)}^{t(z_c)} dt' \frac{R_x^3(t')}{R_0^2} \frac{(1+z')^{\alpha+3}}{(1+z)^{\alpha+1}} \frac{\dot{f}_{\text{coll,g}}}{f_{\text{coll,g}}} \frac{(1+z'_c)^2}{(1+z')^2} \\ &\quad \int_{\nu'_{\text{min}}}^{\infty} d\nu' \frac{e^{-\tau(R_0, \nu')}}{\nu'^{\alpha+4}} \sum_i (\nu' - \nu_i) x_i \sigma_{i,0} \nu_i^3. \end{aligned} \quad (2.19)$$

Here z_\star is the source redshifts corresponding to formation of first sources and $R_x(t')$ is the radius of the given ionized region at time t' in past. This is not a straightforward quantity to calculate as excursion set formulation doesn't give the time evolution of the radius of a particular self-ionized region. Given that the formalism allows us to compute the evolution of the average ionized fraction f_i , we assume $R_x^3(t') =$

$R_x^3(t)(f_i(t')/f_i(t))$. This gives,

$$\frac{dE'_{\text{heat}}}{dV_0} = \frac{h_p n_{b,0}^2}{3} \frac{f_H \alpha N_{\text{heat}} f_{\star} v_{\text{min}}^{\alpha}}{\zeta} \frac{R_x^3}{R_0^2} (1+z'_c)^2 \int_{t(z_{\star})}^{t(z_c)} dt' \frac{f_i(t')}{f_i(t)} \frac{\dot{f}_{\text{coll,g}}}{f_{\text{coll,g}}} \left(\frac{1+z'}{1+z} \right)^{\alpha+1} \int_{v'_{\text{min}}}^{\infty} dv' \frac{e^{-\tau(R_0, v')}}{v'^{\alpha+4}} \sum_i (v' - v_i) x_i \sigma_{i,0} v_i^3. \quad (2.20)$$

Note that if we know the exact collapse and merger history of a particular ionization bubble, then we can replace the $(f_i(t')/f_i(t))(\dot{f}_{\text{coll,g}}/f_{\text{coll,g}})$ factor with appropriate time dependent values. The final increase in temperature at redshift z'_c , due to a self-ionized region of radius R_x at distance R_0 is,

$$\Delta T' = \frac{1}{n_{b,0} k_B} \frac{dE'_{\text{heat}}}{dV_0} = \frac{h_p n_{b,0}}{3 k_B} \frac{f_H \alpha N_{\text{heat}} f_{\star} v_{\text{min}}^{\alpha}}{\zeta} \frac{R_x^3}{R_0^2} (1+z'_c)^2 \int_{t(z_{\star})}^{t(z_c)} dt' \frac{f_i(t')}{f_i(t)} \frac{\dot{f}_{\text{coll,g}}}{f_{\text{coll,g}}} \left(\frac{1+z'}{1+z} \right)^{\alpha+1} \int_{v'_{\text{min}}}^{\infty} dv' \frac{e^{-\tau(R_0, v')}}{v'^{\alpha+4}} \sum_i (v' - v_i) x_i \sigma_{i,0} v_i^3. \quad (2.21)$$

Here we have assumed that the energy of the photoelectron is shared by HI and HeI. If the ionization fraction is large or if baryonic matter is coupled to dark matter particles, the number of particles sharing the energy should be modified accordingly.

2.1.3 Background Temperature

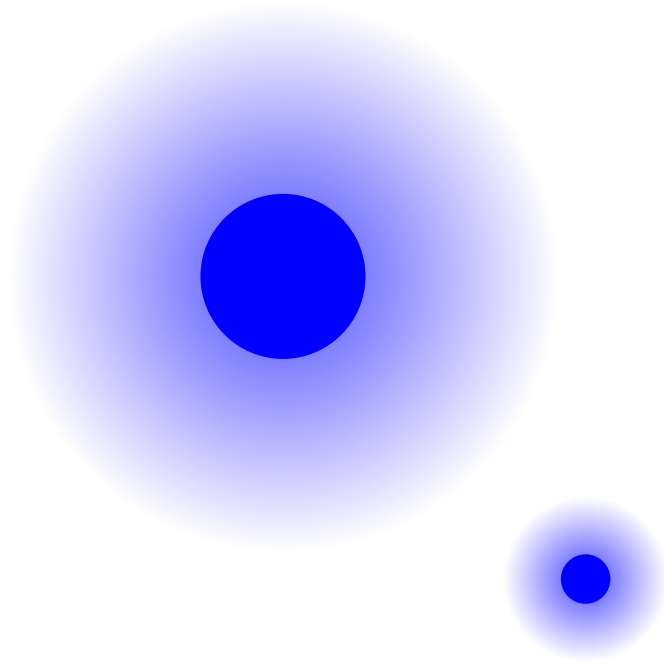
To calculate the average temperature increase of the IGM since z_{\star} , we need to take into account the X-ray photons emitted by all the sources over the history of the universe. We choose a random point and calculate the increase in temperature at that point due to sources that lie in a shell of thickness dR_0 at distance R_0 and integrate over all such shells. The volume of ionized gas inside this shell at comoving distance R_0 is,

$$V_0 = 4\pi R_0^2 dR_0 f_i(z(R_0)), \quad (2.22)$$

where $f_i(z(R_0))$ is the global ionization fraction at the redshift of that shell. Eq. 2.21 gives the increase in temperature due to ionized region of volume $4\pi/3 R_x^3$. Replacing, Eq. 2.22 in it and integrate over R_0 ,

$$\Delta T'_{\text{bg}} = \frac{h_p n_{b,0}}{k_B} \frac{f_H \alpha N_{\text{heat}} f_{\star} v_{\text{min}}^{\alpha}}{\zeta} (1+z'_0)^2 \int_{R_{\text{min}}}^{R_0(z_{\star})} dR_0 \int_{t(z_{\star})}^{t(z)} dt' \frac{\dot{f}_{\text{coll,g}}(t')}{f_{\text{coll,g}}(t')} f_i(t') \left(\frac{1+z'}{1+z} \right)^{\alpha+1} \int_{v'_{\text{min}}}^{\infty} dv' \frac{e^{-\tau(R_0, v')}}{v'^{\alpha+4}} \sum_i (v' - v_i) x_i \sigma_{i,0} v_i^3. \quad (2.23)$$

We take the upper limit of R_0 integration to correspond to the redshift of star formation $R_0(z_{\star})$, where we take $z_{\star} = 35$. However, the lower limit R_{min} is somewhat difficult choice as we discuss in the next subsection. Here we do not correct the value of optical depth due to any intermediate ionized regions between the shell at R_0 and the point of interest P .



2.1.4 Modelling Profiles

There are two major problems with this method of separating the medium in the ‘near zone’ (source profiles) and ‘far zone’ (background). (a) Due to the large mean free paths of heating bubbles, we expect the temperature profiles to be very large. They start overlapping with one another long before the overlap of ionization bubbles. This is problematic while trying to calculate the correlations, as discussed in Chapter 4. (b) The ionization bubbles, and hence their temperature profiles have a wide range of sizes. Therefore it is difficult to define some characteristic scale at which the profiles end and the background begins. This problem is also related to the lower limit R_{\min} of integral in Eq. 2.23. Given that most of the contribution to X-ray heating come from soft photons from nearby sources, it is important to model their contribution properly.

Since the profile of one source is still in the background region for the rest of sources, we need to add the average T_{bg} to the source profile temperature. We use energy conservation to make sure that the average temperature rise over different regions corresponds to the total energy dumped into the medium by all the sources.

Some of the methods to mitigate these problems are explored below, with a brief description and a few pros and cons:

- **Inter-bubble Separation:** At any redshift, we can define \bar{R} as the mean separation between two ionization bubbles. It can be defined as $\bar{R} \sim N^{-1/3}$, where N is the total number density of ionization bubble, or we can take weighed average as,

$$\bar{R} \sim \frac{\sum N(R_x) R_x}{\sum N(R_x)},$$

where, $N(R_x)$ is the number density of bubbles with size R_x and we take the sum over R_x .

We can calculate source profiles up to this distance \bar{R} and use $R_{\min} = \bar{R}$ to calculate background temperature. However, given the large size distribution of bubbles, this method fails in many ways. Profiles of large bubbles are cut-off abruptly, before the temperature levels off, whereas profiles of small bubbles are computed up to a distance where they have negligible influence. Excursion set formalism also gives us ionization bubbles whose radius is larger than \bar{R} , which would result in these bubbles having no temperature profiles. We do not use this method in our work.

- **Region of Influence:** We can try to cutoff source profiles where the temperature increase due to that source, over its history, is equal to the background temperature. This results in the smooth merging of source profiles with the background, however, it undermines the fact that source profiles would also have a small amount of heating due to faraway sources. It also does not give a conclusive value of R_{\min} . We do not use this method in our work.
- **Cutoff Temperature:** We can cutoff source profiles when the temperature increase in a shell of this profile over the entire history of the source is less than T_{cutoff} , or can use cutoff value for $s \equiv T_{\text{CMB}}/T_K$. This prescription works at high redshifts where the heating is yet inefficient and the profiles are small. At low redshift, if T_{cutoff} is too small, this method results in a *very* large number of overlaps. Even though we have attempted and succeeded in incorporating a small amount of overlap of temperature profiles (Section 2.1.5), scenarios where several profiles are bound to overlap on every other profile is a difficult case, which often gives in unphysical artefacts in our formalism. This also does not give us any intuitive value for R_{\min} .

We used this method with $T_{\text{cutoff}} = 1K$ and $R_{\min} = 0$ in [Raste and Sethi \[2018\]](#). Here the photon energy from the source profiles is also included while calculating background temperature. However, we can remove this contribution by subtracting the total amount of energy in the profiles from the final T_{bg} (Method 1 in Section 2.1.5).

- **Relative cutoff Temperature:** We can cut-off source profiles where the temperature difference between two consecutive shells is less than certain cutoff value, which would indicate that the temperature profiles have levelled off. As in the case of absolute cutoff temperature, this would result in large T_S profiles and high amount of overlap at lower redshift. We do not use this method in our work.
- **Volume fraction of Profiles:** We can calculate source profiles up to a very large distance and use a very small value of cutoff temperature ($T_{\text{cutoff}} < 0.1 K$). The total volume fraction occupied by all the profiles $f_{hb} \gg 1$, which suggests a large amount of overlap. After correcting for the effect of overlap, the real volume fraction of these profiles f_h (see Section 2.1.5) is still close to unity.

The average temperature increased due to all the sources should agree with the background temperature calculated using $R_{\min} = 0$. However, instead of calculating background temperature using Eq. 2.23, we shed outer shells from the source profiles until the volume fraction occupied by bubbles and their profiles $f_i + f_h$ is less than 0.5. The energy within these shedded shells is averaged to calculate the background temperature. As we remove more outer shells from source profiles, the sizes of these profiles decrease and the global temperature increases. We have used this method in [Raste and Sethi \[2019\]](#).

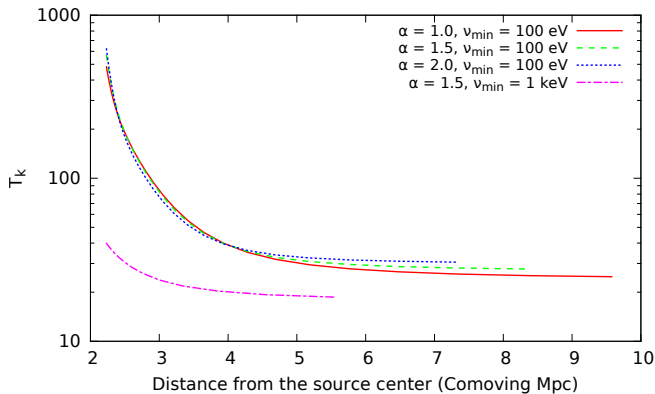


Figure 2.1: Heating (T_K) profiles around a bubble at $z = 17$ for various values of α and v_{\min} with $\zeta = 10$ and $N_{\text{heat}} = 1.0$. For $v_{\min} > 1$ keV the temperature is smaller and the profile around a source is shallow.

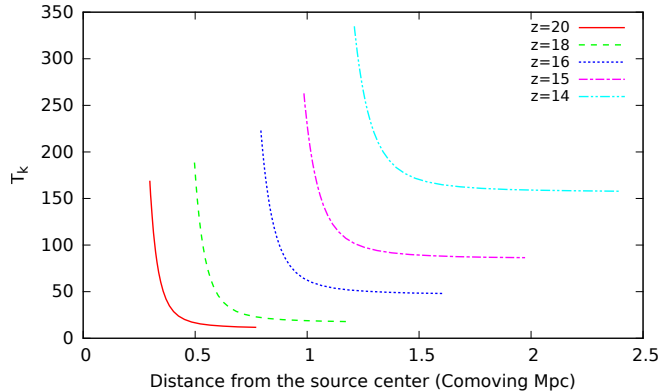


Figure 2.2: Evolution of the T_K profile around a fiducial ionized bubble for $\alpha = 1.5$, $v_{\min} = 100$ eV, $\zeta = 10$, and $N_{\text{heat}} = 1.0$. The size of the ionization bubble is assumed to grow as $R_x \sim f_i^{1/3}$.

With the growth and formation of more sources, the profile, as well as, the background temperature increase. However, the quantity of interest that can be probed directly with the 21 cm signal is not the absolute temperature of the gas T_K , but its contrast with CMB ($1 - T_{\text{CMB}}/T_K$). At lower redshifts, T_{CMB} is small and the kinetic temperature is increasing. Spatial fluctuations in T_K results in significant spatial fluctuations of 21 cm signal only as long as T_K is smaller than T_{CMB} . When the gas has heated to a temperature much higher than T_{CMB} , its spatial fluctuations have negligible effect on 21 cm fluctuations ($T_K \gg T_{\text{CMB}} \Rightarrow 1 - T_{\text{CMB}}/T_K \sim 1$). This is the uniformly heated phase of the universe, even though the actual kinetic temperature can be far from uniform. Therefore, in our work, we primarily focus on accurate modelling of T_K during the early phase of heating.

While deriving Eqs. 2.21 and 2.23, we have assumed that other than adiabatic cooling, no other cooling mechanism are efficient in the IGM. If there were any other uniform heating or cooling mechanisms in the universe, we can incorporate their effect in the value of T_{bg} .

In Figure 2.1 we plot temperature profiles around an ionization bubble at $z = 17$ for $\zeta = 10$, $N_{\text{heat}} = 1.0$, and three values of α . The figure also displays a case when $v_{\min} = 1$ keV. This figure shows that the temperature around an ionization bubble falls sharply unto certain distance, after which the profiles become shallower.

For higher value of α , there are more soft X-ray photons and the profile temperature, as well as the background temperatures, are higher. For smaller value of α , the profiles are shallower and the temperature in the inner shells (right outside ionization bubbles) is small. When we assume that the minimum frequency of photons escaping the halo is 1 keV, the profiles are smaller and shallower. The absence of soft photons, which are the main reasons for temperature fluctuations, results in almost uniform heating of the medium. Also, in this case, the heating is suppressed even in the far zone as high energy photons remain unabsorbed (Fialkov et al. [2014]). For higher value of N_{heat} , there are more photons of every frequency. This results in a higher overall temperature of the medium.

In Figure 2.2 we show the evolution of the heating profile around an ionization bubble (similar results have been obtained by e.g. Venkatesan and Benson [2011], Ghara et al. [2015]). The smallest radius in each

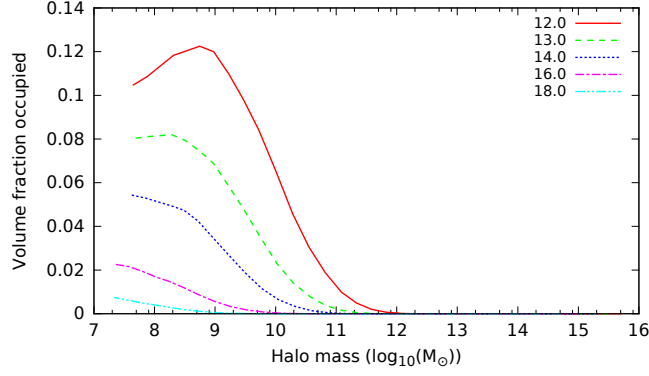


Figure 2.3: Evolution of the size distribution of heated regions as a function of halo mass for $\zeta = 10$, $\alpha = 1.5$ and $N_{\text{heat}} = 1.0$.

profile displayed is the size of the fiducial ionization bubble, which is assumed to grow according to the mean ionized fraction in the universe ($R_x \sim f_i^{1/3}$). With the growth of this bubble, the temperature of the profile and background is increasing.

In Figure 2.3 we show the temperature profile size distribution corresponding to ionization bubbles from Figure 1.6. Here the profile boundaries are calculated using $T_{\text{cutoff}} = 1$ K. The heating profiles are larger than self-ionized regions by roughly a factor of 4.5 for this case. For most of the history of reionization, the maximum contribution comes from the smallest bubble size and only at small redshifts there is a clear peak at intermediate bubble sizes. Sizes of profiles increase with N_{heat} since there are more X-ray photons. For higher value of α , more heating contribution comes from smaller bubble size than larger ones.

2.1.5 Overlap of Profiles

The volume fraction of the universe occupied by the ionization bubbles is,

$$f_i = \sum_{R_x} N(R_x) \frac{4\pi}{3} R_x^3, \quad (2.24)$$

where, $N(R_x)$ is the number density of bubbles with ionization radius R_x and we have assumed that the ionization bubbles do not overlap. Similarly, we can define the volume *fraction* due to source temperature profiles to be,

$$f_{hb} = \sum_{R_x} N(R_x) \frac{4\pi}{3} (R_h^3 - R_x^3), \quad (2.25)$$

where, R_h is the outer radius of the profile around ionization bubble of radius R_x (See Section 4.3 for detailed notations). The value of R_h is depended on what prescription we use to define the source profiles, however, it is generically a function of R_x . When there is a significant overlap between source profiles, the value of f_{hb} can exceed unity, as many parts of the volume are counted more than once as parts of different profiles. Hence, f_{hb} is not really a *fraction*. We define another quantity f_h , as the actual volume fraction occupied by source profiles. We use two methods to calculate f_h .

Method 1: We can imagine a universe filled with ionization bubbles (f_i), their overlapping source profiles (f_h) and a *background* region (f_b) which lies outside any source profile. In this universe we place another ionization bubble with its own source profile, and make sure that the new ionization bubble does not overlap with any other ionization bubble (but it can overlap with any source profile). Therefore within the source profile of the new bubble, f_i fraction of the volume is ionized, f_h fraction of the volume is overlapping with other profiles and only f_b fraction of the volume is un-overlapping. Thus, generally within every profile, there can be part of another profile or ionization bubble¹. We subtract these parts while defining f_h recursively as,

$$\begin{aligned} f_h &= \sum_{R_x} N(R_x) \frac{4\pi}{3} (R_h^3 - R_x^3) (1 - f_i - f_h) \\ &= f_{hb} (1 - f_i - f_h). \end{aligned}$$

This gives us,

$$f_h = \frac{f_{hb}(1 - f_i)}{1 + f_{hb}}, \quad (2.26)$$

$$f_b = 1 - f_i - f_h = \frac{1 - f_i}{1 + f_{hb}}. \quad (2.27)$$

When the value of f_{hb} and f_i is small, f_h approaches f_{hb} . However, even when the value of f_{hb} becomes much larger than unity, f_h remains less than unity.

We also calculate the effect of overlap of source profiles on the average profile and background temperatures. When multiple temperature profiles are likely to overlap, the temperature of any profile should contain contribution due to other overlapping profiles. Hence,

$$T_p = T_q + T_o, \quad (2.28)$$

where, T_p , the resultant temperature, is the sum of the original temperature of this shell T_q and the average contribution due to overlaps T_o . We can write,

$$T_o = \sum_{R_x} \sum_q f_q (T_q + T_o),$$

where, f_q is the real volume fraction of the shell with temperature T_q after taking into account the overlaps. We can write it as,

$$f_q = N(R_x) \frac{4\pi}{3} \frac{f_{hb}}{f_h} ((R_q + \Delta R_q)^3 - R_q^3), \quad (2.29)$$

where, R_q and ΔR_q are the radius and width of the shell. The f_{hb}/f_h factor takes care of the overlaps. The

¹Outside an ionization bubble, the probability of finding *any* temperature profile is $1 - f_i$, since this region is definitely not in the background. But the volume fraction of the profile associated with *this* bubble is $1 - f_i - f_h$ since some of the heated regions are shared with other bubbles and will get counted as profiles associated with those bubbles.

sum of all such volume fractions for all shells of all profiles is f_h . Therefore,

$$\begin{aligned} T_o &= \sum_{R_x} \sum_q f_q T_q + f_h T_o \\ &= \frac{1}{1-f_h} \sum_{R_x} \sum_q \frac{4\pi}{3} N(R_x) \frac{f_{hb}}{f_h} ((R_q + \Delta R_q)^3 - R_q^3) T_q. \end{aligned}$$

Using value of f_h from Eq. 2.26, we get,

$$T_o = \frac{1-f_i}{1+f_i f_{hb}} \sum_{R_x} \sum_q \frac{4\pi}{3} N(R_x) ((R_q + \Delta R_q)^3 - R_q^3) T_q. \quad (2.30)$$

We add T_o to the profiles, but subtract T_o/f_n from background temperature T_{bg} to maintain the energy budget. Here $f_n = 1 - f_i$ is the neutral fraction of the universe, and this factor arises since we need to discard the energy from the profile that overlap with ionized regions¹. If the background temperature calculated using $R_{\min} = 0$ in Eq. 2.23 is T_{bg} , then the average temperature within neutral region is,

$$f_n \bar{T}_K = \sum_{R_x} \sum_q f_q \left(T_q + T_o + \left(T_{bg} - \frac{T_o}{f_n} \right) \right) + f_b \left(T_{bg} - \frac{T_o}{f_n} \right).$$

Here we note again that within a source profile, there is contribution due to overlapping profiles as well as background temperature due to far away sources. This gives,

$$\begin{aligned} f_n \bar{T}_K &= \sum_{R_x} \sum_q f_q (T_o + T_q) + f_h \left(T_{bg} - \frac{T_o}{f_n} \right) + f_b \left(T_{bg} - \frac{T_o}{f_n} \right) \\ &= T_o + f_n \left(T_{bg} - \frac{T_o}{f_n} \right) \\ &= f_n T_b. \end{aligned}$$

This confirms the conservation of energy. We used this method in [Raste and Sethi \[2018\]](#).

Method 2: We want to arrange N ionization bubbles of radius R_x and temperature profile of radius R_h , in a large box of volume V ($V \gg 4\pi/3 R_h^3$). The condition is that the ionization bubbles must not overlap with one another, but the temperature profiles can overlap with other ionization bubbles and profiles. We wish to calculate the total volume fraction occupied by the profiles for such an arrangement.

When $N = 1$, there is only one bubble randomly placed within the box. The fraction of volume of this box occupied by the bubble and profile is, respectively,

$$g_x = \frac{4\pi R_x^3}{3V} \quad \text{and} \quad g_h = \frac{4\pi R_h^3 - R_x^3}{3V},$$

with the total volume fraction occupied, $g_t = g_x + g_h = (4\pi/3) R_h^3/V$. Here we are interested in calculating the volume fraction occupied by the profiles. Thus, this fraction for $N = 1$ is $g_1 = g_h$.

¹In reality, as ionized regions are almost transparent to X-ray photons, we could have accommodated this energy properly, but it is a small factor and we do not attempt more detailed calculations.

For $N = 2$, we need to randomly place the second bubble in the box which already contains the first bubble. Across multiple such placements, the average non-overlapping volume fraction occupied by the profile of the second bubble is $g_h(1 - g_t)$, since its probability of overlapping with first bubble or its profile is g_t . Therefore the total average volume fraction of both bubbles is,

$$g_2 = g_h + g_h(1 - g_t) = g_1 + g_1(1 - (g_1 + g_i)).$$

Placing a third bubble in this scenario ($N = 3$), we get,

$$g_3 = g_2 + g_h(1 - (2g_i + g_2)),$$

where the first term (g_2) is due to the profiles of first the two bubbles, and the second term is due to the profile of the third bubble, which can overlap with the two ionization bubbles ($2g_i$) or their profiles (g_2). This can be expressed recursively for N spheres as,

$$\begin{aligned} g_N &= g_{N-1} + g_1(1 - ((N-1)g_i + g_{N-1})) \\ &= g_{N-1}(1 - g_1) + g_1(1 - (N-1)g_i) \\ &= \sum_{k=0}^{N-1} g_1(1 - g_1)^k(1 - (N-1-k)g_i) \\ &= \left(1 + \frac{g_i}{g_1}\right) (1 - (1 - g_1)^N) - Ng_i. \end{aligned} \quad (2.31)$$

Now the total volume fraction occupied by the ionization bubbles is $f_i = Ng_i$, and the total sum of fractions occupied by the profiles, including the multiple counting of overlapped part is $f_{hb} = Ng_h$. The actual volume fraction occupied by the profiles is,

$$f_h = g_N = \left(1 + \frac{f_i}{f_{hb}}\right) (1 - (1 - g_h)^N) - f_i. \quad (2.32)$$

In the limit where $g_h \ll 1$ and $N \gg 1$, we get $(1 - g_h)^N \simeq \exp(-Ng_h)$. Thus, we finally have,

$$f_h = \left(1 + \frac{f_i}{f_{hb}}\right) (1 - e^{-f_{hb}}) - f_i. \quad (2.33)$$

We extend this result to multiple bubble sizes and temperature profiles with multiple shells by using Eqs. 2.24, and 2.25.

We tried putting a large number of ionization bubbles ($N = 200$) in a simulation box, with the condition that these bubbles do not overlap, but their profiles can, and calculated the total volume fraction occupied by these profiles. These results match very well with Eq. 2.33, but start diverging from Eq. 2.26 for large f_{hb} . In both methods, it has been assumed that the probability of overlap of inner shells is the same as the probability of overlap of the outer shells, however, if we enforce that the ionization bubbles do not overlap, then the outer shells are more likely to be overlap than inner shells.

2.2 Baryon Interaction with Cold Dark Matter

If there was a small fraction of millicharged dark matter in the universe, then there is a possibility that it might interact with baryons through Coulomb scattering (Barkana [2018], Fraser et al. [2018]). The cross section for this interaction is,

$$\sigma_{\text{dm}} = \sigma_1 \left(\frac{1 \text{ km/s}}{v_{\text{rel}}} \right)^4, \quad (2.34)$$

where v_{rel} is the relative velocity between dark matter and baryonic particle and σ_1 is the interaction cross-section when $v_{\text{rel}} = 1 \text{ km/s}$. This interaction cross-section increases with decreasing velocity, which corresponds to lower temperatures as $v \propto T^{1/2}$. Such an interaction would change the evolution of the baryon temperature during dark ages as,

$$\frac{dT_K}{dt} = -\frac{2\dot{a}}{a}T_K + \frac{x_e}{1+x_e} \frac{8\sigma_T}{3} \frac{a_r T_{\text{CMB}}^4}{m_e c} (T_{\text{CMB}} - T_K) + n_{\text{dm}} \sigma_{\text{dm}} v_{\text{rel}} (T_{\text{dm}} - T_K). \quad (2.35)$$

Here, T_K and T_{dm} are baryon and dark matter temperatures respectively and n_{dm} is the dark matter number density. If $T_{\text{dm}} < T_K$, then this interaction results in the cooling of baryons more than what is predicted by the standard physics during dark ages. Dark matter temperature evolves as,

$$\frac{dT_{\text{dm}}}{dt} = -\frac{2\dot{a}}{a}T_{\text{dm}} + n_b \sigma_{\text{dm}} v_{\text{rel}} (T_K - T_{\text{dm}}). \quad (2.36)$$

Here the first term accounts for the cooling of the dark matter temperature and the second term is the change in temperature due to its interaction with baryons with number density n_b . This is a difficult quantity to calculate since we do not know initial *or* final temperature of dark matter.

The evolution of baryon temperature will depend on T_{dm} , n_{dm} and σ_{dm} , which are parameters dependent on the dark matter models. If $n_{\text{dm}} \gg n_b$, then its interaction with baryons does not affect the evolution of dark matter temperature significantly.

Given the strong dependence of σ_{dm} on relative velocity, this interaction would become more important at low temperatures. If the value of σ_{dm} is very high, it would couple dark matter temperature to baryon temperatures at the epoch when the baryons are still coupled to CMB, and this would result in heating of the dark matter, and change the later structure formation scenario. This provides an upper bound for σ_{dm} .

The presence of dark matter-baryons interaction would alter the fluctuations in baryon temperature significantly. Baryonic gas at the same temperature and redshift will cool differently due to its peculiar velocity, which would create additional baryon acoustic oscillations at low redshifts (Fialkov et al. [2018], Muñoz and Loeb [2018]). In our work, we do not model velocity-dependent fluctuations; however, we do explore models where the interaction between baryon and cold dark matter changes the baryon temperature history during dark ages and cosmic dawn, and decreases the efficiency of X-ray heating.

Chapter 3

Spin Temperature Coupling

“Dumbledore beamed at him, and his voice sounded loud and strong, [...] ‘Of course it is happening inside your head, Harry, but why on earth should that mean it is not real?’”

— J. K. Rowling, *Harry Potter and the Deathly Hallows*

3.1 Lyman- α Coupling

Photons of frequency between Lyman- α and Lyman-continuum line ($10.2 \text{ eV} < \nu < 13.6 \text{ eV}$) are emitted by the same sources that ionize the medium. These photons are referred to as the Lyman- α radiation emitted from the source¹. These photons with frequency less than hydrogen ionizing frequency escape the ionized regions and redshift into the outside neutral medium. When their frequency becomes equals the resonant frequency of one of the Lyman series lines, they are absorbed and scattered by the neutral hydrogen of the medium². Lyman series photons with $n > 2$ usually cascade to Lyman- α frequency, and help coupling spin temperature T_S to kinetic temperature T_K (Pritchard and Furlanetto [2006]). Here we have assumed that all of Lyman- n photons are converted to Lyman- α photons ($f_{\text{recycle}} = 1$ for all n).

In the neutral regions, collisional excitation of the hydrogen to first excited state can be safely ignored because the temperature required for such excitations would be high enough to cause significant ionization of the medium. We also ignore the Lyman- α photons produced due to recombination in the ionized regions, because they are either absorbed very close to the boundary of the HII regions or they redshift to frequency lower than Lyman- α and do not interact with the neutral IGM.

3.1.1 Lyman- α in the Intergalactic Medium

In IGM, a Lyman- α photon is scattered repeatedly by neutral hydrogen. It also undergoes redshift between each scattering and will be shifted out of the resonance width after a number of scatterings. This resonance

¹However, the Lyman- α radiation *received* at a point only refers to photons with Lyman- α frequency.

²The scattering cross-section falls with increasing n of the line, so this scenario is applicable if the optical depth of scattering in the expanding medium exceeds unity. This requirement is readily met for the transitions of interest ($n < 20$).

width Δv_α is dominated by the Doppler broadening for Lyman- α . Hence we take¹,

$$\Delta v_\alpha = \sqrt{\frac{k_B T_K}{m_p c^2}} v_\alpha. \quad (3.1)$$

Lyman- α absorption cross-section by HI is,

$$\sigma_\alpha = \frac{\pi e^2}{m_e c} f_\alpha \phi(v - v_\alpha) \quad (3.2)$$

where, $f_\alpha = 0.4162$ is the Lyman- α oscillation strength. It can be written as function of spontaneous decay rate A_α and frequency v_α as,

$$f_\alpha = \frac{3c^2 A_\alpha m_e c}{8\pi v_\alpha^2 \pi e^2}. \quad (3.3)$$

Lyman- α line profile function $\phi(v - v_\alpha)$ is sharply peaked around Lyman- α frequency. Therefore, we can approximate it to $\phi(v - v_\alpha) = 1/2\Delta v_\alpha$.

Optical Depth: Lyman- α optical depth in neutral medium is,

$$\begin{aligned} \tau_\alpha &= \int \sigma_\alpha n_{\text{HI}}(z) dl \\ &= \frac{\pi e^2 f_\alpha}{m_e c} \int \phi(v - v_\alpha) n_{\text{HI}}(z) \frac{c}{H(z)} \frac{dz}{1+z}, \end{aligned}$$

where, dl is the light-travel distance. Since, $\phi(v - v_\alpha)$ is sharply peaked around v_α , we assume that the redshift dependent quantities n_{HI} and $H(z)$ will remain constant over this distance. Using, $dz/(1+z) = dv/v$, we get,

$$\begin{aligned} \tau_\alpha &\simeq \frac{\pi e^2 f_\alpha n_{\text{HI}}(z)}{m_e v_\alpha H(z)} \int \phi(v - v_\alpha) dv \\ &\simeq 1.34 \times 10^{-7} \frac{n_{\text{HI}}(z)}{H(z)}. \end{aligned}$$

Using, approximation of matter-dominated universe, and taking the number density of neutral hydrogen at redshift z to be $n_{\text{HI}}(z) = n_{\text{HI},0} x_{\text{HI}} (1 + \delta) (1 + z)^3$, we derive the Gunn-Peterson optical depth (Section 1.2),

$$\tau_\alpha = 2.04 \times 10^5 x_{\text{HI}} (1 + \delta) (1 + z)^{3/2}. \quad (3.4)$$

Here $n_{\text{HI},0}$ is the neutral hydrogen number density at present; x_{HI} and δ are neutral fraction and overdensity, respectively.

¹ In our work, we have also alternatively used,

$$2\Delta v'_\alpha = \sqrt{\frac{8k_B T_K \ln(2)}{m_p c^2}} v_\alpha,$$

the full-width half-maximum of the line. This makes a small difference since, $\Delta v'_\alpha/\Delta v_\alpha = \sqrt{2\ln(2)} \simeq 1.18$.

Mean Free Path: Using Eq. 3.2, the mean free path of a Lyman- α photon at redshift z is,

$$\bar{l}_\alpha = \frac{1}{n_{\text{HI}}(z)\sigma_\alpha} \simeq \frac{m_e c}{\pi e^2 f_\alpha} \frac{2\Delta v_\alpha}{n_{\text{HI},0}(1+z)^3}. \quad (3.5)$$

While travelling this distance, the Lyman- α photon has redshifted by,

$$\overline{dv}_\alpha = v_\alpha \frac{H(z)}{c} \bar{l}_\alpha \simeq v_\alpha \frac{2m_e}{\pi e^2 f_\alpha} \frac{H(z)}{n_{\text{HI},0}(1+z)^3} \Delta v_\alpha.$$

Therefore, the number of scattering before the photon is redshifted by its resonance width Δv_α is,

$$n_{\text{scatter}} = \frac{\Delta v_\alpha}{\overline{dv}_\alpha} \simeq \frac{(1+z)^3}{H(z)} \frac{n_{\text{HI},0} \pi e^2 f_\alpha}{2m_e v_\alpha} \simeq 1.02 \times 10^4 (1+z)^{3/2}. \quad (3.6)$$

The large number of scattering experienced by a Lyman- α photon before it redshifts out of Doppler resonance width, is sufficient to couple the Lyman- α colour temperature T_α to matter kinetic temperature T_K (Wouthuysen [1952], Field [1959]). Lyman- α line has a constant shape once the steady state is reached (Chen and Miralda-Escudé [2004]). We assume $T_\alpha = T_K$ everywhere in our work.

Influence Region: We define Lyman- n influence region as the comoving distance travelled by the Lyman- $(n+1)$ photons to redshift to Lyman- n frequency. If these photons were emitted at $z = z_e$ and absorbed at $z = z_a$ with $v_e = v_{n+1}$ and $v_a = v_n$, then the comoving distance travelled by the photon before it is absorbed in an expanding matter dominated universe is ($n \geq 2$),

$$\begin{aligned} R_{\text{max}}^{(n)} &= \int_{z_a}^{z_e} \frac{cdz}{H(z)} \simeq \frac{2c}{H_0 \Omega_m^{1/2}} \left[\frac{1}{(1+z_a)^{1/2}} - \frac{1}{(1+z_e)^{1/2}} \right] \\ &\simeq \frac{2c}{H_0 \Omega_m^{1/2}} \frac{1}{(1+z_e)^{1/2}} \left(\sqrt{\frac{v_{n+1}}{v_n}} - 1 \right). \end{aligned}$$

Here, we have used, $(1+z_a)/(1+z_e) = v_a/v_e$. Lyman- n line frequency is $v_n \propto (1 - 1/n^2)$, therefore we can write,

$$\frac{v_{n+1}}{v_n} = \frac{n(n+2)}{(n+1)^2} \frac{n^2}{(n-1)(n+1)}.$$

The Lyman- n influence region is

$$R_{\text{max}}^{(n)} \simeq \frac{1.6 \times 10^4 \text{ Mpc}}{(1+z_e)^{1/2}} \left[\left(\frac{n^3(n+2)}{(n-1)(n+1)^3} \right)^{1/2} - 1 \right]. \quad (3.7)$$

These influence regions become smaller with increasing n , as the frequency difference between v_{n+1} and v_n decreases. The Lyman- α influence region ($n = 2$) is

$$R_{\text{max}}^{(2)} \simeq \frac{1422 \text{ Mpc}}{(1+z_e)^{1/2}}. \quad (3.8)$$

This region is much larger than the mean distance between ionization bubbles at any redshift. For example,

for $\zeta = 7.5$, the values of mean comoving distance between bubbles at redshifts 25, 20, and 15 is 7.85 Mpc, 2.29 Mpc and 0.96 Mpc respectively. Therefore, Lyman- α influence regions are very large and merge very early.

3.1.2 Lyman- α Photons Number Density

The Lyman- α contribution at any point arises from two main factors: Lyman- α emitted from the sources and Lyman- α created due to X-ray photoelectrons (Venkatesan et al. [2001]). The latter is generally small and we neglect it in our work.

Source Luminosity: We assume that the total Lyman- α luminosity of an ionization bubble of size R_x is proportional to its ionizing photons (UV) luminosity¹:

$$\begin{aligned}\dot{N}_t &= f_L \dot{N}_{\text{ion}} \\ &= f_L \frac{4\pi}{3} \left(\frac{R_x}{1+z} \right)^3 \alpha_B C n_0^2(z) \\ &= f_L \frac{4\pi}{3} R_x^3 n_{\text{HI},0}^2 \alpha_B C (1+z)^3.\end{aligned}\tag{3.9}$$

Here we have used the balance between ionization and recombination in the self-ionized HII region (Eq. 1.10) to connect its ionizing luminosity with the size of the HII region. α_B is case-2 recombination coefficient (Section B) and C is the clumping factor of the halo (Section 1.1.4).

The luminosity of ionizing and Lyman- α photons depends on the type of stellar sources (Schaerer [2002], Mirocha et al. [2018]). The ratio of ionizing photons and Lyman- α photons emitted from the sources is between 0.07 and 0.3 (Mirocha et al. [2015]). Lyman- α photons also escape the halo more easily than ionizing photons (Dijkstra et al. [2008a]). Hence, Chen and Miralda-Escudé [2004] has taken the value of f_L to be between 10 and 100. However, for the sake of completeness, we take $0.1 < f_L < 1000$ in our work. Since the stellar population is expected to change with time, the value of f_L should evolve with redshift. We have ignored this effect. We also assume that the sources emit flat spectrum between Lyman- α and Lyman-limit. Therefore, we have

$$\frac{dN}{dt dv} = \frac{\dot{N}_t}{v_{\text{HI}} - v_\alpha}.\tag{3.10}$$

The angle averaged specific intensity of Lyman- α photons (by number) at comoving distance R_0 is,

$$\begin{aligned}J'_\nu &= \frac{1}{4\pi} \frac{dN'}{dt' dv' dA'} \\ &= \frac{1}{4\pi} \frac{\dot{N}_t}{v_{\text{HI}} - v_\alpha} \frac{(1+z')^2}{4\pi R_0^2}.\end{aligned}\tag{3.11}$$

Here, all primed quantities are calculated at the receiving point P , and the unprimed quantities are calculated

¹The Lyman- α photons (photons with frequency between Lyman- α and Lyman-continuum lines) also fall in the ultraviolet spectrum; however, in our work ‘ultraviolet photons’ always refer to ionizing photons with $\nu > 13.6$ eV.

at the source S . The (physical) number density of Lyman- α photons at a P is

$$n'_{\alpha,*} = \frac{dN'_\alpha}{dV'} = \frac{1}{c} \frac{dN'_\alpha}{dA' dt'}.$$

The only frequencies which are absorbed at redshift z' are in the range of Δv_α around v_α . Therefore, we can write,

$$\begin{aligned} n'_{\alpha,*} &\simeq \frac{4\pi}{c} 2\Delta v'_\alpha \int J'_v(x) \phi(x - v_\alpha) dx \\ &\simeq \frac{4\pi}{c} 2\Delta v'_\alpha S'_\alpha J'_\alpha \\ &\simeq \frac{S'_\alpha}{c} \frac{\dot{N}_t}{4\pi R_0^2} \frac{2\Delta v'_\alpha}{v_{\text{HI}} - v_\alpha} (1 + z')^2. \end{aligned} \quad (3.12)$$

Here S_α is a correction factor of order unity as defined in [Chen and Miralda-Escudé \[2004\]](#), which depends on the photon spectrum around Lyman- α line ([Hirata \[2006\]](#), [Pritchard and Loeb \[2012\]](#)). This spectrum is determined by the process of repeated scattering of Lyman- α photons. Using luminosity from Eq. 3.9, we get

$$\begin{aligned} n'_{\alpha,*} &\simeq \frac{S'_\alpha}{c} \frac{1}{4\pi R_0^2} \left(f_L \frac{4\pi}{3} R_x^3 n_{\text{HI},0}^2 \alpha_B C (1+z)^3 \right) \frac{2\Delta v'_\alpha}{v_{\text{HI}} - v_\alpha} (1+z')^2 \\ &\simeq \frac{S'_\alpha f_L n_{\text{HI},0}^2 \alpha_B C}{3c} \frac{R_x^3}{R_0^2} \frac{2\Delta v'_\alpha}{v_{\text{HI}} - v_\alpha} (1+z')^2 (1+z)^3. \end{aligned} \quad (3.13)$$

When a photon redshifts to the frequency corresponding to one of the Lyman series lines, it gets scattered by the neutral hydrogen and eventually cascades to frequency corresponding to Lyman- α . Thus, the number density of Lyman- α photons at any point will be determined by the number of Lyman- n influence regions the points falls within. If the distance of a point from the source R_0 is such that $R_{\text{max}}(n+1) < R_0 < R_{\text{max}}(n)$, then the point in question will have n Lyman- α photons due to this source. This means that Lyman- α flux from the source centre generally falls more rapidly than $1/r^2$ when this effect is taken into account.

The effect of higher order transitions is expected to be subdominant, because for a continuum source, the total number of photons emitted between Lyman- β to Lyman-limit is smaller than in the frequency range between Lyman- β and Lyman- α . Moreover, these photons will be absorbed closer to the source, since their influence region is smaller.

In our work, we only consider Lyman series lines which have influence regions ($R_{\text{max}}^{(n)}$) larger than the ionization bubble radius (R_x):

$$\left(\frac{n^3(n+2)}{(n-1)(n+1)^3} \right)^{1/2} - 1 \geq \frac{R_x(1+z_e)^{1/2}}{1.6 \times 10^4 \text{ Mpc}}.$$

For an ionization bubble of $R_x = 0.3$ comoving Mpc, at $z = 15$, the highest Lyman- n transition that escapes this bubble is, $n_{\text{max}} \simeq 23$. Photons with influence regions smaller than the ionization bubble will redshift to lower and lower Lyman series lines until they cross the ionization region boundary, where they should

get absorbed right away. However, their effect would be very small and very close to the boundary of the ionization region. Here we have assumed that the sources of Lyman- α photon are situated at the exact centre of the ionization bubble, which is not a good assumption at later redshift when these ionization bubbles are created due to merging of HII regions of multiple nearby sources. Therefore, in reality, the photons which escape the ionization bubbles will depend on the distribution of sources within these bubbles and the shapes of ionized regions. However, this would only affect the number density of Lyman- α photons very close to the HII regions boundary¹. As a first approximation, we can distribute the photons of frequency between Lyman- n_{\max} and Lyman-continuum uniformly in a thin shell around ionization bubble.

Background Sources: We also calculate the Lyman- α number density due to faraway source by taking thin shells of width dR_0 at comoving distance R_0 from the receiving point P and integrating over R_0 . We replace the source ionization volume $(4\pi/3) R_x^3$ with $4\pi R_0^2 dR_0 f_i(z)$, which is the contributing ionized volume at R_0 . We take the lower limit of R_0 at 0 and the upper limit $R_{\max}^{(n)}$. This gives, the background number density of Lyman- α photons due to cascading of Lyman- n photons as,

$$n'_{\alpha, \text{bg}}^{(n)} = \frac{S'_\alpha f_L n_{\text{HI},0}^2 \alpha_B C}{c} \frac{2\Delta v'_\alpha}{v_{\text{HI}} - v_\alpha} (1+z')^2 \int_0^{R_{\max}^{(n)}} dR_0 f_i(z) (1+z)^3. \quad (3.14)$$

Equivalence Regions: The Lyman- α coupling can be separated into near and far zone. In the near zone, the emission from a nearby source dominates the coupling. To analyse fluctuations due to inhomogeneous number density of Lyman- α photons, we can define Lyman- n equivalence region as the distance around a source of radius R_x up to which the contribution due to that source is more than the contribution due to all the background sources ($n'_{\alpha,*} = n'_{\alpha, \text{bg}}^{(n)}$). Roughly, this is the distance $R_f^{(n)}$ from the source where the following condition is satisfied:

$$\frac{1}{3} \frac{R_x^3}{\left(R_f^{(n)}\right)^2} (1+z)^3 \simeq \int_0^{R_{\max}^{(n)}} dR_0 f_i(z) (1+z)^3.$$

We can take a simple approximation as,

$$R_f^{(n)} \sim \sqrt{\frac{R_x^3}{3 f_i R_{\max}^{(n)}}}.$$

This would create a new length scale in the correlation function if this distance exceeds the size of the ionization bubbles.

Lyman- α Photons due to Photoionization of the Medium by X-rays: A small fraction (f_{Ly}) of energy of the photoelectron emitted due X-rays goes into creating Lyman- α photons (Shull and van Steenberg [1985], Pritchard and Furlanetto [2007]). Therefore at any point, the number of Lyman- α photons created per unit

¹It is not useful to model them in more detail, since, several other assumptions would break down so close to the boundary (e.g. sphericity of bubbles, sharp boundary of ionization regions).

time per unit volume is

$$\varepsilon_{X,\alpha} = \frac{dN_\alpha}{dt' dV'} = f_{Ly} \frac{dE'_{\text{heat}}}{dt' dV'} \frac{1}{h\nu_\alpha}. \quad (3.15)$$

The number density of the Lyman- α created at any point is above quantity multiplied by the survival time of average Lyman- α photon before they are redshifted out of the resonance width. This survival time is

$$T_\alpha \simeq \frac{\Delta\nu_\alpha}{\nu_\alpha} \frac{1}{H(z)}.$$

Therefore, Lyman- α number density due to X-rays is,

$$n'_{\alpha,X} = \frac{dN_\alpha}{dt' dV'} T_\alpha = f_{Ly} \frac{dE'_{\text{heat}}}{dt' dV'} \frac{1}{h\nu_\alpha} \frac{\Delta\nu_\alpha}{\nu_\alpha} \frac{1}{H(z)}. \quad (3.16)$$

This expression also matches with [Pritchard and Loeb \[2012\]](#). We ignore this effect in our work.

Photons between Lyman- α and Lyman- β frequencies (Lyman-Werner photons) can be absorbed by H_2 molecule, but we ignore this effect as the number density of H_2 is very low in IGM at high redshifts. Also, the possibility of a Lyman- α photon splitting into two photons through a virtual level is negligible ([Field \[1958\]](#)) and we ignore this effect.

3.1.3 Coupling Coefficient

Depending on the number of photons available at frequency corresponding to transition 1s-triplet to 2p state, the atoms in triplet level will be excited to the 2p state. [Figure 3.1](#) shows the levels of 1s and 2p and the relative strength of transitions between them. An atom which is originally in triplet, can get excited to all four 2p states shown in the Figure. However, $2P_{3/2} \rightarrow 0S_{1/2}$ and $0P_{1/2} \rightarrow 0S_{1/2}$ transitions are forbidden through selection rules. Therefore, the triplet atoms which were excited to $2P_{3/2}$ (with probability 5/9) and $0P_{1/2}$ (with probability 1/9) levels will only be de-excited back to triplet level and will not experience hyperfine spin-flip. The triplet atoms which excite to $1P_{3/2}$ (with probability 1/9) and $1P_{1/2}$ (with probability 2/9), can de-excite to singlet level with probability 2/3 and 1/3, respectively. Therefore, the probability of an atom in triplet level absorbing a Lyman- α photon and de-exciting to singlet level is,

$$\frac{P_{10}^\alpha}{P_\alpha} = \sum_x \mathcal{P}(t \rightarrow x) \times \mathcal{P}(x \rightarrow s) = \left(\frac{1}{9} \times \frac{2}{3}\right) + \left(\frac{2}{9} \times \frac{1}{3}\right) = \frac{4}{27}. \quad (3.17)$$

Here P_α is the absorption rate of Lyman- α photons by HI atoms. Similarly, the number of singlet atoms that transition to triplet level after being excited and de-excited from 2p state is

$$\frac{P_{01}^\alpha}{P_\alpha} = \sum_x \mathcal{P}(s \rightarrow x) \times \mathcal{P}(x \rightarrow t) = \left(\frac{2}{3} \times \frac{1}{3}\right) + \left(\frac{1}{3} \times \frac{2}{3}\right) = \frac{4}{9}. \quad (3.18)$$

The de-excitation probability from 2p is independent of the available photons number, as the stimulated emission is negligible. Therefore, the total number of spin-flip transitions depends on the relative intensity of Lyman- α photons at the two frequencies, given by Lyman- α colour temperature T_α (which attains

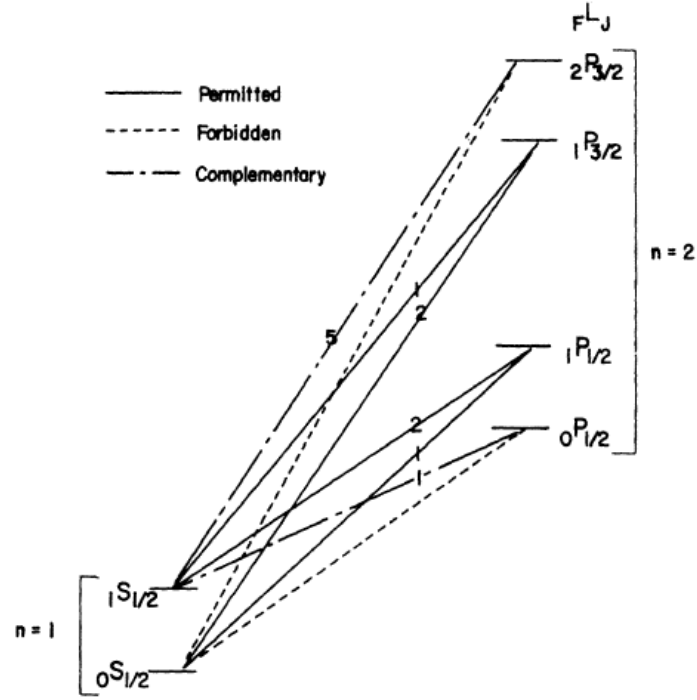


Figure 3.1: The 1s and 2p levels of hydrogen atom. The numbers in the centre are relative strengths. (Courtesy: [Field \[1958\]](#))

equilibrium with T_K through repeated scattering). Therefore, if there are more red photons than blue, then more triplet atoms are excited and cause spin flip, increasing the population of singlet level. The coupling coefficient from Eq. 1.28 is,

$$y_\alpha = \frac{P_{10}^\alpha T_\star}{A_{21} T_\alpha} = \frac{4 P_\alpha T_\star}{27 A_{21} T_\alpha}.$$

The rate of scattering of Lyman- α photons by HI atoms is,

$$P_\alpha = n_\alpha c \sigma_\alpha \simeq \frac{3n_\alpha c^3 A_\alpha}{16\pi v_\alpha^2 \Delta v_\alpha}, \quad (3.19)$$

where we use Eqs. 3.2, and 3.3 for the cross-section of Lyman- α line. This gives the coupling coefficient ([Field \[1958\]](#)),

$$\begin{aligned} y_\alpha &\simeq \frac{4}{27} \frac{1}{A_{21}} \frac{T_\star}{T_\alpha} \frac{3n_\alpha c^3 A_\alpha}{16\pi v_\alpha^2 \Delta v_\alpha} \\ &\simeq \frac{h_p c^4}{36\pi k_B v_\alpha^2} \sqrt{\frac{m_p}{k_B}} \frac{A_\alpha}{A_{21}} \frac{v_{21}}{v_\alpha} \frac{n_\alpha}{T_K^{3/2}} \\ &\simeq 5.9 \times 10^{11} \frac{n_\alpha}{T_K^{3/2}}, \end{aligned} \quad (3.20)$$

where we use Eq. 3.1. Hence, Lyman- α coupling coefficient y_α is a function of Lyman- α photon number

density n_α and temperature T_K . Using Eq. 3.12 in Eq. 3.19, we get

$$\begin{aligned} P_\alpha &= 4\pi \frac{\pi e^2}{m_e c} f_\alpha \int J_\nu(x) \phi(x - \nu_\alpha) dx \\ &= \frac{4\pi^2 e^2}{m_e c} f_\alpha J_\alpha S_\alpha, \end{aligned} \quad (3.21)$$

and the coupling coefficient,

$$y_\alpha = \frac{16\pi^2 e^2 f_\alpha T_\star}{27A_{10} m_e c T_K} S_\alpha J_\alpha, \quad (3.22)$$

which matches with [Pritchard and Loeb \[2012\]](#). Using values of Lyman- α photon number density from Eqs. 3.13 and 3.14, and taking into account the effect of all Lyman-series lines, we have,

$$\begin{aligned} y_{\alpha,\star} T_K &\simeq \sum_{n=2}^{n_{\max}} \frac{h_p c^2 S'_\alpha}{18\pi v_\alpha^2 k_B} \frac{A_\alpha}{A_{21}} \frac{v_{21}}{v_\alpha} \frac{\dot{N}_t}{4\pi R_0^2} \frac{v_\alpha}{v_{n+1} - v_n} (1+z')^2 \\ &\simeq \sum_{n=2}^{n_{\max}} \frac{h_p c^2 \alpha_B}{18\pi k_B} \frac{A_\alpha}{A_{21}} \frac{v_{21}}{v_\alpha^2 (v_{n+1} - v_n)} (S'_\alpha f_L n_{\text{HI},0}^2 C) \frac{R_x^3}{R_0^2} (1+z')^2 (1+z)^3, \end{aligned} \quad (3.23)$$

$$y_{\alpha,\text{bg}} T_K \simeq \sum_{n=2}^{n_{\max}} \frac{h_p c^2 \alpha_B}{18\pi k_B} \frac{A_\alpha}{A_{21}} \frac{v_{21}}{v_\alpha^2 (v_{n+1} - v_n)} (S'_\alpha f_L n_{\text{HI},0}^2 C) (1+z')^2 \int_0^{R_{\max}^{(n)}} dR_0 f_i(z) (1+z)^3. \quad (3.24)$$

The term that appears in the definition of ΔT_B (Eq. 1.39) is $(1 - T_{\text{CMB}}/T_S)$. Rearranging this, and ignoring the effect of collisional coupling, we observe that the influence of y_α only appears through $y_\alpha T_K$ term, since

$$1 - \frac{T_{\text{CMB}}}{T_S} = \left(1 - \frac{T_{\text{CMB}}}{T_K}\right) \left(\frac{y_\alpha T_K}{y_\alpha T_K + T_{\text{CMB}}}\right)$$

From Eqs. 3.23 and 3.24, we can see that $y_\alpha T_K$ is independent of local temperature T_K at the receiving point. Thus, the coupling strength $y_\alpha T_K / (y_\alpha T_K + T_{\text{CMB}})$, is not a function of T_K and for given Lyman- α number density and T_{CMB} , regions with any temperature will couple equally.

Spin temperature profiles: The size of spin temperature profile around a source depends on the Lyman- α modelling parameter f_L as well as the kinetic temperature profiles (Chapter 2). For low value of f_L , spin temperature T_S is weakly coupled to T_K and has value closer to T_{CMB} . For high value of f_L , the coupling of T_S to T_K is stronger. The number density of Lyman- α photons (and value of y_α) falls away from a source. Therefore, at high redshifts, the medium immediately surrounding an ionization bubble is strongly coupled, whereas far away from the source, the coupling can be weak and T_S can relax to T_{CMB} . If the profiles of multiple sources overlap, then there will be stronger coupling in the overlapped regions .

Perfect coupling: If around ionization bubbles certain regions have attained complete coupling, and the background is only partial coupled, then this creates inhomogeneities in Lyman- α coupling on the scales of these regions. As the intensity builds in the background owing to the birth of new self-ionized regions and reaches levels sufficient to cause complete coupling, these inhomogeneities disappear.

We can take $R_L(R_x)$ as the distance around an ionization bubble of size R_x up to which there is perfect

Lyman- α coupling ($y_\alpha \gg T_{\text{CMB}}/T_K$) due to that bubble. If

$$\sum_{R_x} \frac{4\pi}{3} N(R_x) R_L^3 \gtrsim 1, \quad (3.25)$$

then we can assume that Lyman- α coupling is complete and there are no fluctuations due to this field.

3.2 Collisional Coupling

The collisional coupling of spin temperature T_S and matter kinetic temperature T_K due to scattering of neutral hydrogen and electrons can play an important role (Eq. 1.29). The coupling coefficient is proportional to the number density of colliding particles,

$$y_c = \frac{(n_{\text{HI}} k_{21}^{\text{HI}} + n_e k_{21}^e) T_\star}{A_{21} T_K}. \quad (3.26)$$

For collision rate coefficients, we use the following fits (Zygelman [2005], Pritchard and Loeb [2012]):

$$k_{21}^e = \begin{cases} \exp\left(-9.607 + 0.5 \log(T_K) \exp\left(-\frac{(\log(T_K))^{4.5}}{1800}\right)\right) \text{ cm}^3 \text{ s}^{-1} & T_K \leq 10^4 \text{ K} \\ k_{21,e}(T_K = 10^4 \text{ K}) & T_K > 10^4 \text{ K} \end{cases}$$

$$k_{21}^{\text{HI}} = \begin{cases} 3.6 \times 10^{-16} T_K^{3.640} \exp\left(\frac{6.035}{T_K}\right) \text{ cm}^3 \text{ s}^{-1} & T_K \leq 10 \text{ K} \\ 3.1 \times 10^{-11} T_K^{0.357} \exp\left(-\frac{32}{T_K}\right) \text{ cm}^3 \text{ s}^{-1} & T_K > 10 \text{ K}. \end{cases} \quad (3.27)$$

Here we note that $T_K y_c$ is not independent of T_K , because these rates increase with temperature. Therefore, there is stronger collisional coupling for hotter gas than for cold gas. This effect is important if the gas was colder during the cosmic dawn due to exotic physics: the pre-reionization absorption trough might be shallower, in spite of having larger contrast of matter temperature with the CMB temperature. During EoR, the electron scattering is more effective close to the sources where there is partial ionization and high temperature. However, we assume ionization fraction in the neutral regions to be the residual fraction, and this effect is negligible in our work.

Chapter 4

Correlation

“She was also, by the standards of other people, lost. She would not see it like that. She knew where she was, it was just that everywhere else didn’t.”

— Terry Pratchett, *Equal Rites*

Our aim in this work is to analytically calculate the correlation of HI brightness temperature fluctuations from the early phase of CD/EoR owing to scales that emerge due to ionization, heating and Lyman- α coupling inhomogeneities. These inhomogeneities are caused by bubbles of a given size distribution and their surrounding T_S profiles, which evolve with time. For fully coupled and heated universe ($T_S \gg T_{\text{CMB}}$ in the neutral regions), these scales are determined by the size distribution of ionized regions.

We have assumed a topology where there are spherical self-ionized regions, surrounded by isotropic and concentric spin temperature profiles¹. These profiles might overlap with one another and smoothly merge with the background. The ionization bubbles can be treated as isolated and non-overlapping when the ionization volume fraction of the universe is small, which is expected during the early phase of reionization. We further assume that the ionization bubble centres are uncorrelated and later present a simple model where this assumption is relaxed. We neglect the cross-correlation of density with ionization and spin temperature inhomogeneities as they contribute negligibly on the scales of interest. We explore possible effects of our assumptions in Section 5.6.

Our formalism allows us to deal with T_S profile fractions up to $f_h \simeq 0.5$. When f_h exceeds this value, we merge the outer shells of the T_S profiles to the background (Section 4.3). In general, at lower redshifts, when ionization and heating fractions are large, our formalism is not very accurate.

At any redshift, using excursion set formalism (Section 1.1.4) and the matter power spectrum given by Λ CDM model, we generate size distribution of self-ionized regions. Using Eqs. 1.29, 1.39, 2.21, and 3.23, we calculate spin temperature in shells around these bubbles.

¹ Given the statistical isotropy (we neglect redshift-space distortion) and homogeneity of the process of reionization, heating and coupling, our assumption of spherical bubbles and isotropic spin temperature profiles hold even though the individual bubbles might not be spherical.

4.1 Auto-correlation of Brightness Temperature T_B

Dimensionless brightness temperature fluctuation is defined as (Zaldarriaga et al. [2004]):

$$\begin{aligned}\psi &= x_{\text{HI}}(1 + \delta) \left(1 - \frac{T_{\text{CMB}}}{T_S} \right) \\ &= n(1 + \delta)(1 - s),\end{aligned}\tag{4.1}$$

where we have defined $s \equiv T_{\text{CMB}}/T_S$. In our formalism every small volume is either completely neutral or completely ionized, therefore we use a variable n which is unity if the medium is neutral and zero otherwise. Variable n can be generalised to take any value between 0 and 1 if partial ionization is considered.

The statistics of ψ allows us to study the main physical processes that cause brightness temperature fluctuations: δ (density perturbations), n (ionization inhomogeneities) and s (fluctuations of spin temperature). These quantities are functions of the position, and so they contribute to the spatial fluctuation of the signal. We suppress their dependence on position for notational clarity. The auto-correlation of ψ is,

$$\begin{aligned}\mu &= \langle \psi_1 \psi_2 \rangle - \langle \psi \rangle^2 \\ &= \langle n_1(1 + \delta_1)(1 - s_1)n_2(1 + \delta_2)(1 - s_2) \rangle - \langle n_1(1 + \delta_1)(1 - s_1) \rangle^2.\end{aligned}\tag{4.2}$$

Here (n_1, δ_1, s_1) and (n_2, δ_2, s_2) are values of ionization, overdensity and temperature¹ (T_{CMB}/T_S) at point 1 (\mathbf{r}_1) and at point 2 (\mathbf{r}_2), respectively. Since the process of reionization is statistically homogeneous and isotropic, the auto-correlation function μ is function of $r = |\mathbf{r}_2 - \mathbf{r}_1|$. Here, we assume that density has no correlation with ionization or spin temperature. Therefore,

$$\eta = \langle n\delta \rangle = 0 \quad \text{and} \quad \langle s\delta \rangle = 0.\tag{4.3}$$

The average value of ψ is,

$$\begin{aligned}\langle \psi \rangle &= \langle (1 + \delta_1) \rangle \langle n_1(1 - s_1) \rangle \\ &= (1 + \langle \delta_1 \rangle) (\langle n_1 \rangle - \langle n_1 s_1 \rangle) \\ &= f_n - \langle n_1 s_1 \rangle,\end{aligned}$$

where $\langle \delta \rangle = 0$ and $f_n = \langle n \rangle$ is the average neutral volume fraction. We also have,

$$\begin{aligned}\langle \psi_1 \psi_2 \rangle &= \langle (1 + \delta_1)(1 + \delta_2) \rangle \langle n_1 n_2 (1 - s_1)(1 - s_2) \rangle \\ &= (1 + \xi) \langle n_1 n_2 (1 - s_1)(1 - s_2) \rangle,\end{aligned}$$

where, $\xi = \langle \delta(\mathbf{r}_1)\delta(\mathbf{r}_2) \rangle$ is the auto-correlation function of the HI density perturbation. We compute ξ using the Λ CDM model linear power spectrum and assume the relative bias between the dark matter and

¹In this chapter, T_S and s are both referred to as ‘temperature’.

the HI to be $b = 1$. Therefore,

$$\begin{aligned}\mu &= (1 + \xi) \langle n_1 n_2 (1 - s_1)(1 - s_2) \rangle - (f_n - \langle n_1 s_1 \rangle)^2 \\ &= (1 + \xi) (\langle n_1 n_2 \rangle - \langle n_1 n_2 s_1 \rangle - \langle n_1 n_2 s_2 \rangle + \langle n_1 n_2 s_1 s_2 \rangle) - (f_n - \langle n_1 s_1 \rangle)^2.\end{aligned}$$

We can greatly simplify correlation functions higher than second order. Let us first consider $\langle n_1 n_2 s_1 \rangle$. This corresponds to the joint probability that the point 1 is both neutral and heated to a temperature such that $s = s_1$, while point 2 is neutral. However, the variable $s = T_{\text{CMB}}/T_S$ is only defined for neutral medium. In other words, a point can have $s = s_1$ *only if* it has $n = 1$. Therefore the condition of point 1 being neutral ($n_1 = 1$) is fulfilled by it having temperature s_1 . Thus we can write,

$$\begin{aligned}\langle n_1 n_2 s_2 \rangle &= \langle n_1 n_2 s_1 \rangle = \langle n_2 s_1 \rangle = \langle n_1 s_2 \rangle \\ \langle n_1 n_2 s_1 s_2 \rangle &= \langle s_1 s_2 \rangle.\end{aligned}$$

These simplifications are direct consequences of ignoring partially ionized regions. Finally, we have,

$$\mu = (1 + \xi) (\langle n_1 n_2 \rangle - 2\langle n_1 s_2 \rangle + \langle s_1 s_2 \rangle) - (f_n - \langle n_1 s_1 \rangle)^2. \quad (4.4)$$

Here we have introduced cross-correlations between spin temperature and ionization ($\langle n_1 s_2 \rangle$) and auto-correlation of heating ($\langle s_1 s_2 \rangle$). These terms have significant effect in brightness temperature correlation.

We can also write,

$$\begin{aligned}\mu &= (1 + \xi) \langle n_1 n_2 - n_1 n_2 s_1 - n_1 n_2 s_2 + n_1 n_2 s_1 s_2 \rangle - (f_n - \langle n_1 s_1 \rangle)^2 \\ &= (1 + \xi) \langle n_1 n_2 - n_2 s_1 - n_1 s_2 + s_1 s_2 \rangle - (f_n - \langle n_1 s_1 \rangle)^2 \\ &= (1 + \xi) \langle (s_1 - n_1)(s_2 - n_2) \rangle - (f_n - \langle n_1 s_1 \rangle)^2.\end{aligned} \quad (4.5)$$

Ideally, correlation function derived from Eqs. 4.4 and 4.5 should match.

The correlation functions we calculate in our work are analytically derived. However, a function $\mu(r)$ is a valid correlation function only if it follows certain properties:

- It should be a finite positive value at $r = 0$, $\mu(0)$.
- At any $r > 0$, the value of correlation function $\mu(r) < \mu(0)$.
- It should go to 0 at very large distance ($\mu(r \rightarrow \infty) \rightarrow 0$).
- The Fourier transform of the correlation function should be a positive definite function (power spectrum).
- In between $r = 0$ and $r \rightarrow \infty$, the correlation function can be positive or negative, with the condition that its integration over all space must be 0.

We do not satisfy the last condition as we assume an infinite volume (Section 5.6). However, we check for consistency of our formalism with the rest of the conditions.

Given that correlation function $\mu(r) = \mu(-r)$, the power spectrum can be written as

$$\begin{aligned} P(k) &= \int_{-\infty}^{\infty} \mu(r) e^{i2\pi kr} d^3r \\ &= 4\pi \int_0^{\infty} \mu(r) \cos(2\pi kr) r^2 dr. \end{aligned} \quad (4.6)$$

4.2 Simplifying Cases and Limits

4.2.1 Ignoring Density Inhomogeneities ($\xi = 0$)

We define $\phi = n(1-s)$ to explore simplifying cases where we temporarily ignore the effect of density correlation ξ . In such case, the two-point correlation function of ϕ is,

$$\begin{aligned} \mu &= (1 + \xi) \langle n_1 n_2 (1 - s_1)(1 - s_2) \rangle - \langle n(1 - s) \rangle^2 \\ &= (1 + \xi) \langle \phi_1 \phi_2 \rangle - \langle \phi \rangle^2. \end{aligned} \quad (4.7)$$

4.2.2 Uniform Temperature T_S

If the heating and Lyman- α coupling are homogeneous, the neutral gas of the IGM is at the uniform spin temperature T_{bg} . Therefore,

$$\psi = n(1 + \delta)(1 - s_b),$$

where, $s_b = T_{\text{CMB}}/T_{\text{bg}}$. The correlation is,

$$\begin{aligned} \mu &= \langle \psi_1 \psi_2 \rangle - \langle \psi \rangle^2 \\ &= (1 - s_b)^2 \langle n_1(1 + \delta_1)n_2(1 + \delta_2) \rangle - (1 - s_b)^2 \langle n_1(1 + \delta_1) \rangle^2 \\ &= (1 + \xi)(1 - s_b)^2 \langle n_1 n_2 \rangle - (1 - s_b)^2 f_n^2 \\ &= (1 - s_b)^2 ((1 + \xi) \langle n_1 n_2 \rangle - f_n^2). \end{aligned} \quad (4.8)$$

High Redshift: As early times, T_{bg} can approach the adiabatically cooled temperature of the IGM gas which is smaller than T_{CMB} . If ionization fraction is too small, $\langle n_1 n_2 \rangle \simeq f_n^2 \simeq 1$. This gives us,

$$\begin{aligned} \psi &= (1 + \delta)(1 - s_b), \\ \mu &= \xi(1 - s_b)^2. \end{aligned}$$

Here the density fluctuations are enhanced by the temperature contrast between IGM and CMB.

Complete Heating: In later stages of reionization, the gas surrounding ionization regions has heated to

$T_K \gg T_{\text{CMB}}$. Which gives $T_S \gg T_{\text{CMB}}$ (Zaldarriaga et al. [2004]) and $s \sim 0$ everywhere. Therefore,

$$\begin{aligned}\psi &= n(1 + \delta), \\ \mu &= (1 + \xi)\langle n_1 n_2 \rangle - f_n^2.\end{aligned}\tag{4.9}$$

This reduces the correlation function to the one dominated by density and ionization inhomogeneities.

4.2.3 Very Large Scale

Both ionization and T_S inhomogeneities are caused by bubbles of a given size distribution, and their profiles. For scales greater than the largest profiles, the fluctuations due to the ionization, heating, and Lyman- α coupling inhomogeneities vanish, and the HI correlation function is determined by only density perturbations. At these scales,

$$\begin{aligned}\langle n_1 n_2 \rangle &= \langle n_1 \rangle \langle n_2 \rangle = f_n^2 \\ \langle n_1 s_2 \rangle &= \langle n_1 \rangle \langle s_2 \rangle = f_n \langle s \rangle \\ \langle s_1 s_2 \rangle &= \langle s_1 \rangle \langle s_2 \rangle = \langle s \rangle^2.\end{aligned}$$

Therefore, the correlation function is,

$$\begin{aligned}\mu &= (1 + \xi)(f_n^2 - 2f_n \langle s \rangle + \langle s \rangle^2) - (f_n - \langle s \rangle)^2 \\ &= \xi(f_n - \langle s \rangle)^2.\end{aligned}\tag{4.10}$$

Here the HI brightness temperature correlation function μ scales as the density correlation function ξ . Because ξ is very small at large scales, μ becomes very small. If at large scale ξ becomes negative, then we will get negative correlation. We also note that the correlation function at large scale vanishes when $f_n = \langle s \rangle$ (close to global heating transition).

4.2.4 Very Small Scale

When the distance between two points is 0 ($\mathbf{r}_2 = \mathbf{r}_1$),

$$\begin{aligned}\mu_0 &= (1 + \xi_0)(\langle n_1 n_1 \rangle - 2\langle n_1 s_1 \rangle + \langle s_1 s_1 \rangle) - (f_n - \langle n_1 s_1 \rangle)^2 \\ &= (1 + \xi_0)(\langle n \rangle - 2\langle s \rangle + \langle s^2 \rangle) - (f_n - \langle s \rangle)^2.\end{aligned}\tag{4.11}$$

As this quantity is RMS, it is very large and positive. Here $\xi_0 = \xi(0)$ is the correlation function computed at zero lag which equals RMS of density perturbations.

We verify Eqs. (4.10) and (4.11) as the large and small scale limits of the HI correlation function computed using methods described in the next sections.

4.2.5 Complete Coupling

We can also try to separate influence of heating and coupling using Eq. 1.31 and using $x_t = x_c + x_\alpha$ as,

$$\begin{aligned}\psi &= n(1 + \delta) \left(1 - \frac{T_{\text{CMB}}}{T_S} \right) \\ &= n(1 + \delta) \left(1 - \frac{T_{\text{CMB}}}{T_K} \right) \frac{x_t}{1 + x_t} \\ &= n(1 + \delta)(1 - \kappa)(1 - \chi),\end{aligned}\tag{4.12}$$

where,

$$\kappa = \frac{T_{\text{CMB}}}{T_K} \quad \text{and} \quad \chi = \frac{1}{1 + x_t}\tag{4.13}$$

$$s = \kappa + \chi - \kappa\chi.\tag{4.14}$$

While, Eq. 4.1 is easier to use, Eq. 4.12 is useful if x_t is independent of T_K . This condition is only true for Lyman- α coupling and not for collisional coupling (Chapter 3). We check that both the equations give same results in general cases. In case of complete coupling ($x_t \gg 1$),

$$\psi = n(1 + \delta) \left(1 - \frac{T_{\text{CMB}}}{T_K} \right).\tag{4.15}$$

For very weak coupling ($x_t \ll 1$),

$$\psi = n(1 + \delta) \left(1 - \frac{T_{\text{CMB}}}{T_K} \right) x_t = n(1 + \delta) \left(\frac{T_K}{T_\gamma} - 1 \right) y_t.\tag{4.16}$$

4.3 Notations and Modelling

In Figure 4.1 we show the geometry of the self-ionized region and the IGM surrounding it. We assume that at a given z , the ionized bubbles have various radii R_x . The number density of bubbles of radius R_x is $N(R_x)$. Between R_x and R_h (the outer radius of the spin temperature profile for a given R_x), we take shells of thickness $\Delta R(R_x, s)$, having temperature $s = T_{\text{CMB}}/T_S$. Here $R_s = R(s, R_x)$ and $\Delta R_s = \Delta R(s, R_x)$. In our model, s gradually changes as we move away from the source and finally approaches the background value of $s_b = T_{\text{CMB}}/T_{\text{bg}}$. We use prime (R'_x) if we have more than one bubble in focus. A detailed description of notations followed in this work is given in Table 1.

Table 4.1: Notations

Symbols	Explanation
δ	Over-density of HI gas
n	Ionization state of HI gas: Neutral point $n = 1$ and ionized point $n = 0$
s	Temperature state defined as $s = T_{\text{CMB}}/T_S$
ψ	Dimensionless brightness temperature: $\psi = n(1 + \delta)(1 - s)$
ϕ	$\phi = n(1 - s)$
ξ	Auto-correlation of over density δ : $\xi = \langle \delta_1 \delta_2 \rangle$
μ	Auto-correlation of dimensionless brightness temperature ψ : $\mu = \langle \psi_1 \psi_2 \rangle - \langle \psi \rangle^2$
f_i	Average ionized volume fraction
f_n	Average neutral volume fraction: $f_n = 1 - f_i$
f_{hb}	Total volume fraction due to T_S profiles (without correcting for the overlaps)
f_h	Average heated volume fraction after correcting for the overlaps
f_b, f_{bg}	Average background volume fraction: $f_b = 1 - f_i - f_h$
R_x	Radius of given ionization bubble
R_h	Outer radius of given T_S profile of, $R_h = R_h(R_x)$
R_s	Inner radius of the shell with spin temperature $T_S = T_{\text{CMB}}/s$ around given bubble
ΔR_s	Thickness of the shell with spin temperature $T_S = T_{\text{CMB}}/s$ around given bubble
$N(R_x)$	Number density of ionization bubbles of radius R_x
$\mathcal{P}(a_n)$	Probability of point a being neutral
$\mathcal{P}(a_i)$	Probability of point a being ionized
$\mathcal{P}(a_i, R_x)$	Probability that point a belongs to an ionization bubble of radius R_x
$\mathcal{P}(a_s)$	Probability of point a having temperature s
$\mathcal{P}(a_b)$	Probability of point a being in background
$\mathcal{P}(a_s, R_x)$	Probability of point a having temperature s in the profile of an ionization radius R_x
$\mathcal{P}(a_X \cap b_Y)$	Probability of point a having property X and point b having property Y where X and Y can be neutral, ionized, heated or background values

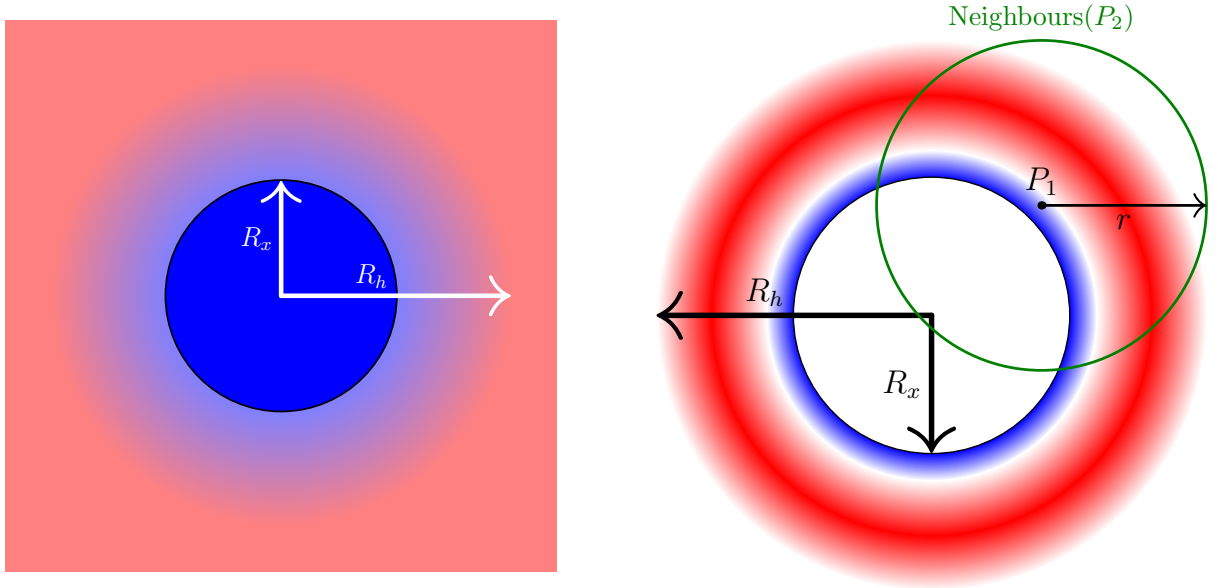


Figure 4.1: Cartoons for topology of the ionized region and its surrounding IGM. The colour scheme shows the kinetic temperature T_K (left panel) and dimensionless brightness temperature ψ (right panel). T_K in the ionization bubble of radius R_x (with sharp boundary) is 10^4 K. It falls as the distance from the source increases and smoothly merges with the background at radius R_h . $\psi_i = 0$ in the ionized region. It might be positive in the neutral, heated and coupled region, and negative in neutral, non-heated and coupled region. The background is not coupled in this case ($\psi_{bg} = 0$). We can randomly choose a point and find correlation with its neighbour at distance r .

If a point a is randomly chosen, then the probability that –

it is in ionization bubble of radius R_x : $\mathcal{P}(a_i, R_x) = N(R_x) \frac{4\pi}{3} R_x^3$

it is ionized: $\mathcal{P}(a_i) = \sum_{R_x} \mathcal{P}(a_i, R_x) = \sum_{R_x} \frac{4\pi}{3} N(R_x) R_x^3 = f_i$

it is neutral: $\mathcal{P}(a_n) = 1 - \sum_{R_x} \mathcal{P}(a_i, R_x) = 1 - \sum_{R_x} N(R_x) \frac{4\pi}{3} R_x^3 = f_n$

it has temp s around ion bub of rad R_x : $\mathcal{P}(a_s, R_x) = N(R_x) \frac{4\pi}{3} \frac{f_h}{f_{hb}} ((R_s + \Delta R_s)^3 - R_s^3)$

it has temperature s : $\mathcal{P}(a_s) = \sum_{R_x} \mathcal{P}(a_s, R_x) = \sum_{R_x} N(R_x) \frac{4\pi}{3} \frac{f_h}{f_{hb}} ((R_s + \Delta R_s)^3 - R_s^3)$

it is in some T_S profile: $\mathcal{P}(a_p) = \sum_s \sum_{R_x} \mathcal{P}(s, R_x) = \sum_{R_x} N(R_x) \frac{4\pi}{3} \frac{f_h}{f_{hb}} (R_h^3 - R_x^3) = f_h$

it is in background region: $\mathcal{P}(a_{bg}) = 1 - \sum_{R_x} \sum_s \mathcal{P}(a_s, R_x) - \sum_{R_x} \mathcal{P}(a_i, R_x)$
 $= 1 - \sum_{R_x} N(R_x) \frac{4\pi}{3} \left(\frac{f_h}{f_{hb}} (R_h^3 - R_x^3) + R_x^3 \right) = f_b.$

Overlap

The total contribution due to all profiles, without taking into account their overlaps is (Eq. 2.25),

$$f_{hb} = \sum_{R_x} \frac{4\pi}{3} N(R_x) (R_h^3 - R_x^3).$$

When spin temperature profiles around ionization bubbles are very large and overlap significantly, f_{hb} can be much larger than unity. After correcting for these overlaps, the volume fraction occupied by heating bubbles is (Section 2.1.5)

$$f_h \simeq \frac{f_{hb}(1 - f_i)}{1 + f_{hb}} \quad \text{or} \quad f_h \simeq \left(1 + \frac{f_i}{f_{hb}}\right) (1 - e^{-f_{hb}}) - f_i,$$

where, the second expression is more accurate. We have used the first expression in [Raste and Sethi \[2018\]](#) and second expression in [Raste and Sethi \[2019\]](#). For both expressions, f_h approaches f_{hb} when f_{hb} and f_i are small. However, f_h remains less than unity even if the value of f_{hb} becomes much larger than unity.

4.4 Complete Model

In this section, we develop a formalism to calculate the correlation of dimensionless brightness temperature ψ for epochs at which ionization volume fraction is small. This ensures that ionization bubbles are separate and non-overlapping. However, as described in Section 2.1.5, our formulation allows us to deal with overlap of T_S profiles. If we strictly enforce that the ionization bubbles of their profiles do not overlap, then we get negative correlation at the intermediate scale. This is clearly an artefact, and so we do not enforce that condition, but still include some of those cases for the sake of completeness.

To calculate two-point correlation function, we need to find all pairs of points which are separated by distance r , and multiply them by the HI signal at those points (Figure 4.1).

4.4.1 Correlation of Neutral Region ($\langle n_1 n_2 \rangle$)

To find two-point correlation function of neutral region, we need to find all pairs of points (a and b) which are separated by distance r and multiply by the neutral fraction n at those points. Since in our work, the value of n is either 0 or 1, we essentially need to count the pairs which have both points in the neutral region. Therefore,

$$\begin{aligned} \langle n_1 n_2 \rangle &= 1^2 \mathcal{P}(a_n \cap b_n) + 0 \mathcal{P}(a_n \cap b_i) + 0 \mathcal{P}(a_i \cap b_n) + 0 \mathcal{P}(a_i \cap b_i) \\ &= \mathcal{P}(a_n \cap b_n). \end{aligned}$$

If there was no correlation between neutral regions, probability of two points being neutral is,

$$\mathcal{P}_{nc}(a_n \cap b_n) = \mathcal{P}(a_n) \mathcal{P}(b_n) = f_n^2.$$

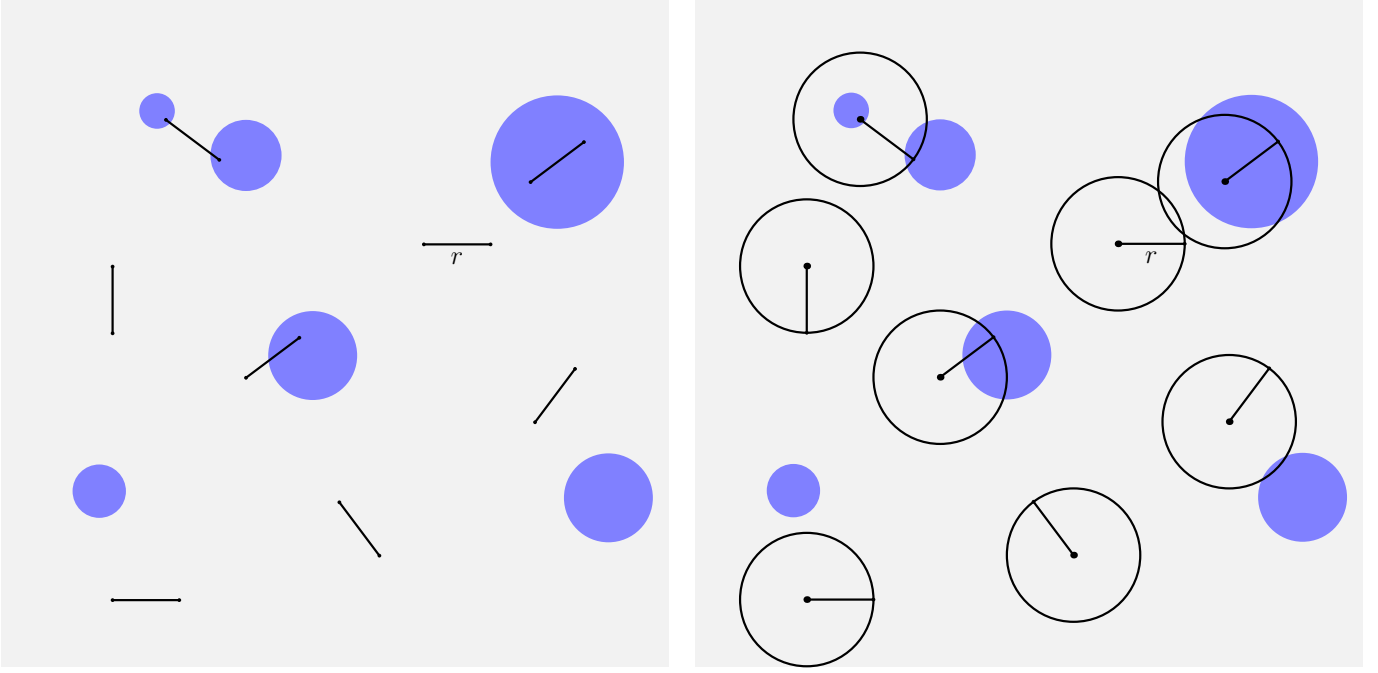


Figure 4.2: Finding pairs of points separated by distance r is equivalent to finding points and their neighbours at distance r .

Here $\mathcal{P}(a_n)$ and $\mathcal{P}(b_n)$ are the probability of one point being neutral, which is equal to average neutral fraction f_n . The statement that the points do not have any correlation implies that the probability of one point being neutral is independent of the ionized state of the other point.

For EoR studies, the ionized points are in the HII bubble. The neutral region has a very irregular shape as it is the remainder of the volume from which spherical bubbles of various sizes have been carved out. Finding a correlation for this random geometry of the neutral regions is very difficult. Therefore it is desirable if we can put one of the two points in an ionized region and find the probability of its neighbour being neutral. Here we choose one point and try to find all its neighbours which are located on the surface of a sphere of radius r (Figure 4.2). Using Eq. E.3 and Eq. E.1,

$$\mathcal{P}(a_n \cap b_n) = \mathcal{P}(a_n) - \mathcal{P}(a_n \cap b_i).$$

Now we calculate the probability that point a is neutral and point b is ionized ($\mathcal{P}(a_n \cap b_i)$). Point b lies in *some* ionized bubble, so the statement that its neighbor (point a) at distance r is neutral means that point a lies outside *that* bubble in which point b is, denoted as *out same*, and also outside *any other* bubble, denoted as *out other* (Figure 4.3). Using Eq. E.2,

$$\begin{aligned} \mathcal{P}(a_n \cap b_i) &= \mathcal{P}((a\{\text{out same}\} \cap a\{\text{out other}\}) \cap b_i) \\ &= \mathcal{P}(a\{\text{out other}\} | (a\{\text{out same}\} \cap b_i)) \mathcal{P}(a\{\text{out same}\} \cap b_i). \end{aligned}$$

$\mathcal{P}(a\{\text{out other}\} | (a\{\text{out same}\} \cap b_i))$ is the probability that it is neutral given that point a lies outside the bubble in which point b is. For large enough distance, this quantity is average neutral fraction f_n , as we assume random bubble distribution.

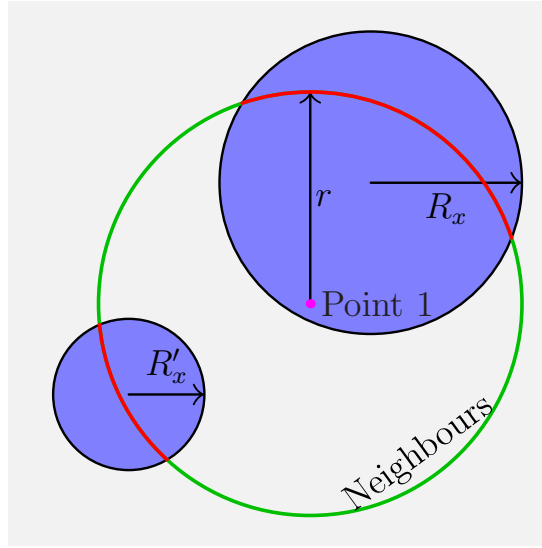


Figure 4.3: If one point is ionized, what is the probability of its neighbour at distance r being neutral?

There are multiple caveats to this simple assumption: (a) If ionization bubble centres were correlated, then that would decrease the probability of finding neutral regions surrounding an ionization bubble on certain scales. (b) If we enforce the condition that the ionization bubbles do not overlap, then the probability of ionized region right outside a bubble is smaller than f_i . This scenario essentially anti-correlates bubble centres. (c) If we assume that the ionization bubbles can overlap, then the resultant shape will not be spherical. This will also affect the neutral fraction surrounding ionization bubbles. (d) If we perform calculations for finite volume (as would be the case for a simulation), the ionized volume fraction around an ionization bubble will be less than the global ionized volume fraction f_i since we need to subtract the volume occupied by the said ionization bubble¹. This effect should cause anti-correlation between bubbles on certain scales. (e) For finite volume, Poisson fluctuations in the distribution of ionization bubbles would also affect the probability of finding an ionized or neutral region.

In our work, we ignore all these complications. We assume that bubbles are spherical, uncorrelated, non-overlapping and randomly distributed. And we assume infinite volume for averaging. Hence, when a point is outside a certain bubble, its probability to be ionized or neutral is equal to f_i or f_n respectively.

Now, we need to find $\mathcal{P}(a\{\text{out same}\} \cap b_i)$, the probability that point b is in an ionization bubble and point a lies out of that bubble. Since point 2 can be in a bubble with any radius R_x , we have

$$\begin{aligned}
 \mathcal{P}(a\{\text{out same}\} \cap b_i) &= \sum_{R_x} \mathcal{P}(a\{\text{out same}\} \cap b_i(R_x)) \\
 &= \sum_{R_x} \mathcal{P}(b_i(R_x)) \mathcal{P}(a\{\text{out same}\} | b_i(R_x)) \\
 &= \sum_{R_x} N(R_x) \frac{4\pi}{3} R_x^3 D(r, R_x),
 \end{aligned}$$

¹ Example: If there are five red and five blue balls in a box and we choose two balls at random, one after the other, then the probability of the first ball being red is $5/10 = 0.5$, but the probability of second ball being red given that first ball is red is not $5/10$, but $4/9 < 0.5$.

where $\mathcal{P}(a\{\text{out same}\}|b_i(R_x)) = D(r, R_x)$ is the probability that point a is out of the bubble given that point b is inside a bubble of radius R_x (Appendix F). $\mathcal{P}(b_i(R_x))$ is the probability of point b being in an ionization bubble of radius R_x , which is $4\pi/3 N(R_x)R_x^3$ (Section 4.3). Therefore,

$$\begin{aligned}\langle n_1 n_2 \rangle &= \mathcal{P}(a_n) - \mathcal{P}(a_n \cap b_i) \\ &= f_n - \mathcal{P}(a\{\text{out other}\}|(a\{\text{out same}\} \cap b_i)) \mathcal{P}(a\{\text{out same}\} \cap b_i) \\ &= f_n - f_n \sum_{R_x} N(R_x) \frac{4\pi}{3} R_x^3 D(r, R_x).\end{aligned}\tag{4.17}$$

This expression reduces to the results of [Zaldarriaga et al. \[2004\]](#), when a single scale corresponding to size of ionized bubbles is taken for a fixed ionization fraction. When the distance between two points $r = 0$, we have $D(0, R_x) = 0$, and

$$\langle n_1 n_2 \rangle = f_n - f_n \sum_{R_x} N(R_x) \frac{4\pi}{3} R_x^3 D(r, R_x) = f_n.\tag{4.18}$$

Enforcing No-Overlap Condition for Temperature Profiles: In the above derivation, we have made no assumptions about the overlap of T_S profiles surrounding these ionization bubbles. For the sake of completeness and to understand our formalism, we can imagine a scenario in which both the ionization bubbles and their T_S profiles are isolated and non-overlapping. For this, we take

$$\begin{aligned}\mathcal{P}(a_n \cap b_n) &= \mathcal{P}(a_n) - \mathcal{P}(b_i) + \mathcal{P}(a_i \cap b_i) \\ &= f_n - f_i + \mathcal{P}(a_i \cap b_i).\end{aligned}$$

Here we need to find the probability of both points being ionized, given that their surrounding heating profiles do not overlap. If point a is inside a bubble of radius R_x , then its neighbour b can be in the same ionization bubble or another ionization bubble, giving,

$$\begin{aligned}\mathcal{P}(a_i \cap b_i) &= \sum_{R_x} \mathcal{P}(b_i \cap a_i(R_x)) \\ &= \sum_{R_x} \mathcal{P}(b\{\text{same}\} \cap a_i(R_x)) + \sum_{R_x} \mathcal{P}(b\{\text{diff}\} \cap a_i(R_x)). \\ &= \sum_{R_x} \mathcal{P}(a_i(R_x)) \mathcal{P}(b\{\text{same}\}|a_i(R_x)) + \sum_{R_x} \mathcal{P}(b\{\text{diff}\} \cap a_i(R_x)).\end{aligned}$$

Here $\mathcal{P}(b\{\text{same}\}|a_i(R_x))$ is the probability that point b is in the same ionization bubble in which point a is, which is given as $(1 - D(r, R_x))$. Therefore,

$$\begin{aligned}\mathcal{P}(a_n \cap b_n) &= f_n - f_i + \sum_{R_x} \mathcal{P}(a_i(R_x)) \mathcal{P}(b\{\text{same}\}|a_i(R_x)) + \sum_{R_x} \mathcal{P}(b\{\text{diff}\} \cap a_i(R_x)) \\ &= f_n - f_i + \sum_{R_x} N(R_x) \frac{4\pi}{3} R_x^3 - \sum_{R_x} N(R_x) \frac{4\pi}{3} R_x^3 D(r, R_x) + \sum_{R_x} \mathcal{P}(b\{\text{diff}\} \cap a_i(R_x)) \\ &= f_n - \sum_{R_x} N(R_x) \frac{4\pi}{3} R_x^3 D(r, R_x) + \sum_{R_x} \mathcal{P}(a_i(R_x)) \mathcal{P}(b\{\text{diff}\}|a_i(R_x)).\end{aligned}$$

To evaluate this expression, we need to compute $\mathcal{P}(b\{\text{diff}\}|a_i(R_x))$, the probability of point b lying in some other ionization bubble given that point a lies in an ionization bubble of radius R_x . Point b can be in bubble of any size R'_x , therefore,

$$\sum_{R_x} \mathcal{P}(b\{\text{diff}\} \cap a_i(R_x)) = \sum_{R_x} \sum_{R'_x} \mathcal{P}(a_i(R_x)) \mathcal{P}(b_i(R'_x)\{\text{diff}\}|a_i(R_x)).$$

$\mathcal{P}(b_i(R'_x)\{\text{diff}\}|a_i(R_x))$ is the probability that if point a is inside ionization bubble of radius R_x , then point b is inside another ionization bubble with radius R'_x . To satisfy the condition of non-overlap, we need point b to be farther away than distance X from the centre of the bubble which contains point a . Therefore we have,

$$\mathcal{P}(b_i(R'_x)\{\text{diff}\}|a_i(R_x)) = E(r, R_x, X) \mathcal{P}(b_i(R'_x)).$$

And finally,

$$\begin{aligned} \mathcal{P}(n_1 \cap n_2) &= f_n - \sum_{R_x} N(R_x) \frac{4\pi}{3} R_x^3 D(r, R_x) + \sum_{R_x} \sum_{R'_x} \mathcal{P}(a_i(R_x)) \mathcal{P}(b_i(R'_x)) E(r, R_x, X) \\ &= f_n + \sum_{R_x} N(R_x) \frac{4\pi}{3} R_x^3 \left(\sum_{R'_x} N(R'_x) \frac{4\pi}{3} R'^3_x E(r, R_x, X) - D(r, R_x) \right). \end{aligned} \quad (4.19)$$

When there we do not enforce any condition on overlap of T_S profiles, we can take $X = R_x$, which results in $E(r, R_x, R_x) = D(r, R_x)$ (Appendix F) and Eq. 4.19 reduces to Eq. 4.17. If we take $X = R_h$, it ensures that there are no other ionization bubbles within the T_S profiles of an ionization bubble; however, it allows the T_S profiles to overlap with one another. To ensure that the temperature profiles themselves do not overlap, we can take $X = R_{ha} + R_{hb} - R_{xb}$. It should be noted that for small ionized fraction f_i , Eq. 4.19 reduces to Eq. 4.17 irrespective of other assumptions, which shows that Eq. 4.17 is a good assumption at early times.

Eq. 4.19 is not symmetric with respect to R_{xa} and R_{xb} . Given two points, the correlation will depend on which point is taken as point a . However, since we sum over all R_x , the final expression is symmetric with respect to points a and b .

4.4.2 Correlation between Neutral region and Temperature ($\langle n_1 s_2 \rangle$)

Here we need to find the correlation between neutral and regions with temperature s . The point b needs to be in the neutral region because the spin temperature is not even defined within an ionized region. Therefore,

$$\langle n_1 s_2 \rangle = s_b \mathcal{P}(a_n \cap b_{s_b}) + \sum_s s \mathcal{P}(a_n \cap b_s) \quad (4.20)$$

Here, s_b corresponds to the background temperature at any redshift and the summation is over temperature profiles. The first term can be written as

$$\mathcal{P}(a_n \cap b_{s_b}) = \mathcal{P}(b_{s_b}) - \mathcal{P}(b_{s_b} \cap a_i).$$

Here $\mathcal{P}(b_{s_b})$ is the average background fraction f_b and $\mathcal{P}(b_{s_b} \cap a_i)$ is the probability that point a is ionized and point b is in background. Point a lies in *some* ionization bubble, so the statement that its neighbor (point b) at distance r is in background region means that point b is outside the T_S profile corresponding to *that* ionization bubble, denoted by *out same*, and that it is outside *any other* T_S profile, denoted by *out other*. Hence,

$$\begin{aligned}\mathcal{P}(b_{s_b} \cap a_i) &= \mathcal{P}((b_{s_b} \{\text{out same}\} \cap b_{s_b} \{\text{out other}\}) \cap a_i) \\ &= \mathcal{P}(b_{s_b} \{\text{out other}\} | (b_{s_b} \{\text{out same}\} \cap a_i)) \mathcal{P}(b_{s_b} \{\text{out same}\} \cap a_i).\end{aligned}$$

$\mathcal{P}(b_{s_b} \{\text{out other}\} | (b_{s_b} \{\text{out same}\} \cap a_i))$ gives the probability that point b is in background region given that point a lies in *some* ionization bubble and point b lies outside T_S profile corresponding to *that* ionization bubble. If we assume that the bubbles are non-overlapping and uncorrelated then, this probability equals the fraction of universe heated at background temperature, f_b ¹.

$\mathcal{P}(b_{s_b} \{\text{out same}\} \cap a_i)$ is the probability of point a being in an ionization bubble and point b being out of the T_S profile corresponding to that ionization bubble. Given the distribution of radii of ionization bubbles R_x , we have,

$$\begin{aligned}\mathcal{P}(b_{s_b} \{\text{out same}\} \cap a_i) &= \sum_{R_x} \mathcal{P}(b_{s_b} \{\text{out same}\} \cap a_i(R_x)) \\ &= \sum_{R_x} N(R_x) \frac{4\pi}{3} R_x^3 \mathcal{P}(b_{s_b} \{\text{out same}\} | a_i(R_x)).\end{aligned}$$

We see that $\mathcal{P}(b_{s_b} \{\text{out same}\} | a_i(R_x))$, the probability that point b is out of the T_S profile (of radius R_h) corresponding to the ionization bubble of radius R_x in which point a lies is $E(r, R_x, R_h)$. Thus we have

$$\begin{aligned}\mathcal{P}(a_n \cap b_s) &= \mathcal{P}(b_{s_b}) - \mathcal{P}(b_{s_b} \{\text{out other}\} | (b_{s_b} \{\text{out same}\} \cap a_i)) \mathcal{P}(b_{s_b} \{\text{out same}\} \cap a_i) \\ &= f_b - f_b \sum_{R_x} N(R_x) \frac{4\pi}{3} R_x^3 E(r, R_x, R_h).\end{aligned}\tag{4.21}$$

When there are no T_S profiles (i.e. in the case of uniform heating), we have $R_h \rightarrow R_x$, $f_b \rightarrow f_n$, and $E(r, R_x, R_h) \rightarrow D(r, R_x)$, and the Eq. 4.21 reduces to the Eq. 4.53.

Now, we need to find $\mathcal{P}(a_n \cap b_s)$. Here, point b is in a T_S profile, but outside the ionization bubble. This can be done in two ways.

Method 1

Point b can be in T_S profile of any radius, thus,

$$\begin{aligned}\mathcal{P}(a_n \cap b_s) &= \sum_{R_x} \mathcal{P}(s, R_x) \mathcal{P}(a_n | b_s(R_x)) \\ &= \sum_{R_x} N(R_x) \frac{4\pi}{3} \frac{f_h}{f_{hb}} ((R_s + \Delta R_s)^3 - R_s^3) \mathcal{P}(a_n | b_s(R_x)),\end{aligned}$$

¹Refer to the discussion in the previous section.

where $\mathcal{P}(s, R_x)$ is the probability of a point being in the shell with temperature s around an ionization bubble of radius R_x , and $\mathcal{P}(a_n|b_s(R_x))$ is the probability that point a is in some neutral region given that point b is in the T_S profile of ionization bubble of radius R_x with temperature s . This can be calculated in multiple ways. None of them is entirely correct.

Overlap Allowed: If point a is outside the ionization bubble corresponding to T_S profile in which point b is, then its probability to be ionized is the probability of there being an ionization bubble at distance r from a neutral point b . If we assume that the ionization bubbles are randomly distributed and that they can overlap with the T_S profile of one another, then we can use the result of section 4.4.1, and get¹,

$$\mathcal{P}(a_n|b_s(R_x)) = \left(1 - \sum_{R'_x} N(R'_x) \frac{4\pi}{3} R'_x{}^3 D(r, R'_x) \right) C(r, R_s, R_s + \Delta R_s, R_x).$$

Here the $C()$ term accounts for the fact that if point a is inside the ionization bubble corresponding to profile of point b , then it is definitely not neutral. Therefore we have,

$$\mathcal{P}(a_n \cap b_s) = \sum_{R_x} N(R_x) \frac{4\pi}{3} \frac{f_h}{f_{hb}} ((R_s + \Delta R_s)^3 - R_s^3) \left(1 - \sum_{R'_x} N(R'_x) \frac{4\pi}{3} R'_x{}^3 D(r, R'_x) \right) C(r, R_s, R_s + \Delta R_s, R_x),$$

and the final expression is

$$\begin{aligned} \langle n_1 s_2 \rangle &= s_b f_b - s_b f_b \sum_{R_x} N(R_x) \frac{4\pi}{3} R_x^3 E(r, R_x, R_h) \\ &+ \left(1 - \sum_{R'_x} N(R'_x) \frac{4\pi}{3} R'_x{}^3 D(r, R'_x) \right) \sum_{R_x} N(R_x) \frac{4\pi}{3} \frac{f_h}{f_{hb}} \\ &\quad \sum_{s(R_x)} s ((R_s + \Delta R_s)^3 - R_s^3) C(r, R_s, R_s + \Delta R_s, R_x). \end{aligned} \quad (4.22)$$

We use this expression in our calculations. We can also calculate correlation between neutral region and spin temperature at the same point:

$$\langle s \rangle = \langle a_n a_s \rangle = b_{s_b} f_b + \sum_{R_x} N(R_x) \frac{4\pi}{3} \frac{f_h}{f_{hb}} \sum_{s(R_x)} s ((R_s + \Delta R_s)^3 - R_s^3). \quad (4.23)$$

No Overlap: If we enforce that no ionization bubble overlaps with the T_S profile of another bubble, then we get a different answer. If point b is in T_S profile of a bubble, then its neighbour is definitely ionized if it is within the ionization bubble, definitely neutral if it is within the profile, and neutral with probability f_n if it is outside the profile. Therefore,

$$\mathcal{P}(a_n|b_s(R_x)) = (0)\mathcal{P}(a_n\{\text{bubble}\}|b_s(R_x)) + (1)\mathcal{P}(a_n\{\text{profile}\}|b_s(R_x)) + f_n\mathcal{P}(a_n\{\text{out}\}|b_s(R_x)).$$

And if point b is between distance R_s and $R_s + \Delta R_s$ from the centre of the bubble, then the probability of

¹This expression is not the exact answer even if it gives correct result in various limits, because such approximations might create other problems (e.g. negative power spectrum).

its neighbour at distance r being at distance between R_x and R_h from the centre of the bubble and outside distance R_h is respectively,

$$\begin{aligned}\mathcal{P}(a_n\{\text{profile}\}|b_s(R_x)) &= C(r, R_s, R_s + \Delta R_s, R_x) - C(r, R_s, R_s + \Delta R_s, R_h) \\ \mathcal{P}(a_n\{\text{out}\}|b_s(R_x)) &= C(r, R_s, R_s + \Delta R_s, R_h).\end{aligned}$$

Therefore,

$$\mathcal{P}(a_n|b_s(R_x)) = C(r, R_s, R_s + \Delta R_s, R_x) - (1 - f_n)C(r, R_s, R_s + \Delta R_s, R_h),$$

and the final expression is

$$\begin{aligned}\langle n_1 s_2 \rangle &= s_b f_b - s_b f_b \sum_{R_x} N(R_x) \frac{4\pi}{3} R_x^3 E(r, R_x, R_h) \\ &+ \sum_{R_x} N(R_x) \frac{4\pi}{3} \sum_{s(R_x)} s ((R_s + \Delta R_s)^3 - R_s^3) \\ &\quad (C(r, R_s, R_s + \Delta R_s, R_x) - (1 - f_n)C(r, R_s, R_s + \Delta R_s, R_h)).\end{aligned}\tag{4.24}$$

Here we do not need to include the f_h/f_{hb} factor, since overlaps are explicitly forbidden in this scenario. This is not a good approximation, and we do not use it in our work.

Method 2

Now, instead of putting one point in a T_S profile shell and finding the probability of its neighbour being neutral, we can put one point in an ionization bubble and find the probability of its neighbour being in certain shell of a T_S profile:

$$\begin{aligned}\mathcal{P}(a_n \cap b_s) &= \mathcal{P}(s) - \mathcal{P}(b_s \cap a_i) \\ &= \sum_{R_x} \sum_s \mathcal{P}(s, R_x) - (\mathcal{P}(b_s\{\text{same}\} \cap a_i) + \mathcal{P}(b_s\{\text{diff}\} \cap a_i)),\end{aligned}$$

where, $\mathcal{P}(b_s\{\text{same}\} \cap a_i)$ is the probability point b is in the T_S profile corresponding to the *same* ionization bubble in which point a is, and $\mathcal{P}(b_s\{\text{diff}\} \cap a_i)$ is the probability that point b is in the T_S profile of some *other* ionization bubble. Because point a can be in ionization bubble of any radius R_x , we have,

$$\begin{aligned}\sum_s \mathcal{P}(b_s\{\text{same}\} \cap a_i) &= \sum_{R_x} \sum_{s(R_x)} \mathcal{P}(a_i(R_x)) \mathcal{P}(b_s\{\text{same}\}|a_i(R_x)) \\ &= \sum_{R_x} N(R_x) \frac{4\pi}{3} R_x^3 \sum_{s(R_x)} [E(r, R_x, R_s) - E(r, R_x, R_s + \Delta R_s)].\end{aligned}$$

In the case where the two points are in different bubbles, we have,

$$\sum_s \mathcal{P}(b_s\{\text{diff}\} \cap a_i) = \sum_{R_x} \sum_{R'_x} \sum_{s(R'_x)} \mathcal{P}(b_s(R'_x)\{\text{diff}\} \cap a_i(R_x))$$

$$= \sum_{R_x} N(R_x) \frac{4\pi}{3} R_x^3 \sum_{R'_x} \sum_{s(R'_x)} \mathcal{P}(b_s(R'_x) \{\text{diff}\} | a_i(R_x)),$$

where $\mathcal{P}(b_s(R'_x) \{\text{diff}\} | a_i(R_x))$ is the probability that if a is in the ionization bubble of radius R_x , then point b is in some different bubble with radius R'_x and has temperature s . Again, we can derive this in multiple ways.

Overlap Allowed: For these two points to be in different bubbles, the main requirement is that point b has to be outside the T_S profile of the bubble in which point a is. Therefore,

$$\begin{aligned} \mathcal{P}(b_s(R'_x) \{\text{diff}\} | a_i(R_x)) &= \mathcal{P}(s, R'_x) C(r, 0, R_x, R_h) \\ &= N(R'_x) \frac{4\pi}{3} \frac{f_h}{f_{hb}} ((R'_s + \Delta R'_s)^3 - R'_s{}^3) C(r, 0, R_x, R_h). \end{aligned}$$

Putting all terms together, we have

$$\begin{aligned} \langle n_2 s_2 \rangle &= s_b f_b - s_b f_b \sum_{R_x} N(R_x) \frac{4\pi}{3} R_x^3 E(r, R_x, R_h) + \sum_{R_x} N(R_x) \frac{4\pi}{3} \frac{f_h}{f_{hb}} \sum_s s ((R_s + \Delta R_s)^3 - R_s^3) \\ &\quad - \sum_{R_x} N(R_x) \frac{4\pi}{3} R_x^3 \sum_s s [E(r, R_x, R_s) - E(r, R_x, R_s + \Delta R_s)] \\ &\quad - \sum_{R_x} N(R_x) \frac{4\pi}{3} R_x^3 C(r, 0, R_x, R_h) \sum_{R'_x} N(R'_x) \frac{4\pi}{3} \frac{f_h}{f_{hb}} \sum_{s(R'_x)} s ((R'_s + \Delta R'_s)^3 - R'_s{}^3). \end{aligned} \quad (4.25)$$

No Overlap: If we assume that the T_S profiles of two bubbles does not overlap, then the main requirement is that point b has to be further away than $R_h + R'_h - (R'_s + \Delta R'_s)$ from the centre of the bubble in which point a is, otherwise these profiles would be overlapping. Therefore,

$$\mathcal{P}(b_s(R'_x) \{\text{diff}\} | a_i(R_x)) = C(r, 0, R_x, R_h + R'_h - (R'_s + \Delta R'_s)) \mathcal{P}(s, R'_x).$$

The final result is,

$$\begin{aligned} \langle n_1 s_2 \rangle &= s_b f_b - s_b f_b \sum_{R_x} N(R_x) \frac{4\pi}{3} R_x^3 E(r, R_x, R_h) + \sum_{R_x} N(R_x) \frac{4\pi}{3} \sum_s s ((R_s + \Delta R_s)^3 - R_s^3) \\ &\quad - \sum_{R_x} N(R_x) \frac{4\pi}{3} R_x^3 \sum_s s [E(r, R_x, R_s) - E(r, R_x, R_s + \Delta R_s)] \\ &\quad - \sum_{R_x} \sum_{R'_x} N(R_x) N(R'_x) \left(\frac{4\pi}{3} \right)^2 R_x^3 \sum_{s(R'_x)} s ((R'_s + \Delta R'_s)^3 - R'_s{}^3) C(r, 0, R_x, R_h + R'_h - (R'_s + \Delta R'_s)). \end{aligned} \quad (4.26)$$

4.4.3 Correlation of Temperature ($\langle s_1 s_2 \rangle$)

To calculate auto-correlation of temperature, we need to find pairs where both points can be in background, one of them in background and another in a T_S profile, or both of them some in profiles. Therefore we have,

$$\langle s_1 s_2 \rangle = s_b^2 \mathcal{P}(a_{s_b} \cap b_{s_b}) + 2s_b \sum_s s \mathcal{P}(a_{s_b} \cap b_s) + \sum_s \sum_{s'} s s' \mathcal{P}(a_s \cap b_{s'}),$$

where the summation is over profiles. The first term can be written as,

$$\mathcal{P}(a_{s_b} \cap b_{s_b}) = \mathcal{P}(a_{s_b}) - \mathcal{P}(a_{s_b} \cap b_{\tilde{s}_b}),$$

where, $\mathcal{P}(a_{s_b} \cap b_{\tilde{s}_b})$ is the probability that point a is in background region, and point b is not. Therefore, point b is either in ionized region or profile region, and its neighbour point a will be in background region only if it is outside the profile of the bubble in which point b is, therefore,

$$\begin{aligned} \mathcal{P}(a_{s_b} \cap b_{s_b}) &= f_b - \mathcal{P}(a_{s_b}|b_i)\mathcal{P}(i) - \sum_s \mathcal{P}(a_{s_b}|b_s)\mathcal{P}(s) \\ &= f_b - f_b \sum_{R_x} N(R_x) \frac{4\pi}{3} \left(R_x^3 E(r, R_x, R_h) + (R_h^3 - R_x^3) \frac{f_h}{f_{hb}} C(r, R_x, R_h, R_h) \right). \end{aligned} \quad (4.27)$$

When point a is in background and point b is in a T_S profile, point a needs to be outside the profile corresponding the bubble in which point b is and also out of any other profile. Therefore,

$$\begin{aligned} \mathcal{P}(a_{s_b} \cap b_s) &= \mathcal{P}((a\{\text{out same}\} \cap a\{\text{out other}\}) \cap b_s) \\ &= \mathcal{P}(a\{\text{out other}\} | (a\{\text{out same}\} \cap b_s)) \mathcal{P}(a\{\text{out same}\} \cap b_s), \end{aligned}$$

where, $\mathcal{P}(a\{\text{out other}\} | (a\{\text{out same}\} \cap b_s))$ is the probability that point a is in background region given that it is out the profile of the bubble in which point b with temperature s . This probability equals the average background volume fraction, f_b . $\mathcal{P}(a\{\text{out same}\} \cap b_s)$ is the probability that point a is out of T_S profile in which point b is has temperature s . As point b can be in bubble with any ionization radius R_x , we have,

$$\begin{aligned} \mathcal{P}(a\{\text{out same}\} \cap b_s) &= \sum_{R_x} \mathcal{P}(s, R_x) \mathcal{P}(a\{\text{out same}\} | b_s(R_x)) \\ &= \sum_{R_x} N(R_x) \frac{4\pi}{3} \frac{f_h}{f_{hb}} ((R_s + \Delta R_s)^3 - R_s^3) C(r, R_s, R_s + \Delta R_s, R_h). \end{aligned}$$

$\mathcal{P}(a\{\text{out same}\} | b_s(R_x))$ is the probability that point a is out of the T_S profile which has ionization radius R_x and which contains point b with temperature s . Finally,

$$\mathcal{P}(a_{s_b} \cap b_s) = f_b \sum_{R_x} N(R_x) \frac{4\pi}{3} \frac{f_h}{f_{hb}} ((R_s + \Delta R_s)^3 - R_s^3) C(r, R_s, R_s + \Delta R_s, R_h). \quad (4.28)$$

In the case where both points are partially heated, these points can belong to the same bubble or different bubbles, which gives

$$\mathcal{P}(a_s \cap b_{s'}) = \mathcal{P}(a_s \cap b_{s'} \{\text{same}\}) + \mathcal{P}(a_s \cap b_{s'} \{\text{diff}\}). \quad (4.29)$$

$\mathcal{P}(a_s \cap b_{s'} \{\text{same}\})$ is the probability that point a and b have temperature s and s' respectively and that they belong to the same bubble. We can further take cases when they are within the same shell or different shells, but it doesn't make any difference in our final expression. Given the distribution of R_x ,

$$\mathcal{P}(a_s \cap b_{s'} \{\text{same}\}) = \sum_{R_x} \mathcal{P}(s, R_x) \mathcal{P}(b_{s'} \{\text{same}\} | a_s(R_x))$$

$$= \sum_{R_x} N(R_x) \frac{4\pi}{3} \frac{f_h}{f_{hb}} ((R_s + \Delta R_s)^3 - R_s^3) \mathcal{P}(b_{s'} \{\text{same}\} | a_s(R_x)),$$

where, $\mathcal{P}(b_{s'} \{\text{same}\} | a_s(R_x))$ is the probability that if point a is in the profile of an ionization bubble of radius R_x and has temperature s , then point b is in the same profile with temperature s' . However, since we allow T_S profiles to overlap with other ionization bubbles, we get

$$\begin{aligned} \sum_s \sum_{s'} ss' \mathcal{P}(a_s \cap b_{s'} \{\text{same}\}) &= \sum_{R_x} N(R_x) \frac{4\pi}{3} \sum_{s(R_x)} \sum_{s'(R_x)} ss' \frac{f_h}{f_{hb}} ((R_s + \Delta R_s)^3 - R_s^3) \\ &\quad (C(r, R_s, R_s + \Delta R_s, R_{s'}) - C(r, R_s, R_s + \Delta R_s, R_{s'} + \Delta R_{s'})) \\ &\quad \left(1 - \sum_{R'_x} N(R'_x) \frac{4\pi}{3} R_x^3 D(r, R'_x) \right). \end{aligned} \quad (4.30)$$

Now $\mathcal{P}(a_s \cap b_{s'} \{\text{diff}\})$ is the probability that point a has temperature s , point b has temperature s' and they both belong to different bubbles, therefore,

$$\mathcal{P}(a_s \cap b_{s'} \{\text{diff}\}) = \sum_{R_x} \mathcal{P}(s, R_x) \mathcal{P}((b_{s'} \{\text{diff}\}) | a_s(R_x)).$$

Here we take a simple assumption that if point b is outside the profile in which point a is, then its probability of having temperature s' is equal to the global probability of s' temperature shell. Therefore, we have,

$$\begin{aligned} \sum_{s'} \mathcal{P}((b_{s'} \{\text{diff}\}) | a_s(R_x)) &= C(r, R_s, R_s + \Delta R_s, R_h) \sum_{R'_x} \sum_{s'(R'_x)} \mathcal{P}(s', R'_x) \\ &= C(r, R_s, R_s + \Delta R_s, R_h) \sum_{R'_x} N(R'_x) \frac{4\pi}{3} \frac{f_h}{f_{hb}} \sum_{s'(R'_x)} ((R'_{s'} + \Delta R'_{s'})^3 - R'^3_{s'}), \end{aligned}$$

which gives,

$$\begin{aligned} \sum_s \sum_{s'} ss' \mathcal{P}(s \cap s' \{\text{diff}\}) &= \sum_{R_x} N(R_x) \frac{4\pi}{3} \sum_{s(R_x)} s f_b ((R_s + \Delta R_s)^3 - R_s^3) \\ &\quad C(r, R_s, R_s + \Delta R_s, R_h) \\ &\quad \sum_{R'_x} N(R'_x) \frac{4\pi}{3} \sum_{s'(R'_x)} s' f_b ((R'_{s'} + \Delta R'_{s'})^3 - R'^3_{s'}). \end{aligned} \quad (4.31)$$

Using Eqs. 4.27, 4.28, 4.30, and 4.31, we get the final expression,

$$\begin{aligned} \langle s_1 s_2 \rangle &= s_b^2 f_b - s_b^2 f_b \sum_{R_x} N(R_x) \frac{4\pi}{3} \left(\frac{f_h}{f_{hb}} (R_h^3 - R_x^3) C(r, R_x, R_h, R_h) + R_x^3 E(r, R_x, R_h) \right) \\ &\quad + \sum_{R_x} N(R_x) \frac{4\pi}{3} \frac{f_h}{f_{hb}} \sum_{s(R_x)} s ((R_s + \Delta R_s)^3 - R_s^3) C(r, R_s, R_s + \Delta R_s, R_h) \\ &\quad \left(2s_b f_b + \sum_{R'_x} N(R'_x) \frac{4\pi}{3} \frac{f_h}{f_{hb}} \sum_{s'(R'_x)} s' ((R'_{s'} + \Delta R'_{s'})^3 - R'^3_{s'}) \right) \end{aligned}$$

$$\begin{aligned}
& + \sum_{R_x} N(R_x) \frac{4\pi}{3} \frac{f_h}{f_{hb}} \sum_{s(R_x)} \sum_{s'(R_x)} ss' ((R_s + \Delta R_s)^3 - R_s^3) \\
& \times (C(r, R_s, R_s + \Delta R_s, R_{s'}) - C(r, R_s, R_s + \Delta R_s, R_{s'} + \Delta R_{s'})) \\
& \left(1 - \sum_{R'_x} N(R'_x) \frac{4\pi}{3} R_x^3 D(r, R'_x) \right). \tag{4.32}
\end{aligned}$$

We use this expression in our work. We also calculate the correlation of temperature at the same point ($r = 0$):

$$\langle s^2 \rangle = \langle ss \rangle = s_b^2 f_b + \sum_{R_x} N(R_x) \frac{4\pi}{3} \frac{f_h}{f_{hb}} \sum_{s(R_x)} s^2 ((R_s + \Delta R_s)^3 - R_s^3).$$

Enforcing Non-Overlap of Temperature Profiles: If we assume that the profiles of bubbles do not overlap, then the calculation is different. Eq. 4.27 is modified as,

$$\mathcal{P}(a_{s_b} \cap b_{s_b}) = f_b - f_b \sum_{R_x} N(R_x) \frac{4\pi}{3} R_h^3 D(r, R_h), \tag{4.33}$$

since we can take the ionization bubble and its profile as one bubble of radius R_h and calculate probability of a point being outside that. In Eq. 4.28, we ignore the correction term due to overlap and get,

$$\mathcal{P}(a_{s_b} \cap b_s) = f_b \sum_{R_x} N(R_x) \frac{4\pi}{3} ((R_s + \Delta R_s)^3 - R_s^3) C(r, R_s, R_s + \Delta R_s, R_h). \tag{4.34}$$

When both points are in the same bubble, we do not need to consider the modification in the probability due to overlap, so Eq. 4.30 is modified as

$$\begin{aligned}
\sum_s \sum_{s'} ss' \mathcal{P}(s \cap s' \{ \text{same} \}) & = \sum_{R_x} N(R_x) \frac{4\pi}{3} \sum_s \sum_{s'} ss' ((R_s + \Delta R_s)^3 - R_s^3) \\
& \times (C(r, R_s, R_s + \Delta R_s, R_{s'}) - C(r, R_s, R_s + \Delta R_s, R_{s'} + \Delta R_{s'})). \tag{4.35}
\end{aligned}$$

When both points are in different bubbles, they both can belong to bubble of any size, therefore,

$$\begin{aligned}
\sum_s \sum_{s'} \mathcal{P}(a_s \cap b_{s'} \{ \text{diff} \}) & = \sum_{R_x} \sum_{R'_x} \sum_{s(R_x)} \sum_{s'(R'_x)} \mathcal{P}(s, R_x) \mathcal{P}(b_{s'}(R'_x) \{ \text{diff} \} | a_s(R_x)), \\
& = \sum_{R_x} \sum_{R'_x} N(R_x) N(R'_x) \left(\frac{4\pi}{3} \right)^2 \sum_{s(R_x)} \sum_{s'(R'_x)} ((R_s + \Delta R_s)^3 - R_s^3) ((R'_{s'} + \Delta R'_{s'})^3 - R'^3_{s'}) \\
& C(r, R_s, R_s + \Delta R_s, R_h + R'_h - (R'_{s'} + \Delta R'_{s'})) \tag{4.36}
\end{aligned}$$

where, $\mathcal{P}(b_{s'}(R'_x) \{ \text{diff} \} | a_s(R_x))$ is the probability that if point a has temperature s in profile of an ionization bubble of radius R_x , then point b has temperature s' in profile of a different ionization bubble with radius R'_x . For these two profiles to not overlap, the main requirement is that point b has to be further away than distance $R_h + R'_h - (R'_{s'} + \Delta R'_{s'})$ from the centre of the bubble in which point a is.

Using Eqs. 4.33, 4.28, 4.35, and 4.36, we finally obtain the expression for the heating correlation function,

$$\begin{aligned}
\langle s_1 s_2 \rangle &= s_b^2 f_b - s_b^2 f_b \sum_{R_x} N(R_x) \frac{4\pi}{3} R_h^3 D(r, R_h) \\
&+ 2s_b f_b \sum_{R_x} N(R_x) \frac{4\pi}{3} \sum_{s(R_x)} s ((R_s + \Delta R_s)^3 - R_s^3) C(r, R_s, R_s + \Delta R_s, R_h) \\
&+ \sum_{R_x} N(R_x) \frac{4\pi}{3} \sum_{s(R_x)} \sum_{s'(R_x)} s s' ((R_s + \Delta R_s)^3 - R_s^3) \\
&\quad (C(r, R_s, R_s + \Delta R_s, R_{s'}) - C(r, R_s, R_s + \Delta R_s, R_{s'} + \Delta R_{s'})) \\
&+ \sum_{R_x} \sum_{R'_x} N(R_x) N(R'_x) \left(\frac{4\pi}{3} \right)^2 \sum_{s(R_x)} \sum_{s'(R'_x)} s s' ((R_s + \Delta R_s)^3 - R_s^3) ((R'_{s'} + \Delta R'_{s'})^3 - R'^3_{s'}) \\
&\quad C(r, R_s, R_s + \Delta R_s, R_h + R'_h - (R'_{s'} + \Delta R'_{s'})). \tag{4.37}
\end{aligned}$$

4.4.4 Alternative Method ($\langle \phi_1 \phi_2 \rangle$)

Since we have already assumed that the cross correlation of density with ionization or spin temperature is negligible, we try to find the auto-correlation of $\phi = n(1 - s)$ (henceforth referred to as ‘temperature’ in this section) (Eq. 4.7). Therefore to calculate correlation at scale r , we need to find pairs of points a and b which are separated by distance r and multiply them by temperatures at those points as,

$$\begin{aligned}
\langle \phi_1 \phi_2 \rangle &= \phi_{\text{bg}}^2 \mathcal{P}(a_{\text{bg}} \cap b_{\text{bg}}) + 2\phi_{\text{bg}} \sum_{R_x} \sum_{s(R_x)} \phi_s \mathcal{P}(a_{\text{bg}} \cap b_s) \\
&+ \sum_{R_x} \sum_{s(R_x)} R'_x \sum_{s'(R'_x)} \phi_s \phi_{s'} \mathcal{P}(a_s \cap b_{s'}). \tag{4.38}
\end{aligned}$$

When both points are in background, we get

$$\mathcal{P}(a_{\text{bg}} \cap b_{\text{bg}}) = \mathcal{P}(a_{\text{bg}}) - \mathcal{P}(a_{\text{bg}} \cap b_i) - \sum_{R_x} \sum_{s(R_x)} \mathcal{P}(a_{\text{bg}} \cap b_s). \tag{4.39}$$

In the case where both points are partially heated, these points can be within the same bubble or different bubbles. Within the same bubble, they can be in the same shell or different shells. This gives,

$$\begin{aligned}
\sum_{R_x} \sum_{s(R_x)} \sum_{R'_x} \sum_{s'(R'_x)} \phi_s \phi_{s'} \mathcal{P}(a_s \cap b_{s'}) &= \sum_{R_x} \sum_{s(R_x)} \phi_s^2 \mathcal{P}(a_s \cap b_s \{\text{same}\}) \\
&+ \sum_{R_x} \sum_{s(R_x)} \sum_{s'(R_x) \neq s} \phi_s \phi_{s'} \mathcal{P}(a_s \cap b_{s'} \{\text{same}\}) \\
&+ \sum_{R_x} \sum_{s(R_x)} \sum_{R'_x} \sum_{s'(R'_x)} \phi_s \phi_{s'} \mathcal{P}(a_s \cap b_{s'} \{\text{diff}\}), \tag{4.40}
\end{aligned}$$

where, $\mathcal{P}(a_s \cap b_s \{\text{same}\})$ is the probability that both points are in the same bubble with the same temperature ϕ_s . This is straightforward to calculate. However, since we allow overlap of heated profiles, the simplest

derivation is not necessarily correct. Instead, we expand it further,

$$\begin{aligned}
\sum_{R_x} \sum_{s(R_x)} \phi_s^2 \mathcal{P}(a_s \cap b_s \{\text{same}\}) &= \sum_{R_x} \sum_{s(R_x)} \phi_s^2 \left(\mathcal{P}(a_s) - \mathcal{P}(a_s \cap b_{\text{bg}}) - \mathcal{P}(a_s \cap b_i) \right) \\
&\quad - \sum_{R_x} \sum_{s(R_x)} \sum_{s'(R_x) \neq s} \phi_s^2 \mathcal{P}(a_s \cap b_{s'} \{\text{same}\}) \\
&\quad - \sum_{R_x} \sum_{s(R_x)} \sum_{R'_x} \sum_{s'(R'_x)} \phi_s^2 \mathcal{P}(a_s \cap b_{s'} \{\text{diff}\}). \tag{4.41}
\end{aligned}$$

Putting Eqs. 4.39, 4.40 and 4.41 in Eq. 4.38, we get,

$$\begin{aligned}
\langle \phi_1 \phi_2 \rangle &= \phi_{\text{bg}}^2 \mathcal{P}(a_{\text{bg}}) - \phi_{\text{bg}}^2 \mathcal{P}(a_{\text{bg}} \cap b_i) + \langle \phi_s^2 \rangle \\
&\quad - \sum_{R_x} \sum_{s(R_x)} \phi_s^2 \mathcal{P}(a_s \cap b_i) - \sum_{R_x} \sum_{s(R_x)} (\phi_{\text{bg}} - \phi_s)^2 \mathcal{P}(a_{\text{bg}} \cap b_s) \\
&\quad + \sum_{R_x} \sum_{s(R_x)} \sum_{s'(R_x)} \phi_s (\phi_{s'} - \phi_s) \mathcal{P}(a_s \cap b_{s'} \{\text{same}\}) \\
&\quad + \sum_{R_x} \sum_{s(R_x)} \sum_{R'_x} \sum_{s'(R'_x)} \phi_s (\phi_{s'} - \phi_s) \mathcal{P}(a_s \cap b_{s'} \{\text{diff}\}), \tag{4.42}
\end{aligned}$$

where we define,

$$\begin{aligned}
\langle \phi_s \rangle &= \sum_{R_x} \frac{4\pi}{3} N(R_x) \sum_{s(R_x)} \phi_s \frac{f_h}{f_{hb}} ((R_s + \Delta R_s)^3 - R_s^3) \\
\langle \phi_s^2 \rangle &= \sum_{R_x} \frac{4\pi}{3} N(R_x) \sum_{s(R_x)} \phi_s^2 \frac{f_h}{f_{hb}} ((R_s + \Delta R_s)^3 - R_s^3). \tag{4.43}
\end{aligned}$$

The probability of point a being in background and point b being ionized is

$$\mathcal{P}(a_{\text{bg}} \cap b_i) = f_b \sum_{R_x} N(R_x) \frac{4\pi}{3} R_x^3 C(r, 0, R_x, R_h). \tag{4.44}$$

Here the probability of point a being in background region is f_b , given that it is outside the temperature profile of the bubble in which point b is. Similarly, the probability of point a being in background and point b having temperature ϕ_s is,

$$\sum_{R_x} \sum_{s(R_x)} \mathcal{P}(a_{\text{bg}} \cap b_s) = f_b \sum_{R_x} N(R_x) \frac{4\pi}{3} \sum_{s(R_x)} \frac{f_h}{f_{hb}} ((R_s + \Delta R_s)^3 - R_s^3) C(r, R_s, R_s + \Delta R_s, R_h). \tag{4.45}$$

When point a has temperature ϕ_s and point b is ionized, they both can be in the same bubble or in different bubbles, which respectively give first and second terms on the right hand side of the following equation:

$$\begin{aligned}
\sum_{R_x} \sum_{s(R_x)} \phi_s^2 \mathcal{P}(a_s \cap b_i) &= \sum_{R_x} \sum_{s(R_x)} \phi_s^2 \frac{4\pi}{3} N(R_x) R_x^3 (1 - f_i) [C(r, 0, R_x, R_s) - C(r, 0, R_x, R_s + \Delta R_s)] \\
&\quad + \sum_{R_x} \frac{4\pi}{3} N(R_x) R_x^3 C(r, 0, R_x, R_h) \langle \phi_s^2 \rangle. \tag{4.46}
\end{aligned}$$

Here we have taken a simple assumption that if point a is outside the profile of the bubble in which point b is, then its probability of having temperature ϕ_s is equal to the global probability of shell with that temperature. And because ionization bubbles can overlap with profiles, point a can be neutral with probability $1 - f_i$. Now, $\mathcal{P}(a_s \cap b_{s'} \{\text{diff}\})$ is the probability that points a and b are in profiles of different bubbles and have temperature ϕ_s and $\phi_{s'}$ respectively. Here, we can pick either point a or b to be in a profile and find the probability of it neighbour in another profile. Therefore,

$$\begin{aligned} \sum_{R_x} \sum_{s(R_x)} \sum_{R'_x} \sum_{s'(R'_x)} \phi_s(\phi_{s'} - \phi_s) \mathcal{P}(a_s \cap b_{s'} \{\text{diff}\}) &= \sum_{R_x} N(R_x) \frac{4\pi}{3} \sum_{s(R_x)} \frac{f_h}{f_{hb}} ((R_s + \Delta R_s)^3 - R_s^3) \\ &\quad \sum_{R'_x} N(R'_x) \frac{4\pi}{3} \sum_{s'(R'_x)} \frac{f_h}{f_{hb}} ((R'_{s'} + \Delta R'_{s'})^3 - R'_{s'}{}^3) \phi_s(\phi_{s'} - \phi_s) \\ &\quad \frac{C(r, R_s, R_s + \Delta R_s, R_h) + C(r, R'_{s'}, R'_{s'} + \Delta R'_{s'}, R'_h)}{2}. \end{aligned} \quad (4.47)$$

The probability that points a and b have temperatures ϕ_s and $\phi_{s'} \neq \phi_s$, respectively, and they both belong to the same bubble is,

$$\begin{aligned} \sum_{R_x} \sum_{s(R_x)} \sum_{s'(R_x) \neq s} \phi_s \phi_{s'} \mathcal{P}(a_s \cap b_{s'} \cap (\text{same})) &= \sum_{R_x} N(R_x) \frac{4\pi}{3} \sum_{s(R_x)} \frac{f_h}{f_{hb}} ((R_s + \Delta R_s)^3 - R_s^3) \\ &\quad \sum_{s'(R_x) \neq s} \phi_s \phi_{s'} (1 - f_i) [C(r, R_s, R_s + \Delta R_s, R_{s'}) \\ &\quad - C(r, R_s, R_s + \Delta R_s, R_{s'} + \Delta R_{s'})]. \end{aligned} \quad (4.48)$$

We put Eqs. 4.44, 4.45, 4.46, 4.47, and 4.48 in Eq. 4.42, include the influence of ξ and simplify in terms of $F(x, P, Q, R) = 1 - C(x, P, Q, R)$, getting

$$\begin{aligned} \mu &= \xi (f_b \phi_{bg} + \langle \phi_s \rangle)^2 + (1 + \xi) \left((\phi_{bg}^2 f_b + \langle \phi_s^2 \rangle) \sum_{R_x} \frac{4\pi}{3} N(R_x) R_x^3 F(r, 0, R_x, R_h) \right. \\ &\quad + f_b \sum_{R_x} \frac{4\pi}{3} N(R_x) \sum_{s(R_x)} (\phi_{bg} - \phi_s)^2 \frac{f_h}{f_{hb}} ((R_s + \Delta R_s)^3 - R_s^3) F(r, R_s, R_s + \Delta R_s, R_h) \\ &\quad + \sum_{R_x} \frac{4\pi}{3} N(R_x) R_x^3 \sum_{s(R_x)} \phi_s^2 (1 - f_i) [F(r, 0, R_x, R_s) - F(r, 0, R_x, R_s + \Delta R_s)] \\ &\quad - \sum_{R_x} \frac{4\pi}{3} N(R_x) \sum_{s(R_x)} \frac{f_h}{f_{hb}} ((R_s + \Delta R_s)^3 - R_s^3) \sum_{s'(R_x)} \phi_s(\phi_{s'} - \phi_s) (1 - f_i) \\ &\quad \quad [F(r, R_s, R_s + \Delta R_s, R_{s'}) - F(r, R_s, R_s + \Delta R_s, R_{s'} + \Delta R_{s'})] \\ &\quad - \sum_{R_x} \frac{4\pi}{3} N(R_x) \sum_{s(R_x)} \frac{f_h}{f_{hb}} ((R_s + \Delta R_s)^3 - R_s^3) \sum_{R'_x} \frac{4\pi}{3} N(R'_x) \sum_{s'(R'_x)} \frac{f_h}{f_{hb}} ((R'_{s'} + \Delta R'_{s'})^3 - R'_{s'}{}^3) \\ &\quad \quad \left. \phi_s(\phi_{s'} - \phi_s) \frac{1}{2} [F(r, R_s, R_s + \Delta R_s, R_h) + F(r, R'_{s'}, R'_{s'} + \Delta R'_{s'}, R'_h)] \right). \end{aligned} \quad (4.49)$$

The correlation for $r = 0$ is,

$$\begin{aligned}
\mu_0 = \langle \phi^2 \rangle &= (1 + \xi_0)(\phi_{\text{bg}}^2 f_b + \langle \phi_s^2 \rangle) - (f_b \phi_{\text{bg}} + \langle \phi_s \rangle)^2 \\
&= (1 + \xi_0) \left(f_b \phi_{\text{bg}}^2 + \sum_{R_x} N(R_x) \frac{4\pi}{3} \sum_{s(R_x)} \phi_s^2 \frac{f_h}{f_{hb}} ((R_s + \Delta R_s)^3 - R_s^3) \right) \\
&\quad - \left(f_b \phi_{\text{bg}} + \sum_{R_x} \frac{4\pi}{3} N(R_x) \sum_{s(R_x)} \phi_s \frac{f_h}{f_{hb}} ((R_s + \Delta R_s)^3 - R_s^3) \right)^2. \tag{4.50}
\end{aligned}$$

Comparing Eq. 4.49 with results from previous subsections (Eqs. 4.17, 4.22, and 4.32), we see they match very well. Therefore,

$$\langle \phi_1 \phi_2 \rangle \simeq \langle n_1 n_2 \rangle - 2 \langle n_1 s_2 \rangle + \langle s_1 s_2 \rangle, \tag{4.51}$$

which agrees with Eq. 4.4. However, we find that Eq. 4.49 is more robust during extreme cases. It is also possible to taken into account effects of ionization and temperature cross correlation with density and the velocity fluctuations if we expand ϕ to include those effects; however, we do not attempt such model in our work.

4.5 Simple Models

In the early phase of CD/EoR, the fluctuations have scales linked to the sizes of heated and coupled regions. It is difficult to analyse these scales for our complete formalism, where we try to realistically model the condition of the early universe. However, to understand our formalism, we study a few simple models.

4.5.1 Uniform Temperature T_S

We can assume a scenario where there are no T_S profiles around ionization bubbles. Therefore the sum over heating shells is 0. In this limit, we obtain,

$$\begin{aligned}
R_h &= R_x, & E(r, R_x, R_x) &= D(r, R_x), \\
f_b &= f_n, & \text{and} & \quad \Delta R_s = 0.
\end{aligned}$$

Simplifying result of section 4.4.4, we get

$$\begin{aligned}
\mu &= \xi f_n^2 \phi_{\text{bg}}^2 + (1 + \xi) f_n \phi_{\text{bg}}^2 \sum_{R_x} \frac{4\pi}{3} N(R_x) R_x^3 (1 - D(r, R_x)) \\
&= f_n \phi_{\text{bg}}^2 (1 + \xi) \left(1 - \sum_{R_x} \frac{4\pi}{3} N(R_x) R_x^3 D(r, R_x) \right) - f_n^2 \phi_{\text{bg}}^2 \\
&= \phi_{\text{bg}}^2 ((1 + \xi) \langle n_1 n_2 \rangle - f_n^2). \tag{4.52}
\end{aligned}$$

We also get the same expression after simplifying results from section 4.4.1, 4.4.2, 4.4.3 with $\phi_{bg} = 1 - s_b$. This expression agrees with Eq. 4.8 from section 4.2.2, where

$$\langle n_1 n_2 \rangle = f_n - f_n \sum_{R_x} N(R_x) \frac{4\pi}{3} R_x^3 D(r, R_x). \quad (4.53)$$

This result is derived and explored in [Zaldarriaga et al. \[2004\]](#). Here if we take, only one bubble size, we have,

$$\mu = f_n \phi_{bg}^2 ((1 + \xi)(1 - f_i D(r, R_x)) - f_n). \quad (4.54)$$

4.5.2 Uniform Bubble Size

We try to reduce the final expression of μ (Eq. 4.49) for the case where there is only one bubble size, we have,

$$\begin{aligned} \mu = & \xi (f_b \phi_{bg} + \langle \phi_s \rangle)^2 + (1 + \xi) \left((\phi_{bg}^2 f_b + \langle \phi_s^2 \rangle) f_i F(r, 0, R_x, R_h) \right. \\ & + f_b \sum_s \mathcal{P}(s) (\phi_{bg} - \phi_s)^2 F(r, R_s, R_s + \Delta R_s, R_h) \\ & + f_i \sum_s \phi_s^2 (1 - f_i) [F(r, 0, R_x, R_s) - F(r, 0, R_x, R_s + \Delta R_s)] \\ & - \sum_s \mathcal{P}(s) \sum_{s'} \phi_s (\phi_{s'} - \phi_s) (1 - f_i) [F(r, R_s, R_s + \Delta R_s, R_{s'}) - F(r, R_s, R_s + \Delta R_s, R_{s'} + \Delta R_{s'})] \\ & \left. - \sum_s \mathcal{P}(s) \sum_{s'} \mathcal{P}(s') \phi_s (\phi_{s'} - \phi_s) \frac{1}{2} [F(r, R_s, R_s + \Delta R_s, R_h) + F(r, R_{s'}, R_{s'} + \Delta R_{s'}, R_h)] \right). \quad (4.55) \end{aligned}$$

Two Shells

If there are only two T_S shells, then replacing $R_s \rightarrow R_x$, $R_s + \Delta R_s = R_{s'} \rightarrow R_t$ and $R_{s'} + \Delta R_{s'} \rightarrow R_h$ gives,

$$\begin{aligned} \mu = & \xi (f_b \phi_{bg} + \langle \phi_s \rangle)^2 + (1 + \xi) \left((\phi_{bg}^2 f_b + \langle \phi_s^2 \rangle) f_i F(r, 0, R_x, R_h) \right. \\ & + f_b (\mathcal{P}(s) (\phi_{bg} - \phi_s)^2 F(r, R_x, R_t, R_h) + \mathcal{P}(s') (\phi_{bg} - \phi_{s'})^2 F(r, R_t, R_h, R_h)) \\ & + f_i f_n (\phi_s^2 [F(r, 0, R_x, R_x) - F(r, 0, R_x, R_t)] + \phi_{s'}^2 [F(r, 0, R_x, R_t) - F(r, 0, R_x, R_h)]) \\ & - f_n \mathcal{P}(s) \phi_s (\phi_{s'} - \phi_s) [F(r, R_x, R_t, R_t) - F(r, R_x, R_t, R_h)] \\ & - f_n \mathcal{P}(s') \phi_{s'} (\phi_s - \phi_{s'}) [F(r, R_t, R_h, R_x) - F(r, R_t, R_h, R_t)] \\ & \left. + \mathcal{P}(s) \mathcal{P}(s') (\phi_s - \phi_{s'})^2 \frac{1}{2} [F(r, R_x, R_t, R_h) + F(r, R_t, R_h, R_h)] \right). \quad (4.56) \end{aligned}$$

If in Eq. 4.56 we assume $\xi = 0$ and $\phi_{bg} = 0$, then

$$\begin{aligned} \mu = & f_i (\mathcal{P}(s) \phi_s^2 + \mathcal{P}(s') \phi_{s'}^2) F(r, 0, R_x, R_h) \\ & + f_b (\mathcal{P}(s) \phi_s^2 F(r, R_x, R_t, R_h) + \mathcal{P}(s') \phi_{s'}^2 F(r, R_t, R_h, R_h)) \end{aligned}$$

$$\begin{aligned}
& + f_i f_n (\phi_s^2 [F(r, 0, R_x, R_x) - F(r, 0, R_x, R_t)] + \phi_{s'}^2 [F(r, 0, R_x, R_t) - F(r, 0, R_x, R_h)]) \\
& - f_n \mathcal{P}(s) \phi_s (\phi_{s'} - \phi_s) [F(r, R_x, R_t, R_t) - F(r, R_x, R_t, R_h)] \\
& - f_n \mathcal{P}(s') \phi_{s'} (\phi_s - \phi_{s'}) [F(r, R_t, R_h, R_x) - F(r, R_t, R_h, R_t)] \\
& + \mathcal{P}(s) \mathcal{P}(s') (\phi_s - \phi_{s'})^2 \frac{1}{2} [F(r, R_x, R_t, R_h) + F(r, R_t, R_h, R_h)]. \tag{4.57}
\end{aligned}$$

Further assuming $f_i = 0$ ($R_x = 0$) in Eq. 4.57, we have

$$\begin{aligned}
\mu & = f_b (\mathcal{P}(s) \phi_s^2 F(r, 0, R_t, R_h) + \mathcal{P}(s') \phi_{s'}^2 F(r, R_t, R_h, R_h)) \\
& - f_n \mathcal{P}(s) \phi_s (\phi_{s'} - \phi_s) [F(r, 0, R_t, R_t) - F(r, 0, R_t, R_h)] \\
& - f_n \mathcal{P}(s') \phi_{s'} (\phi_s - \phi_{s'}) [1 - F(r, R_t, R_h, R_t)] \\
& + \mathcal{P}(s) \mathcal{P}(s') (\phi_s - \phi_{s'})^2 \frac{1}{2} [F(r, 0, R_t, R_h) + F(r, R_t, R_h, R_h)]. \tag{4.58}
\end{aligned}$$

If we instead assume $\mathcal{P}(s) = \mathcal{P}(s') = f_s/2$ in Eq. 4.57, we have

$$\begin{aligned}
\mu & = f_i \frac{f_s}{2} (\phi_s^2 + \phi_{s'}^2) F(r, 0, R_x, R_h) + f_b \frac{f_s}{2} (\phi_s^2 F(r, R_x, R_t, R_h) + \phi_{s'}^2 F(r, R_t, R_h, R_h)) \\
& + f_i f_n (\phi_s^2 [F(r, 0, R_x, R_x) - F(r, 0, R_x, R_t)] + \phi_{s'}^2 [F(r, 0, R_x, R_t) - F(r, 0, R_x, R_h)]) \\
& - f_n \frac{f_s}{2} (\phi_{s'} - \phi_s) (\phi_s [F(r, R_x, R_t, R_t) - F(r, R_x, R_t, R_h)] - \phi_{s'} [F(r, R_t, R_h, R_x) - F(r, R_t, R_h, R_t)]) \\
& + \frac{f_s^2}{4} (\phi_s - \phi_{s'})^2 \frac{1}{2} [F(r, R_x, R_t, R_h) + F(r, R_t, R_h, R_h)]. \tag{4.59}
\end{aligned}$$

Assuming $\phi_s = -\phi_{s'} = \phi$ in Eq. 4.57, we have

$$\begin{aligned}
\mu & = \phi^2 \left(f_i (\mathcal{P}(s) + \mathcal{P}(s')) F(r, 0, R_x, R_h) + f_i f_n [F(r, 0, R_x, R_x) - F(r, 0, R_x, R_h)] \right. \\
& + f_b (\mathcal{P}(s) + \mathcal{P}(s')) F(r, R_x, R_h, R_h) \\
& + 2 f_n \mathcal{P}(s) [F(r, R_x, R_t, R_t) - F(r, R_x, R_t, R_h)] + \mathcal{P}(s') [F(r, R_t, R_h, R_x) - F(r, R_t, R_h, R_t)] \\
& \left. + 2 \mathcal{P}(s) \mathcal{P}(s') [F(r, R_x, R_t, R_h) + F(r, R_t, R_h, R_h)] \right), \tag{4.60}
\end{aligned}$$

because $\mathcal{P}(s) F(r, R_x, R_t, R_h) + \mathcal{P}(s') F(r, R_t, R_h, R_h) = (\mathcal{P}(s) + \mathcal{P}(s')) F(r, R_x, R_h, R_h)$. Assuming $\mathcal{P}(s) = \mathcal{P}(s') = f_s/2$ in Eq. 4.60, we have,

$$\begin{aligned}
\mu & = \phi^2 \left(f_i f_s F(r, 0, R_x, R_h) + f_i f_n [F(r, 0, R_x, R_x) - F(r, 0, R_x, R_h)] \right. \\
& \left. + f_n f_s [F(r, R_x, R_h, R_h) + F(r, R_x, R_t, R_t) - F(r, R_x, R_t, R_h) + F(r, R_t, R_h, R_x) - F(r, R_t, R_h, R_t)] \right). \tag{4.61}
\end{aligned}$$

Assuming $f_i \rightarrow 0$ ($R_x = 0$) in Eq. 4.61, we get,

$$\mu = \phi^2 f_s [F(r, 0, R_h, R_h) + F(r, 0, R_t, R_t) - F(r, 0, R_t, R_h) - F(r, R_t, R_h, R_t)]. \tag{4.62}$$

One Shell

If there is only one T_S shell, then simplifying Eq. 4.49 gives,

$$\begin{aligned} \mu = \xi(f_b\phi_{bg} + f_h\phi_s)^2 + (1 + \xi) & \left((\phi_{bg}^2 f_b + \phi_s^2 f_h) f_i F(r, 0, R_x, R_h) \right. \\ & \left. + f_b f_h (\phi_{bg} - \phi_s)^2 F(r, R_x, R_h, R_h) + f_i f_n \phi_s^2 [F(r, 0, R_x, R_x) - F(r, 0, R_x, R_h)] \right). \end{aligned} \quad (4.63)$$

Assuming $\xi = 0$ and $\phi_{bg} = 0$ in Eq. 4.63, we get,

$$\mu = \phi_s^2 \left(f_h f_i F(r, 0, R_x, R_h) + f_b f_h F(r, R_x, R_h, R_h) + f_i f_n [F(r, 0, R_x, R_x) - F(r, 0, R_x, R_h)] \right). \quad (4.64)$$

If we instead assume $f_i \rightarrow 0$ ($R_x = 0$) in Eq. 4.63, we get,

$$\mu = \xi(f_b\phi_{bg} + f_h\phi_s)^2 + (1 + \xi) f_b f_h (\phi_{bg} - \phi_s)^2 F(r, 0, R_h, R_h). \quad (4.65)$$

Further assuming $\xi = 0$ and $\phi_{bg} = 0$ in Eq. 4.65, we get,

$$\mu = f_b f_h \phi_s^2 F(r, 0, R_h, R_h). \quad (4.66)$$

4.5.3 Toy Model: One Bubble Size, Flat Temperature Profile

We take a simple toy model with a single bubble size and a shell with a uniform spin temperature around it (flat profile). Thus there are small ionization bubbles embedded in larger heated bubbles (Figure 4.4). We first ignore density fluctuations (ξ) for simplicity in this section and later present the results including ξ . In this case, there are only three values of $\phi = n(1 - s)$ in the universe: in the ionized region, $\phi_i = 0$ as $n = 0$; in the heated and the background regions respectively,

$$\begin{aligned} \phi_h = (1 - s_h) &= 1 - \frac{T_{\text{CMB}}}{T_{\text{heat}}} \\ \text{and} \quad \phi_{bg} = (1 - s_{bg}) &= 1 - \frac{T_{\text{CMB}}}{T_{bg}}. \end{aligned}$$

If N is the number density of bubbles, R_x the ionization bubble radius and R_h the heating bubble radius, then the total ionized volume fraction, heated volume fraction after correcting for overlap (Section 2.1.5), and the remaining background volume fraction are respectively,

$$f_i = N \frac{4\pi}{3} R_x^3, \quad f_h = \frac{f_{hb}(1 - f_i)}{1 + f_{hb}} \quad \text{and} \quad f_{bg} = 1 - f_i - f_h.$$

Here the total dimensionless temperature correlation at distance r is,

$$\begin{aligned} \mu_\phi(r) &= \langle \phi_1 \phi_2 \rangle - \langle \phi \rangle^2 \\ &= \phi_h^2 P(a_h \cap b_h) + 2\phi_h \phi_{bg} \mathcal{P}(a_h \cap b_{bg}) + \phi_{bg}^2 \mathcal{P}(a_{bg} \cap b_{bg}) - \langle \phi \rangle^2. \end{aligned} \quad (4.67)$$

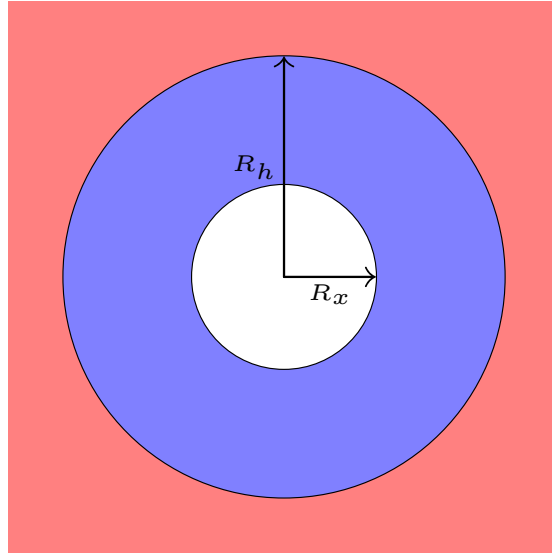


Figure 4.4: A toy model: an ionization bubble ($\phi_i = 0$) has one T_S shells around it. Background is unheated.

Now we derive each term separately. When both points a and b are heated,

$$\begin{aligned}\mathcal{P}(a_h \cap b_h) &= \mathcal{P}(a_h) - \mathcal{P}(b_{\bar{h}} \cap a_h) \\ &= f_h - \mathcal{P}(b_{\text{bg}} \cap a_h) - \mathcal{P}(b_i \cap a_h).\end{aligned}\quad (4.68)$$

Here $\mathcal{P}(a_h)$ is the probability that point a is heated; this is equal to the total heated volume fraction f_h . $\mathcal{P}(b_{\text{bg}} \cap a_h)$ is the probability that point a is heated and point b is in background. We assume that if point b is outside the heated shell in which point a is then its probability to be in background is equal to the background volume fraction f_{bg} . Therefore,

$$\mathcal{P}(b_{\text{bg}} \cap a_h) = f_h f_{\text{bg}} C(r, R_x, R_h, R_h). \quad (4.69)$$

$\mathcal{P}(b_i \cap a_h)$ is the probability that point a is heated and point b is ionized. If point b is ionized, then point a can be in the heated shell of the same bubble or different bubble. Therefore,

$$\mathcal{P}(b_i \cap a_h) = \mathcal{P}(b_i) \mathcal{P}(a_h(\text{same})|b_i) + \mathcal{P}(b_i) \mathcal{P}(a_h(\text{diff})|b_i).$$

Here $\mathcal{P}(b_i)$ is the probability of point b being ionized, which is equal to f_i . The probability of point a being in the shell of the ionization bubble in which point b is ($C(r, 0, R_x, R_x) - C(r, 0, R_x, R_h)$), and its probability to be heated in this shell is $1 - f_i$ since this shell is allowed to overlap with other ionization bubbles. The probability of point a being outside the shell corresponding to ionization bubble in which point b is $C(r, 0, R_x, R_h)$ and its probability to be heated outside this shell is f_h . Therefore, we have,

$$\begin{aligned}\mathcal{P}(b_i \cap a_h) &= \mathcal{P}(b_i) \mathcal{P}(a_h(\text{same})|b_i) + \mathcal{P}(b_i) \mathcal{P}(a_h(\text{diff})|b_i) \\ &= f_i (1 - f_i) [C(r, 0, R_x, R_x) - C(r, 0, R_x, R_h)] + f_i f_h C(r, 0, R_x, R_h).\end{aligned}\quad (4.70)$$

Putting, Eqs. 4.69 and 4.70 in Eq. 4.68, we get

$$\begin{aligned}\mathcal{P}(a_h \cap b_h) &= f_h - f_h f_{bg} C(r, R_x, R_h, R_h) - f_i f_h C(r, 0, R_x, R_h) \\ &\quad - f_i (1 - f_i) [C(r, 0, R_x, R_x) - C(r, 0, R_x, R_h)].\end{aligned}\quad (4.71)$$

When both points are in background region,

$$\begin{aligned}\mathcal{P}(a_{bg} \cap b_{bg}) &= \mathcal{P}(a_{bg}) - \mathcal{P}(a_{bg} \cap \widetilde{b_{bg}}) \\ &= \mathcal{P}(a_{bg}) - \mathcal{P}(a_{bg} \cap b_h) - \mathcal{P}(a_{bg} \cap b_i),\end{aligned}\quad (4.72)$$

where $\mathcal{P}(a_{bg})$ is the probability of point a being in background, and it is equal to f_b . $\mathcal{P}(a_{bg} \cap b_i)$ is the probability that point a in background region given that point b is ionized. The probability of point a being in background is f_{bg} if it is outside the shell of the bubble in which point b is. Therefore,

$$\mathcal{P}(a_{bg} \cap b_i) = f_i f_b C(r, 0, R_x, R_h). \quad (4.73)$$

Using Eqs. 4.69 and 4.73 in Eq. 4.72, we get,

$$\mathcal{P}(a_{bg} \cap b_{bg}) = f_{bg} - f_{bg} f_h C(r, R_x, R_h, R_h) - f_{bg} f_i C(r, 0, R_x, R_h). \quad (4.74)$$

Putting Eqs. 4.71, 4.69 and 4.72 in Eq. 4.67, we get

$$\begin{aligned}\mu &= \phi_h^2 (f_h - f_h f_{bg} C(r, R_x, R_h, R_h) - f_i f_h C(r, 0, R_x, R_h) \\ &\quad - f_i (1 - f_i) [C(r, 0, R_x, R_x) - C(r, 0, R_x, R_h)]) \\ &\quad + 2\phi_h \phi_{bg} f_h f_{bg} C(r, R_x, R_h, R_h) \\ &\quad + \phi_{bg}^2 f_{bg} (1 - f_h C(r, R_x, R_h, R_h) - f_i C(r, 0, R_x, R_h)) - (f_h \phi_h + f_{bg} \phi_{bg})^2.\end{aligned}\quad (4.75)$$

If the impact of density correlation ξ is included we finally have,

$$\begin{aligned}\mu &= (1 + \xi) \left(\phi_h^2 (f_h - f_h f_{bg} C(r, R_x, R_h, R_h) - f_i f_h C(r, 0, R_x, R_h) \right. \\ &\quad \left. - f_i (1 - f_i) [C(r, 0, R_x, R_x) - C(r, 0, R_x, R_h)]) \right. \\ &\quad \left. + 2\phi_h \phi_{bg} f_h f_{bg} C(r, R_x, R_h, R_h) \right. \\ &\quad \left. + \phi_{bg}^2 f_{bg} (1 - f_h C(r, R_x, R_h, R_h) - f_i C(r, 0, R_x, R_h)) \right) - (\phi_{bg} f_{bg} + \phi_h f_h)^2.\end{aligned}\quad (4.76)$$

Writing this in terms of $F(r, \dots, \dots) = 1 - C(r, \dots, \dots)$, we can simplify further as,

$$\begin{aligned}\mu &= \xi (f_b \phi_{bg} + f_h \phi_h)^2 + (1 + \xi) \left((\phi_{bg}^2 f_b + \phi_h^2 f_h) f_i F(r, 0, R_x, R_h) \right. \\ &\quad \left. + f_b f_h (\phi_{bg} - \phi_h)^2 F(r, R_x, R_h, R_h) \right. \\ &\quad \left. + f_i f_h \phi_h^2 [F(r, 0, R_x, R_x) - F(r, 0, R_x, R_h)] \right),\end{aligned}\quad (4.77)$$

which matches with Eq. 4.63 with ϕ_s replaced with ϕ_h . To verify the validity of our formalism, we need to consider Eqs. 4.75 and 4.76 in different limits:

- **Small Scale:** At $r = 0$, $\mu_0 = (1 + \xi_0)(\phi_h^2 f_h + \phi_{bg}^2 f_{bg}) - (\phi_{bg} f_{bg} + \phi_h f_h)^2$, which is the expected result.
- **Large Scale:** At $r \rightarrow \infty$, all the functions $C(\dots, \dots)$ tend to unity. In this case, Eq. 4.75 vanishes and Eq. 4.76 approaches the correct large scale limit (Eq. 4.10).
- **No Heating Profile:** If we take $R_h \rightarrow R_x$, $f_h = 0$, and $f_{bg} = f_n$, we get,

$$\begin{aligned}\mu &= (1 + \xi) \left[\phi_{bg}^2 f_n (1 - f_i C(r, 0, R_x, R_x)) \right] - (\phi_{bg} f_n)^2 \\ &= \phi_{bg}^2 f_n [(1 + \xi)(1 - f_i C(r, 0, R_x, R_x)) - f_n].\end{aligned}$$

This is the same result as Eq. 4.54.

- **Uniform Heating:** We also get Eq. 4.54 if we take $\phi_h = \phi_{bg}$ and $f_n = f_h + f_b$. In this case there is no distinction between the heated bubble and the background.

This simple case does not allow for negative correlation since within the heated shell, the ϕ is positively correlated and it is un-correlation outside it. However, if we add a little negative correlation between bubble centres then the overall correlation does become negative for large scales.

Enforcing No-Overlap of Heated Shells: If we assume that there is no overlap between heated shells of different ionization bubbles, then the calculations are different. When both point a and b are heated they can belong to the same shell or different shells, therefore,

$$\begin{aligned}P(a_h \cap b_h) &= \mathcal{P}(a_h) \mathcal{P}(b_h(\text{same})|a_h) + \mathcal{P}(a_h) \mathcal{P}(b_h(\text{diff})|a_h) \\ &= f_h [(C(r, R_x, R_h, R_x) - C(r, R_x, R_h, R_h)) + f_h C(r, R_x, R_h, R_h)].\end{aligned}\quad (4.78)$$

When both the points are in the background region, we get,

$$\begin{aligned}\mathcal{P}(a_{bg} \cap b_{bg}) &= \mathcal{P}(a_{bg}) - \mathcal{P}(b_{bg}^{\sim}) \mathcal{P}(a_{bg}|b_{bg}^{\sim}) \\ &= f_{bg} - (1 - f_{bg}) f_{bg} C(r, 0, R_h, R_h),\end{aligned}\quad (4.79)$$

as probability of point a being in background is f_{bg} if it outside the ionization bubble and shell in which point a is. Putting Eqs. 4.78, 4.69 and 4.79 in Eq. 4.67, and including the impact of density correlations, we get,

$$\begin{aligned}\mu &= (1 + \xi) \left(\phi_{bg}^2 f_{bg} (1 - (1 - f_{bg}) C(r, 0, R_h, R_h)) \right. \\ &\quad + 2 \phi_{bg} \phi_h f_{bg} f_h C(r, R_x, R_h, R_h) \\ &\quad \left. + \phi_h^2 f_h (C(r, R_x, R_h, R_x) - (1 - f_h) C(r, R_x, R_h, R_h)) \right) \\ &\quad - (\phi_{bg} f_{bg} + \phi_h f_h)^2.\end{aligned}\quad (4.80)$$

This expression does not reduce to correct values for some of the limiting cases explored above.

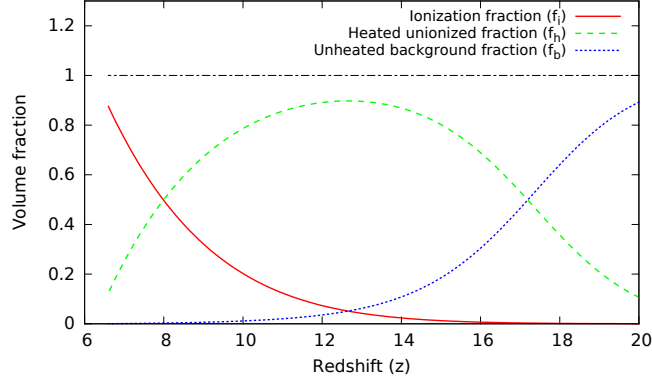


Figure 4.5: Evolution of ionized and heating fractions for a fiducial model for $\zeta = 10$, $N_{\text{heat}} = 1.0$ and $\alpha = 1.5$

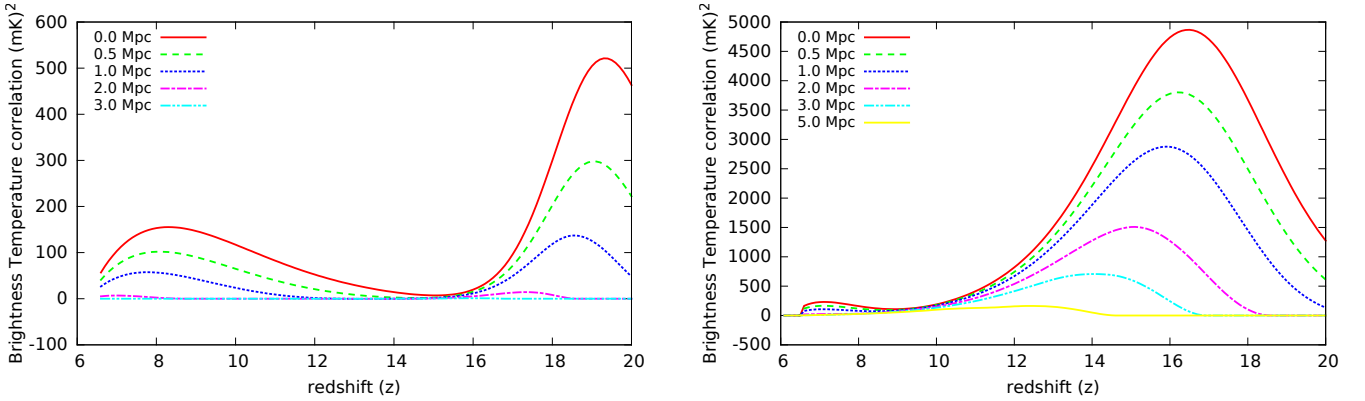


Figure 4.6: Evolution of correlation function for a set of scales for a model in Figure 4.5. The background temperature and profile temperature is allowed to increase in the left panel, whereas they are held constant in the right panel.

Results

We show the evolution of ionized, heated, and background fractions (f_i , f_h and f_{bg}) in Figure 4.5. Here, we have kept the ratio of heating shell radius R_h to ionization bubble radius R_x constant. We have also neglected the impact of density perturbations. The initial radius of the ionization bubble (heated shell) is assumed to be 0.1 Mpc (0.7 Mpc). The initial ratio of the heated and ionized fraction is the cube of the ratio of these radii. Initially, nearly 90% of the universe is in the background region. As the universe evolves, the ionization bubbles grow and so do the heated regions, resulting in an increase in both f_i and f_h with a decrement in f_b . This process is accompanied by an increase in the background and heated temperature. At certain redshift, the heated shells begin to merge, driving the background fraction to zero. Eventually, the ionized fraction becomes large enough to drive the heated fraction to zero.

The evolution of correlation function (normalized using Eq. 1.39) for a set of scales is shown in Figure 4.6. Here the background temperature is assumed to evolve according Eq. 2.23 for modelling parameters: $\zeta = 10$, $N_{\text{heat}} = 1.0$ and $\alpha = 1.5$, while the heating bubble temperature is kept at a constant value above the background temperature. Initially, the correlation function is small which is expected, because f_i and f_h approach zero in the absence of density perturbations. The correlation function rises as f_h increases and then decreases again as the background and shell temperatures rise (s decreases).

This behaviour is generic to all models even though the evolution in the range of scales displayed in Figure 4.6 could change as it is determined by the sizes of the bubbles. For instance, in Figure 4.6 the correlation on the scales of $\simeq 3$ Mpc remains close to zero at all times owing to our choices of initial scales. $T_h^{-1} f_h + T_{\text{bg}}^{-1} f_{\text{bg}}$ reaches T_{CMB}^{-1} at $z \simeq 16$; at this redshift, the global HI signal vanishes and the universe makes a transition from being observable in the HI signal from absorption to emission. However, the redshift at which the correlation function reaches its minimum is determined by a multitude of other causes. The minimum of the correlation function at $z \simeq 15$ signals the beginning of the phase in which the universe is uniformly heated. The signal at this time reaches nearly zero for all scales in our case because at this redshift, the ionization inhomogeneities are small ($f_i \simeq 0.01$) and we ignore density perturbations. As f_i increases, the ionization inhomogeneities start rising, reaching a peak at around $f_i \simeq 0.5$ and subsequently decline as the universe becomes fully ionized. The peak of the correlation function when it is dominated by ionization inhomogeneities is smaller than when it is determined by heating inhomogeneities because s is larger than unity in the earlier phase and it is zero during the latter phase.

To isolate the impact of merging of heating profiles from the effect of heating of the medium on the evolution of correlation function, we show a different model in the right panel of Figure 4.6. This model is also based on the evolution of ionization and heating fractions shown Figure 4.5, but here the background temperature and the temperature inside the heated shell is kept at is 5 K and 10 K, respectively, throughout the redshift evolution. Therefore, in this case, the temperature inhomogeneities are destroyed by merging of heating bubbles and not heating, which delays the transition to the uniform heating regime as compared to Figure 4.6 from $z \sim 15$ to $z \sim 9$.

Figure 4.6 allows us to identify the relevant physical processes involved in the modelling of the correlation function in the phase when heating inhomogeneities dominate, the end of this phase (owing to either heating of the medium above CMB temperature or merger of profiles), and the transition to ionization inhomogeneities domination phase. As we shall notice later, the features seen in the Figures are also present for complete models.

4.5.4 Toy Model: One Bubble Size, Two Shells, $\langle \phi \rangle = 0$

We can construct another simple scenario where there is only one bubble size and the heating profile around the sources have two shells. The first shell is heated and coupled through Lyman- α radiation. The second shell is non-heated but still coupled. The region outside the second shell (background region) is neither heated nor coupled (Figure 4.7).

This gives three values of $\phi = n(1-s)$ when we ignore density fluctuations: $\phi_i = 0$ in the ionized regions; $\phi_h = \phi > 0$ in the first shell where $T_S > T_{\text{CMB}}$; $\phi_u = -\phi < 0$ in the second shell since $T_S < T_{\text{CMB}}$; and $\phi_b = 0$ in the background region which is uncoupled. For simplicity we have assumed that the volume occupied by the two shells is the same, $f_h = f_u = f_s/2$ and $\phi_h = -\phi_u = \phi$. Therefore, $\langle \phi \rangle = f_h \phi_h + f_u \phi_u = 0$. Here we allow the shells of different bubbles to overlap with one another and with other ionization bubbles.

From Figure 4.7, we can see that the correlation will be positive ($\propto \phi^2$) if both points are either in shell 1 or both in shell 2. If one point is in shell 1 and another in shell 2, then the correlation is negative ($\propto -\phi^2$).

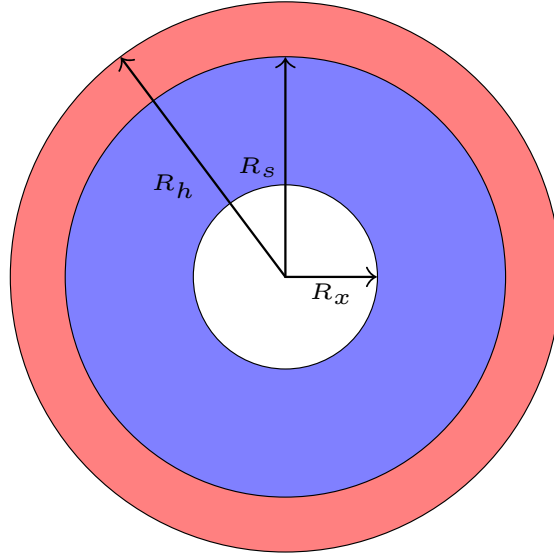


Figure 4.7: A toy model: an ionization bubble ($\phi_i = 0$) has two T_S shells around it. The background is uncoupled ($\phi_b = 0$).

When one point is out of the bubble, its average value is 0. Therefore, we essentially only count pairs of points which belong to the same bubble. The two-point correlation function without density perturbation is,

$$\begin{aligned}\mu &= \phi_h^2 \mathcal{P}(a_h \cap b_h) + \phi_u^2 \mathcal{P}(a_u \cap b_u) + \phi_h \phi_u (\mathcal{P}(a_h \cap b_u) + \mathcal{P}(a_u \cap b_h)) \\ &= \phi^2 (\mathcal{P}(a_h \cap b_h) + \mathcal{P}(a_u \cap b_u) - \mathcal{P}(a_h \cap b_u) - \mathcal{P}(a_u \cap b_h)).\end{aligned}\quad (4.81)$$

When both the points are in the first (heated) shell or second (unheated) shell, then we have, respectively,

$$\begin{aligned}\mathcal{P}(a_h \cap b_h) &= \mathcal{P}(a_h) - \mathcal{P}(a_h \cap b_i) - \mathcal{P}(a_h \cap b_{bg}) - \mathcal{P}(a_h \cap b_u), \\ \mathcal{P}(a_u \cap b_u) &= \mathcal{P}(a_u) - \mathcal{P}(a_u \cap b_i) - \mathcal{P}(a_u \cap b_{bg}) - \mathcal{P}(a_u \cap b_h).\end{aligned}$$

Putting them in Eq. 4.81, we get

$$\begin{aligned}\mu &= \phi^2 \left(f_h - \mathcal{P}(a_h \cap b_i) - \mathcal{P}(a_h \cap b_{bg}) - 2\mathcal{P}(a_h \cap b_u) \right. \\ &\quad \left. + f_u - \mathcal{P}(b_u \cap a_i) - \mathcal{P}(b_u \cap a_{bg}) - 2\mathcal{P}(a_u \cap b_h) \right).\end{aligned}\quad (4.82)$$

Now, the probability of point a being in a shell and point b being ionized is,

$$\begin{aligned}\mathcal{P}(a_h \cap b_i) &= f_i(1 - f_i)[C(r, 0, R_x, R_x) - C(r, 0, R_x, R_s)] + f_i f_h C(r, 0, R_x, R_h) \\ \mathcal{P}(b_u \cap a_i) &= f_i(1 - f_i)[C(r, 0, R_x, R_s) - C(r, 0, R_x, R_h)] + f_i f_u C(r, 0, R_x, R_h)\end{aligned}\quad (4.83)$$

where, the first terms and second terms of both equations give probability of both point being in the same bubble (and its profile), and probability of them being in different bubble (and their profiles), respectively.

The probability of point a being in a shell and point b being in the background is,

$$\begin{aligned}\mathcal{P}(a_h \cap b_{\text{bg}}) &= f_h f_{\text{bg}} C(r, R_x, R_s, R_h) \\ \mathcal{P}(a_u \cap b_{\text{bg}}) &= f_u f_{\text{bg}} C(r, R_s, R_h, R_x).\end{aligned}\quad (4.84)$$

And the probability of both point being in different shells is,

$$\begin{aligned}\mathcal{P}(a_h \cap b_u) &= (1 - f_i) f_h [C(r, R_x, R_s, R_s) - C(r, R_x, R_s, R_h)] + f_h f_u C(r, R_x, R_s, R_h) \\ \mathcal{P}(a_h \cap b_u) &= (1 - f_i) f_u [C(r, R_s, R_h, R_x) - C(r, R_s, R_h, R_s)] + f_h f_u C(r, R_s, R_h, R_h),\end{aligned}\quad (4.85)$$

where the first terms and second terms give probability of both points being in shells of the same bubble and in shells of different bubbles, respectively. Note that $\mathcal{P}(a_h \cap b_u) = \mathcal{P}(a_u \cap b_h)$; however, we still keep both these terms, because it makes the final expression more symmetric. Using Eqs. 4.83, 4.84, and 4.85 in Eq. 4.82, and substituting $f_h = f_u = f_s/2$ we get,

$$\begin{aligned}\mu &= \phi^2 \left(f_s - f_i f_n [C(r, 0, R_x, R_x) - C(r, 0, R_x, R_h)] - f_i f_s C(r, 0, R_x, R_h) \right. \\ &\quad \left. - f_n [f_h C(r, R_x, R_s, R_h) + f_u C(r, R_s, R_h, R_h)] \right. \\ &\quad \left. - f_s f_n [C(r, R_x, R_s, R_s) - C(r, R_x, R_s, R_h) + C(r, R_s, R_h, R_x) - C(r, R_s, R_h, R_s)] \right) \\ &= \phi^2 \left(f_s - f_i f_n [C(r, 0, R_x, R_x) - C(r, 0, R_x, R_h)] - f_i f_s C(r, 0, R_x, R_h) \right. \\ &\quad \left. - f_s f_n [C(r, R_x, R_h, R_h) + C(r, R_x, R_s, R_s) - C(r, R_x, R_s, R_h) + C(r, R_s, R_h, R_x) - C(r, R_s, R_h, R_s)] \right).\end{aligned}\quad (4.86)$$

Here we have used, $f_h C(r, R_x, R_s, R_h) + f_u C(r, R_s, R_h, R_h) = f_s C(r, R_x, R_h, R_h)$ (Appendix F) in the last step. This result matches Eq. 4.61 when we use $F(r, \dots, \dots) = 1 - C(r, \dots, \dots)$. To verify the validity of our formalism, we need to consider this model in different limits:

- **Large Scales:** At large scales, all the functions $C(\dots, \dots, \dots)$ tend to unity. In this case, Eq. 4.86 approaches 0. This is expected, as for $r > 2R_h$, the two-point correlation should vanish without ξ .
- **Small Scale:** When $r = 0$, $\mu = f_s \phi^2$, this is also as expected because there is no probability of two points being in different shells when they are so close.

Eq. 4.86 takes negative value for a range of r , where the two points are more likely to be in different shells than in the same shell. In Figure 4.8, we have shown one such case where the auto-correlation is negative at certain scales. For scales $R_x + R_s < r < R_s + R_h$, depending on the values of various radii, two randomly chosen points can have a higher probability of being in different shells than in the same shell, driving the correlation to negative value. For larger scales, $R_s + R_h < r < 2R_h$, both the points have a finite probability of being in the outer shell, and zero probability of being in different shells of the same bubble, which leads the overall correlation at these scales to be positive. On scales $r > 2R_h$, the correlation function is zero. We note that the possibility of negative correlation at any scale depends on values of R_x , R_s and R_h and their differences. It is entirely possible to have models where correlation function remains positive at all scales.

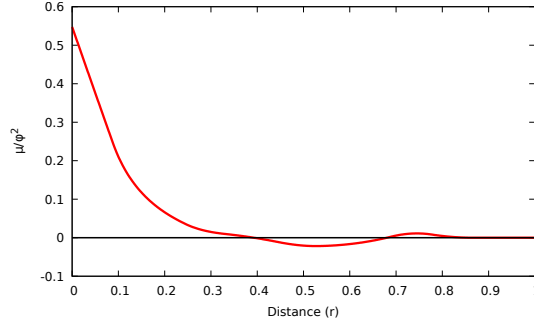


Figure 4.8: A case with negative correlation for certain scales. The ionization fraction $f_i = 0.01$ and heated fraction $f_s = 0.55$. The distance scale would depend on the size of ionization bubble, which is chosen to be 0.1 Mpc.

4.6 Correlation between Ionization Bubble Centres

To analyse the effect of correlation between ionization bubbles centres, we can again study the simple model introduced in Section 4.5.3. We choose an ionization bubble and a shell of width Δl at distance $l > R_x$ from its centre. The fraction of volume within this shell being ionized by another bubble at distance x from the centre of the first bubble is (Appendix F),

$$\lim_{\Delta l \rightarrow 0} \frac{V(x, l + \frac{\Delta l}{2}, R_x) - V(x, l - \frac{\Delta l}{2}, R_x)}{\frac{4\pi}{3} \left[\left(l + \frac{\Delta l}{2} \right)^3 - \left(l - \frac{\Delta l}{2} \right)^3 \right]} = \frac{A(x, l, R_x)}{4\pi l^2}. \quad (4.87)$$

If we assume that there is no correlation between ionization bubble centres, then the probability of there being another bubble at distance x (in a shell of volume $4\pi x^2 dx$) from the centre of an ionization bubble is $N4\pi x^2 dx$. Therefore, using Eq. 4.87, the probability of a point at distance l from the centre of an ionization bubble being ionized is

$$\mathcal{P}_{i,0} = \int N 4\pi x^2 \frac{A(x, l, R_x)}{4\pi l^2} dx = N \frac{4\pi}{3} R_x^3.$$

This is the global ionization fraction f_i , as expected.

Now if we assume that there is correlation between ionization bubble centres, then the probability of there being another bubble at distance x (in a shell of volume $4\pi x^2 dx$) from the centre of an ionization bubble is $N4\pi x^2 dx [1 + I(x)]$, where $I(x)$ is the correlation function of ionization bubble centres at distance x . Now, the probability of a point at distance l from the centre of a bubble in a shell of width Δl to be ionized is

$$\begin{aligned} \mathcal{P}_i &= \int N 4\pi x^2 [1 + I(x)] \frac{A(x, l, R_x)}{4\pi l^2} dx \\ &= f_i + \frac{N}{l^2} \int x^2 I(x) A(x, l, R_x) dx \\ &= f_i (1 + G_i(l, R_x)). \end{aligned} \quad (4.88)$$

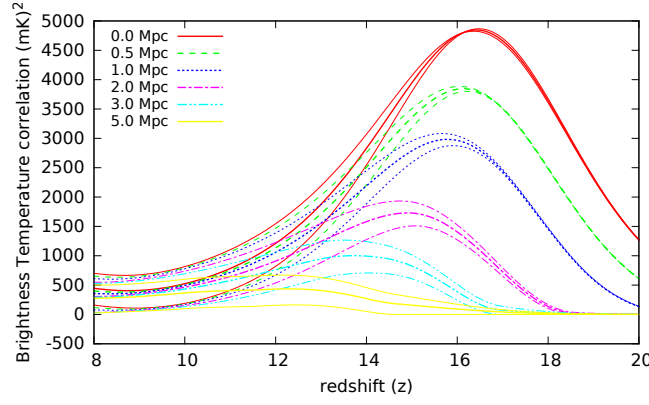


Figure 4.9: Evolution of correlation function for a set of scales for a model in which the background temperature is held constant. Here the curves from bottom to top show cases for no correlation (left panel of Figure 4.6), correlation with $b = 1$ and with $b = 2$.

Using a similar argument, the probability of there being a heated region at distance l from a centre of an ionization bubble given the correlation between bubble centres is,

$$\begin{aligned}
\mathcal{P}_h &= \int N 4\pi x^2 [1 + I(x)] \frac{f_h}{f_{hb}} \frac{A(x, l, R_h) - A(x, l, R_x)}{4\pi l^2} dx \\
&= f_h + \frac{N}{l^2} \frac{f_h}{f_{hb}} \int x^2 I(x) [A(x, l, R_h) - A(x, l, R_x)] dx \\
&= f_h(1 + G_h(l, R_x, R_h)).
\end{aligned} \tag{4.89}$$

When $I(x) = 0$, we have $\mathcal{P}_i = f_i$ and $\mathcal{P}_h = f_h$. Hence, we can get the probability of there being an ionized or heated region at a distance l from a centre of an ionization bubble if we know the correlation function between ionization bubble centres:

$$\begin{aligned}
f_i G_i(l, R_x) &= \frac{N}{l^2} \int x^2 I(x) A(x, l, R_x) dx \\
f_{hb} G_h(l, R_x, R_h) &= f_i [G_i(l, R_h) - G_i(l, R_x)].
\end{aligned} \tag{4.90}$$

If there was positive correlation between ionization bubble centres, the overlap of heated profiles would increase, and the heated volume fraction (f_h) would decrease. Eq. 4.75 will be modified as

$$\begin{aligned}
\mu &= (\phi_h^2 f_h + \phi_b^2 f_b) - (f_h \phi_h + f_b \phi_b)^2 \\
&+ \int_{R_h}^{R_h+r} \left((\phi_h - \phi_b)^2 f_h (1 - f_i (1 + G_i(y))) - f_h (1 + G_h(y)) \right) \frac{dC(r, R_x, R_h, y)}{dy} \\
&+ (\phi_b^2 f_i (1 - f_i (1 + G_i(y))) - f_h (1 + G_h(y))) + \phi_h^2 f_i f_h (1 + G_h(y)) \frac{dC(r, 0, R_x, y)}{dy} dy \\
&+ \int_{R_x}^{R_h} \phi_h^2 f_i (1 - f_i (1 + G_i(y))) \frac{dC(r, 0, R_x, y)}{dy} dy.
\end{aligned} \tag{4.91}$$

We further assume that the correlation of ionization bubble centres follows the same form as the density auto-correlation $I(r) = b\xi(r)$ with a constant bias b . We take two possible values of bias: $b = 1$ and $b = 2$. Figure 4.9 shows the modified correlation for these two cases for the model considered in Figure 4.6. We notice that the HI signal increases due to the correlation of ionization bubble centres. This effect is more significant at later times and on larger scales. This might also introduce correlations on scales at which the signal would be very small or zero without bubble centre correlations, e.g. correlation at $r = 5$ Mpc in Figure 4.9.

Chapter 5

Results

*“I daresay you haven’t had much practice,’ said the Queen.
‘When I was your age, I always did it for half-an-hour a day.
Why, sometimes I’ve believed as many as six impossible things
before breakfast.’”*

— Lewis Carroll, *Through the Looking-Glass*

To compute the global 21 cm brightness temperature and its fluctuating component, we calculate the size distribution of ionization bubbles through excursion set formalism (Eq. 1.19), and the spin temperature profiles around them due to X-ray heating (Eq. 2.21), collisional coupling (Eq. 3.27) and Lyman- α coupling (Eq. 3.13). These profiles have a number of shells and they might overlap with one another due to the random distribution of ionization bubbles. The sizes of these profiles, their temperatures and the background temperature depend on multiple physical processes and modelling parameters.

We first present results for the complete model (Section 4.4.4) for the Λ CDM universe in the redshift range 10–30. However, the results below redshift $z \sim 12$ are not entirely reliable since several approximations used in our formalism (including excursion set formalism) become less valid and eventually break down when the ionization volume fraction is large ($f_i > 0.1$).

5.1 Modelling Parameters

In our work, we have explored five modelling parameters:

1. ζ = Ionization efficiency factor. ζ (Eq. 1.15) determines the size distribution of ionization bubbles and through that, temperature profiles (Figure 1.5). For smaller value of ζ , the ionization bubbles are smaller and the heating is less efficient. However, this does not significantly affect the overall temperature, since the number of X-ray photons is determined from collapse fraction and other parameters, which are independent of ζ . The value of ζ affects Lyman- α coupling strongly because we assume that number of Lyman- α photons emitted is proportional to the number of ionizing photons, which is determined by ζ .

In our model, ζ is constrained by reionization optical depth τ_{reion} . We usually take $\zeta \sim 7.5$, which corresponds to $\tau_{\text{reion}} \simeq 0.055$ (Planck Collaboration et al. [2018]). We also present some results for $\zeta \sim 10.0$, which was in agreement $\tau_{\text{reion}} \simeq 0.066$ (Planck Collaboration et al. [2016a]).

2. N_{heat} = Number of X-ray photons emitted per stellar baryon. For higher value of N_{heat} , more X-ray photons are emitted. This increases the temperature of the medium in the background as well as profiles around ionization bubbles. For our study, we assume N_{heat} in the range: 0.1–10.0.
3. α = X-Ray spectrum power index. For higher value of α , there are more photons at low frequency. These soft photons more efficiently heat up the medium, as they have a higher probability of being absorbed (Figure 2.1). We take three possible values of α , 1.0, 1.5 and 2.0, with $\alpha = 1.5$ to be the standard case.
4. ν_{min} = Minimum X-ray frequency escaping source halo with the number of X-ray photons kept constant. For a given N_{heat} , a higher value of ν_{min} implies that the emitted photons are more energetic with smaller interaction cross-section with neutral atoms. These photons are ineffective for heating the gas. They free stream into the medium and heat it with uniformly. We take two possible values of ν_{min} , 100 eV and 1 keV. Unless mentioned otherwise, we always use $\nu_{\text{min}} = 100$ eV.
5. f_L = Ratio of source luminosity in the range between Lyman- α and Lyman-limit to the luminosity of ionizing photons. As the value of f_L increases, the coupling between T_S and T_K is stronger, and T_S has higher contrast with T_{CMB} . Therefore, it increases the absolute value of ΔT_B in both emission and absorption. In our work, we take f_L in the range: 0.1–1000 (Section 3.1.2).

We present results for only a subset of these parameters. We have not considered scenarios for which the modelling parameters evolve with time. For such models, the shape of the power spectrum and correlation functions would change. To explore more complicated models where the X-ray spectrum is not power law (e.g. Fialkov et al. [2014]), we can take N_{heat} and α to be a function of frequency ν and time. However, we do not explore such models in our work.

5.2 Global Brightness Temperature

In Figures 5.1 and 5.2, we show the evolution of global HI brightness temperature (Eq. 1.40) as function of redshift for various combination of modelling parameters. At $z \simeq 30$, the global signal starts slightly negative as weak collisional coupling drives the spin temperature towards matter temperature which is below the CMB temperature (Eq. 1.29). This coupling becomes inefficient at lower redshift due to decreasing number density of particles.

At $z < 30$, Lyman- α photons start coupling T_S once again to T_K , which is colder than the CMB, and the global 21 cm signal is seen in absorption. The gas is soon heated due to X-ray heating and the signal approaches 0 when $\langle T_K \rangle \simeq T_{\text{CMB}}$. This point is called the ‘heating transition’ from absorption to emission. The maximum strength of the emission signal is determined by the redshift of this transition and ionization fraction. At lower redshifts, the global signal again declines as the medium becomes ionized and goes to zero with the completion of reionization. We do not show results from this last epoch since our formalism

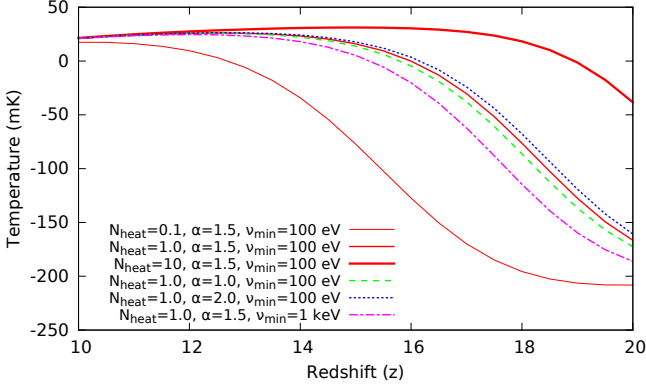


Figure 5.1: Global brightness temperature as function of redshift for various values of α , N_{heat} , and v_{min} . All plots have $\zeta = 10.0$ and $f_L \rightarrow \infty$ ($T_S = T_K$).

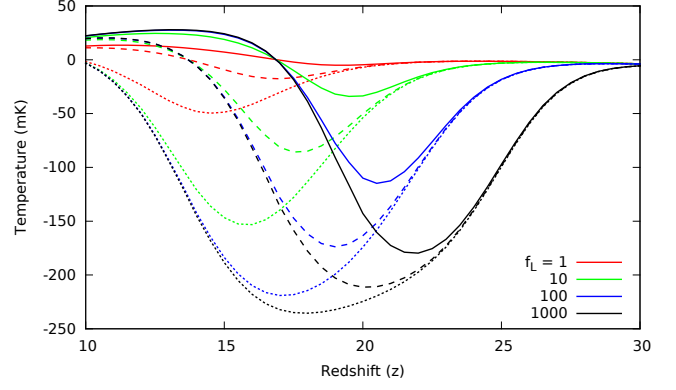


Figure 5.2: Global brightness temperature as function of redshift for various values of f_L ranging from 1.0 to 1000 and for $N_{\text{heat}} = 10$ (solid lines), 1.0 (long dashed lines), and 0.1 (short dashed lines). All plots have $\zeta = 7.5$, $\alpha = 1.5$, and $v_{\text{min}} = 100$ eV.

is only applicable when the ionization fraction is small ($f_i < 0.1$).

The shape of the global brightness temperature signal is completely determined by the modelling parameters. The value of N_{heat} is proportional to the total number of X-ray photons; therefore it is determined by the efficiency of X-ray sources and the escape fraction of these photons from source halos. For higher efficiency and escape fraction (higher value of N_{heat}), the heating starts earlier and the absorption troughs are shallower (Pacucci et al. [2014], Mirocha et al. [2015], Cohen et al. [2017]). Hard X-ray photons generated in X-ray Binaries and mini-quasar are inefficient compared to soft photons to heat up the medium (Fialkov et al. [2014], Pacucci et al. [2014]). For higher value of α and lower value of v_{min} , there are more soft X-ray photons. This increases global temperature faster with shallower absorption trough. However, for the values of α and v_{min} explored in our work, the effect of X-ray spectra on the global signal is smaller compared to the effect of overall X-ray luminosity (N_{heat}).

If the stellar population has more low mass stars (e.g. Pop II stars), then there are more Lyman- α photons emitted compared to ionizing photons and the value of f_L is larger (Furlanetto et al. [2006], Mirocha et al. [2015]). This value is also higher if the escape fraction of ionizing photons is smaller (Mirocha et al. [2018]). For higher value of f_L , the coupling starts earlier, and the overall strength of the signal is larger at all redshifts before the complete coupling is achieved. This corresponds to deeper and earlier absorption troughs. The emission signal for very small f_L is smaller than the maximum value, which shows that the coupling has not saturated. The values of ζ we explored in our work do not change the global brightness temperature significantly for the redshift range of interest. Its only effect is to slightly shift the whole brightness temperature curve in redshift.

The redshift of heating transition is dependent on the heating (N_{heat} , α and v_{min}) and is almost independent of Lyman- α coupling (f_L). It happens sooner for higher value of N_{heat} and α , and lower value of v_{min} .

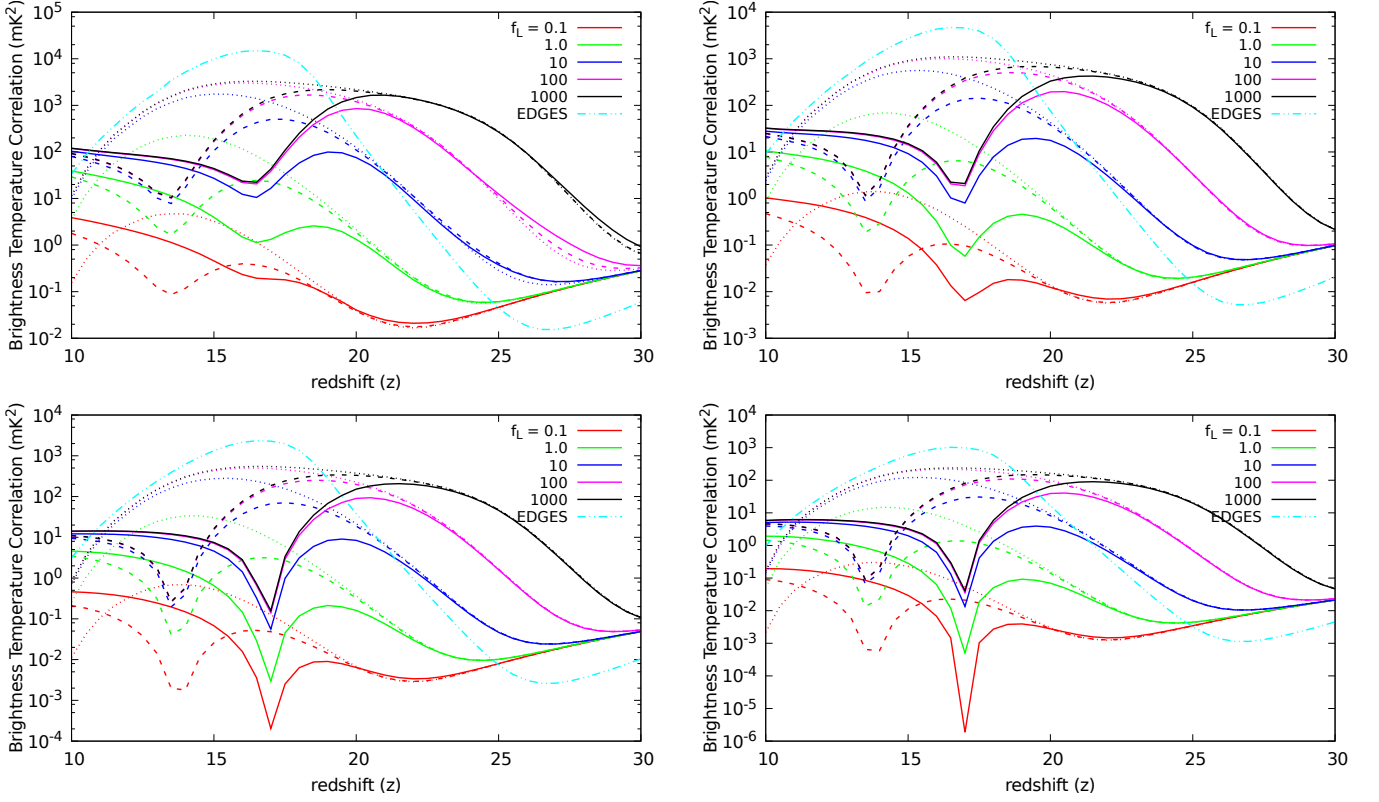


Figure 5.3: Evolution of auto-correlation of HI brightness temperature for $r = 0.5$ Mpc (top left panel), $r = 2.0$ Mpc (top right panel), $r = 4$ Mpc (bottom left panel) and $r = 8$ Mpc (bottom right panel) for $\zeta = 7.5$, a range of f_L varying from 0.1 to 1000 and three values of N_{heat} : 10 (solid lines), 1.0 (long dashed curves) and 0.1 (short dashed lines). The dot-dashed line represents a fiducial model that matches with EDGES observations.

5.3 Two-point Correlation Function

During the epoch of cosmic dawn and reionization, the inhomogeneous X-ray heating and Lyman- α coupling are expected to introduce fluctuations of spin temperature in addition to density and ionization inhomogeneities. The size distribution of ionization bubbles (Figure 1.6) introduces a range of scales in the correlation function. The X-ray photons create shallow temperature profiles around these bubbles (Figures 2.1 and 2.2), but their size distribution (Figure 2.3) makes it harder to identify the direct impact of heating and coupling on the correlation function.

Most of the studies of fluctuation in 21 cm brightness temperature from CD/EoR have been in the Fourier space. However, studying the correlation function in real space allows us to readily understand the impact of various parameters and physical processes. Our formalism has been built on geometric arguments, which are intuitively easier to visualize in real space. Our entire correlation structure can be written in terms of a single polynomial function: $C(\cdot, \cdot, \cdot, \cdot)$ and its limits given by the functions $E(\cdot, \cdot, \cdot)$ and $D(\cdot, \cdot)$ (Appendix F). Taking Fourier transform with respect to the first argument r of this function yields the power spectrum.

In Figure 5.3, we show the evolution of correlation function at scales $r = 0.5$ –8 Mpc for different values of N_{heat} and f_L , using Eqs. 1.39, 2.21, 3.13, and 4.49. In Figure 5.4, we show the evolution of the correlation

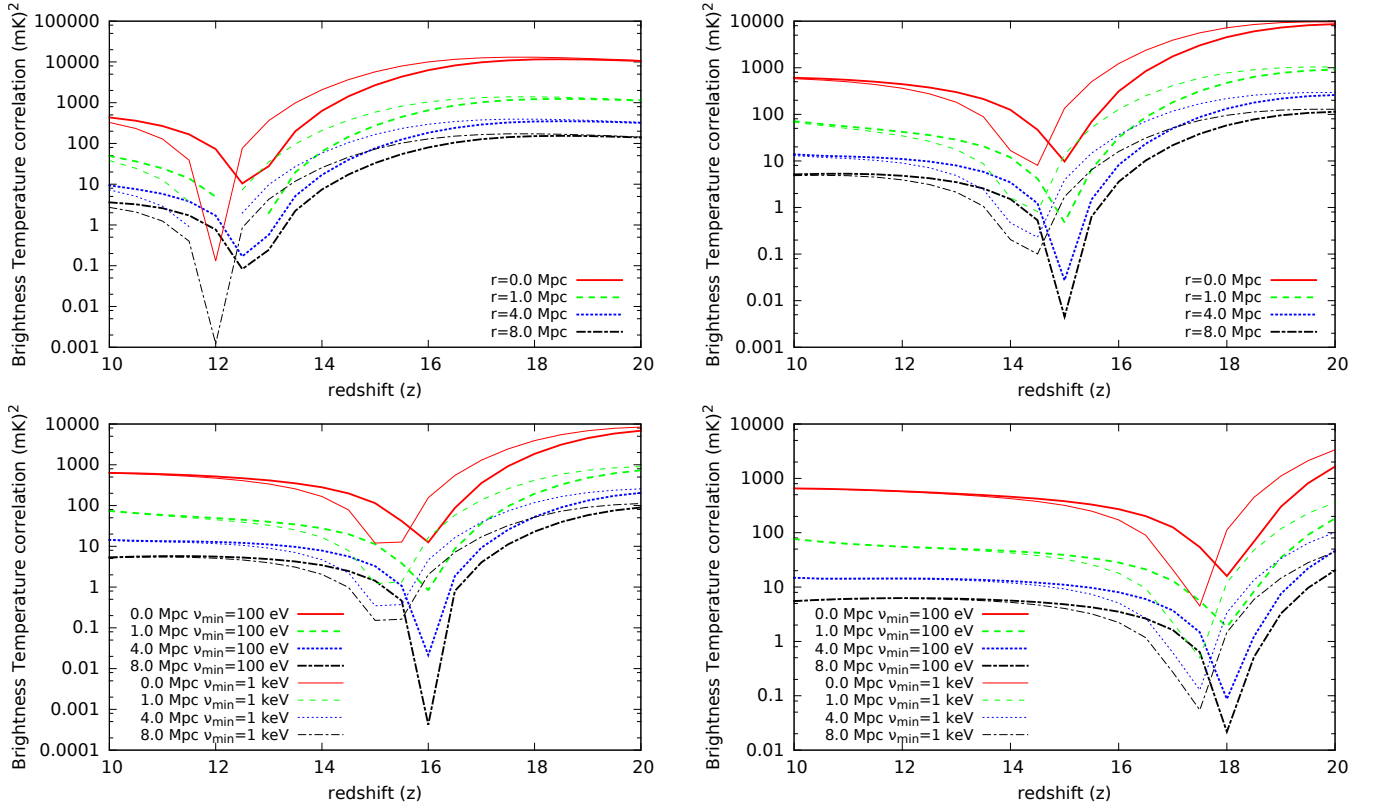


Figure 5.4: Evolution of two-point correlation function for a range of scales (including the RMS corresponding to $r = 0$) for $\alpha = 1.5$, and $\zeta = 10$. The thick curves are for $v_{\min} = 100$ eV and the thin curves are for $v_{\min} = 1$ keV. N_{heat} is 0.1 (top left panel), 0.5 (top right panel), 1.0 (bottom left panel), and 5.0 (bottom right panel).

function for a range of scales¹ for different values of N_{heat} and v_{\min} , assuming perfect Lyman- α coupling at $z \leq 20$ ($f_L \rightarrow \infty$).

At $z \simeq 30$, only the weak collisional coupling is effective, so all the curves shown in Figure 5.3 start with small values, and the correlation functions have similar strength for different modelling parameters. For small f_L , the correlations decline with time as the collisional coupling weakens. This situation is only reversed when Lyman- α coupling becomes efficient. For higher value of f_L , this coupling occurs sooner, leading to an increase in fluctuations with time until complete coupling is achieved. After this period, the fluctuations are determined by only heating, ionization and density inhomogeneities.

At high redshifts, the correlation function is large due to smaller background temperature. The fluctuations are dominated by density perturbations because the number density of ionizing sources is small and the volume fraction of ionization bubbles and spin temperature profiles is tiny. The position of the first peak at high redshift in Figure 5.3 depends strongly on the thermal evolution of the medium, and hence on heating parameters. For higher value of N_{heat} , the gas temperature is higher everywhere; this results in a decrease in the correlation function, which scales as $(1 - T_{\text{CMB}}/T_S)$ during this phase.

¹We also show the evolution of the RMS which corresponds to the plot for $r = 0$ to guide the eye. For an experiment, the relevant quantity would be the RMS smoothed with the three-dimensional resolution of the radio interferometer, which, as discussed below could be around 3–5 Mpc for ongoing and upcoming experiments. Therefore, the measured RMS would always be smaller than the quantity shown in Figure 4.6.

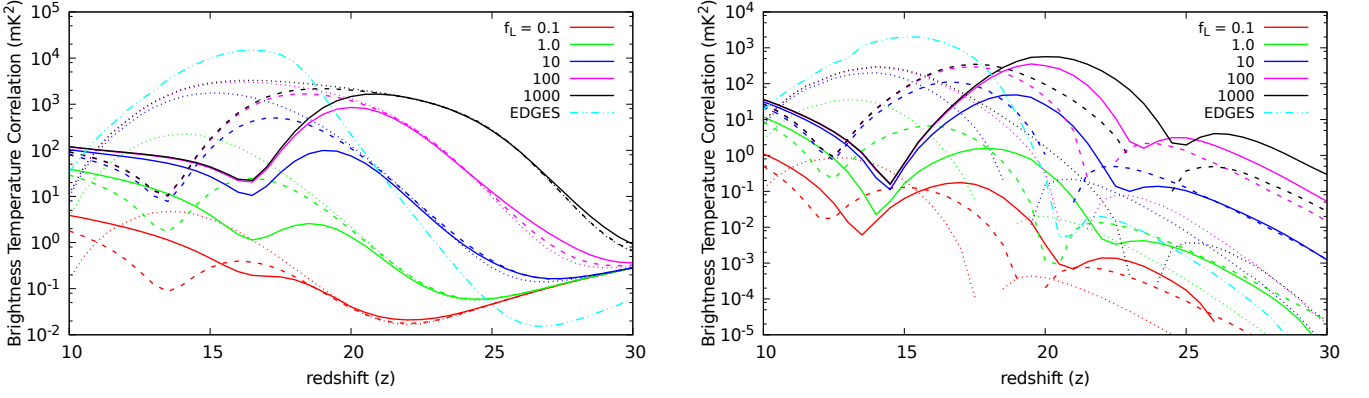


Figure 5.5: Evolution of auto-correlation of HI brightness temperature for $r = 0.5$ Mpc, including density perturbations (left panel) and without density perturbations ($\xi = 0$) (right panel), for $\zeta = 7.5$, a range of f_L varying from 0.1 to 1000 and three values of N_{heat} : 10 (solid lines), 1.0 (long dashed curves) and 0.1 (short dashed lines). The dot-dashed line represents a fiducial model that matches with EDGES observations.

There are three distinct mechanisms that can wipe out the information on the correlation scales generated by T_S inhomogeneities: (1) Increase in temperature in the profiles and the background: when these temperatures rise substantially above T_{CMB} , $s = T_{\text{CMB}}/T_S$ is driven to zero causing both autocorrelation of s and its cross-correlation with ionization inhomogeneities to approach zero. (2) Decrease in the gradient of temperature between the heated profiles and the background: This can happen at later stages when the higher number density of X-ray sources would raise the temperature uniformly. It can also be achieved when v_{min} is increased or α is decreased as seen in Figure 2.1; in this case, the heating around the bubble decreases and most of the X-ray photons are used in raising the background temperature homogeneously. (3) Merging of profiles: this process destroys the distinction between heated profile and background thereby erasing correlation information on the scales of the profiles. The difference between this case and case (2) is that the latter is possible for even small spin temperature profile fractions, f_h . All these reasons play some role in determining the transition from heating to ionization inhomogeneities regime. For the parameters we consider in our work, the effect of both (1) and (3) can be suppressed by considering a small N_{heat} while the scenario considered in (2) can be achieved by varying v_{min} .

When $\langle T_{\text{CMB}}/T_S \rangle$ decreases, reaching f_n at a certain redshift, the correlation function at large scales become negligible (Eq. 4.10). This happens very close to heating transition since $f_n \sim 1$ at large redshifts. For smaller value of N_{heat} and larger value of v_{min} the heating transition is delayed and the signal is larger during the era of partial heating. This result is in qualitative agreement with similar analyses on delayed heating (e.g. Fialkov et al. [2014]). Inhomogeneous collisional coupling and shape of the temperature profiles, which are determined by spectrum of X-ray photons (α and v_{min}), can potentially change the redshift and depth of heating transition by a small amount. We do not study this effect.

An increase in v_{min} causes shallow heating profiles, which results in reducing the gradient of temperature between the heating bubbles and the background, thereby reducing the correlation on a given scale for the same average temperature. Similarly, for smaller value of α , the temperature is more uniform and the correlation function is smaller. However, assuming a very large value of α does not change the correlation structure substantially, as this only increases the temperature right outside the ionization bubbles and the T_S

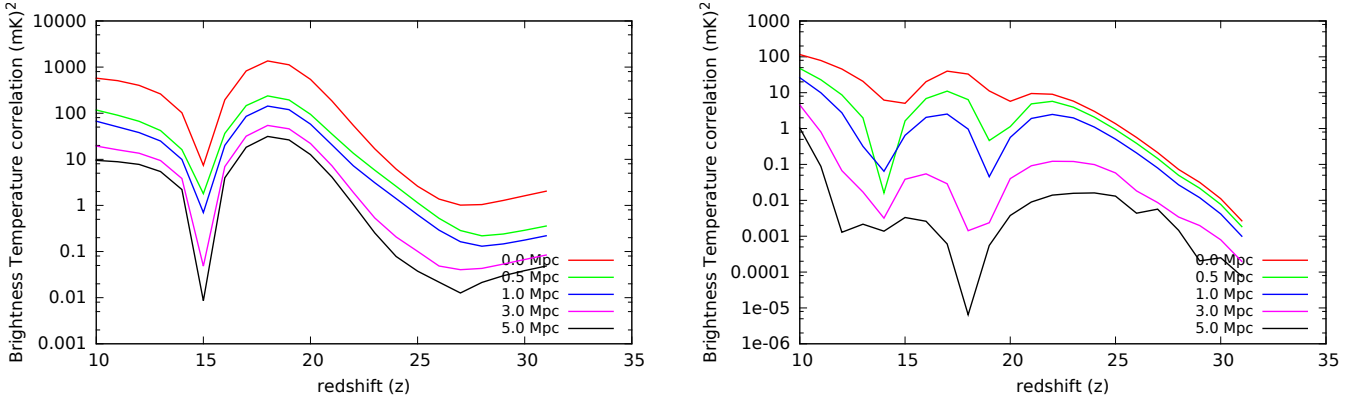


Figure 5.6: The evolution of auto-correlation of HI brightness temperature at various scales, including density perturbations (left panel) and without density perturbations ($\xi = 0$) (right panel), for $\zeta = 10$, $f_L = 10$, and $N_{\text{heat}} = 0.5$.

profile sizes remain the same. Generically, a larger N_{heat} for a fixed R_x results in larger temperature profiles and therefore causes correlation at larger scales. However, these profiles also merge sooner and wipe out heating fluctuations at those scales. All these parameters have a much stronger effect on correlation than ζ for most of the relevant redshifts in our work.

After the heating transition, the effect of inhomogeneous T_S decreases and the main source of fluctuations is ionization inhomogeneity. Their effect is suppressed if the heating or coupling is not saturated (very small values of N_{heat} and f_L).

The correlation functions are generally large at small scales (Eq. 4.11) and decrease as the distance between two points increases. At very large scale, they approach Eq. 4.10, where the density inhomogeneity is enhanced by $\langle 1 - T_{\text{CMB}}/T_S \rangle$, which could be large at early times. Therefore, large scales correlation function at early times could be a reliable measure of density correlation (ξ) and its statistical anisotropy, in agreement with results of Tashiro and Sugiyama [2013], Mesinger et al. [2013].

In Figure 5.5 and 5.6 the evolution of correlation function is shown without taking into account the correlation of density inhomogeneities ($\xi = 0$). The impact of Lyman- α coupling, heating and ionization fluctuations can be clearly observed in these figures. In Figure 5.5, the correlation goes slightly negative (also see Figure 5.9) at certain redshifts which depends strongly on N_{heat} and f_L . As the density correlation function, ξ is positive for all the scales we consider in our work, inclusion of this term generally makes our overall correlation function positive.

5.4 Power Spectrum

In Figure 5.7, we show the evolution of the power spectrum $\Delta^2 = k^3 P(k)/2\pi^2$ for a range of k^1 and various values of N_{heat} and f_L . In Figure 5.8, we present a range of Fourier modes k for different values of N_{heat} and v_{min} , assuming complete coupling at $z \leq 20$ ($f_L \rightarrow \infty$). These figures show similar evolutionary trend as the correlation functions (Figures 5.3 and 5.4). They are also in agreement with analyses that have studied

¹Generally, a wavenumber k will contribute to a range of spatial scales, but for making a comparison between real space correlation function and power spectrum, one can use the approximate conversion $r \simeq \pi/k$.

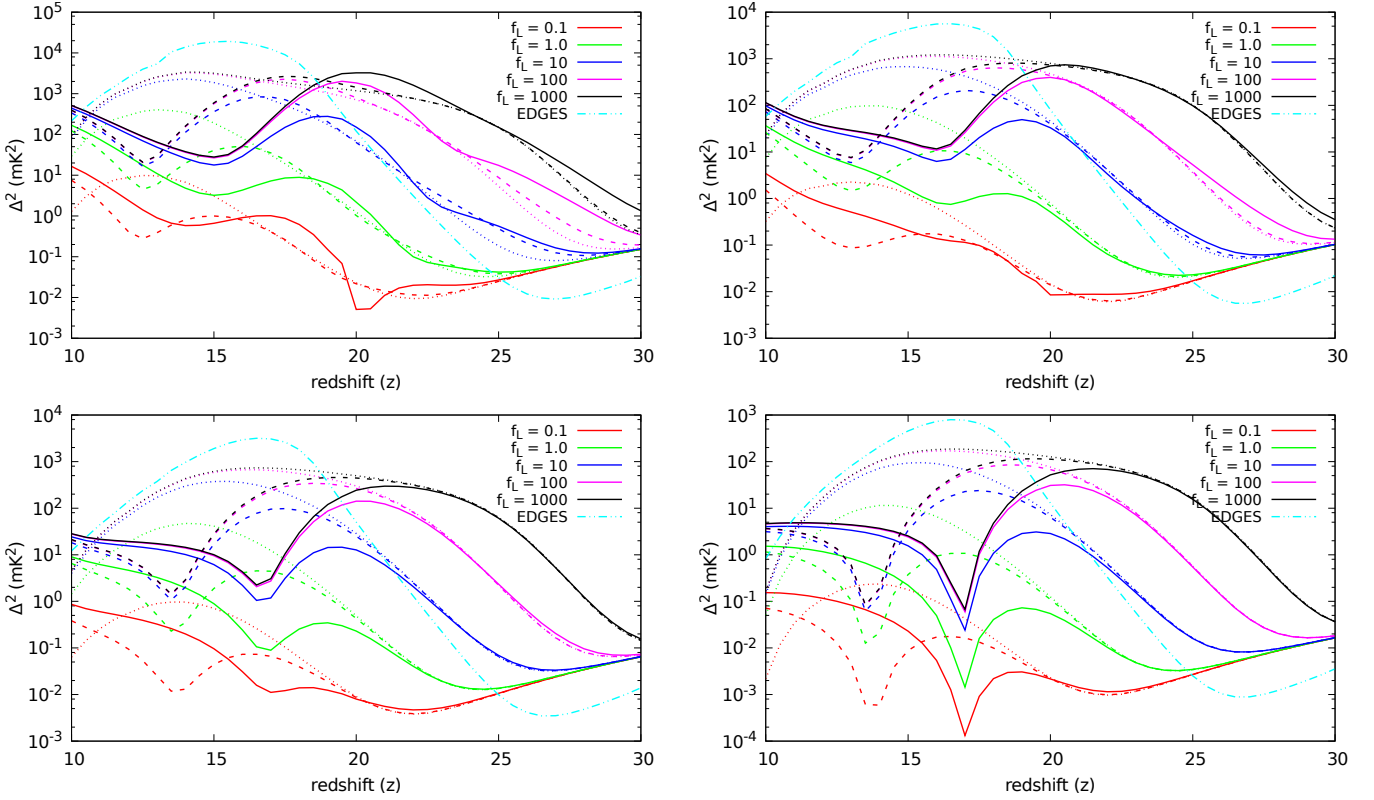


Figure 5.7: Evolution of $\Delta^2(k) = k^3 P(k)/2\pi^2$ for $k = 2 \text{ Mpc}^{-1}$ (top left panel), $k = 1 \text{ Mpc}^{-1}$ (top right panel), $k = 0.5 \text{ Mpc}^{-1}$ (bottom left panel) and $k = 0.125 \text{ Mpc}^{-1}$ (bottom right panel) for $\zeta = 7.5$, a range of f_L varying from 0.1 to 1000 and three values of N_{heat} : 10 (solid lines), 1.0 (long dashed lines) and 0.1 (short dashed lines). The dot-dashed line represents a fiducial model that matches with EDGES detection.

the impact of partial heating and density perturbations at large scales (e.g. [Tashiro and Sugiyama \[2013\]](#), [Mesinger et al. \[2013\]](#)) or the impact of late heating on the fluctuating component of the signal ([Fialkov et al. \[2014\]](#)).

While comparing our results with simulations, we have focused on three features: (a) the number of peaks in the power spectrum, (b) the amplitude of $\Delta^2(k)$ for a range of scales $k \sim 0.1\text{--}0.5 \text{ Mpc}^{-1}$ and (c) the difference between the redshift of heating transition and the redshift of the power spectrum minimum.

Existing results in the literature show that, for $k \simeq 0.1\text{--}0.5 \text{ Mpc}^{-1}$, there are generally two or three peaks of power spectrum as a function of redshift ([Santos et al. \[2008\]](#), [Baek et al. \[2010\]](#), [Mesinger et al. \[2013\]](#), [Ghara et al. \[2015\]](#), [Mesinger et al. \[2016\]](#), [Fialkov et al. \[2017\]](#)). At high redshifts, when the Lyman- α coupling and X-ray heating commence, they will create fluctuations of T_S in the medium. If fluctuations in these two fields dominate at widely different times, there will be two distinct peaks at high redshift: one due to coupling inhomogeneities and the other (generally at lower redshift than former) due to heating inhomogeneities ([Chen and Miralda-Escudé \[2008\]](#), [Pritchard and Furlanetto \[2007\]](#), [Ahn et al. \[2015a\]](#)). After the heating transition, there is a third, smaller peak at low redshifts, when the power spectrum is dominated by ionization inhomogeneities (e.g. [Pritchard and Furlanetto \[2007\]](#), [Fialkov et al. \[2014\]](#), [Ghara et al. \[2015\]](#)).

In our results, for the modelling parameters that we have used, we do not have separate Lyman- α and X-ray heating peaks; there is one peak due to T_S fluctuations at high redshift and a smaller peak due to

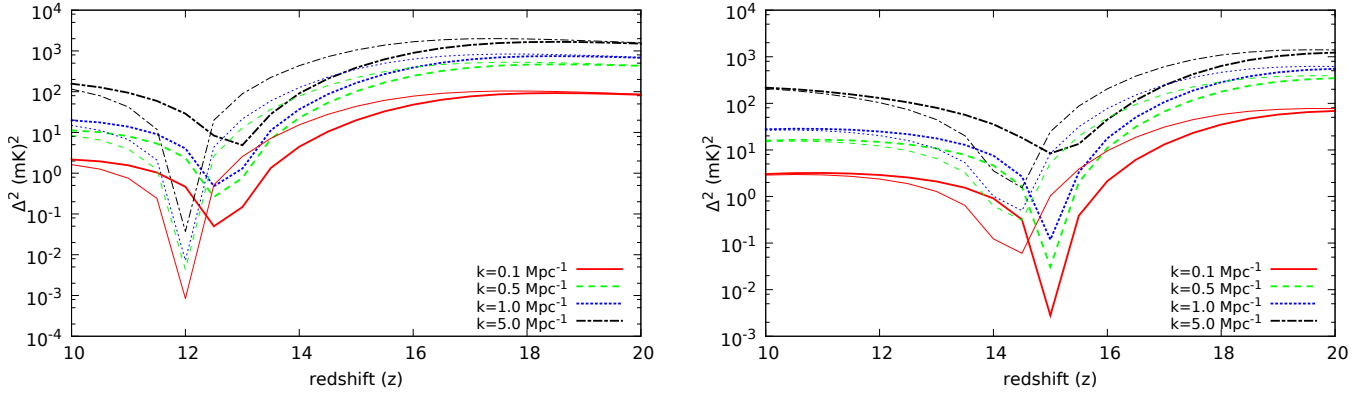


Figure 5.8: Evolution of $\Delta^2 = k^3 P(k)/2\pi^2$ ($(mK)^2$) for a range of scales for $\alpha = 1.5$, and $\zeta = 10$. The thick curves are for $v_{\min} = 100$ eV and the thin curves are for $v_{\min} = 1$ keV. The left and right panels correspond to $N_{\text{heat}} = 0.1$ and $N_{\text{heat}} = 0.5$, respectively.

ionization inhomogeneities at low redshifts. Generally, the possible additional peak is masked by density perturbations. When we neglect the impact of density perturbations in Figures 5.5 and 5.6, we see an additional peak. However, in the complete model, we find a weak peak owing to this effect only at small scales in the power spectrum ($k = 2 \text{ Mpc}^{-1}$ in Figure 5.7). Also, this feature is generally absent from plots of the evolution of correlation function (Figure 5.3).

The strength of the high redshift peak can be understood in terms of the evolution of number density of large self-ionized regions at early times and influence region of Lyman- α photons. For $z < 30$, the number density of self-ionized regions build exponentially in the excursion set formalism. While this creates inhomogeneities owing to geometry seen in Figure 4.7, it also causes a rapid build-up of the background Lyman- α photons, destroying the contrast between the near and far zone. At any point the background flux gets nearly equal contribution from sources within the (comoving) radius $R_{\text{max}}^{(n)}$ (Eq. 3.7). This radius is close to 600 Mpc for $n = 2$ at $z \simeq 25$. This large influence region contributes to wiping out the contrast in Lyman- α number density a short span. After this, the inhomogeneities in Lyman- α coupling arises owing to the influence regions $R_{\text{max}}^{(n)}$ for large principal quantum numbers n , which affects the medium very close to the sources. These fluctuations are destroyed only when complete Lyman- α coupling is established.

We note that $R_{\text{max}}^{(n)}$ (for small principle quantum numbers $n > 2$) determines the length scale at which the physics needs to be captured to study the Lyman- α generated inhomogeneities. It might be difficult to achieve it using an N -body simulation as the box size is generally smaller than this length scale. In our results for large N_{heat} and small f_L , we get three peaks at large k (top left panel of Figure 5.7), since the heating, and by extension collisional coupling inhomogeneities dominate *before* the Lyman- α inhomogeneities commence.

While our $\Delta^2(k)$ agrees with the results of simulations for smaller scales, for $k \simeq 0.1 \text{ Mpc}^{-1}$, our results give less power as compared to simulations (bottom right panel of Figure 5.7). Given the small sizes of ionization bubbles at high redshifts, the only contribution to fluctuations at $k \sim 0.1 \text{ Mpc}^{-1}$ is due to density and spin temperature inhomogeneities. For the models of heating and Lyman- α coupling used in our work, the contribution due to heating and coupling is dominated by faraway sources which diminish fluctuations at large scales. Therefore at these scales, the spin temperature inhomogeneities are negligible and only the

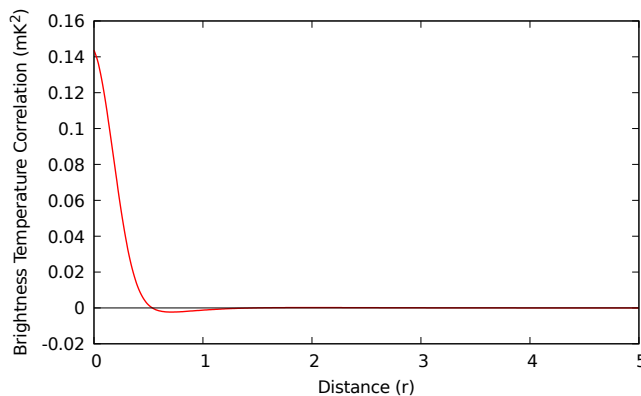


Figure 5.9: Neglecting density perturbations ($\xi = 0$), the auto-correlation of HI signal at $z = 20$ for $\zeta = 7.5$, $f_L = 1.0$ and $N_{\text{heat}} = 1.0$.

density fluctuations are enhanced by the average contrast of HI spin temperature with the CMB temperature. While it is conceivable that the higher power at large scales in simulation is owing to finite box size (for a discussion see Zahn et al. [2011], Ghara et al. [2015]), which might not allow one to take into account the contribution of far-away sources whose impact tends to homogenize the fluctuations of T_S at large scales, a more detailed comparison with simulations is hard as the parameter range used is generally not the same.

When the average spin temperature equals the CMB temperature during the heating transition, the power spectrum at small k reaches a minimum value (Figure 5.7). However, for larger k (small r), even during the heating transition there are significant fluctuations due to inhomogeneities of spin temperature and ionization which delays the minima of the power spectrum. Figure 5.7 shows that, for $k = 2\text{Mpc}^{-1}$, the minima of power spectrum depends on the value of f_L even though the heating transition is independent of it. In general, the minimum of power spectrum occurs during or after the global heating transition, depending on scales and modelling parameters. This is in agreement with simulations that have explored the dependence of these inhomogeneities on modelling parameters (Mesinger et al. [2013], Ghara et al. [2015], Mesinger et al. [2016], Fialkov et al. [2017]).

5.5 Non-Standard Scenarios

5.5.1 Negative Correlation

Our formalism allows for negative correlation, but we do not encounter cases with negative μ in our complete model. If we ignore ξ , which is positively correlated at all scales of interest, we can still identify cases where the auto-correlation of ϕ goes negative. We show one such case in Figure 5.9. Also, if the ionization bubble centres were anti-correlated (Section 4.6), then we can get negative correlations even after including the impact of density fluctuations. While such a situation doesn't obtain for ΛCDM model, except at much larger scales, the detection of negative correlation might point to another source of density fluctuations during the early universe.

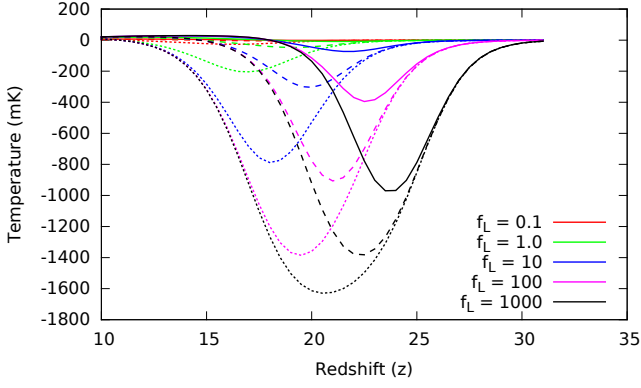


Figure 5.10: Global brightness temperature as function of redshift for $\zeta = 7.5$, various values of f_L ranging from 0.1 to 1000, and three value of N_{heat} : 10 (solid lines), 1.0 (long dashed lines) and 0.1 (short dashed lines). We have assumed dark matter-baryon interaction with $\sigma_1 = 5 \times 10^{-24} \text{ cm}^2$ and $m_{\text{dm}}/m_p = 0.001$.

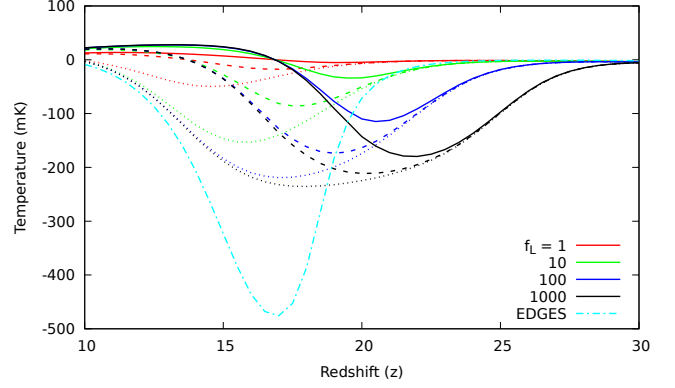


Figure 5.11: Global brightness temperature as function of redshift for $\zeta = 7.5$, various values of f_L ranging from 1.0 to 1000, and three value of N_{heat} : 10 (solid lines), 1.0 (long dashed lines) and 0.1 (short dashed lines). The dot-dashed line represents the fiducial model of Figure 5.10 with $f_L = 2$ and $N_{\text{heat}} = 0.08$.

5.5.2 Possible Explanations for EDGES Detection

An observation by Experiment to Detect the Global Epoch of Reionization Signature (EDGES) low band instrument reported a global brightness temperature absorption trough of strength $\Delta T \simeq -500 \text{ mK}$ in the frequency range of 70–90 MHz, corresponding to a redshift range of 15–19 (Bowman et al. [2018]). This detection implies a sharp trough in the signal at $z \simeq 19$ and an equally sharp rise at $z \simeq 15$. This detection can be explained using Eqs. 1.29 and 1.39 if $T_K \lesssim 2.5 \text{ K}$ at $z \simeq 17$. For standard recombination and thermal history, the minimum temperature of the gas at $z \simeq 17$ is $T_K \sim 7 \text{ K}$, and the absorption trough can have a maximum amplitude of $\sim 200 \text{ mK}$ at $z \simeq 17$. Therefore, this detection might indicate additional exotic channels of cooling the medium.

As the noise level for the detection is $\simeq 20 \text{ mK}$, the drop at higher redshift can arise from strong Lyman- α coupling ($T_K \gamma_\alpha \gg T_{\text{CMB}}$) being established close to $z \simeq 19$, with the rapid heating being responsible for the sharp rise at $z \simeq 15$. It should be noted that one of the implications of the EDGES results is that f_L cannot be too large, otherwise the complete Lyman- α coupling would be established at a higher redshift and even in the absence of additional cooling, the signal would be close to -150 mK at $z > 19$, which should be observable but is not seen by EDGES. Mirocha and Furlanetto [2019] have suggested that the star formation efficiency at high redshift should be higher than expected to account for the rapid buildup of Lyman- α photons and rapid T_S coupling.

Dark Matter-Baryon Interaction

One possible explanation of EDGES result is the additional cooling of baryons through their interactions with dark matter (Barkana [2018], Muñoz and Loeb [2018], Fialkov et al. [2018]). To understand our formalism better, we have taken a fiducial model of the form described in Barkana [2018] which fits the EDGES data: We have assumed dark matter-baryon interaction with cross-section $\sigma_1 = 5 \times 10^{-24} \text{ cm}^2$ and

the ratio of dark matter to proton mass $m_{\text{dm}}/m_p = 0.001$. Such an interaction helps cooling the baryon gas temperature much below what is predicted by the standard scenario, resulting in very large absorption troughs (Figure 5.10). For $f_L = 2$ and $N_{\text{heat}} = 0.08$, we get an absorption trough in the global signal similar to the one observed by EDGES data (Figure 5.11).

In Figures 5.3 and 5.7, we have shown the correlation functions and power spectrum for a range of scales, taking into account this fiducial model to replicate the EDGES results. The main impact of these observation on the fluctuating component is to boost the signal by nearly an order of magnitude in the redshift range $15 < z < 19$, even as compared to the most optimistic models¹ (low N_{heat} and high f_L) in the usual case. Even when the T_S field is uniform, with complete Lyman- α coupling and unheated gas, the low T_S would enhance the underlying density inhomogeneities. As we have shown in Section 4.5.4, the spin temperature field can be negatively correlated at some scales. In such scenarios, the fluctuating component of the signal could be less than given by Eq. 4.8. We tried to produce such models for parameters needed to explain the EDGES data and found it very difficult to anti-correlate the T_S field. Hence we infer that the minimum value of correlation function which corresponds to the EDGES signal is given by Eq. 4.8, using the value of T_K derived from the trough in the global signal. If the global signal has a trough of ~ 500 mK at $z \simeq 17$, then assuming complete coupling and no heating (no fluctuations due to these two fields), the autocorrelation function at $r = 2$ Mpc and $r = 4$ Mpc should be ~ 5100 (mK)² and ~ 2500 (mK)² respectively.

As EDGES results imply a smaller value of f_L , it results in smaller signal for $z > 19$ as compared to models with larger f_L that give a significantly higher signal (Figure 5.7). We also notice a decrease in the signal $z \simeq 30$, which is owing to cooler baryons causing a decrease in the efficiency of collisional coupling.

Effect of Residual Ionization Fraction

With residual ionization at the time of cosmic dawn $x_{\text{res}} \simeq 2 \times 10^{-4}$, the minimum matter temperature is $T_K \simeq 7.15$ K (Figure 1.3), which leads to maximum absorption signal of $\Delta T_B \sim 225$ mK. If we take $x_{\text{res}} \simeq 2 \times 10^{-6}$, we have minimum $T_K \simeq 1.32$ K and maximum absorption signal of $\Delta T_B \sim 1.3$ K. The EDGES absorption trough can be achieved by reducing x_{res} by one order of magnitude. However, there are no known phenomena which can lower the residual ionization fraction, as its value is fixed by the physics of recombination epoch which is extremely well constrained by the observation of CMB anisotropies.

Excess Radio Background

Another possible explanation of the EDGES result is the additional radio background at $z \leq 19$. In this case we can replace T_{CMB} with $T_{\text{CMB}} + T_{\text{radio}}$ in Eq. 1.29 (Feng and Holder [2018], Ewall-Wice et al. [2018], Sharma [2018]), and with suitable choice of T_{radio} , we can re-derive all our results for compatibility with EDGES detection. The results of the previous two mechanisms would hold even when this excess radio background is responsible for the deep absorption feature, as s increases by a similar factor in that case too. It might be possible to distinguish this scenario from the ones involving lower spin temperature if the radio background sources themselves exhibit spatial fluctuations with their own characteristic scales.

¹We have not incorporated the enhancement in the signal due to the inhomogeneous velocity-dependent cooling of gas within this model (Fialkov et al. [2018], Muñoz et al. [2018]).

5.6 Certain Assumptions and their Impact on Results

In our work, we have made many assumptions to simplify our formalism. We list some of the major assumptions and their possible impact below.

Λ CDM Model of the Universe and the HI Bias

The size distribution of self-ionized regions is calculated using the excursion set formalism, which assumes that the density perturbations at small scales are given by the Λ CMD model. In many extensions of this model, the power at small scales can differ substantially from the standard model (e.g. Sethi and Subramanian [2009], Sarkar et al. [2016]). Our formalism can be extended to such models by using their matter power spectrum to generate the size distribution of self-ionized regions. This would result in different T_S profiles, correlation functions and power spectrum strengths at various scales.

We assume the HI bias to be unity. If the HI distribution was biased with respect to underlying dark matter, the signal owing to density perturbations could be larger/smaller depending on the value of this bias.

Minimum Mass and Cooling

We have assumed the minimum mass of the collapsed objects (M_{\min}) to correspond to virial temperature $T_{\text{vir}} = 10^4$ K. However, if there were other channels of cooling (e.g. H_2), then this minimum mass could be smaller, which would lead to smaller ionization bubbles. This would shift the correlation function and power spectrum strength to lower scales. Conversely, if there were heating mechanisms which hampered the atomic cooling, the minimum mass of halos and ionization bubbles would be larger.

Excursion Set Formalism

For the Λ CDM model, the sources of radiation are expected to be highly clustered at high redshifts. Thus, within a self-ionized region, there are many such clustered sources. We assume that these self-ionized regions are unclustered and non-overlapping.

At smaller redshift ($z \lesssim 12$, depending on the parameter ζ), the excursion set formalism begins to break down when the ionization fraction (f_i) becomes large and there is substantial overlap between ionization bubbles (Furlanetto and Oh [2016], Giri et al. [2018]). In this regime, our results are not very accurate, however, we still show results up to $z \simeq 10$, to emphasize the transition from the era of T_S inhomogeneities to ionization inhomogeneities.

Correlation of Ionization Bubble Centres

We have assumed that the ionization bubbles are uncorrelated in space. The correlation of these bubble centres is expected to follow the correlation function of the density field with a bias (e.g. Dodelson [2003] and references therein). The mean bubble separation is large at high redshifts, where the density correlation function is much smaller than unity and the HI density fluctuations do not have a large bias with respect to

underlying dark matter density field. Thus, this assumption has greater validity at higher redshifts when the mean separation between the bubble centres is large.

If HI field is highly biased with respect to the underlying density field, the centres of ionization bubbles can be correlated (Ahn et al. [2015b]). In that scenario, there can be a significant correlation at scales much larger than sizes of the spin temperature profiles. We consider the case of correlated ionization bubble centres in Section 4.6 for a toy model and show that while this effect doesn't alter our results qualitatively it can introduce correlations at new scales.

Sphericity of Ionization Bubbles

Given the statistically isotropic and homogeneous process of the photoionization, X-ray heating and Lyman- α coupling, our assumption of spherical bubbles and isotropic spin temperature profiles hold even though the individual bubbles might not be spherical. At low redshifts, when the ionization fraction is very large, the ionized region geometry would vary substantially from spherical bubbles.

Ignoring Partly Ionized Regions

We have assumed that a small point in space is either completely ionized ($n = 0$) or completely neutral ($n = 1$). This is a good assumption as the HII regions have sharp boundaries. The boundary thickness is of the order of mean free path of an ionizing photon in the neutral medium, which is smaller than the sizes of ionization bubbles and spin temperature profiles.

We have also ignored the partial ionization caused by X-rays. It has been shown that X-rays can ionize medium up to 10% (Shull and van Steenberg [1985], Venkatesan et al. [2001]). This effect can be easily accommodated in our results (Section 4.4.4) by changing the value of $\phi = x_{\text{HI}}(1 - s)$. This would reduce the correlations by a small amount. However, Shull and van Steenberg [1985] have shown that the fraction of energy of a photoelectron which goes into heating the medium increases from $f_H \sim 0.15$ for a completely neutral medium to $f_H > 0.5$ for a medium with ionization fraction $x_i \sim 0.1$. Thus, the temperature within the partially ionized regions will increase faster. This would increase the global temperature as well as profile temperature for the same number and spectrum of X-ray photons. We have ignored this effect in our work.

Spectra of X-rays and Lyman- α Radiation

We have assumed that the X-ray luminosity is power-law with power index α and minimum frequency ν_{min} (Furlanetto [2006], Pritchard and Loeb [2012], Mesinger et al. [2011]). However, if this spectrum had a more complicated shape (Fialkov et al. [2014]), then we would be required to use multiple combinations of these two parameters to capture such a shape. In that case, the effect of these modelling parameters would be more difficult to analyze.

We have also assumed that the spectrum of radiation between Lyman- α and Lyman-limit is flat. If this spectrum had a different shape, then the Lyman- α contribution to a point from different distances would depend on this spectrum. For example, if there were more photons emitted at a frequency just below Lyman-

β than the number of photons at frequency just above Lyman- α , then for the same number of photons, the coupling would be more homogeneous, since more photons originate from far-away sources (with more redshifting) than from nearby sources.

Coupling of T_α to T_K

Throughout our work, we have assumed that the Lyman- α colour temperature T_α is coupled to matter kinetic temperature T_K through repeated scattering (Wouthuysen [1952], Field [1958]). Given the high number of scatterings undergone by every Lyman- α photon in the neutral medium, this is a good assumption. However, if for any reason, $T_\alpha < T_K$, then the Lyman- α photons can bring T_S to a temperature colder than given by the kinetic temperature of the medium and increase the strength of both global signal and its fluctuating component.

Redshift Space Distortion

We have neglected redshift-space distortion in our work, which would add anisotropy to the observed HI field. However, this effect is small and our formalism is still valid for scales perpendicular to the line of sight. As long as the ionization and heating sources are isotropic, their correlation is not affected by this anisotropy. Moreover, the regions which are most affected by the redshift space distortion, are the sites of structure formation and first regions to be ionized (McQuinn et al. [2006], Mesinger et al. [2011]). This reduces the anisotropy due to redshift space distortion at later redshifts.

Density Cross-correlation with Ionization and Temperature

For the sake of simplicity, we have ignored cross-correlation of density with ionization and temperature in this work. Most of the non-linear density fluctuation peaks are sites of source formation and these regions will be first to ionize. Thus, density is positively correlated with ionization. Using excursion set formalism, Furlanetto et al. [2004] computed this cross-correlation and showed that it is generally subdominant compared to auto-correlation terms (section 3.5, Figure 5 of their paper).

Similarly, high-density regions are more likely to produce and capture X-ray photons and heat up, which results in positive density-temperature correlation. High density and high-temperature regions would have higher collisional coupling. High-density regions near the sources will also receive more Lyman- α photons, which would suggest a positive correlation between the density and T_S coupling. However, on the scale of T_S profiles, the density correlation is smaller at high redshifts. Simulations show that the density-heating cross-correlation is sub-dominant compared to other contributions (Ghara et al. [2015]).

Overlap of Spin Temperature Profiles

Due to the assumption of random distribution of ionization bubbles, there is a finite probability that their spin temperature profiles will overlap with one another even when the total volume fraction occupied by such profiles is much smaller than unity. We have taken into account this effect in Section 4.3. However, in cases where there is a large overlap of profiles, our formalism gives unexpected results (e.g. negative power

spectrum). To avoid such unphysical results, we enforce that the total volume fraction of T_S profiles in our formalism remains small.

Evolution of Modelling Parameters

In our work, we have not considered scenarios for which the modelling parameters evolve with time. If these parameters are allowed to evolve, the ionization bubbles size distribution, spin temperature profiles and the background heating and coupling would require more complicated modelling. For instance, if R_x is larger at an earlier epoch owing to the evolution of ζ , the heating bubbles could be larger causing correlations on much larger scales than shown in our work. Our formalism can be easily extended to take into account such effects.

Infinite Volume for Correlation Calculation

While calculating correlations, if one point is inside a bubble or its profile, and the second point is outside that bubble and profile, then we have assumed that the probability of the second point being ionized or heated with certain temperature is the global volume fraction of ionized regions or regions with that temperature. However, we should ideally correct this fraction by taking into account the existence of ionization bubble and profile in which the first point is (see discussion in Section 4.4.1). This is a minor effect and we ignore it since we have assumed an infinite universe with an infinite number of bubbles; therefore, the presence of one bubble does not significantly alter the global fractions.

If correlation function was calculated on a box of finite length L with periodic boundary condition, then the conservation of the number of bubbles will introduce negative correlations at scales close to the half the box size. In our formalism, the negative correlations should appear at much larger scales than given by simulations. For Λ CDM universe, the correlation function of density is negative for very large scales and we can assume that the ionization and spin temperature correlations would also have negative values for such scales. A small value of negative correlation at very large scale will compensate for large positive correlation at small scale. This effect is quantifiable for finite volume, but difficult to calculate for an infinite volume. Since we do not calculate correlations on such large scales, we do not attempt to satisfy the condition that the integration of correlation overall space should be zero.

Chapter 6

Conclusion

*“And she never could remember; and ever since that day what
Lucy means by a good story is a story which reminds her of
the forgotten story in the Magician’s Book.”*

— C. S. Lewis, *The Voyage of the Dawn Treader*

Theoretically understanding the physical processes during the epoch of cosmic dawn and reionization remains a challenge given a large amount of uncertainty in the physics of ionizing sources, IGM, feedback mechanisms, etc. The detection of 21 cm signal from this time period is an outstanding goal of modern cosmology, which can not only shed light on the first sources of radiation but also help us gain a deeper understanding of cosmological structure formation.

6.1 Detecting HI 21 cm Signal

The global brightness temperature of 21 cm signal from the CD/EoR (redshift range of $25 > z > 8$) is expected to be in the range of -200 mK to 20 mK (Eq. 1.39), corresponding to the frequency range of 50 – 150 MHz (Madau et al. [1997], Tozzi et al. [2000], Gnedin and Shaver [2004]). The fluctuating component of the signal is likely to be an order of magnitude smaller on scales in the range 3 – 100 Mpc, which implies angular scales of $\simeq 1$ – 30 arc-minutes (e.g. Pritchard and Furlanetto [2007], Pritchard and Loeb [2012], Natarajan and Yoshida [2014], Morales and Wyithe [2010]). Currently, many ongoing and planned experiments are attempting to detect both the global HI signal and its fluctuating component from the CD/EoR. This signal is very weak, and it is buried under foregrounds, ionospheric distortion as well as terrestrial noise and systematic errors – all of which are orders of magnitude stronger than the signal.

Radio Foregrounds: Synchrotron continuous emission from galactic and extragalactic sources are the main sources of contaminations to the redshifted 21 cm signal from the EoR. The foreground flux, $S(\nu) \propto \nu^{-0.7}$, is higher at lower frequencies, which means that the HI signal from higher redshifts is more contaminated. Various methods have been developed to mitigate the impact of foregrounds (Harker et al. [2009], Bernardi et al. [2015], Chapman et al. [2015], Sathyanarayana Rao et al. [2017]). Iteratively removing point sources, along with modelling diffuse emission should ideally leave only signal and Gaussian noise in the

data. However, there is a possibility that residual from point sources might contaminate the signal (Harker et al. [2009]). Other methods try to exploit the difference in spectral properties of the signal and foregrounds to isolate the latter from the former in the data. As the frequency structure of the signal translates to the evolution of the HI spatial structure with redshift, the signal is not spectrally smooth; whereas the foregrounds are expected to have smooth frequency response due to their power-law spectra. Delay transform methodology can be used to make a certain region of the spectrum (EoR window) arbitrarily clean (Parsons et al. [2012], Paul et al. [2016]).

Ionosphere: Earth’s atmosphere is transparent to radio waves, but the free electrons in the ionosphere distort the signal through refraction and absorption (Vedantham et al. [2014], Sokolowski et al. [2015b], Datta et al. [2016]). This effect is dependent on the ionospheric electron density, which varies with time and place. To avoid contamination of the 21 cm signal due to this effect, observational projects have been proposed to study this signal from the far side of the moon (Dark Ages Radio Explorer (DARE) - frequency range of 40-120 MHz) (Burns et al. [2017]).

Radio Frequency Interference: The radio frequency interference (RFI) due to terrestrial sources such as FM and TV transmission, power lines, satellites and radio communications can also contaminate data. Given the time and place dependent nature of such interference, radio-quiet zones are chosen as sites of observations.

6.1.1 Global Signal

The thermal noise level required to detect the global 21 cm signal can be achieved within a few minutes to a few hours of integration time. However, the main challenge is in designing an instrument which does not introduce any spectral shapes that can confuse or distort the original signal. It is also important to develop algorithms to separate this signal from foregrounds, ionospheric distortions and internal systematics of the instrument. Observational projects that are attempting to detect the global signal are,

- **LEDA:** Large Aperture Experiment to Detect the Dark Ages (Bernardi et al. [2015], Price et al. [2018]), operating in the frequency range of 40-85 MHz has constrained the amplitude of the signal $\Delta T_B \lesssim -890$ mK with width greater than 6.5 MHz (corresponding to $\Delta z > 1.9$ at redshift $z = 20$) in the range $13.2 < z < 27.4$ ($100 > \nu > 50$ MHz) at the 95% confidence level (Bernardi et al. [2016]).
- **BIGHORNS:** Broadband Instrument for Global HydrOgen ReioNisation Signal is operating in the frequency range of 70-200 MHz (Sokolowski et al. [2015a]).
- **SCI-HI:** Sonda Cosmológica de las Islas para la Detección de Hidrógeno Neutro is operating in the frequency range of 40-130 MHz (Voytek et al. [2014]).
- **SARAS:** Shaped Antenna measurement of the background Radio Spectrum (Singh et al. [2017, 2018]), operating in the frequency range of 40-200 MHz has examined a large number models for 21 cm global signal predicted by the semi-numerical simulation of Cohen et al. [2017]. With data acquired over 13 nights, they have rejected models where the reionization was rapid and the IGM temperature T_K (and T_S , which is coupled with it) was very low due to late or no heating.

- **EDGES:** Experiment to Detect the Global EoR Signature (Bowman et al. [2018]) is operating in the frequency range of 50-200 MHz. They have ruled out rapid reionization ($\Delta z < 0.06$) in the redshift range of $6 < z < 13$ at 95% confidence level (Bowman and Rogers [2010]). Assuming $T_S \gg T_{\text{CMB}}$, their high-band instrument predicts $\Delta z \leq 1$ at $z \approx 8.5$ and $\Delta z \geq 0.4$ across most of the observed redshift range. For T_S not being heated to a large temperature, they reject $\Delta z \leq 2$ over most of the observed redshift range at $\geq 2\sigma$ significance (Monsalve et al. [2017]).

Their recent detection of a broad global absorption trough of strength 500 mK at $\nu \simeq 78 \pm 10$ MHz is the only positive detection of global HI signal (Bowman et al. [2018]). This result cannot be explained by the standard scenario of cosmic dawn and reionization (Section 5.5.2). Models have been proposed where interaction of baryons with cold dark matter will cool the gas and increase its contrast with the CMB (Barkana [2018], Muñoz and Loeb [2018], Fialkov et al. [2018]). Increased radio background due to early the radio sources has also been considered (Ewall-Wice et al. [2018], Sharma [2018]). It was also proposed that the signal could have been mimicked by spinning dust in the local universe (Draine and Miralda-Escudé [2018]) or might be an artefact of the data modelling (Hills et al. [2018], Singh and Subrahmanyam [2019]). If confirmed, this unexpectedly deep absorption trough will open new avenues to investigate exotic physics.

Apart from these single-element radiometers, interferometers can also be used to detect the global 21 cm signal. They have the advantage of reduced systematics level, at the cost of less sensitivity to the monopole component (Presley et al. [2015], Vedantham et al. [2015], Singh et al. [2015], Mahesh et al. [2015], McKinley et al. [2018]).

6.1.2 Fluctuating Components

In principle, radio interferometers can image the spatial fluctuations of 21 cm signal. However, given the nature of foregrounds, which are orders of magnitude brighter than the underlying HI signal (Pritchard and Loeb [2012]), it is easier to probe the statistical properties of the signal instead of directly imaging the field. It is customary in the literature to present the sensitivity of radio interferometers for the detection of HI signal in terms of power spectrum, partly because the radio interferometers measure the Fourier component of the HI signal. These radio interferometers directly measure visibilities; their correlations can be related to the power spectrum of the HI signal (Bharadwaj and Sethi [2001], Zaldarriaga et al. [2004]).

Many of the ongoing and upcoming experiments have the capability to detect the fluctuating component of the HI signal in hundreds of hours of data integration in the redshift range $8 < z < 25$ (e.g. Ahn et al. [2015a], Mesinger et al. [2014]). The best upper limits of $\Delta^2(k) \simeq (50\text{mK})^2$ for $k \simeq 0.1 \text{ Mpc}^{-1}$ has been obtained by these experiments:

- **GMRT:** The Giant Metrewave Radio Telescope Epoch of Reionization experiment provided the first upper limit of $\Delta^2(k) \leq (248 \text{ mK})^2$ for $k = 0.50 h \text{ Mpc}^{-1}$ at $z \approx 8.6$ (Paciga et al. [2013]).
- **LOFAR:** The ongoing experiment Low-Frequency Array High-Band Antenna's best upper limit correspond to $\Delta^2(k) = (79.6 \text{ mK})^2$ ($k \simeq 0.053 h \text{ cMpc}^{-1}$) in the redshift range $9.6 < z < 10.6$ in 13 hours of integration (Patil et al. [2017]). LOFAR has the frequency range to probe the redshift range of glo-

bal trough observed by EDGES. If the noise properties at smaller frequencies ($\simeq 80$ MHz) behave roughly as the one observed at higher frequencies ($\simeq 110$ MHz), LOFAR might be able to detect the signal in a few hundred hours of integration.

- **MWA:** The Murchison Widefield Array placed a systematic-limited upper limit on the HI power spectrum of $\Delta^2(k) \leq 2.7 \times 10^4 \text{ mK}^2$ at $k = 0.27 h \text{ Mpc}^{-1}$ and $z = 7.1$ with integration of 32 hours of data (Beardsley et al. [2016]). At frequency between 113 and 75 MHz ($11.6 \lesssim z \lesssim 17.9$) they have placed upper limit of $\Delta^2(k) \leq (10^4 \text{ mK})^2$ at comoving scales $k \lesssim 0.5 h \text{ Mpc}^{-1}$ with three hours of observations (Ewall-Wice et al. [2016]).
- **PAPER:** Precision Array for Probing the Epoch of Reionization claimed upper limit of $\Delta^2(k) \leq (22.4 \text{ mK})^2$ in the range $0.15 < k < 0.5 h \text{ Mpc}^{-1}$ at $z = 8.4$ with observation of 135 days (Ali et al. [2015]). However, due to signal loss estimation issue, they have retracted this limit (Cheng et al. [2018]).
- **HERA:** Hydrogen Epoch of Reionization Array is the successor of PAPER experiment and it is expected to observe the HI signal from CD/EoR in the range of 50-250 MHz (DeBoer et al. [2017]).
- **SKA:** For a deep survey with Square Kilometre Array (SKA1-LOW), the error on the power spectrum ($\Delta^2(k)$) is expected to vary from 0.1 (mK)^2 at $z \simeq 9$ to 5 (mK)^2 at $z \simeq 25$ for $k = 0.1 \text{ Mpc}^{-1}$. At $z \simeq 16$, it is expected to detect the HI signal with a signal-to-noise varying from 100 to 10 for $0.1 < k < 0.6 \text{ Mpc}^{-1}$ for a signal strength of $\Delta^2(k) \simeq 100 \text{ (mK)}^2$. The expected error is 2 (mK)^2 at $k = 0.1 \text{ Mpc}^{-1}$, and it increases to 10 (mK)^2 for $k \simeq 0.5 \text{ Mpc}^{-1}$. SKA1-LOW (and SKA2) have the capability to detect the EoR signal in the redshift range $20 < z < 25$. A signal of 100 (mK)^2 at $z \simeq 25$ is detectable by a deep SKA1-LOW survey with signal-to-noise of 5 for $k < 0.1 \text{ Mpc}^{-1}$. SKA1-LOW will also be able to directly image the HI field from scales of arc-minutes to degrees over most of the redshift range $z \sim 6 - 28$ (Ahn et al. [2015a], Koopmans et al. [2015]).

The angular scale above which the HI signal can be reliably measured for most ongoing and upcoming radio interferometers is a few arcminutes. $1'$ corresponds to nearly 3 Mpc (comoving) at $z \simeq 15$. Therefore, these telescopes are sensitive to linear scales larger than 5–10 Mpc (comoving). However, these telescopes have frequency resolution which correspond to much smaller linear scales (e.g. MWA's frequency resolution of 40 kHz corresponds to nearly 1 Mpc (comoving) along the line of sight).

Data analysis of these interferometers can readily be extended to the image plane (which is a byproduct of the analysis pipeline e.g. Patil et al. [2017] for LOFAR). This means real-space correlation functions can also be used for computation of the signal (Sethi and Haiman [2008]). Along with the global HI signal, the statistical detection of the fluctuating component can be used to constrain the epoch of Lyman- α coupling, X-ray heating and ionization, which would help us understand the properties of first sources and their surrounding medium better.

6.2 Summary and Conclusions

The main aim of our work is to present a new analytic formalism to study the HI 21 cm signal fluctuations from CD/EoR due to density, ionization, heating, and spin temperature coupling inhomogeneities. Our formalism takes into account size distribution of ionization bubbles using excursion set formalism for the Λ CDM model, and isotropic spin temperature profiles surrounding them using X-ray heating, collisional coupling and Lyman- α coupling. These profiles might overlap with one another and merge smoothly with the background. We study the evolution of these HII bubbles and their surrounding medium in the redshift range $10 \leq z \leq 30$ for five modelling parameters: efficiency of ionization (ζ), number of X-ray photons per stellar baryon (N_{heat}), the spectral index of X-ray photons (α), the minimum frequency of X-ray photons (ν_{min}) and the ratio of number of Lyman- α to ionizing photons (f_L).

We use geometric and probabilistic arguments to calculate two-point correlation function and power spectrum for this geometry. We compute the ionization autocorrelation, spin temperature autocorrelation, and spin temperature-ionization cross-correlations while neglecting the density cross-correlation with ionization and T_S . We explicitly show that our formalism reduces to the correct form in various limits. We study two simple toy models to understand the prediction of our formalism.

We also apply our method to study the fluctuating signal which would correspond to the global HI signal detected by EDGES group in the redshift range $15 < z < 19$. Generically, EDGES detection results in higher correlation signal in the redshift range of the detection but lower signal at higher redshifts, as compared to the most optimistic standard models (Figures 5.3 and 5.7). We do not attempt to physically explain the anomalous EDGES result in our work, but merely wish to demonstrate the power of our formalism to study such cases.

We find reasonable agreement with existing semi-analytic and N -body simulation results. As we compute correlation functions in both real and Fourier space, we find a possible case where the correlation function in real space is negative owing to partial heating and Lyman- α coupling (Figure 4.8). Since our formalism is not limited by the size of the simulation box, we can easily incorporate a variety of physical processes at very small or very large scale, e.g. the influence region of Lyman- α photons. This formalism is computationally cheaper, which means we can explore a large set of modelling parameters and their degeneracies at a fraction of computation resources taken by N -body simulation. While N -body simulations are important to understand and image the HI field, analytic methods, like the one presented in this thesis, are suitable to compute the statistical quantities like the correlation function and the power spectrum. Since N -body simulations, semi-analytic, and analytic formalisms each have their own set of assumptions, strengths, and weaknesses, it is beneficial to apply all these methods to unravel the complex physics of reionization.

6.3 Future Prospects

While developing our formalism, we have made several assumptions (Section 5.6). We can extend our formalism by taking into account the redshift space distortion and cross-correlation of density with ionization and T_S fields; these terms can help us better understand of the underlying dark matter model and its effect

on 21 cm signal. This would also allow us to investigate alternative dark matter models.

We can also apply our formalism to study cross-correlation of various lines at high redshift (e.g. 21 cm hyperfine line, 3 cm fine structure line, recombination lines, He lines). In the post-recombination era, such methods can be applied to study the Lyman- α forests. We can also extend our formalism to compute three-point correlation function to study non-gaussianity in the early universe. Establishing general properties of two- and three-point correlation functions of the 21 cm signal (or power spectrum and bispectrum in Fourier space) can help us distinguish the HI signal from foregrounds and other contaminants, which have different statistical properties.

Appendix

A Physical Constants

c	$3 \times 10^{10} \text{ cm s}^{-1}$	speed of light
h_p	$6.626 \times 10^{-27} \text{ cgs}$	Planck constant
G	$6.67 \times 10^{-8} \text{ cm}^2 \text{ g}^{-1} \text{ s}^{-2}$	gravitational constant
m_e	$9.11 \times 10^{-28} \text{ g}$	mass of electron
m_p	$1.67 \times 10^{-24} \text{ g}$	mass of proton
e	$4.8 \times 10^{-10} \text{ esu}$	charge of electron
k_B	$1.38 \times 10^{-16} \text{ erg/K}$ $8.617 \times 10^{-5} \text{ eV/K}$	Boltzmann constant
a_r	$7.56 \times 10^{-15} \text{ cgs}$	radiation constant
σ_T	$6.65 \times 10^{-25} \text{ cm}^2$	Thomson cross-section
1 eV	$1.602 \times 10^{-12} \text{ erg}$ $\simeq 10^4 \text{ K}$	
1 parsec	$3.0857 \times 10^{18} \text{ cm}$	
M_\odot	$1.99 \times 10^{33} \text{ g}$	Solar mass

B Hydrogen and Helium

21 cm Hyperfine Transition of HI			Ionization of Hydrogen and Helium	
ΔE_{21}	$5.9 \times 10^{-6} \text{ eV}$	energy difference	E_{HI}	13.6 eV
λ_{21}	21.1 cm	wavelength	E_{HeI}	24.6 eV
ν_{21}	1420.4 MHz	frequency	E_{HeII}	54.4 eV
A_{21}	$2.85 \times 10^{-15} \text{ s}^{-1}$	spontaneous transition rate	$\sigma_{0,\text{HI}}$	$6.3 \times 10^{-18} \text{ cm}^2$
T_\star	0.068	$h_p \nu_{21} / k_B$	$\sigma_{0,\text{HeI}}$	$7.4 \times 10^{-18} \text{ cm}^2$

Lyman-series		
ΔE_α	10.2 eV	Lyman- α energy difference
λ_α	1216×10^{-8} cm	Lyman- α wavelength
ν_α	2.468×10^{15} Hz	Lyman- α frequency
ν_β	2.925×10^{15} Hz	Lyman- β frequency
ν_γ	3.083×10^{15} Hz	Lyman- γ frequency
A_α	6.2581×10^8 s $^{-1}$	Lyman- α spontaneous transition rate
f_α	0.4162	Lyman- α oscillation strength

Case A and B recombination coefficient: Case A recombination coefficient takes into account recombination to all the states of the hydrogen atom, whereas Case B recombination coefficient only takes into account recombination to $n \geq 2$. When the matter is optically thick for the recombination photon, we use Case B recombination coefficient.

$$\alpha_A = 4.2 \times 10^{-13} \text{ cm}^3 \text{ s}^{-1} \quad \text{at } 10^4 \text{ K}$$

$$\alpha_B = \frac{2.6 \times 10^{-13}}{(T_K/10^4 \text{ K})^{0.8}} \text{ cm}^3 \text{ s}^{-1}$$

C Cosmology

Cosmological Parameters (Planck Collaboration et al. [2018])		
T_0	2.725 K	CMB temperature at $z = 0$
h	0.677	Hubble parameter
Ω_m	0.310	matter density fraction
Ω_b	0.049	baryon density fraction
Ω_Λ	0.690	dark energy density fraction
$\Omega_b h^2$	0.022	
$\Omega_m h^2$	0.142	
σ_8	0.808	density fluctuations at $8 h^{-1} \text{ Mpc}$ at $z = 0$
n_s	0.967	power spectrum spectral index
τ_{reion}	0.055	reionization optical depth

Redshift: In the expanding universe, if the photons were emitted at redshift $z = z_e$, and observed at $z = z_o$:

$$\frac{a(t_o)}{a(t_e)} = \frac{1 + z_e}{1 + z_o} = \frac{\nu_e}{\nu_o} = \frac{\lambda_o}{\lambda_e}$$

$$\frac{dz}{1 + z} = \frac{d\nu}{\nu} = -\frac{da}{a}$$

Λ CDM Universe: We assume that the universe is statistically homogeneous and isotropic.

$$\begin{aligned}\dot{\rho} + 3\frac{\dot{a}}{a}(\rho + p) &= 0 \\ \frac{\ddot{a}}{a} &= -\frac{4\pi G}{3}(\rho + 3p) + \frac{\Lambda}{3} \\ \frac{\dot{a}^2}{a^2} &= \frac{8\pi G}{3}(\rho_m + \rho_\gamma + \rho_\Lambda + \rho_k) = \frac{8\pi G}{3}(\rho_m + \rho_\gamma) + \frac{\Lambda}{3} - \frac{k}{a^2}\end{aligned}$$

Hubble's constant: $H(z) = \frac{\dot{a}}{a} = H_0 \left(\Omega_\gamma (1+z)^4 + \Omega_m (1+z)^3 + \Omega_k (1+z)^2 + \Omega_\Lambda \right)^{1/2}$

Critical density for $k = 0$: $\rho_c = \frac{3H_0^2}{8\pi G}$

Matter-radiation equality: $\Omega_m (1+z)^3 = \Omega_\gamma (1+z)^4 \Rightarrow 1 + z_{\text{eq}} = \frac{\Omega_m}{\Omega_r} \simeq 3380$

Matter-dark energy equality: $\Omega_m (1+z)^3 = \Omega_\Lambda \Rightarrow 1 + z_{\text{eq2}} = \left(\frac{\Omega_\Lambda}{\Omega_m} \right)^{1/3} \simeq 1.306$

Matter dominated epoch: $(z_{\text{eq}} > z > z_{\text{eq2}}) \quad H(z) \simeq H_0 \Omega_m^{1/2} (1+z)^{3/2}$.

valid assumption for epochs of dark ages, cosmic dawn and reionization.

Baryons:

$$\begin{aligned}\text{mass density fraction at } z = 0: \quad \Omega_{\text{H}} &= x_{\text{H}} \Omega_b \simeq \frac{3}{4} \Omega_b & \text{and} & \quad \Omega_{\text{He}} = x_{\text{He}} \Omega_b \simeq \frac{1}{4} \Omega_b \\ \text{number density at } z = 0: \quad n_{\text{H},0} &= \frac{\Omega_{\text{H}} \rho_c}{m_p} \simeq \frac{3}{4} \frac{\Omega_b \rho_c}{m_p} & \text{and} & \quad n_{\text{He},0} = \frac{\Omega_{\text{He}} \rho_c}{m_{\text{He}}} \simeq \frac{1}{4} \frac{\Omega_b \rho_c}{4m_p} \\ \text{number density fraction:} \quad \frac{n_{\text{H}}}{n_b} &= \frac{n_{\text{H}}}{n_{\text{H}} + n_{\text{He}}} \simeq \frac{12}{13} & \text{and} & \quad \frac{n_{\text{He}}}{n_b} = \frac{n_{\text{He}}}{n_{\text{H}} + n_{\text{He}}} \simeq \frac{1}{13}.\end{aligned}$$

number density of baryons at $z = 0$: $n_{b,0} = n_{\text{H},0} + n_{\text{He},0} \simeq \frac{13}{16} \frac{\Omega_b \rho_c}{m_p} = 1.125 \times 10^{-5} \frac{13}{16} \Omega_b h^2$.

number density of hydrogen: $n_{\text{HI}} = 1.125 \times 10^{-5} x_{\text{HI}} x_{\text{H}} \Omega_b h^2 (1+z)^3$

Cosmological Parameters		
H_0	$h \times 100 \text{ km s}^{-1} \text{Mpc}^{-1}$ $h \times 3.24 \times 10^{-18} \text{ s}^{-1}$	Hubble's constant
ρ_c	$h^2 \times 1.8786 \times 10^{-29} \text{ g cm}^{-3}$	critical density $z = 0$
$n_{b,0}$	$9.140 \times 10^{-6} \Omega_b h^2 \text{ cm}^{-3}$	number density of nucleons at $z = 0$
$n_{\text{H},0}$	$8.437 \times 10^{-6} \Omega_b h^2 \text{ cm}^{-3}$	number density of hydrogen at $z = 0$

Distances: Line element in spatially flat ($k = 0$) FRW metric is

$$ds^2 = dt^2 - a^2(t)(dr_0^2 + r_0^2 d\Omega),$$

where, r_0 is the coordinate (comoving) distance between two points. This distance remains constant with the expansion of the universe. If we trace the path of a photon between two points, we need to take into account the evolution of the scale factor a while the photon is travelling by using the light-travel distance r_γ . If a photon was emitted at t_e (z_e) and observed at t_o (z_o), then

$$\begin{aligned} \text{Comoving distance:} \quad r_0 &= \int_{t_e}^{t_o} \frac{c}{a} dt = \int_{z_o}^{z_e} \frac{c}{H(z)} dz \\ \text{Light-travel distance:} \quad r_\gamma &= \int_{t_e}^{t_o} c dt = \int_{z_o}^{z_e} \frac{c}{H(z)(1+z)} dz \\ \text{Physical (proper) distance:} \quad dr &= a(t) dr_0 \\ \text{Luminosity distance:} \quad r_L &= r_0 \frac{1+z_e}{1+z_o} \\ \text{Angular diameter distance:} \quad r_A &= r_0 \frac{1+z_o}{1+z_e}. \end{aligned}$$

Structure Formation with Linear Perturbation Theory:

$$\begin{aligned} \text{Position and Motion of Particle:} \quad \vec{r} &= a(t) \vec{x}, & \dot{\vec{r}} &= a \dot{\vec{x}} + \vec{x} \dot{a} \\ \text{Linear Perturbation Theory:} \quad \dot{\vec{v}} + \vec{v} H &= -\frac{\vec{\nabla} \phi}{a}, & \dot{\delta} + \frac{\vec{\nabla} \cdot \vec{v}}{a} &= 0 \\ & \ddot{\delta} + 2\frac{\dot{a}}{a} \dot{\delta} &= \frac{\nabla^2 P}{\rho_b a^2} + 4\pi G \rho_b \delta \\ \text{Solutions:} \quad \delta_1 &= \frac{X^{1/2}}{a} \int^a \frac{1}{X^{3/2}} da, & \delta_2 &= \frac{X^{1/2}}{a} \\ & X &= \frac{8\pi}{3} G \rho_b a^2 + \frac{\Lambda}{3} a^2 - k \end{aligned}$$

D Radiative Transfer

Specific intensity: $I_\nu = \frac{dE}{dt d\Omega dA dv}$ (Rybicki and Lightman [1979])

Angle averaged specific intensity: $J_\nu = \frac{1}{4\pi} \int I_\nu d\Omega$, $\bar{J} = \int \phi(\nu) J_\nu d\nu$

Flux: $F_\nu = \int I_\nu \cos\theta d\Omega = \frac{dE}{dt dA dv}$

Energy density: $\mu_\nu = \frac{1}{c} \int I_\nu d\Omega = \frac{4\pi}{c} J_\nu = \frac{dE}{dV dv}$

Number density of photons: $n_\nu = \frac{4\pi}{c} \frac{2\Delta\nu}{h_p \nu} J_\nu = \frac{dN}{dV}$

Emission coefficient: $j_\nu = \frac{h_p \nu}{4\pi} n_2 A_{21} \phi(\nu) = \frac{dE}{dV d\Omega dt dv}$

Absorption coefficient: $\alpha_\nu = \frac{h_p \nu}{4\pi} (n_1 B_{12} - n_2 B_{21}) \phi(\nu) = \sigma_\nu n_1 \left(1 - \frac{g_1 n_2}{g_2 n_1}\right)$

Optical depth: $\tau_\nu = \int n \sigma_\nu ds = \int \alpha_\nu ds$

Source function: $S_\nu = \frac{j_\nu}{\alpha_\nu} = \frac{n_2 A_{21}}{n_1 B_{12} - n_2 B_{21}}$

Mean free path: $\bar{l}_\nu = \frac{1}{\alpha_\nu} = \frac{1}{n \sigma_\nu}$

Cross-section: $\sigma_\nu = \frac{h_p \nu}{4\pi} B_{12} \phi(\nu) = \frac{g_2}{g_1} \frac{A_{21} \lambda^2}{8\pi} \phi(\nu)$

Doppler broadening line profile: $\phi(\nu) = \frac{1}{\sqrt{\pi}} \frac{1}{\Delta\nu_D} \exp\left[-\left(\frac{\nu - \nu_0}{\Delta\nu_D}\right)^2\right]$; $\int \phi(\nu) d\nu = 1$

Einstein coefficients: $g_1 B_{12} = g_2 B_{21}$ and $A_{21} = \frac{2h_p \nu^3}{c^2} B_{21}$

Without medium, static universe: $\frac{dI_\nu}{ds} = 0$

Without medium, expanding universe: $\frac{I_{\nu_o}}{\nu_o^3} = \frac{I_{\nu_e}}{\nu_e^3}$

Medium: $\frac{dI_\nu}{ds} = -\alpha_\nu I_\nu + j_\nu$; $\frac{dI_\nu}{d\tau_\nu} = -I_\nu + S_\nu$

$\therefore I_\nu(\tau_\nu) = I_\nu(0)e^{-\tau_\nu} + S_\nu(1 - e^{-\tau_\nu})$

Planck law for blackbody: $B_\nu(T) = \frac{2h_p \nu^3}{c^2} \frac{1}{\exp\left(\frac{h_p \nu}{k_B T}\right) - 1}$

Rayleigh-Jeans limit ($h_p \nu \ll k_B T$): $B_\nu(T) \simeq \frac{2\nu^2 k_B T}{c^2}$

Brightness temperature in RJ limit: $T_B \simeq \frac{c^2}{2\nu^2 k_B} I_\nu$

$T_B(\tau_\nu) \simeq T_B(0)e^{-\tau_\nu} + T(1 - e^{-\tau_\nu})$.

E Probability

$$\mathcal{P}(A|B) = \frac{\mathcal{P}(A \cap B)}{\mathcal{P}(B)} \quad (\text{E.1})$$

$$\begin{aligned} \mathcal{P}((A \cap B)|C) &= \frac{\mathcal{P}(A \cap B \cap C)}{\mathcal{P}(C)} \\ &= \frac{\mathcal{P}(A \cap B \cap C)}{\mathcal{P}(B \cap C)} \frac{\mathcal{P}(B \cap C)}{\mathcal{P}(C)} \\ &= \mathcal{P}(A|(B \cap C)) \mathcal{P}(B|C) \end{aligned} \quad (\text{E.2})$$

$$\begin{aligned} \mathcal{P}(A) &= \mathcal{P}(A \cap B) + \mathcal{P}(A \cap \tilde{B}) \\ \therefore \mathcal{P}(A \cap B) &= \mathcal{P}(A) - \mathcal{P}(A \cap \tilde{B}) \end{aligned} \quad (\text{E.3})$$

F Geometry

$A(d, P, Q)$

When two spheres of radius P and Q overlap, then the surface area of the sphere with radius P that lies in sphere of radius Q is (Weisstein [2007a,b]),

$$A(d, P, Q) = \frac{\pi P(Q - P + d)(Q + P - d)}{d},$$

where d is the distance between two sphere centres. If $d > P + Q$, then these two spheres do not overlap. If $Q > P$ and $d < Q - P$, then the first sphere lies entirely within the second sphere. If $P > Q$ and $d < P - Q$, then the first sphere entirely encloses the second sphere. Therefore,

$$A(d, P, Q) = \begin{cases} 0 & d > P + Q \\ 0 & d < P - Q \\ 4\pi P^2 & d < Q - P \\ \frac{\pi P(Q - P + d)(Q + P - d)}{d} & \text{Otherwise.} \end{cases} \quad (\text{F.1})$$

$V(d, P, Q)$

Given two spheres of radius P and Q , the overlapped volume is

$$V(d, P, Q) = \begin{cases} 0 & d > P + Q \\ \frac{4\pi}{3} Q^2 & d < P - Q \\ \frac{4\pi}{3} P^2 & d < Q - P \\ \frac{\pi(Q + P - d)^2(d^2 + 2d(P + Q) - 3(P - Q)^2)}{12d} & \text{Otherwise,} \end{cases} \quad (\text{F.2})$$

where d is the distance between two sphere centres. Here we note that,

$$\frac{d}{dP}V(d,P,Q) = A(d,P,Q). \quad (\text{F.3})$$

F.1 $D(x,R)$

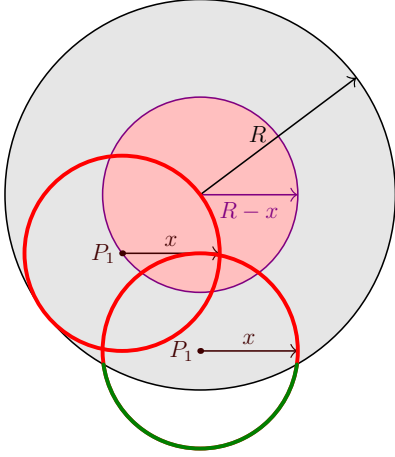


Figure F.1: Case a: $x \leq R$

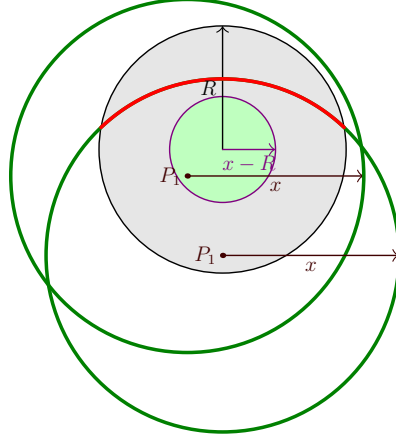


Figure F.2: Case b: $R \leq x \leq 2R$

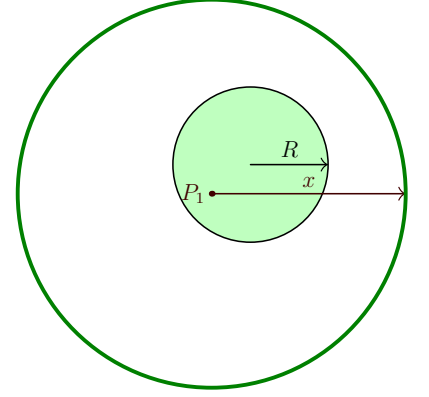


Figure F.3: Case c: $x \geq 2R$

If point 1 is inside a sphere of radius R , then the probability that its neighbour (point 2) at distance x is outside the sphere is $D(x,R)$. Here we take a to be the distance of point 1 from the centre of the sphere.

(a) $x < R$: If $a < R - x$, then all the neighbors of point 1 are inside the sphere. For $a > R - x$, we can use Eq. F.1 (Figure F.1) and get,

$$D(x,R) = \left[\frac{\frac{4\pi}{3}(R-x)^3}{\frac{4\pi}{3}R^3} \right] (0) + \int_{R-x}^R \left(1 - \frac{A(x,R,a)}{A_x} \right) \frac{4\pi a^2}{\frac{4\pi}{3}R^3} da = \frac{3x}{4R} - \frac{x^3}{16R^3}.$$

Here $A_x = 4\pi x^2$ is the surface area of a sphere with radius x .

(b) $R < x < 2R$: If $a < x - R$, then all neighbors of point 1 are outside the sphere (Figure F.2). Therefore,

$$D(x,R) = \left[\frac{\frac{4\pi}{3}(x-R)^3}{\frac{4\pi}{3}R^3} \right] (1) + \int_{x-R}^R \left(1 - \frac{A(x,R,a)}{A_x} \right) \frac{4\pi a^2}{\frac{4\pi}{3}R_x^3} da = \frac{3x}{4R} - \frac{x^3}{16R^3}.$$

(c) $2R < x$: All neighbors of point 1 are outside the sphere (Figure F.3), giving $D(x,R) = 1$.

Putting them all together, we finally get,

$$D(x,R) = \begin{cases} \frac{3x}{4R} - \frac{x^3}{16R^3} & x < 2R \\ 1 & x > 2R. \end{cases} \quad (\text{F.4})$$

Also note that,

$$1 - D(x, R) = \frac{V(x, R, R)}{V_R}. \quad (\text{F.5})$$

Here $V_R = 4\pi R^3/3$. Therefore, the probability that neighbour of a point in sphere of radius R lies within that sphere is the fraction of volume that is overlapped by two spheres of radius R at distance x .

F.2 $E(x, Q, R)$

If point 1 is inside a sphere of radius Q , then the probability that its neighbour (point 2) at distance x is outside the concentric sphere of radius R is $E(x, Q, R)$. a is the distance of point 1 from the centre of the sphere.

(a) $R > Q$ and $x < R - Q$: All neighbors of point 1 are inside the sphere of radius R , giving $E(x, Q, R) = 0$.

(b) $R > Q$ and $R - Q < x < R$: $R - x < Q$. If $a < R - x$, all neighbors of point 1 are inside the sphere with radius R . For $a > R - x$, we can use Eq. F.1, and get

$$\begin{aligned} E(x, Q, R) &= \left[\frac{\frac{4\pi}{3}(R-x)^3}{\frac{4\pi}{3}Q^3} \right] (0) + \int_{R-x}^Q \left(1 - \frac{A(x, R, a)}{A_x} \right) \frac{4\pi a^2}{\frac{4\pi}{3}Q^3} da \\ &= \frac{1}{2} - \frac{R^3}{2Q^3} + \frac{3R^4}{16Q^3x} - \frac{3R^2}{8Qx} + \frac{3Q}{16x} + \frac{3R^2x}{8Q^3} + \frac{3x}{8Q} - \frac{x^3}{16Q^3}. \end{aligned}$$

(c) $R > Q$ and $R < x < R + Q$: $x - R < Q$. If $a < x - R$, all neighbors of point 1 are outside the sphere with radius R . We have,

$$\begin{aligned} E(x, Q, R) &= \left[\frac{\frac{4\pi}{3}(x-R)^3}{\frac{4\pi}{3}Q^3} \right] (1) + \int_{x-R}^Q \left(1 - \frac{A(x, R, a)}{A_x} \right) \frac{4\pi a^2}{\frac{4\pi}{3}Q^3} da \\ &= \frac{1}{2} - \frac{R^3}{2Q^3} + \frac{3R^4}{16Q^3x} - \frac{3R^2}{8Qx} + \frac{3Q}{16x} + \frac{3R^2x}{8Q^3} + \frac{3x}{8Q} - \frac{x^3}{16Q^3}. \end{aligned}$$

(d) $R + Q < x$: All neighbors of point 1 are outside the sphere of radius R , giving $E(x, Q, R) = 1$.

(e) $Q > R$, $x < Q - R$ and $x < R$: $R - x > 0$ and $x + R < Q$. If $a < R - x$, all neighbors of point 1 are inside the sphere of radius R . If $a > R + x$, all neighbors of point 1 are inside the sphere with radius R . We have,

$$E(x, Q, R) = \left[\frac{\frac{4\pi}{3}(R-x)^3}{\frac{4\pi}{3}Q^3} \right] (0) + \int_{R-x}^{x+R} \left(1 - \frac{A(x, R, a)}{A_x} \right) \frac{4\pi a^2}{\frac{4\pi}{3}Q^3} da + \left[\frac{\frac{4\pi}{3}(R+x)^3}{\frac{4\pi}{3}Q^3} \right] (1) = 1 - \frac{R^3}{Q^3}.$$

(f) $Q > R$, $x < Q - R$ and $R < x < Q + R$: $x - R > 0$ and $x + R < Q$. If $a < x - R$, all neighbors of point 1 are outside the sphere of radius R . If $a > R + x$, all neighbors of point 1 are inside the sphere with radius R .

We have,

$$E(x, Q, R) = \left[\frac{\frac{4\pi}{3}(x-R)^3}{\frac{4\pi}{3}Q^3} \right] (1) + \int_{x-R}^{x+R} \left(1 - \frac{A(x, R, a)}{A_x} \right) \frac{4\pi a^2}{\frac{4\pi}{3}Q^3} da + \left[\frac{\frac{4\pi}{3}(R+x)^3}{\frac{4\pi}{3}Q^3} \right] (1) = 1 - \frac{R^3}{Q^3}.$$

(g) $Q > R$, $x > Q - R$ and $x < R$: $R - x > 0$. If $a < R - x$, all neighbors of point 1 are inside the sphere of radius R . We have,

$$\begin{aligned} E(x, Q, R) &= \left[\frac{\frac{4\pi}{3}(R-x)^3}{\frac{4\pi}{3}Q^3} \right] (0) + \int_{R-x}^Q \left(1 - \frac{A(x, R, a)}{A_x} \right) \frac{4\pi a^2}{\frac{4\pi}{3}Q^3} da \\ &= \frac{1}{2} - \frac{R^3}{2Q^3} + \frac{3R^4}{16Q^3x} - \frac{3R^2}{8Qx} + \frac{3Q}{16x} + \frac{3R^2x}{8Q^3} + \frac{3x}{8Q} - \frac{x^3}{16Q^3}. \end{aligned}$$

(h) $Q > R$, $x > Q - R$ and $R < x < Q + R$: $x - R > 0$. If $a < x - R$, all neighbors of point 1 are outside the sphere of radius R . We have,

$$\begin{aligned} E(x, Q, R) &= \left[\frac{\frac{4\pi}{3}(x-R)^3}{\frac{4\pi}{3}Q^3} \right] (1) + \int_{x-R}^Q \left(1 - \frac{A(x, R, a)}{A_x} \right) \frac{4\pi a^2}{\frac{4\pi}{3}Q^3} da \\ &= \frac{1}{2} - \frac{R^3}{2Q^3} + \frac{3R^4}{16Q^3x} - \frac{3R^2}{8Qx} + \frac{3Q}{16x} + \frac{3R^2x}{8Q^3} + \frac{3x}{8Q} - \frac{x^3}{16Q^3}. \end{aligned}$$

Putting all cases together, we get,

$$E(x, Q, R) = \begin{cases} 0 & x < R - Q \\ 1 - \frac{R^3}{Q^3} & R - Q < x < Q - R \\ \frac{1}{2} - \frac{R^3}{2Q^3} + \frac{3R^4}{16Q^3x} - \frac{3R^2}{8Qx} + \frac{3Q}{16x} + \frac{3R^2x}{8Q^3} + \frac{3x}{8Q} - \frac{x^3}{16Q^3} & |R - Q| < x < R + Q \\ 1 & x > R + Q. \end{cases} \quad (\text{F.6})$$

Also note that,

$$1 - E(x, Q, R) = \frac{V(x, Q, R)}{V_Q}. \quad (\text{F.7})$$

F.3 $C(x, P, Q, R)$

If point 1 is located between distance P and Q from the centre of a sphere ($Q > P$), then $C(x, P, Q, R)$ is the probability that its neighbour at distance x (point 2) is located outside the concentric sphere of radius R . We take a to be the distance of point 1 from the centre of the sphere.

(a) $x \leq R - Q$: None of the neighbours of point 1 are outside the sphere of radius R (Figure F.4), giving $C(x, P, Q, R) = 0$.

(b) $x \leq P - R$: All of the neighbours of point 1 are outside the sphere of radius R (Figure F.5), giving

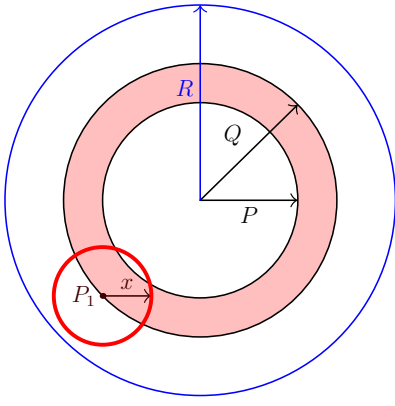


Figure F.4: Case a: $x \leq R - Q$

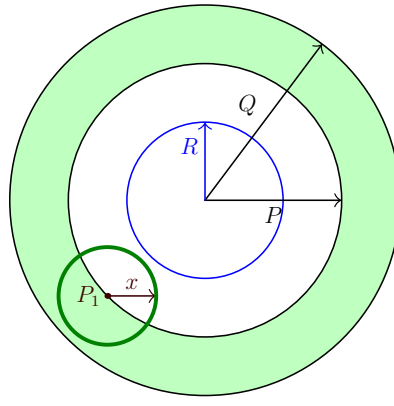


Figure F.5: Case b: $x \leq P - R$

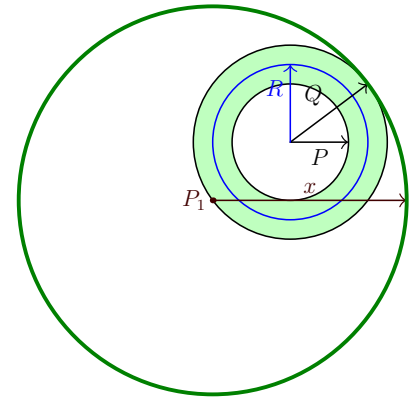


Figure F.6: Case c: $x \geq R + Q$

$$C(x, P, Q, R) = 1.$$

(c) $x \geq R + Q$: All of the neighbours of point 1 are outside the sphere of radius R (Figure F.6), giving $C(x, P, Q, R) = 1$.

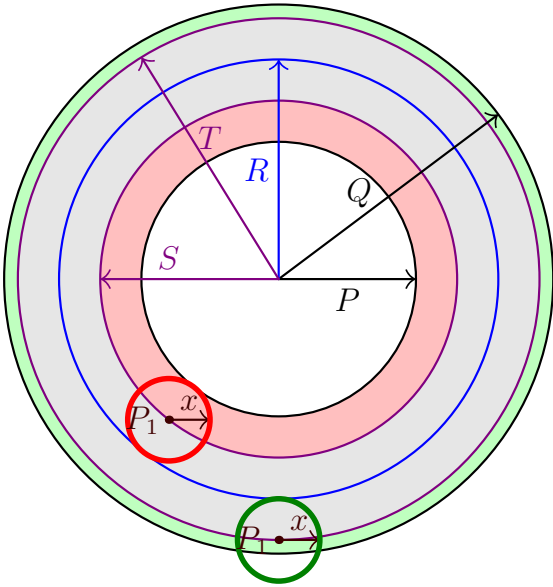


Figure F.7: Case d.a: $R - Q \leq x \leq R - P$,
 $x \leq Q - R$

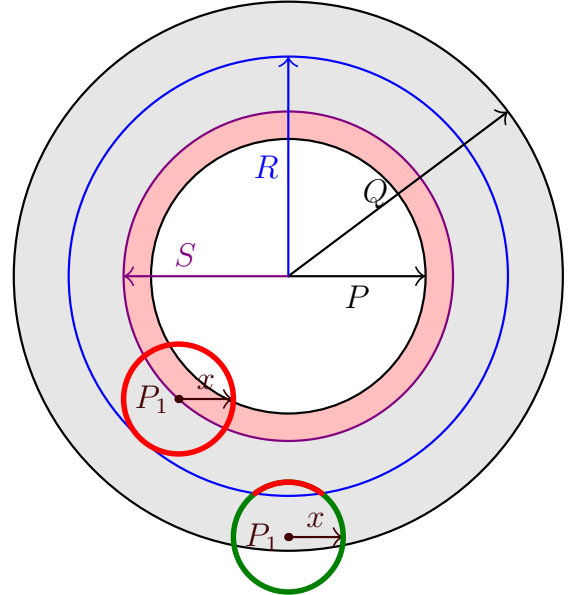


Figure F.8: Case d.b: $R - Q \leq x \leq R - P$,
 $x \geq Q - R$

(d) $R - Q \leq x \leq R - P$: Taking $S = R - x$, we can see that all the neighbours of the points between distance P and S (the red shaded area in Figure F.7 and Figure F.8) are inside the sphere of radius R . Therefore we have,

$$C(x, P, Q, R) = \left[\frac{4\pi}{3}(S^3 - P^3) \right] (0) + \int_S^Q \left(1 - \frac{A(x, R, a)}{A_x} \right) \frac{4\pi a^2}{3(Q^3 - P^3)} da.$$

(d.a) If $x \leq Q - R$: Taking $T = x + R$, we see that all neighbours of points between distance T and Q (the

green shaded area in Figure F.7) are outside the sphere of radius R . Therefore,

$$\begin{aligned} C(x, P, Q, R) &= \int_S^T \left(1 - \frac{A(x, R, a)}{A_x}\right) \frac{4\pi a^2}{\frac{4\pi}{3}(Q^3 - P^3)} da + \int_T^Q \left(1 - \frac{0}{A_x}\right) \frac{4\pi a^2}{\frac{4\pi}{3}(Q^3 - P^3)} da \\ &= \frac{1}{2} \frac{T^3 - S^3}{Q^3 - P^3} + \frac{3}{8x} \frac{T^2 - S^2}{Q^3 - P^3} \left[\frac{T^2 + S^2}{2} + (x^2 - R^2) \right] + \frac{Q^3 - T^3}{Q^3 - P^3} \\ &= \frac{Q^3 - R^3}{Q^3 - P^3}. \end{aligned}$$

(d.b) Otherwise (Figure F.8),

$$\begin{aligned} C(x, P, Q, R) &= \frac{1}{2} \frac{Q^3 - S^3}{Q^3 - P^3} + \frac{3}{8x} \frac{Q^2 - S^2}{Q^3 - P^3} \left[\frac{Q^2 + S^2}{2} + (x^2 - R^2) \right] \\ &= \frac{1}{2} \frac{Q^3 - (R-x)^3}{Q^3 - P^3} + \frac{3}{8x} \frac{Q^2 - (R-x)^2}{Q^3 - P^3} \left[\frac{Q^2 + (R-x)^2}{2} + (x^2 - R^2) \right]. \end{aligned}$$

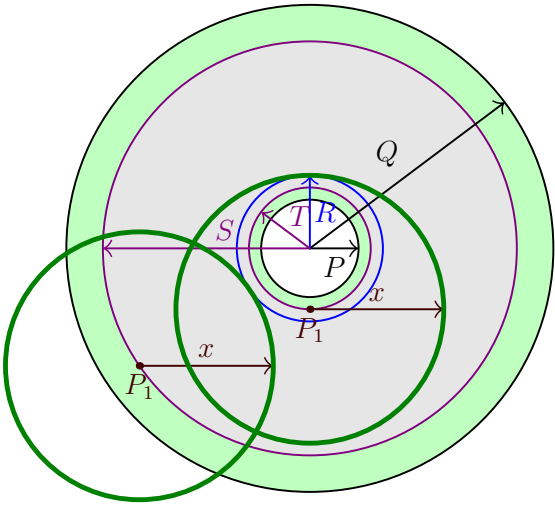


Figure F.9: Case e.a: $P - R \leq x \leq Q - R$, $x \geq P + R$

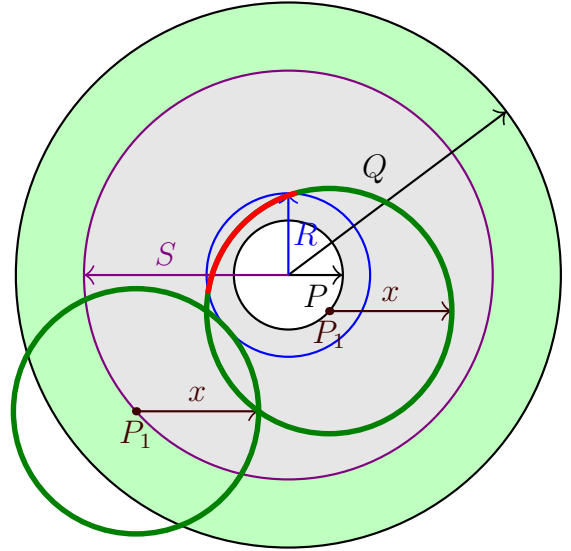


Figure F.10: Case e.b: $P - R \leq x \leq Q - R$, $x \leq P + R$

(e) $P - R \leq x \leq Q - R$: Taking $S = R + x$, we can see that all the neighbours of the points between distance S and Q (the larger green shaded area in Figure F.9 and Figure F.10) are outside the sphere of radius R . Therefore we have,

$$C(x, P, Q, R) = \left[\frac{4\pi}{3}(Q^3 - S^3) \right] (1) + \int_P^S \left(1 - \frac{A(x, R, a)}{A_x}\right) \frac{4\pi a^2}{\frac{4\pi}{3}(Q^3 - P^3)} da.$$

(e.a) If $x \geq P + R$: $T = x - R$, we can see that all the neighbours of the points between distance P and Q (the smaller green shaded area in Figure F.9) are outside the sphere of radius R . Therefore we have,

$$C(x, P, Q, R) = \left[\frac{4\pi}{3}(Q^3 - S^3) \right] (1) + \int_P^T \left(1 - \frac{0}{A_x}\right) \frac{4\pi a^2}{\frac{4\pi}{3}(Q^3 - P^3)} da + \int_T^S \left(1 - \frac{A(x, R, a)}{A_x}\right) \frac{4\pi a^2}{\frac{4\pi}{3}(Q^3 - P^3)} da$$

$$= 1 - \frac{R^3}{Q^3 - P^3}.$$

(e.b) For $x \leq P + R$, there are two probabilities. If $x < R - P$, we are left with the case **(d.b)** (Figure F.8). Otherwise (Figure F.10),

$$\begin{aligned} C(x, P, Q, R) &= \frac{Q^3 - S^3}{Q^3 - P^3} + \frac{1}{2} \frac{S^3 - P^3}{Q^3 - P^3} + \frac{3}{8x} \frac{S^2 - P^2}{Q^3 - P^3} \left[\frac{S^2 + P^2}{2} + (x^2 - R^2) \right] \\ &= \frac{Q^3 - (R+x)^3/2 - P^3/2}{Q^3 - P^3} + \frac{3}{8x} \frac{(R+x)^2 - P^2}{Q^3 - P^3} \left[\frac{(R+x)^2 + P^2}{2} + (x^2 - R^2) \right] \end{aligned}$$

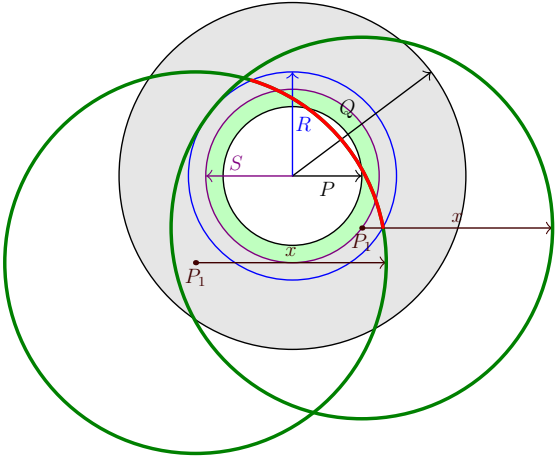


Figure F.11: Case f.b: $R + P \leq x \leq R + Q$,
 $x \geq Q - R$

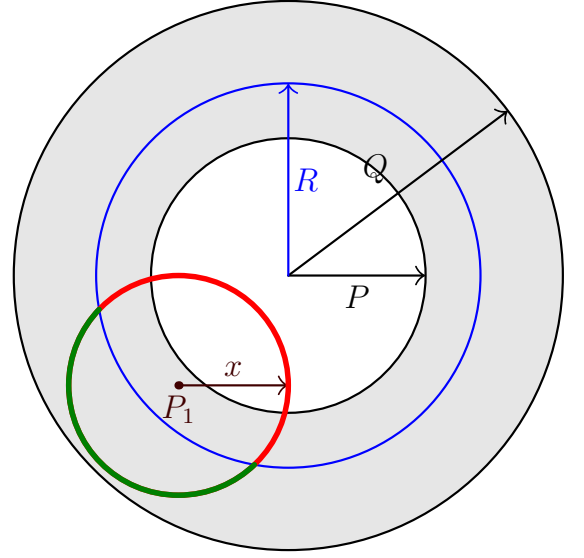


Figure F.12: Case g: $x \geq Q - R$, $x \geq R - P$,
 $x \leq P + R$

(f) $R + P \leq x \leq R + Q$: Taking $S = x - R$, we can see that all the neighbours of the points between distance S and P (the green shaded area in Figure F.11 and the smaller green shaded area in Figure F.9) are outside the sphere of radius R . Therefore we have,

$$C(x, P, Q, R) = \left[\frac{\frac{4\pi}{3}(S^3 - P^3)}{\frac{4\pi}{3}(Q^3 - P^3)} \right] (1) + \int_S^Q \left(1 - \frac{A(x, R, a)}{A_x} \right) \frac{4\pi a^2}{\frac{4\pi}{3}(Q^3 - P^3)} da.$$

(f.a) If $x \leq Q - R$: Taking $T = x + R$, we can see that all the neighbours of the points between distance T and Q (the larger green shaded area in Figure F.9) are outside the sphere of radius R . This is the same case as **(e.a)** (Figure F.9) (with T and S exchanged). Therefore we have,

$$C(x, P, Q, R) = 1 - \frac{R^3}{Q^3 - P^3}.$$

(f.b) Otherwise (Figure F.11),

$$C(x, P, Q, R) = \frac{S^3 - P^3}{Q^3 - P^3} + \frac{1}{2} \frac{Q^3 - S^3}{Q^3 - P^3} + \frac{3}{8x} \frac{Q^2 - S^2}{Q^3 - P^3} \left[\frac{Q^2 + S^2}{2} + (x^2 - R^2) \right]$$

$$= \frac{(x-R)^3 - P^3}{Q^3 - P^3} + \frac{1}{2} \frac{Q^3 - (x-R)^3}{Q^3 - P^3} + \frac{3}{8x} \frac{Q^2 - (x-R)^2}{Q^3 - P^3} \left[\frac{Q^2 + (x-R)^2}{2} + (x^2 - R^2) \right].$$

(g) For the last case, when $x \geq Q - R$, $x \geq R - P$, $x \leq P + R$ (Figure F.12), we have

$$\begin{aligned} C(x, P, Q, R) &= \int_P^Q \left(1 - \frac{A(x, R, a)}{A_x} \right) \frac{4\pi a^2}{\frac{4\pi}{3}(Q^3 - P^3)} da \\ &= \frac{1}{2} + \frac{3}{8x} \frac{P+Q}{P^2 + PQ + Q^2} \left[\frac{P^2 + Q^2}{2} + (x^2 - R^2) \right]. \end{aligned}$$

$$C(x, P, Q, R) = \begin{cases} 0 & x \leq R - Q \\ 1 & x \leq P - R \\ 1 & x \geq R + Q \\ \frac{1}{2} \frac{Q^3 - (R-x)^3}{Q^3 - P^3} + \frac{3}{8x} \frac{Q^2 - (R-x)^2}{Q^3 - P^3} \left[\frac{Q^2 + (R-x)^2}{2} + (x^2 - R^2) \right] & R - Q \leq x \leq R - P, x > Q - R \\ \frac{Q^3 - R^3}{Q^3 - P^3} & R - Q \leq x \leq R - P, x \leq Q - R \\ \frac{1}{2} \frac{2Q^3 - (R+x)^3 - P^3}{Q^3 - P^3} + \frac{3}{8x} \frac{(R+x)^2 - P^2}{Q^3 - P^3} \left[\frac{(R+x)^2 + P^2}{2} + (x^2 - R^2) \right] & |P - R| \leq x \leq Q - R, x < P + R \\ \frac{1 - \frac{R^3}{Q^3 - P^3}}{Q^3 - P^3} & P + R \leq x \leq Q - R, \\ \frac{1}{2} \frac{(x-R)^3 + Q^3 - 2P^3}{Q^3 - P^3} + \frac{3}{8x} \frac{Q^2 - (x-R)^2}{Q^3 - P^3} \left[\frac{Q^2 + (x-R)^2}{2} + (x^2 - R^2) \right] & R + P \leq x \leq R + Q, x > Q - R \\ \frac{1}{2} + \frac{3}{8x} \frac{P+Q}{P^2 + PQ + Q^2} \left[\frac{P^2 + Q^2}{2} + (x^2 - R^2) \right] & R - P \leq x \leq P + R, x \geq Q - R \end{cases} \quad (\text{F.8})$$

We note that $C(x, P, Q, R)$ always appear as $(Q^3 - P^3)C(r, P, Q, R)$ in Chapter 4, where the first term $(Q^3 - P^3)$ cancels out the denominator from above equation. We note that $D(x, R)$, $E(x, P, R)$ and $C(x, P, Q, R)$ are functions with values between 0 and 1:

$$D(x, R) = E(x, R, R) = C(x, 0, R, R) \quad (\text{F.9})$$

$$E(x, Q, R) = C(x, 0, Q, R). \quad (\text{F.10})$$

We can also write,

$$\begin{aligned} 1 - C(x, P, Q, R) &= \int_P^Q \frac{4\pi a^2 da}{\frac{4\pi}{3}(Q^3 - P^3)} \left(\frac{A(x, R, a)}{A_x} \right) \\ &= \frac{V(x, Q, R) - (x, P, R)}{V_Q - V_P} \end{aligned} \quad (\text{F.11})$$

$$\frac{d}{dR} C(x, P, Q, R) = \frac{A(x, P, R) - A(x, Q, R)}{V_Q - V_P}.$$

$$(Q^3 - P^3)C(r, P, Q, y) + (R^3 - Q^3)C(r, Q, R, y) = (R^3 - P^3)C(r, P, R, y) \quad (\text{F.12})$$

$$Q^3 C(r, 0, Q, y) - P^3 C(r, 0, P, y) = (Q^3 - P^3)C(r, P, Q, y) \quad (\text{F.13})$$

$$P^3 E(r, P, Q) = Q^3 E(r, Q, P). \quad (\text{F.14})$$

Fourier Transform

Three dimensional Fourier transform of $1 - C(x, P, Q, R)$ is useful while calculating power spectrum:s

$$\begin{aligned} FT(1 - C(x, P, Q, R)) &= \int_0^\infty (1 - C(x, P, Q, R)) \frac{\sin(kr)}{kr} dx x^2 \\ &= \frac{12\pi([kQ \cos(kQ) - \sin(kQ)] - [kP \cos(kP) - \sin(kP)])[kR \cos(kR) - \sin(kR)]}{k^6(Q^3 - P^3)}. \end{aligned} \tag{F.15}$$

Bibliography

- K. Ahn, A. Mesinger, M. A. Alvarez, and X. Chen. Probing the First Galaxies and Their Impact on the Intergalactic Medium through 21-cm Observations of the Cosmic Dawn with the SKA. *Advancing Astrophysics with the Square Kilometre Array (AASKA14)*, art. 3, April 2015a. [94](#), [105](#), [106](#)
- K. Ahn, H. Xu, M. L. Norman, M. A. Alvarez, and J. H. Wise. Spatially Extended 21 cm Signal from Strongly Clustered UV and X-Ray Sources in the Early Universe. *ApJ*, 802:8, March 2015b. doi: 10.1088/0004-637X/802/1/8. [100](#)
- Z. S. Ali, A. R. Parsons, H. Zheng, J. C. Pober, A. Liu, J. E. Aguirre, R. F. Bradley, G. Bernardi, C. L. Carilli, C. Cheng, D. R. DeBoer, M. R. Dexter, J. Grobbelaar, J. Horrell, D. C. Jacobs, P. Klima, D. H. E. MacMahon, M. Maree, D. F. Moore, N. Razavi, I. I. Stefan, W. P. Walbrugh, and A. Walker. PAPER-64 Constraints on Reionization: The 21 cm Power Spectrum at $z = 8.4$. *ApJ*, 809:61, August 2015. doi: 10.1088/0004-637X/809/1/61. [106](#)
- S. Baek, B. Semelin, P. Di Matteo, Y. Revaz, and F. Combes. Reionization by UV or X-ray sources. *A&A*, 523:A4, November 2010. doi: 10.1051/0004-6361/201014347. [23](#), [94](#)
- R. Barkana. Possible interaction between baryons and dark-matter particles revealed by the first stars. *Nature*, 555:71–74, March 2018. doi: 10.1038/nature25791. [39](#), [97](#), [105](#)
- Rennan Barkana and Abraham Loeb. In the beginning: The First sources of light and the reionization of the Universe. *PhR*, 349:125–238, 2001. doi: 10.1016/S0370-1573(01)00019-9. [xvii](#), [7](#), [8](#), [9](#)
- A. P. Beardsley, B. J. Hazelton, I. S. Sullivan, P. Carroll, N. Barry, M. Rahimi, B. Pindor, C. M. Trott, J. Line, D. C. Jacobs, M. F. Morales, J. C. Pober, G. Bernardi, J. D. Bowman, M. P. Busch, F. Briggs, R. J. Cappallo, B. E. Corey, A. de Oliveira-Costa, J. S. Dillon, D. Emrich, A. Ewall-Wice, L. Feng, B. M. Gaensler, R. Goeke, L. J. Greenhill, J. N. Hewitt, N. Hurley-Walker, M. Johnston-Hollitt, D. L. Kaplan, J. C. Kasper, H. S. Kim, E. Kratzenberg, E. Lenc, A. Loeb, C. J. Lonsdale, M. J. Lynch, B. McKinley, S. R. McWhirter, D. A. Mitchell, E. Morgan, A. R. Neben, N. Thyagarajan, D. Oberoi, A. R. Offringa, S. M. Ord, S. Paul, T. Prabu, P. Procopio, J. Ridding, A. E. E. Rogers, A. Roshi, N. Udaya Shankar, S. K. Sethi, K. S. Srivani, R. Subrahmanyan, M. Tegmark, S. J. Tingay, M. Waterson, R. B. Wayth, R. L. Webster, A. R. Whitney, A. Williams, C. L. Williams, C. Wu, and J. S. B. Wyithe. First Season MWA EoR Power spectrum Results at Redshift 7. *ApJ*, 833:102, December 2016. doi: 10.3847/1538-4357/833/1/102. [106](#)

- R. H. Becker, X. Fan, R. L. White, M. A. Strauss, V. K. Narayanan, R. H. Lupton, J. E. Gunn, J. Annis, N. A. Bahcall, J. Brinkmann, A. J. Connolly, I. Csabai, P. C. Czarapata, M. Doi, T. M. Heckman, G. S. Hennessy, Ž. Ivezić, G. R. Knapp, D. Q. Lamb, T. A. McKay, J. A. Munn, T. Nash, R. Nichol, J. R. Pier, G. T. Richards, D. P. Schneider, C. Stoughton, A. S. Szalay, A. R. Thakar, and D. G. York. Evidence for Reionization at $z \sim 6$: Detection of a Gunn-Peterson Trough in a $z=6.28$ Quasar. *AJ*, 122:2850–2857, December 2001. doi: 10.1086/324231. [14](#), [16](#)
- A. Benson, A. Venkatesan, and J. M. Shull. The Escape Fraction of Ionizing Radiation from Galaxies. *ApJ*, 770:76, June 2013. doi: 10.1088/0004-637X/770/1/76. [11](#)
- G. Bernardi, M. McQuinn, and L. J. Greenhill. Foreground Model and Antenna Calibration Errors in the Measurement of the Sky-averaged $\lambda 21$ cm Signal at $z \sim 20$. *ApJ*, 799:90, January 2015. doi: 10.1088/0004-637X/799/1/90. [103](#), [104](#)
- G. Bernardi, J. T. L. Zwart, D. Price, L. J. Greenhill, A. Mesinger, J. Dowell, T. Eftekhari, S. W. Ellingson, J. Kocz, and F. Schinzel. Bayesian constraints on the global 21-cm signal from the Cosmic Dawn. *MNRAS*, 461:2847–2855, September 2016. doi: 10.1093/mnras/stw1499. [104](#)
- S. Bharadwaj and S. K. Sethi. HI Fluctuations at Large Redshifts: I–Visibility correlation. *Journal of Astrophysics and Astronomy*, 22:293–307, December 2001. doi: 10.1007/BF02702273. [105](#)
- G. R. Blumenthal, S. M. Faber, J. R. Primack, and M. J. Rees. Formation of galaxies and large-scale structure with cold dark matter. *Nature*, 311:517–525, October 1984. doi: 10.1038/311517a0. [2](#)
- A. M. Boesgaard and G. Steigman. Big bang nucleosynthesis - Theories and observations. *ARA&A*, 23: 319–378, 1985. doi: 10.1146/annurev.aa.23.090185.001535. [2](#)
- J. R. Bond, S. Cole, G. Efstathiou, and N. Kaiser. Excursion set mass functions for hierarchical Gaussian fluctuations. *ApJ*, 379:440–460, October 1991. doi: 10.1086/170520. [12](#)
- J. D. Bowman and A. E. E. Rogers. A lower limit of $\Delta z < 0.06$ for the duration of the reionization epoch. *Nature*, 468:796–798, December 2010. doi: 10.1038/nature09601. [105](#)
- J. D. Bowman, A. E. E. Rogers, R. A. Monsalve, T. J. Mozdzen, and N. Mahesh. An absorption profile centred at 78 megahertz in the sky-averaged spectrum. *Nature*, 555:67–70, March 2018. doi: 10.1038/nature25792. [17](#), [97](#), [105](#)
- J. O. Burns, R. Bradley, K. Tauscher, S. Furlanetto, J. Mirocha, R. Monsalve, D. Rapetti, W. Purcell, D. Newell, D. Draper, R. MacDowall, J. Bowman, B. Nhan, E. J. Wollack, A. Fialkov, D. Jones, J. C. Kasper, A. Loeb, A. Datta, J. Pritchard, E. Switzer, and M. Bica. A Space-based Observational Strategy for Characterizing the First Stars and Galaxies Using the Redshifted 21 cm Global Spectrum. *ApJ*, 844: 33, July 2017. doi: 10.3847/1538-4357/aa77f4. [104](#)
- J. E. Carlstrom, G. P. Holder, and E. D. Reese. Cosmology with the Sunyaev-Zel’dovich Effect. *ARA&A*, 40:643–680, 2002. doi: 10.1146/annurev.astro.40.060401.093803. [16](#)

- Renyue Cen. The Universe Was Reionized Twice. *ApJ*, 591:12–37, Jul 2003. doi: 10.1086/375217. [16](#)
- E. Chapman, A. Bonaldi, G. Harker, V. Jelic, F. B. Abdalla, G. Bernardi, J. Bobin, F. Dulwich, B. Mort, M. Santos, and J. L. Starck. Cosmic Dawn and Epoch of Reionization Foreground Removal with the SKA. In *Advancing Astrophysics with the Square Kilometre Array (AASKA14)*, page 5, Apr 2015. [103](#)
- X. Chen and J. Miralda-Escudé. The Spin-Kinetic Temperature Coupling and the Heating Rate due to Ly α Scattering before Reionization: Predictions for 21 Centimeter Emission and Absorption. *ApJ*, 602:1–11, February 2004. doi: 10.1086/380829. [18](#), [42](#), [43](#), [44](#)
- X. Chen and J. Miralda-Escudé. The 21 cm Signature of the First Stars. *ApJ*, 684:18-33, September 2008. doi: 10.1086/528941. [94](#)
- Carina Cheng, Aaron R. Parsons, Matthew Kolopanis, Daniel C. Jacobs, Adrian Liu, Saul A. Kohn, James E. Aguirre, Jonathan C. Pober, Zaki S. Ali, Gianni Bernardi, Richard F. Bradley, Chris L. Carilli, David R. DeBoer, Matthew R. Dexter, Joshua S. Dillon, Pat Klima, David H. E. MacMahon, David F. Moore, Chuneeta D. Nunhokee, William P. Walbrugh, and Andre Walker. Characterizing Signal Loss in the 21 cm Reionization Power Spectrum: A Revised Study of PAPER-64. *ApJ*, 868(1):26, Nov 2018. doi: 10.3847/1538-4357/aae833. [106](#)
- Tirthankar Roy Choudhury, Martin G. Haehnelt, and John Regan. Inside-out or outside-in: the topology of reionization in the photon-starved regime suggested by Ly α forest data. *MNRAS*, 394:960–977, Apr 2009. doi: 10.1111/j.1365-2966.2008.14383.x. [10](#)
- B. Ciardi and A. Ferrara. The First Cosmic Structures and Their Effects. *Space Sci. Rev.*, 116:625–705, February 2005. doi: 10.1007/s11214-005-3592-0. [9](#)
- A. Cohen, A. Fialkov, R. Barkana, and M. Lotem. Charting the parameter space of the global 21-cm signal. *MNRAS*, 472:1915–1931, December 2017. doi: 10.1093/mnras/stx2065. [89](#), [104](#)
- A. Datta, R. Bradley, J. O. Burns, G. Harker, A. Komjathy, and T. J. W. Lazio. The Effects of the Ionosphere on Ground-based Detection of the Global 21 cm Signal from the Cosmic Dawn and the Dark Ages. *ApJ*, 831:6, November 2016. doi: 10.3847/0004-637X/831/1/6. [104](#)
- P. Dayal and A. Ferrara. Early galaxy formation and its large-scale effects. *Phys. Rep.*, 780:1–64, December 2018. doi: 10.1016/j.physrep.2018.10.002. [8](#)
- D. R. DeBoer, A. R. Parsons, J. E. Aguirre, P. Alexander, Z. S. Ali, A. P. Beardsley, G. Bernardi, J. D. Bowman, R. F. Bradley, C. L. Carilli, C. Cheng, E. de Lera Acedo, J. S. Dillon, A. Ewall-Wice, G. Fadana, N. Fagnoni, R. Fritz, S. R. Furlanetto, B. Glendenning, B. Greig, J. Grobbelaar, B. J. Hazelton, J. N. Hewitt, J. Hickish, D. C. Jacobs, A. Julius, M. Kariseb, S. A. Kohn, T. Lekalake, A. Liu, A. Loots, D. MacMahon, L. Malan, C. Malgas, M. Maree, Z. Martinot, N. Mathison, E. Matsetela, A. Mesinger, M. F. Morales, A. R. Neben, N. Patra, S. Pieterse, J. C. Pober, N. Razavi-Ghods, J. Ringuette, J. Robnett, K. Rosie, R. Sell, C. Smith, A. Syce, M. Tegmark, N. Thyagarajan, P. K. G. Williams, and H. Zheng. Hydrogen Epoch of Reionization Array (HERA). *PASP*, 129(4):045001, April 2017. doi: 10.1088/1538-3873/129/974/045001. [106](#)

- R. H. Dicke, P. J. E. Peebles, P. G. Roll, and D. T. Wilkinson. Cosmic Black-Body Radiation. *ApJ*, 142: 414–419, July 1965. doi: 10.1086/148306. [1](#)
- M. Dijkstra. Constraining Reionization with Ly α Emitting Galaxies. In A. Mesinger, editor, *Understanding the Epoch of Cosmic Reionization: Challenges and Progress*, volume 423 of *Astrophysics and Space Science Library*, page 145, 2016. doi: 10.1007/978-3-319-21957-8_5. [14](#)
- M. Dijkstra, Z. Haiman, A. Mesinger, and J. S. B. Wyithe. Fluctuations in the high-redshift Lyman-Werner background: close halo pairs as the origin of supermassive black holes. *MNRAS*, 391:1961–1972, December 2008a. doi: 10.1111/j.1365-2966.2008.14031.x. [43](#)
- M. Dijkstra, A. Lidz, J. R. Pritchard, L. J. Greenhill, D. A. Mitchell, S. M. Ord, and R. B. Wayth. On the detectability of the hydrogen 3-cm fine-structure line from the epoch of reionization. *MNRAS*, 390: 1430–1436, November 2008b. doi: 10.1111/j.1365-2966.2008.13680.x. [17](#)
- S. Dodelson. *Modern Cosmology*. Academic Press, 2003. [3](#), [99](#)
- B. T. Draine and J. Miralda-Escudé. Absorption by Spinning Dust: A Contaminant for High-redshift 21 cm Observations. *ApJ*, 858:L10, May 2018. doi: 10.3847/2041-8213/aac08a. [105](#)
- R. S. Ellis, R. J. McLure, J. S. Dunlop, B. E. Robertson, Y. Ono, M. A. Schenker, A. Koekemoer, R. A. A. Bowler, M. Ouchi, A. B. Rogers, E. Curtis-Lake, E. Schneider, S. Charlot, D. P. Stark, S. R. Furlanetto, and M. Cirasuolo. The Abundance of Star-forming Galaxies in the Redshift Range 8.5-12: New Results from the 2012 Hubble Ultra Deep Field Campaign. *ApJ*, 763:L7, January 2013. doi: 10.1088/2041-8205/763/1/L7. [17](#)
- A. Ewall-Wice, J. S. Dillon, J. N. Hewitt, A. Loeb, A. Mesinger, A. R. Neben, A. R. Offringa, M. Tegmark, N. Barry, A. P. Beardsley, G. Bernardi, J. D. Bowman, F. Briggs, R. J. Cappallo, P. Carroll, B. E. Corey, A. de Oliveira-Costa, D. Emrich, L. Feng, B. M. Gaensler, R. Goeke, L. J. Greenhill, B. J. Hazelton, N. Hurley-Walker, M. Johnston-Hollitt, D. C. Jacobs, D. L. Kaplan, J. C. Kasper, H. Kim, E. Kratzenberg, E. Lenc, J. Line, C. J. Lonsdale, M. J. Lynch, B. McKinley, S. R. McWhirter, D. A. Mitchell, M. F. Morales, E. Morgan, N. Thyagarajan, D. Oberoi, S. M. Ord, S. Paul, B. Pindor, J. C. Pober, T. Prabu, P. Procopio, J. Riding, A. E. E. Rogers, A. Roshi, N. U. Shankar, S. K. Sethi, K. S. Srivani, R. Subrahmanyan, I. S. Sullivan, S. J. Tingay, C. M. Trott, M. Waterson, R. B. Wayth, R. L. Webster, A. R. Whitney, A. Williams, C. L. Williams, C. Wu, and J. S. B. Wyithe. First limits on the 21 cm power spectrum during the Epoch of X-ray heating. *MNRAS*, 460:4320–4347, August 2016. doi: 10.1093/mnras/stw1022. [106](#)
- A. Ewall-Wice, T.-C. Chang, J. Lazio, O. Doré, M. Seiffert, and R. A. Monsalve. Modeling the Radio Background from the First Black Holes at Cosmic Dawn: Implications for the 21 cm Absorption Amplitude. *ApJ*, 868:63, November 2018. doi: 10.3847/1538-4357/aae51d. [20](#), [98](#), [105](#)
- H. I. Ewen and E. M. Purcell. Observation of a Line in the Galactic Radio Spectrum: Radiation from Galactic Hydrogen at 1,420 Mc./sec. *Nature*, 168:356, September 1951. doi: 10.1038/168356a0. [17](#)

- X. Fan, R. L. White, M. Davis, R. H. Becker, M. A. Strauss, Z. Haiman, D. P. Schneider, M. D. Gregg, J. E. Gunn, G. R. Knapp, R. H. Lupton, J. E. Anderson, Jr., S. F. Anderson, J. Annis, N. A. Bahcall, W. N. Boroski, R. J. Brunner, B. Chen, A. J. Connolly, I. Csabai, M. Doi, M. Fukugita, G. S. Hennessy, R. B. Hindsley, T. Ichikawa, Ž. Ivezić, J. Loveday, A. Meiksin, T. A. McKay, J. A. Munn, H. J. Newberg, R. Nichol, S. Okamura, J. R. Pier, M. Sekiguchi, K. Shimasaku, C. Stoughton, A. S. Szalay, G. P. Szokoly, A. R. Thakar, M. S. Vogeley, and D. G. York. The Discovery of a Luminous $Z=5.80$ Quasar from the Sloan Digital Sky Survey. *AJ*, 120:1167–1174, September 2000. doi: 10.1086/301534. [16](#)
- X. Fan, C. L. Carilli, and B. Keating. Observational Constraints on Cosmic Reionization. *ARA&A*, 44: 415–462, September 2006a. doi: 10.1146/annurev.astro.44.051905.092514. [14](#)
- X. Fan, M. A. Strauss, R. H. Becker, R. L. White, J. E. Gunn, G. R. Knapp, G. T. Richards, D. P. Schneider, J. Brinkmann, and M. Fukugita. Constraining the Evolution of the Ionizing Background and the Epoch of Reionization with $z \sim 6$ Quasars. II. A Sample of 19 Quasars. *AJ*, 132:117–136, July 2006b. doi: 10.1086/504836. [xvii](#), [14](#), [15](#)
- C. Feng and G. Holder. Enhanced Global Signal of Neutral Hydrogen Due to Excess Radiation at Cosmic Dawn. *ApJ*, 858:L17, May 2018. doi: 10.3847/2041-8213/aac0fe. [20](#), [98](#)
- A. Fialkov, R. Barkana, and E. Visbal. The observable signature of late heating of the Universe during cosmic reionization. *Nature*, 506:197–199, February 2014. doi: 10.1038/nature12999. [23](#), [25](#), [34](#), [88](#), [89](#), [92](#), [94](#), [100](#)
- A. Fialkov, R. Barkana, and A. Cohen. Reconstructing the Nature of the First Cosmic Sources from the Anisotropic 21-cm Signal. *Physical Review Letters*, 114(10):101303, March 2015. doi: 10.1103/PhysRevLett.114.101303. [23](#)
- A. Fialkov, A. Cohen, R. Barkana, and J. Silk. Constraining the redshifted 21-cm signal with the unresolved soft X-ray background. *MNRAS*, 464:3498–3508, January 2017. doi: 10.1093/mnras/stw2540. [23](#), [94](#), [96](#)
- A. Fialkov, R. Barkana, and A. Cohen. Constraining Baryon-Dark-Matter Scattering with the Cosmic Dawn 21-cm Signal. *Physical Review Letters*, 121(1):011101, July 2018. doi: 10.1103/PhysRevLett.121.011101. [39](#), [97](#), [98](#), [105](#)
- G. B. Field. Excitation of the Hydrogen 21-CM Line. *Proceedings of the IRE*, 46:240–250, January 1958. doi: 10.1109/JRPROC.1958.286741. [xvii](#), [18](#), [46](#), [47](#), [101](#)
- G. B. Field. The Time Relaxation of a Resonance-Line Profile. *ApJ*, 129:551, May 1959. doi: 10.1086/146654. [18](#), [42](#)
- G. B. Field. Absorption by Intergalactic Hydrogen. *ApJ*, 135:684–693, May 1962. doi: 10.1086/147312. [14](#)

- S. Fraser, A. Hektor, G. Hütsi, K. Kannike, C. Marzo, L. Marzola, A. Racioppi, M. Raidal, C. Spethmann, V. Vaskonen, and H. Veermäe. The EDGES 21 cm anomaly and properties of dark matter. *Physics Letters B*, 785:159–164, October 2018. doi: 10.1016/j.physletb.2018.08.035. [39](#)
- S. R. Furlanetto. The global 21-centimeter background from high redshifts. *MNRAS*, 371:867–878, September 2006. doi: 10.1111/j.1365-2966.2006.10725.x. [100](#)
- S. R. Furlanetto and S. P. Oh. Reionization through the lens of percolation theory. *MNRAS*, 457:1813–1827, April 2016. doi: 10.1093/mnras/stw104. [99](#)
- S. R. Furlanetto, M. Zaldarriaga, and L. Hernquist. The Growth of H II Regions During Reionization. *ApJ*, 613:1–15, September 2004. doi: 10.1086/423025. [11](#), [13](#), [101](#)
- S. R. Furlanetto, S. P. Oh, and F. H. Briggs. Cosmology at low frequencies: The 21 cm transition and the high-redshift Universe. *Phys. Rep.*, 433:181–301, October 2006. doi: 10.1016/j.physrep.2006.08.002. [17](#), [28](#), [89](#)
- R. Ghara, T. R. Choudhury, and K. K. Datta. 21 cm signal from cosmic dawn: imprints of spin temperature fluctuations and peculiar velocities. *MNRAS*, 447:1806–1825, February 2015. doi: 10.1093/mnras/stu2512. [23](#), [34](#), [94](#), [96](#), [101](#)
- S. K. Giri, G. Mellema, K. L. Dixon, and I. T. Iliev. Bubble size statistics during reionization from 21-cm tomography. *MNRAS*, 473:2949–2964, January 2018. doi: 10.1093/mnras/stx2539. [99](#)
- N. Y. Gnedin and P. A. Shaver. Redshifted 21 Centimeter Emission from the Pre-Reionization Era. I. Mean Signal and Linear Fluctuations. *ApJ*, 608:611–621, June 2004. doi: 10.1086/420735. [22](#), [103](#)
- Nickolay Y. Gnedin, Andrey V. Kravtsov, and Hsiao-Wen Chen. Escape of Ionizing Radiation from High-Redshift Galaxies. *ApJ*, 672(2):765–775, Jan 2008. doi: 10.1086/524007. [11](#)
- J. E. Gunn and B. A. Peterson. On the Density of Neutral Hydrogen in Intergalactic Space. *ApJ*, 142:1633–1641, November 1965. doi: 10.1086/148444. [14](#)
- Z. Haiman, M. J. Rees, and A. Loeb. Destruction of Molecular Hydrogen during Cosmological Reionization. *ApJ*, 476:458–463, February 1997. doi: 10.1086/303647. [9](#)
- Z. Haiman, T. Abel, and M. J. Rees. The Radiative Feedback of the First Cosmological Objects. *ApJ*, 534:11–24, May 2000. doi: 10.1086/308723. [9](#)
- G. Harker, S. Zaroubi, G. Bernardi, M. A. Brentjens, A. G. de Bruyn, B. Ciardi, V. Jelić, L. V. E. Koopmans, P. Labropoulos, G. Mellema, A. Offringa, V. N. Pandey, J. Schaye, R. M. Thomas, and S. Yatawatta. Non-parametric foreground subtraction for 21-cm epoch of reionization experiments. *MNRAS*, 397:1138–1152, August 2009. doi: 10.1111/j.1365-2966.2009.15081.x. [103](#), [104](#)
- R. Hills, G. Kulkarni, P. D. Meerburg, and E. Puchwein. Concerns about Modelling of Foregrounds and the 21-cm Signal in EDGES data. *ArXiv e-prints*, May 2018. [105](#)

- G. Hinshaw, D. Larson, E. Komatsu, D. N. Spergel, C. L. Bennett, J. Dunkley, M. R. Nolta, M. Halpern, R. S. Hill, N. Odegard, L. Page, K. M. Smith, J. L. Weiland, B. Gold, N. Jarosik, A. Kogut, M. Limon, S. S. Meyer, G. S. Tucker, E. Wollack, and E. L. Wright. Nine-year Wilkinson Microwave Anisotropy Probe (WMAP) Observations: Cosmological Parameter Results. *ApJS*, 208:19, October 2013. doi: 10.1088/0067-0049/208/2/19. [1](#), [16](#)
- C. M. Hirata. Wouthuysen-Field coupling strength and application to high-redshift 21-cm radiation. *MNRAS*, 367:259–274, March 2006. doi: 10.1111/j.1365-2966.2005.09949.x. [44](#)
- W. Hu and M. White. A CMB polarization primer. *New A*, 2:323–344, October 1997. doi: 10.1016/S1384-1076(97)00022-5. [16](#)
- H. Jensen, P. Laursen, G. Mellema, I. T. Iliev, J. Sommer-Larsen, and P. R. Shapiro. On the use of Ly α emitters as probes of reionization. *MNRAS*, 428:1366–1381, January 2013. doi: 10.1093/mnras/sts116. [14](#)
- H.-S. Kim, J. S. B. Wyithe, J. Park, and C. G. Lacey. Variation in the escape fraction of ionizing photons from galaxies and the redshifted 21-cm power spectrum during reionization. *MNRAS*, 433:2476–2484, August 2013. doi: 10.1093/mnras/stt918. [11](#)
- E. W. Kolb and M. S. Turner. *The early universe*. 1990. [2](#)
- L. Koopmans, J. Pritchard, G. Mellema, J. Aguirre, K. Ahn, R. Barkana, I. van Bemmell, G. Bernardi, A. Bonaldi, F. Briggs, A. G. de Bruyn, T. C. Chang, E. Chapman, X. Chen, B. Ciardi, P. Dayal, A. Ferrara, A. Fialkov, F. Fiore, K. Ichiki, I. T. Iliev, S. Inoue, V. Jelic, M. Jones, J. Lazio, U. Maio, S. Majumdar, K. J. Mack, A. Mesinger, M. F. Morales, A. Parsons, U. L. Pen, M. Santos, R. Schneider, B. Semelin, R. S. de Souza, R. Subrahmanyam, T. Takeuchi, H. Vedantham, J. Wagg, R. Webster, S. Wyithe, K. K. Datta, and C. Trott. The Cosmic Dawn and Epoch of Reionisation with SKA. *Advancing Astrophysics with the Square Kilometre Array (AASKA14)*, art. 1, April 2015. [106](#)
- C. Lacey and S. Cole. Merger Rates in Hierarchical Models of Galaxy Formation - Part Two - Comparison with N-Body Simulations. *MNRAS*, 271:676, December 1994. doi: 10.1093/mnras/271.3.676. [12](#)
- A. Loeb and R. Barkana. The Reionization of the Universe by the First Stars and Quasars. *ARA&A*, 39: 19–66, 2001. doi: 10.1146/annurev.astro.39.1.19. [9](#)
- P. Madau, A. Meiksin, and M. J. Rees. 21 Centimeter Tomography of the Intergalactic Medium at High Redshift. *ApJ*, 475:429–444, February 1997. doi: 10.1086/303549. [22](#), [103](#)
- N. Mahesh, R. Subrahmanyam, N. Udaya Shankar, and A. Raghunathan. A wideband resistive beam-splitter screen. *Antennas and Propagation, IEEE Transactions on*, 63(11):4835–4847, Nov 2015. ISSN 0018-926X. doi: 10.1109/TAP.2015.2478443. [105](#)
- S. Malhotra and J. E. Rhoads. Luminosity Functions of Ly α Emitters at Redshifts $z=6.5$ and $z=5.7$: Evidence against Reionization at $z\leq 6.5$. *ApJ*, 617:L5–L8, December 2004. doi: 10.1086/427182. [14](#)

- J. C. Mather, E. S. Cheng, R. E. Eplee, Jr., R. B. Isaacman, S. S. Meyer, R. A. Shafer, R. Weiss, E. L. Wright, C. L. Bennett, N. W. Boggess, E. Dwek, S. Gulkis, M. G. Hauser, M. Janssen, T. Kelsall, P. M. Lubin, S. H. Moseley, Jr., T. L. Murdock, R. F. Silverberg, G. F. Smoot, and D. T. Wilkinson. A preliminary measurement of the cosmic microwave background spectrum by the Cosmic Background Explorer (COBE) satellite. *ApJ*, 354:L37–L40, May 1990. doi: 10.1086/185717. [1](#)
- B. McKinley, G. Bernardi, C. M. Trott, J. L. B. Line, R. B. Wayth, A. R. Offringa, B. Pindor, C. H. Jordan, M. Sokolowski, S. J. Tingay, E. Lenc, N. Hurley-Walker, J. D. Bowman, F. Briggs, and R. L. Webster. Measuring the global 21-cm signal with the MWA-I: improved measurements of the Galactic synchrotron background using lunar occultation. *MNRAS*, 481(4):5034–5045, Dec 2018. doi: 10.1093/mnras/sty2437. [105](#)
- M. McQuinn, S. R. Furlanetto, L. Hernquist, O. Zahn, and M. Zaldarriaga. The Kinetic Sunyaev-Zel’dovich Effect from Reionization. *ApJ*, 630:643–656, September 2005. doi: 10.1086/432049. [16](#)
- M. McQuinn, O. Zahn, M. Zaldarriaga, L. Hernquist, and S. R. Furlanetto. Cosmological Parameter Estimation Using 21 cm Radiation from the Epoch of Reionization. *ApJ*, 653:815–834, December 2006. doi: 10.1086/505167. [101](#)
- M. McQuinn, A. Lidz, O. Zahn, S. Dutta, L. Hernquist, and M. Zaldarriaga. The morphology of HII regions during reionization. *MNRAS*, 377:1043–1063, May 2007. doi: 10.1111/j.1365-2966.2007.11489.x. [10](#)
- A. A. Meiksin. The physics of the intergalactic medium. *Reviews of Modern Physics*, 81:1405–1469, October 2009. doi: 10.1103/RevModPhys.81.1405. [17](#)
- A. Mesinger, S. Furlanetto, and R. Cen. 21CMFAST: a fast, seminumerical simulation of the high-redshift 21-cm signal. *MNRAS*, 411:955–972, February 2011. doi: 10.1111/j.1365-2966.2010.17731.x. [13](#), [23](#), [25](#), [100](#), [101](#)
- A. Mesinger, A. Ferrara, and D. S. Spiegel. Signatures of X-rays in the early Universe. *MNRAS*, 431:621–637, May 2013. doi: 10.1093/mnras/stt198. [23](#), [93](#), [94](#), [96](#)
- A. Mesinger, A. Ewall-Wice, and J. Hewitt. Reionization and beyond: detecting the peaks of the cosmological 21 cm signal. *MNRAS*, 439:3262–3274, April 2014. doi: 10.1093/mnras/stu125. [105](#)
- Andrei Mesinger, Bradley Greig, and Emanuele Sobacchi. The Evolution Of 21 cm Structure (EOS): public, large-scale simulations of Cosmic Dawn and reionization. *MNRAS*, 459:2342–2353, Jul 2016. doi: 10.1093/mnras/stw831. [23](#), [94](#), [96](#)
- J. Miralda-Escude. On the He II Gunn-Peterson effect and the He II forest. *MNRAS*, 262:273–276, May 1993. doi: 10.1093/mnras/262.1.273. [14](#)
- J. Miralda-Escudé, M. Haehnelt, and M. J. Rees. Reionization of the Inhomogeneous Universe. *ApJ*, 530:1–16, February 2000. doi: 10.1086/308330. [10](#)
- Jordan Mirocha and Steven R. Furlanetto. What does the first highly redshifted 21-cm detection tell us about early galaxies? *MNRAS*, 483(2):1980–1992, Feb 2019. doi: 10.1093/mnras/sty3260. [97](#)

- Jordan Mirocha, Geraint J. A. Harker, and Jack O. Burns. Interpreting the Global 21-cm Signal from High Redshifts. II. Parameter Estimation for Models of Galaxy Formation. *ApJ*, 813(1):11, Nov 2015. doi: 10.1088/0004-637X/813/1/11. [43](#), [89](#)
- Jordan Mirocha, Richard H. Mebane, Steven R. Furlanetto, Krishma Singal, and Donald Trinh. Unique signatures of Population III stars in the global 21-cm signal. *MNRAS*, 478(4):5591–5606, Aug 2018. doi: 10.1093/mnras/sty1388. [43](#), [89](#)
- R. A. Monsalve, A. E. E. Rogers, J. D. Bowman, and T. J. Mozdzen. Results from EDGES High-band. I. Constraints on Phenomenological Models for the Global 21 cm Signal. *ApJ*, 847:64, September 2017. doi: 10.3847/1538-4357/aa88d1. [105](#)
- M. F. Morales and J. S. B. Wyithe. Reionization and Cosmology with 21-cm Fluctuations. *ARA&A*, 48: 127–171, September 2010. doi: 10.1146/annurev-astro-081309-130936. [9](#), [103](#)
- S. Morrison, M. M. Pieri, D. Syphers, and T.-S. Kim. Probing Inhomogeneity in the Helium Ionizing UV Background. *arXiv e-prints*, March 2019. [13](#), [14](#)
- J. B. Muñoz and A. Loeb. A small amount of mini-charged dark matter could cool the baryons in the early Universe. *Nature*, 557:684–686, May 2018. doi: 10.1038/s41586-018-0151-x. [39](#), [97](#), [105](#)
- J. B. Muñoz, C. Dvorkin, and A. Loeb. 21-cm Fluctuations from Charged Dark Matter. *Physical Review Letters*, 121(12):121301, September 2018. doi: 10.1103/PhysRevLett.121.121301. [98](#)
- A. Natarajan and N. Yoshida. The Dark Ages of the Universe and hydrogen reionization. *Progress of Theoretical and Experimental Physics*, 2014(6):06B112, June 2014. doi: 10.1093/ptep/ptu067. [9](#), [103](#)
- P. A. Oesch, R. J. Bouwens, G. D. Illingworth, I. Labbé, M. Franx, P. G. van Dokkum, M. Trenti, M. Stiavelli, V. Gonzalez, and D. Magee. Probing the Dawn of Galaxies at $z \sim 9$ -12: New Constraints from HUDF12/XDF and CANDELS data. *ApJ*, 773:75, August 2013. doi: 10.1088/0004-637X/773/1/75. [17](#)
- P. A. Oesch, G. Brammer, P. G. van Dokkum, G. D. Illingworth, R. J. Bouwens, I. Labbé, M. Franx, I. Momcheva, M. L. N. Ashby, G. G. Fazio, V. Gonzalez, B. Holden, D. Magee, R. E. Skelton, R. Smit, L. R. Spitler, M. Trenti, and S. P. Willner. A Remarkably Luminous Galaxy at $z=11.1$ Measured with Hubble Space Telescope Grism Spectroscopy. *ApJ*, 819(2):129, Mar 2016. doi: 10.3847/0004-637X/819/2/129. [17](#)
- D. E. Osterbrock. *Astrophysics of Gaseous Nebulae and Active Galactic Nuclei*. 1989. [27](#)
- G. Paciga, J. G. Albert, K. Bandura, T.-C. Chang, Y. Gupta, C. Hirata, J. Odegova, U.-L. Pen, J. B. Peterson, J. Roy, J. R. Shaw, K. Sigurdson, and T. Voytek. A simulation-calibrated limit on the H I power spectrum from the GMRT Epoch of Reionization experiment. *MNRAS*, 433:639–647, July 2013. doi: 10.1093/mnras/stt753. [105](#)
- F. Pacucci, A. Mesinger, S. Mineo, and A. Ferrara. The X-ray spectra of the first galaxies: 21 cm signatures. *MNRAS*, 443:678–686, September 2014. doi: 10.1093/mnras/stu1240. [23](#), [89](#)

- T. Padmanabhan. *Structure Formation in the Universe*. May 1993. [7](#)
- A. R. Parsons, J. C. Pober, J. E. Aguirre, C. L. Carilli, D. C. Jacobs, and D. F. Moore. A Per-baseline, Delay-spectrum Technique for Accessing the 21 cm Cosmic Reionization Signature. *ApJ*, 756:165, September 2012. doi: 10.1088/0004-637X/756/2/165. [104](#)
- A. H. Patil, S. Yatawatta, L. V. E. Koopmans, A. G. de Bruyn, M. A. Brentjens, S. Zaroubi, K. M. B. Asad, M. Hatef, V. Jelić, M. Mevius, A. R. Offringa, V. N. Pandey, H. Vedantham, F. B. Abdalla, W. N. Brouw, E. Chapman, B. Ciardi, B. K. Gehlot, A. Ghosh, G. Harker, I. T. Iliev, K. Kakiichi, S. Majumdar, G. Mellema, M. B. Silva, J. Schaye, D. Vrbanec, and S. J. Wijnholds. Upper Limits on the 21 cm Epoch of Reionization Power Spectrum from One Night with LOFAR. *ApJ*, 838:65, March 2017. doi: 10.3847/1538-4357/aa63e7. [105](#), [106](#)
- S. Paul, S. K. Sethi, M. F. Morales, K. S. Dwarkanath, N. Udaya Shankar, R. Subrahmanyam, N. Barry, A. P. Beardsley, J. D. Bowman, F. Briggs, P. Carroll, A. de Oliveira-Costa, J. S. Dillon, A. Ewall-Wice, L. Feng, L. J. Greenhill, B. M. Gaensler, B. J. Hazelton, J. N. Hewitt, N. Hurley-Walker, D. J. Jacobs, H.-S. Kim, P. Kittiwisit, E. Lenc, J. Line, A. Loeb, B. McKinley, D. A. Mitchell, A. R. Neben, A. R. Offringa, B. Pindor, J. C. Pober, P. Procopio, J. Riding, I. S. Sullivan, M. Tegmark, N. Thyagarajan, S. J. Tingay, C. M. Trott, R. B. Wayth, R. L. Webster, J. S. B. Wyithe, R. Cappallo, M. Johnston-Hollitt, D. L. Kaplan, C. J. Lonsdale, S. R. McWhirter, E. Morgan, D. Oberoi, S. M. Ord, T. Prabu, K. S. Srivani, A. Williams, and C. L. Williams. Delay Spectrum with Phase-tracking Arrays: Extracting the HI Power Spectrum from the Epoch of Reionization. *ApJ*, 833:213, December 2016. doi: 10.3847/1538-4357/833/2/213. [104](#)
- P. J. E. Peebles. *The large-scale structure of the universe*. 1980. [7](#)
- P. J. E. Peebles. *Principles of Physical Cosmology*. 1993. [3](#), [5](#)
- A. A. Penzias and R. W. Wilson. A Measurement of Excess Antenna Temperature at 4080 Mc/s. *ApJ*, 142: 419–421, July 1965. doi: 10.1086/148307. [1](#)
- Planck Collaboration, P. A. R. Ade, N. Aghanim, C. Armitage-Caplan, M. Arnaud, M. Ashdown, F. Atrio-Barandela, J. Aumont, C. Baccigalupi, A. J. Banday, and et al. Planck 2013 results. XVI. Cosmological parameters. *A&A*, 571:A16, November 2014. doi: 10.1051/0004-6361/201321591. [16](#)
- Planck Collaboration, R. Adam, N. Aghanim, M. Ashdown, J. Aumont, C. Baccigalupi, M. Ballardini, A. J. Banday, R. B. Barreiro, N. Bartolo, S. Basak, R. Battye, K. Benabed, J.-P. Bernard, M. Bersanelli, P. Bielewicz, J. J. Bock, A. Bonaldi, L. Bonavera, J. R. Bond, J. Borrill, F. R. Bouchet, F. Boulanger, M. Bucher, C. Burigana, E. Calabrese, J.-F. Cardoso, J. Carron, H. C. Chiang, L. P. L. Colombo, C. Combet, B. Comis, F. Couchot, A. Coulais, B. P. Crill, A. Curto, F. Cuttaia, R. J. Davis, P. de Bernardis, A. de Rosa, G. de Zotti, J. Delabrouille, E. Di Valentino, C. Dickinson, J. M. Diego, O. Doré, M. Douspis, A. Ducout, X. Dupac, F. Elsner, T. A. Enßlin, H. K. Eriksen, E. Falgarone, Y. Fantaye, F. Finelli, F. Forastieri, M. Frailis, A. A. Fraisse, E. Franceschi, A. Frolov, S. Galeotta, S. Galli, K. Ganga, R. T. Génova-Santos, M. Gerbino, T. Ghosh, J. González-Nuevo, K. M. Górski, A. Gruppuso, J. E. Gudmundsson, F. K. Hansen, G. Helou, S. Henrot-Versillé, D. Herranz, E. Hivon, Z. Huang, S. Ilić, A. H.

- Jaffe, W. C. Jones, E. Keihänen, R. Keskitalo, T. S. Kisner, L. Knox, N. Krachmalnicoff, M. Kunz, H. Kurki-Suonio, G. Lagache, A. Lähteenmäki, J.-M. Lamarre, M. Langer, A. Lasenby, M. Lattanzi, C. R. Lawrence, M. Le Jeune, F. Levrier, A. Lewis, M. Liguori, P. B. Lilje, M. López-Caniego, Y.-Z. Ma, J. F. Macías-Pérez, G. Maggio, A. Mangilli, M. Maris, P. G. Martin, E. Martínez-González, S. Matarrese, N. Mauri, J. D. McEwen, P. R. Meinhold, A. Melchiorri, A. Mennella, M. Migliaccio, M.-A. Miville-Deschênes, D. Molinari, A. Moneti, L. Montier, G. Morgante, A. Moss, P. Naselsky, P. Natoli, C. A. Oxborrow, L. Pagano, D. Paoletti, B. Partridge, G. Patanchon, L. Patrizii, O. Perdereau, L. Perotto, V. Pettorino, F. Piacentini, S. Plaszczynski, L. Polastri, G. Polenta, J.-L. Puget, J. P. Rachen, B. Racine, M. Reinecke, M. Remazeilles, A. Renzi, G. Rocha, M. Rossetti, G. Roudier, J. A. Rubiño-Martín, B. Ruiz-Granados, L. Salvati, M. Sandri, M. Savelainen, D. Scott, G. Sirri, R. Sunyaev, A.-S. Suur-Uski, J. A. Tauber, M. Tenti, L. Toffolatti, M. Tomasi, M. Tristram, T. Trombetti, J. Valiviita, F. Van Tent, P. Vielva, F. Villa, N. Vittorio, B. D. Wandelt, I. K. Wehus, M. White, A. Zacchei, and A. Zonca. Planck intermediate results. XLVII. Planck constraints on reionization history. *A&A*, 596:A108, December 2016a. doi: 10.1051/0004-6361/201628897. 16, 88
- Planck Collaboration, P. A. R. Ade, N. Aghanim, M. Arnaud, M. Ashdown, J. Aumont, C. Baccigalupi, A. J. Banday, R. B. Barreiro, J. G. Bartlett, and et al. Planck 2015 results. XIII. Cosmological parameters. *A&A*, 594:A13, September 2016b. doi: 10.1051/0004-6361/201525830. 16, 24
- Planck Collaboration, N. Aghanim, Y. Akrami, M. Ashdown, J. Aumont, C. Baccigalupi, M. Ballardini, A. J. Banday, R. B. Barreiro, N. Bartolo, S. Basak, R. Battye, K. Benabed, J.-P. Bernard, M. Bersanelli, P. Bielewicz, J. J. Bock, J. R. Bond, J. Borrill, F. R. Bouchet, F. Boulanger, M. Bucher, C. Burigana, R. C. Butler, E. Calabrese, J.-F. Cardoso, J. Carron, A. Challinor, H. C. Chiang, J. Chluba, L. P. L. Colombo, C. Combet, D. Contreras, B. P. Crill, F. Cuttaia, P. de Bernardis, G. de Zotti, J. Delabrouille, J.-M. Delouis, E. Di Valentino, J. M. Diego, O. Doré, M. Douspis, A. Ducout, X. Dupac, S. Dusini, G. Efstathiou, F. Elsner, T. A. Enßlin, H. K. Eriksen, Y. Fantaye, M. Farhang, J. Fergusson, R. Fernandez-Cobos, F. Finelli, F. Forastieri, M. Frailis, E. Franceschi, A. Frolov, S. Galeotta, S. Galli, K. Ganga, R. T. Génova-Santos, M. Gerbino, T. Ghosh, J. González-Nuevo, K. M. Górski, S. Gratton, A. Gruppuso, J. E. Gudmundsson, J. Hamann, W. Handley, D. Herranz, E. Hivon, Z. Huang, A. H. Jaffe, W. C. Jones, A. Karakci, E. Keihänen, R. Keskitalo, K. Kiiveri, J. Kim, T. S. Kisner, L. Knox, N. Krachmalnicoff, M. Kunz, H. Kurki-Suonio, G. Lagache, J.-M. Lamarre, A. Lasenby, M. Lattanzi, C. R. Lawrence, M. Le Jeune, P. Lemos, J. Lesgourgues, F. Levrier, A. Lewis, M. Liguori, P. B. Lilje, M. Lilley, V. Lindholm, M. López-Caniego, P. M. Lubin, Y.-Z. Ma, J. F. Macías-Pérez, G. Maggio, D. Maino, N. Mandolesi, A. Mangilli, A. Marcos-Caballero, M. Maris, P. G. Martin, M. Martinelli, E. Martínez-González, S. Matarrese, N. Mauri, J. D. McEwen, P. R. Meinhold, A. Melchiorri, A. Mennella, M. Migliaccio, M. Millea, S. Mitra, M.-A. Miville-Deschênes, D. Molinari, L. Montier, G. Morgante, A. Moss, P. Natoli, H. U. Nørgaard-Nielsen, L. Pagano, D. Paoletti, B. Partridge, G. Patanchon, H. V. Peiris, F. Perrotta, V. Pettorino, F. Piacentini, L. Polastri, G. Polenta, J.-L. Puget, J. P. Rachen, M. Reinecke, M. Remazeilles, A. Renzi, G. Rocha, C. Rosset, G. Roudier, J. A. Rubiño-Martín, B. Ruiz-Granados, L. Salvati, M. Sandri, M. Savelainen, D. Scott, E. P. S. Shellard, C. Sirignano, G. Sirri, L. D. Spencer, R. Sunyaev, A.-S. Suur-Uski, J. A. Tauber, D. Tavagnacco, M. Tenti, L. Toffolatti, M. Tomasi, T. Trombetti, L. Valenziano, J. Valiviita, B. Van Tent, L. Vibert, P. Vielva, F. Villa, N. Vittorio, B. D. Wandelt, I. K. Wehus, M. White,

- S. D. M. White, A. Zacchei, and A. Zonca. Planck 2018 results. VI. Cosmological parameters. *ArXiv e-prints*, July 2018. [1](#), [3](#), [16](#), [24](#), [88](#), [110](#)
- M. E. Presley, A. Liu, and A. R. Parsons. Measuring the Cosmological 21 cm Monopole with an Interferometer. *ApJ*, 809:18, August 2015. doi: 10.1088/0004-637X/809/1/18. [105](#)
- W. H. Press and P. Schechter. Formation of Galaxies and Clusters of Galaxies by Self-Similar Gravitational Condensation. *ApJ*, 187:425–438, February 1974. doi: 10.1086/152650. [11](#)
- D. C. Price, L. J. Greenhill, A. Fialkov, G. Bernardi, H. Garsden, B. R. Barsdell, J. Kocz, M. M. Anderson, S. A. Bourke, J. Craig, M. R. Dexter, J. Dowell, M. W. Eastwood, T. Eftekhari, S. W. Ellingson, G. Hallinan, J. M. Hartman, R. Kimberk, T. J. W. Lazio, S. Leiker, D. MacMahon, R. Monroe, F. Schinzel, G. B. Taylor, E. Tong, D. Werthimer, and D. P. Woody. Design and characterization of the Large-aperture Experiment to Detect the Dark Age (LEDA) radiometer systems. *MNRAS*, 478:4193–4213, August 2018. doi: 10.1093/mnras/sty1244. [104](#)
- J. R. Pritchard and S. R. Furlanetto. Descending from on high: Lyman-series cascades and spin-kinetic temperature coupling in the 21-cm line. *MNRAS*, 367:1057–1066, April 2006. doi: 10.1111/j.1365-2966.2006.10028.x. [40](#)
- J. R. Pritchard and S. R. Furlanetto. 21-cm fluctuations from inhomogeneous X-ray heating before reionization. *MNRAS*, 376:1680–1694, April 2007. doi: 10.1111/j.1365-2966.2007.11519.x. [23](#), [45](#), [94](#), [103](#)
- J. R. Pritchard and A. Loeb. 21 cm cosmology in the 21st century. *Reports on Progress in Physics*, 75(8): 086901, August 2012. doi: 10.1088/0034-4885/75/8/086901. [9](#), [17](#), [20](#), [44](#), [46](#), [48](#), [49](#), [100](#), [103](#), [105](#)
- J. Raste and S. Sethi. An Analytic Formulation of the 21 cm Signal from the Early Phase of the Epoch of Reionization. *ApJ*, 860:55, June 2018. doi: 10.3847/1538-4357/aac2d8. [33](#), [37](#), [58](#)
- J. Raste and S. Sethi. Analytic formulation of 21 cm signal from cosmic dawn: Ly α fluctuations. *ApJ*, 876: 56, May 2019. doi: 10.3847/1538-4357/ab13a6. [33](#), [58](#)
- M. J. Rees. Polarization and Spectrum of the Primeval Radiation in an Anisotropic Universe. *ApJ*, 153:L1, July 1968. doi: 10.1086/180208. [16](#)
- H. E. Ross, K. L. Dixon, I. T. Iliev, and G. Mellema. Simulating the impact of X-ray heating during the cosmic dawn. *MNRAS*, 468:3785–3797, July 2017. doi: 10.1093/mnras/stx649. [23](#)
- G. B. Rybicki and I. P. dell’Antonio. The time development of a resonance line in the expanding universe. *ApJ*, 427:603–617, June 1994. doi: 10.1086/174170. [18](#)
- G. B. Rybicki and A. P. Lightman. *Radiative processes in astrophysics*. 1979. [20](#), [21](#), [113](#)
- A. D. Sakharov. Violation of CP Invariance, C Asymmetry, and Baryon Asymmetry of the Universe. *Soviet Journal of Experimental and Theoretical Physics Letters*, 5:24, January 1967. [2](#)

- M. G. Santos, A. Amblard, J. Pritchard, H. Trac, R. Cen, and A. Cooray. Cosmic Reionization and the 21 cm Signal: Comparison between an Analytical Model and a Simulation. *ApJ*, 689:1-16, December 2008. doi: 10.1086/592487. [23](#), [94](#)
- M. G. Santos, L. Ferramacho, M. B. Silva, A. Amblard, and A. Cooray. Fast large volume simulations of the 21-cm signal from the reionization and pre-reionization epochs. *MNRAS*, 406:2421–2432, August 2010. doi: 10.1111/j.1365-2966.2010.16898.x. [23](#)
- A. Sarkar, R. Mondal, S. Das, S. K. Sethi, S. Bharadwaj, and D. J. E. Marsh. The effects of the small-scale DM power on the cosmological neutral hydrogen (HI) distribution at high redshifts. *J. Cosmology Astropart. Phys.*, 4:012, April 2016. doi: 10.1088/1475-7516/2016/04/012. [99](#)
- M. Sathyanarayana Rao, R. Subrahmanyam, N. Udaya Shankar, and J. Chluba. Modeling the Radio Foreground for Detection of CMB Spectral Distortions from the Cosmic Dawn and the Epoch of Reionization. *ApJ*, 840:33, May 2017. doi: 10.3847/1538-4357/aa69bd. [103](#)
- D. Schaerer. On the properties of massive Population III stars and metal-free stellar populations. *A&A*, 382:28–42, Jan 2002. doi: 10.1051/0004-6361:20011619. [43](#)
- P. A. G. Scheuer. A Sensitive Test for the Presence of Atomic Hydrogen in Intergalactic Space. *Nature*, 207:963, August 1965. doi: 10.1038/207963a0. [14](#)
- U. Seljak and M. Zaldarriaga. A Line-of-Sight Integration Approach to Cosmic Microwave Background Anisotropies. *ApJ*, 469:437, October 1996. doi: 10.1086/177793. [xvii](#), [5](#), [24](#)
- S. Sethi and Z. Haiman. Can We Detect the Anisotropic Shapes of Quasar H II Regions during Reionization through the Small-Scale Redshifted 21 cm Power Spectrum? *ApJ*, 673:1-13, January 2008. doi: 10.1086/523787. [106](#)
- S. K. Sethi. HI signal from re-ionization epoch. *MNRAS*, 363:818–830, November 2005. doi: 10.1111/j.1365-2966.2005.09485.x. [9](#), [10](#), [22](#)
- S. K. Sethi and K. Subramanian. Primordial magnetic fields and the HI signal from the epoch of reionization. *J. Cosmology Astropart. Phys.*, 11:021, November 2009. doi: 10.1088/1475-7516/2009/11/021. [99](#)
- P. R. Shapiro and M. L. Giroux. Cosmological H II regions and the photoionization of the intergalactic medium. *ApJ*, 321:L107–L112, October 1987. doi: 10.1086/185015. [10](#)
- P. R. Shapiro, M. L. Giroux, and A. Babul. Reionization in a cold dark matter universe: The feedback of galaxy formation on the intergalactic medium. *ApJ*, 427:25–50, May 1994. doi: 10.1086/174120. [14](#)
- P. Sharma. Astrophysical radio background cannot explain the EDGES 21-cm signal: constraints from cooling of non-thermal electrons. *MNRAS*, 481:L6–L10, November 2018. doi: 10.1093/mnrasl/sly147. [98](#), [105](#)

- P. A. Shaver, R. A. Windhorst, P. Madau, and A. G. de Bruyn. Can the reionization epoch be detected as a global signature in the cosmic background? *A&A*, 345:380–390, May 1999. [22](#)
- R. K. Sheth. An excursion set model for the distribution of dark matter and dark matter haloes. *MNRAS*, 300:1057–1070, November 1998. doi: 10.1046/j.1365-8711.1998.01976.x. [12](#)
- R. K. Sheth and G. Tormen. Large-scale bias and the peak background split. *MNRAS*, 308:119–126, September 1999. doi: 10.1046/j.1365-8711.1999.02692.x. [12](#)
- R. K. Sheth, H. J. Mo, and G. Tormen. Ellipsoidal collapse and an improved model for the number and spatial distribution of dark matter haloes. *MNRAS*, 323:1–12, May 2001. doi: 10.1046/j.1365-8711.2001.04006.x. [12](#)
- F. H. Shu. *The physics of astrophysics. Volume II: Gas dynamics*. 1992. [10](#)
- J. M. Shull and M. E. van Steenberg. X-ray secondary heating and ionization in quasar emission-line clouds. *ApJ*, 298:268–274, November 1985. doi: 10.1086/163605. [27](#), [45](#), [100](#)
- J. Silk. Cosmic Black-Body Radiation and Galaxy Formation. *ApJ*, 151:459, February 1968. doi: 10.1086/149449. [2](#)
- S. Singh and R. Subrahmanyan. The redshifted 21-cm signal in the EDGES low-band spectrum. *arXiv e-prints*, March 2019. [105](#)
- S. Singh, R. Subrahmanyan, N. Udaya Shankar, M. Sathyanarayana Rao, A. Fialkov, A. Cohen, R. Barkana, B. S. Girish, A. Raghunathan, R. Somashekar, and K. S. Srivani. First Results on the Epoch of Reionization from First Light with SARAS 2. *ApJ*, 845:L12, August 2017. doi: 10.3847/2041-8213/aa831b. [104](#)
- S. Singh, R. Subrahmanyan, N. Udaya Shankar, M. Sathyanarayana Rao, A. Fialkov, A. Cohen, R. Barkana, B. S. Girish, A. Raghunathan, R. Somashekar, and K. S. Srivani. SARAS 2 Constraints on Global 21 cm Signals from the Epoch of Reionization. *ApJ*, 858:54, May 2018. doi: 10.3847/1538-4357/aabae1. [104](#)
- Saurabh Singh, Ravi Subrahmanyan, N. Udaya Shankar, and A. Raghunathan. On the Detection of Global 21-cm Signal from Reionization Using Interferometers. *ApJ*, 815(2):88, Dec 2015. doi: 10.1088/0004-637X/815/2/88. [105](#)
- M. Sokolowski, S. E. Tremblay, R. B. Wayth, S. J. Tingay, N. Clarke, P. Roberts, M. Waterson, R. D. Ekers, P. Hall, M. Lewis, M. Mossammaparast, S. Padhi, F. Schlagenhauer, A. Sutinjo, and J. Tickner. BIG-HORNS - Broadband Instrument for Global Hydrogen Reionisation Signal. *PASA*, 32:e004, February 2015a. doi: 10.1017/pasa.2015.3. [104](#)
- M. Sokolowski, R. B. Wayth, S. E. Tremblay, S. J. Tingay, M. Waterson, J. Tickner, D. Emrich, F. Schlagenhauer, D. Kenney, and S. Padhi. The Impact of the Ionosphere on Ground-based Detection of the Global Epoch of Reionization Signal. *ApJ*, 813:18, November 2015b. doi: 10.1088/0004-637X/813/1/18. [104](#)

- D. N. Spergel, L. Verde, H. V. Peiris, E. Komatsu, M. R. Nolta, C. L. Bennett, M. Halpern, G. Hinshaw, N. Jarosik, A. Kogut, M. Limon, S. S. Meyer, L. Page, G. S. Tucker, J. L. Weiland, E. Wollack, and E. L. Wright. First-Year Wilkinson Microwave Anisotropy Probe (WMAP) Observations: Determination of Cosmological Parameters. *ApJS*, 148:175–194, September 2003. doi: 10.1086/377226. 16
- R. A. Sunyaev and Y. B. Zeldovich. The Observations of Relic Radiation as a Test of the Nature of X-Ray Radiation from the Clusters of Galaxies. *Comments on Astrophysics and Space Physics*, 4:173, November 1972. 16
- E. R. Switzer and C. M. Hirata. Primordial helium recombination. I. Feedback, line transfer, and continuum opacity. *Phys. Rev. D*, 77(8):083006, April 2008. doi: 10.1103/PhysRevD.77.083006. 3
- H. Tashiro and N. Sugiyama. The effect of primordial black holes on 21-cm fluctuations. *MNRAS*, 435:3001–3008, November 2013. doi: 10.1093/mnras/stt1493. 23, 93, 94
- T. Theuns, J. Schaye, S. Zaroubi, T.-S. Kim, P. Tzanavaris, and B. Carswell. Constraints on Reionization from the Thermal History of the Intergalactic Medium. *ApJ*, 567:L103–L106, March 2002. doi: 10.1086/339998. 17
- P. Tozzi, P. Madau, A. Meiksin, and M. J. Rees. The first light seen in the redshifted 21-cm radiation. *Nuclear Physics B Proceedings Supplements*, 80:05, January 2000. 103
- H. C. Van De Hulst. *Origin of the Radio Waves from Space*, pages 302–316. Springer Netherlands, Dordrecht, 1982. ISBN 978-94-009-7752-5. doi: 10.1007/978-94-009-7752-5_34. URL https://doi.org/10.1007/978-94-009-7752-5_34. 17
- E. O. Vasiliev, S. K. Sethi, and Y. A. Shchekinov. Observing the Influence of Growing Black Holes on the Pre-reionization IGM. *ApJ*, 865:130, October 2018. doi: 10.3847/1538-4357/aadd12. 17
- H. K. Vedantham, L. V. E. Koopmans, A. G. de Bruyn, S. J. Wijnholds, B. Ciardi, and M. A. Brentjens. Chromatic effects in the 21 cm global signal from the cosmic dawn. *MNRAS*, 437:1056–1069, January 2014. doi: 10.1093/mnras/stt1878. 104
- H. K. Vedantham, L. V. E. Koopmans, A. G. de Bruyn, S. J. Wijnholds, M. Brentjens, F. B. Abdalla, K. M. B. Asad, G. Bernardi, S. Bus, E. Chapman, B. Ciardi, S. Daiboo, E. R. Fernandez, A. Ghosh, G. Harker, V. Jelic, H. Jensen, S. Kazemi, P. Lambropoulos, O. Martinez-Rubi, G. Mellema, M. Mevius, A. R. Offringa, V. N. Pandey, A. H. Patil, R. M. Thomas, V. Veligatla, S. Yatawatta, S. Zaroubi, J. Anderson, A. Asgekar, M. E. Bell, M. J. Bentum, P. Best, A. Bonafede, F. Breitling, J. Broderick, M. Brüggen, H. R. Butcher, A. Corstanje, F. de Gasperin, E. de Geus, A. Deller, S. Duscha, J. Eislöffel, D. Engels, H. Falcke, R. A. Fallows, R. Fender, C. Ferrari, W. Frieswijk, M. A. Garrett, J. Gießmeier, A. W. Gunst, T. E. Hassall, G. Heald, M. Hoeft, J. Hörandel, M. Iacobelli, E. Jette, V. I. Kondratiev, M. Kuniyoshi, G. Kuper, G. Mann, S. Markoff, R. McFadden, D. McKay-Bukowski, J. P. McKean, D. D. Mulcahy, H. Munk, A. Nelles, M. J. Norden, E. Orru, M. Pandey-Pommier, R. Pizzo, A. G. Polatidis, W. Reich, A. Renting, H. Röttgering, D. Schwarz, A. Shulevski, O. Smirnov, B. W. Stappers, M. Steinmetz, J. Swinbank, M. Tagger, Y. Tang, C. Tasse, S. ter Veen, S. Thoudam, C. Toribio, C. Vocks, M. W.

- Wise, O. Wucknitz, and P. Zarka. Lunar occultation of the diffuse radio sky: LOFAR measurements between 35 and 80 MHz. *MNRAS*, 450:2291–2305, July 2015. doi: 10.1093/mnras/stv746. 105
- A. Venkatesan and A. Benson. X-rays and hard ultraviolet radiation from the first galaxies: ionization bubbles and 21-cm observations. *MNRAS*, 417:2264–2275, November 2011. doi: 10.1111/j.1365-2966.2011.19407.x. 34
- A. Venkatesan, M. L. Giroux, and J. M. Shull. Heating and Ionization of the Intergalactic Medium by an Early X-Ray Background. *ApJ*, 563:1–8, December 2001. doi: 10.1086/323691. 27, 43, 100
- E. Visbal, R. Barkana, A. Fialkov, D. Tseliakhovich, and C. M. Hirata. The signature of the first stars in atomic hydrogen at redshift 20. *Nature*, 487:70–73, July 2012. doi: 10.1038/nature11177. 23
- T. C. Voytek, A. Natarajan, J. M. Jáuregui García, J. B. Peterson, and O. López-Cruz. Probing the Dark Ages at $z \sim 20$: The SCI-HI 21 cm All-sky Spectrum Experiment. *ApJ*, 782:L9, February 2014. doi: 10.1088/2041-8205/782/1/L9. 104
- R. V. Wagoner. Big-Bang Nucleosynthesis Revisited. *ApJ*, 179:343–360, January 1973. doi: 10.1086/151873. 2
- Eric W. Weisstein. Sphere-Sphere Intersection, mathworld—a wolfram web resource. <http://mathworld.wolfram.com/Sphere-SphereIntersection.html>, 2007a. 114
- Eric W. Weisstein. Zone, mathworld—a wolfram web resource. <http://mathworld.wolfram.com/Zone.html>, 2007b. 114
- S. A. Wouthuysen. On the excitation mechanism of the 21-cm (radio-frequency) interstellar hydrogen emission line. *AJ*, 57:31–32, 1952. doi: 10.1086/106661. 18, 42, 101
- O. Zahn, A. Mesinger, M. McQuinn, H. Trac, R. Cen, and L. E. Hernquist. Comparison of reionization models: radiative transfer simulations and approximate, seminumeric models. *MNRAS*, 414:727–738, June 2011. doi: 10.1111/j.1365-2966.2011.18439.x. 96
- M. Zaldarriaga, S. R. Furlanetto, and L. Hernquist. 21 Centimeter Fluctuations from Cosmic Gas at High Redshifts. *ApJ*, 608:622–635, June 2004. doi: 10.1086/386327. 51, 54, 61, 74, 105
- B. Zygelman. Hyperfine Level-changing Collisions of Hydrogen Atoms and Tomography of the Dark Age Universe. *ApJ*, 622:1356–1362, April 2005. doi: 10.1086/427682. 49